Mitigation Techniques for Acoustic Noise and Vibration in Switched Reluctance Drives

Ruchao Pupadubsin

A thesis submitted for the degree of
Doctor of Philosophy

Electrical Power Group
Electrical and Electronic Engineering, School of Engineering

Abstract

Switched reluctance machines (SRM) have become an attractive rotating electrical machine in many applications because they have no permanent magnets, have robust structures and high fault tolerance. However, the crucial drawback of the SRM that limits the range of applications, is the acoustic noise and vibration often associated with this technology. The major source of vibration comes from the high deformation of the SRM stator stack, caused primarily by high radial magnetic forces. Vibration behaviour of different SRM topologies is analyzed by using finite element software to calculate the magnitude, mode shape and the resonant frequencies of the SRM. This includes determination of the generating magnetic force characteristic for each topology. To improve the accuracy of the vibration model of the SRM stator, which is built from laminated steel sheet, calculation of the mechanical material properties of the stator are developed for structural simulations. The simulation and testing results of the resonant frequency of the SRM are compared to determine the accuracy of the simulation model. There are two main strategies for reducing the vibration in an SRM. I) structural design and II) control technique. In this thesis, the structural design of six types of SRM segmented stator, each shrink-fitted into an aluminium housing, are investigated, both in terms of the structural stiffness and resonant frequency. The impact of varying temperature on the resonant frequency of the stator is tested to show the rate of change of the resonant frequency and damping ratio of the stator structure. Furthermore, the control technique of the SRM has also been shown to have a significant impact on the vibration produced in the SRM. Improvement of the control technique based on an active vibration cancellation (AVC) method is implemented under load conditions with different operating speeds of the SRM and compared with the conventional control method.

Acknowledgements

I would like to express my deepest gratitude to all those who have involved in this project.

Firstly, my supervisor team, Barrie Mecrow, James Widmer and Andrew Steven for their contribution time, guidance, and support throughout for me to develop to become a better researcher.

I wish to thank all the technicians within the electrical & electronic engineering group for their help in construction and testing of my prototypes and Adam Richardson from the mechanical engineering group for his help in the mechanical testing.

I gratefully acknowledge the Royal Thai government for giving me a scholarship that made my project work possible.

I would also like to thank all my friends in Newcastle upon Tyne who gave me a good relationship and funny moment and my colleagues from NECTEC for their help, support, and advice throughout.

Finally, my heartfelt thanks to my family for their faith in me. I am infinitely grateful to my parents for their love and support all my life.

ขอกราบขอบพระคุณ คุณยายกิมริ้น แซ่เลี้ยว ผู้ล่วงลับ คุณพ่อศรียง คุณแม่ห้วยลี่ ภู่ประดับศิลป์ และญาติพี่น้องทุกท่าน ที่ให้การสั่งสอนสนับสนุนและเป็นกำลังใจเสมอมา

Contents

List of Figures

List of Tables

Chapter 1. Introduction

Electrical machines are used in many applications, such as industrial manufacturing systems, transportation systems and household appliances. High torque, high power density and high efficiency characteristics are required in modern electrical machines [1], which are consequently designed with high magnetic flux densities to achieve high torque density. However, high magnetic flux density in the air gap causes high magnetic force production, acting on the stator poles and resulting in high vibration and acoustic noise.

1.1 Main Sources of Vibration and Acoustic Noise in Rotating Machine

There are various sources that cause acoustic noise in electrical machines. The main sources of noise in electrical machines [2] can be divided into four categories: I) Magnetic, II) Electronic control, III) Aerodynamic and IV) Mechanical. A classification of noise sources in electrical machines is shown in Fig. 1.1.

I) Magnetic Sources of Noise [3]: The magnetic force can be split up into the radial force, which affects the deformation of the stator outer diameter, and the tangential force, which deflects the stator pole, as magnetic flux passes across the air gap between rotor and stator poles. The radial force is considered to be the main cause of noise from magnetic sources. Resonance occurs when one of the radial force frequencies and one of the natural frequencies of the machine vibration modes are coincident, leading to high acoustic noise. The material properties, physical geometry and control method of the electrical machine also have an effect on magnetic

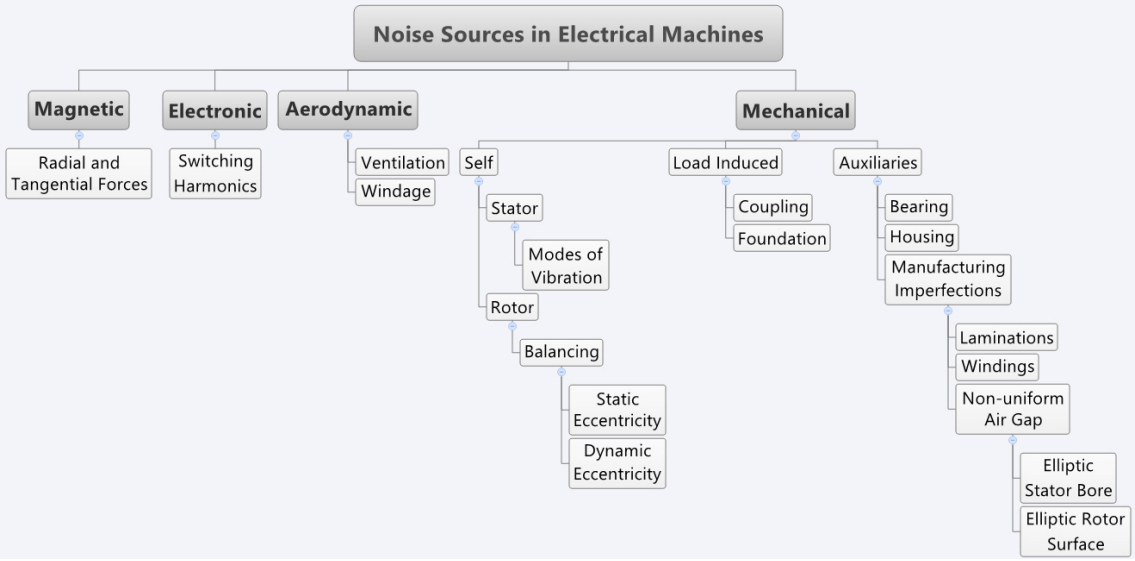

Figure 1.1: Groups of noise sources in electrical machines

force production.

II) Electronic Sources of Noise [4]: The harmonic frequencies of the phase current and voltage, excited by an inverter, are the main source of electronic noise. The electronic sources have a wide range of harmonic frequency components. In 3-phase induction machine variable speed drive, an odd order harmonic, for example, the 5^{th}, the 7^{th} and the 11^{th} must be considered when one of harmonic frequency components is close to the natural frequency of the machine. Higher order harmonics can be neglected as they are small enough not to cause significant acoustic noise.

III) Aerodynamic Sources of Noise [1, 2]: The interaction of moving parts, such as rotor and fan blades of ventilation systems with the air flow produces windage noise. This is one of the major sources of acoustic noise in electrical machines. Windage noise in the ventilation systems, which are used for heat removal from electrical machines, is caused by disturbance in the air flow and predominates when the speed of the machine increases. Salient machine types have high windage because salient rotor poles behave like blades. Therefore, a windage effect appears when the machine is turning the rotor poles.

IV) Mechanical Sources of Noise [1, 3]: Machine structures can generate a source of noise themselves. The stator structure is one of the main sources of noise, which exhibits itself via its natural frequencies of vibration modes. When the natural

frequency of the stator aligns with the excitation frequencies of the magnetic forces, resonance occurs and produces high acoustic noise. Therefore, it is important to know the stator natural frequency accurately in order to avoid resonance. However, it is difficult to avoid the coincidence of the two frequencies over a wide speed range drive, so resonance may occur. Rotor unbalance gives a rise in vibration through dynamic eccentricity of the rotor, which is not aligned to the centre of the stator. This dynamic eccentricity causes acoustic noise when the mass centre of the rotor is out of alignment with the centre of the stator. The load induced becomes a noise source when inadequately mounted, in a similar manner to the misalignment of the coupling of the machine with the load.

Auxiliary mechanical sources of noise occur as a result of various causes. Bearings can produce noise due to the coincidence of the natural frequency of the bearing and the natural frequency of the machine, or through misalignment of the machine with the load. Therefore, a good alignment of the machine with the load and the mismatch of two frequencies can reduce the noise generated by the bearings. Noise produced by the housing of electrical machines is caused by discrete contact points at the interconnection between the stator outer surface and the housing due to the manufacturing process. The manufacturing imperfections of electrical machines can lead to noise generation. For instance, magnetostrictive forces, caused by poorly made stator and rotor lamination stacks, and an improper mounting of the phase windings in the stator slots can allow the whole winding to move when phase windings are excited, generating additional noise. Furthermore, non-uniformity of the air gap, which results in non-uniform distribution of the radial force is caused by manufacturing imperfections, creating an elliptical stator bore and rotor surface. The non-uniform radial force distribution in the air gap leads to rotor vibration and acoustic noise.

1.2 Switched Reluctance Machine

The Switched Reluctance Machine (SRM) [5–8] is the electrical machine type which has perhaps the largest vibration and acoustic noise problem compared with other

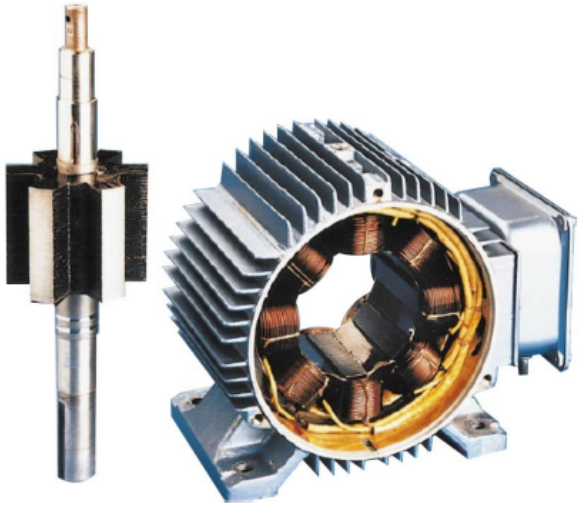

Figure 1.2: Switched reluctance machine structures

electrical machine types. The SRM is a double salient machine, having a simple and robust magnetic structure as shown in Fig. 1.2. It has only concentrated windings on the stator without any coil winding or permanent magnet on the rotor, resulting in cost saving in the manufacturing process. Other advantages of the SRM compared to the standard induction motor include high starting torque, high fault tolerance, high efficiency over wide speed range and broad choice of converters, depending on the application requirements; these make an SRM an attractive alternative to conventional drives in numerous applications. However, the major drawbacks of SRMs, which limit its range applications, are torque ripple and high acoustic noise emissions. While the torque ripple problem of an SRM has been solved successfully by a modified control algorithm [9, 10] and machine design techniques [11, 12], the techniques of acoustic noise reduction are still unsatisfactory, and acoustic noise become the main drawback of SRMs.

1.3 Aims and Objectives

This project focuses on analysis of the main sources of vibration and acoustic noise in the SRM, including the behaviour of the vibration and acoustic noise production mechanisms and develops the most effective and convenient techniques to eliminate

high vibration and acoustic noise. The objectives of this project are as follows:

1. Comparison of magnetic force and vibration and acoustic noise behaviour in different SRM topologies
2. The development of calculation techniques and mechanical material properties for structural simulation models of the SRM
3. The investigation of stator deformation between different segment joints of the segmental stator SRM
4. The design of a new control technique for vibration and acoustic noise reduction

1.4 Outline of Thesis

This thesis has four main parts. The first part is the investigation and comparison of the behaviour of magnetic force generation and how it relates to the vibration and acoustic noise emitted including the effect of machine geometry and winding arrangement in different SRM topologies. The second part presents a new technique for mechanical material property computation for use in structural simulation models for predicting the vibration data in an SRM. The third part is the investigation of the stator deformation which relates to the generation of vibration in an SRM. This reveals the stiffness calculation of the stator and comparison of the stiffness between different segment joint types of the segmental SRM stator, including resonant frequency. In the final part, a new control technique for vibration and acoustic noise reduction is proposed. This thesis consists of eight chapters, including this introductory chapter, a list of references and an appendix. Each chapter of the thesis is briefly described as follows:

Chapter 2 reviews the previous research about vibration sources and techniques to reduce the vibration and acoustic noise in SRMs. There are two main methods used. The first technique is a control technique, aiming to reduce the radial forces acting on the stator and to avoid coincidence between the harmonic component of radial magnetic forces and the stator resonant frequency. The second technique is the modification of SRM structures (stator and rotor) to improve the stiffness and

reduce deformation of the SRM stator. Furthermore, the initial study of the vibration and acoustic noise behaviours shows the effect of changing the SRM geometry, stator frame and control parameters including magnetostrictive effect which have a significant impact on the vibration and acoustic noise.

Chapter 3 investigates of the magnetic radial force and vibration and acoustic noise behaviour between different SRM topologies. In this chapter, four topologies of SRM are simulated using a multiphysics technique. The simulation results in each SRM topology are compared and discussed.

Chapter 4 presents the calculation technique for a mechanical property of the material for the structural simulation model of an SRM. This method can reduce the percentage of error of the resonant frequency prediction of the SRM. Finite element analysis software was used with the analytical method in this computation. Experimental modal testing was done to verify the simulation results of this technique.

Chapter 5 introduces the technique for vibration measurement in an SRM. This technique is a modal testing which is applied to find the resonant frequency of the mechanical structure. An accelerometer was mounted on the SRM stator to measure the vibration signal. The excitation force was applied to the SRM stator by mechanical excitation (impact hammer) or electromagnetic excitation (control unit). The vibration signal was captured and used to calculate the resonant frequency of the SRM stator and the damping ratio.

Chapter 6 discusses and investigates the stiffness and resonant frequency of different segment joint types of the segmented stator core, with an aluminium casing shrink fitted. Finite element analysis software is used in this analysis. The stator prototypes are built and tested to verify the simulation result. The testing is done both of stiffness and modal testing including the impact of temperature on the stator prototype.

Chapter 7 proposes a new control technique for vibration and acoustic noise reduction in an SRM. The proposed technique is a smooth voltage PWM technique based on the active vibration cancellation method. This proposed method utilizes

the PWM technique to reduce the rate change of voltage during the turn-off commutation angle. Both simulation and experimental testing are implemented to confirm the capability of this technique.

Chapter 8 gives conclusions from this research work and recommendation for future work that can be done to enhance and develop a new technique for mitigation of vibration and acoustic noise in an SRM.

1.5 Contributions to Knowledge

The contributions to knowledge in this thesis are as follows:

1. Presenting the radial magnetic force characteristic of different SRM topologies which generate different levels of vibration and acoustic noise (Chapter 3);
2. Development of computation techniques for mechanical material properties for a structural simulation model (Chapter 4 and 5);
3. Development of the SRM stator stiffness simulation and testing (Chapter 6);
4. Development of a control technique for mitigation of vibration and acoustic noise in an SRM (Chapter 7);

1.6 Published Works

The following publications have stemmed from this project:

1. R. Pupadubsin, J. D. Widmer, A. Steven and B. C. Mecrow, "Comparison of vibration and magnetic force behaviours between different switched reluctance machine topologies," *2015 IEEE International Electric Machines & Drives Conference (IEMDC)*, Coeur d'Alene, ID, 2015, pp. 1373-1379.
2. R. Pupadubsin, A. Steven, J. D. Widmer and B. C. Mecrow, "Mechanical material properties for structural simulation model of switched reluctance machines," *2016 XXII International Conference on Electrical Machines (ICEM)*, Lausanne, 2016, pp. 2293-2299.

A series of peer reviewed publications are currently being prepared for submission in 2018.

Chapter 2.
Literature Review and Initial Study

To increase the effectiveness of the techniques used to eliminate acoustic noise in the SRM, it is important to look back to the previous research that has been conducted in the area of acoustic noise and vibration in the SRM. The first known publication of a vibration and acoustic noise study for the SRM was done by Cameron et al. [13]. The experimental results on a 0.5-hp 8/6 SRM rated at 7000 r/min with 4-phase (stator outer diameter of 94 mm and stack length of 51 mm) showed that vibration of the stator is induced by the radial magnetic force when either the natural frequency or the large harmonic frequencies occur at the stator natural frequency. Vibration of the stator in turn results in significant acoustic noise in the SRM.

Cameron et al. proposed two methods of predicting the natural frequency and mode shapes of the stator vibration. Both methods use a procedure based on the Rayleigh-Ritz method, which is often applied to approximate the resonant frequency of multi degree of freedom systems in mechanical engineering and to predict the amplitude of the radial force using the linear stator model as a lumped mass-spring-damper system. However, the performance of these two natural frequency models is unsatisfactory. In Cameron et al.'s second published article about acoustic noise [14], using the same experimental tests in the previous article, two control techniques for acoustic noise reduction are presented. The first technique is a current shaping method which can control the acoustic noise level in the range of 86 to 92 dB by adjusting the turn-on and turn-off angles. Fixed turn-on and turn-off angles, in comparison, generated an acoustic noise level of 92 dB. However, this first technique affects motor efficiency. The other technique, which is more effective, uses random excitation phase angles which randomly select turn-on and turn-off angles by $\pm$ 1 mechanical degree. This second technique drops the acoustic noise level from 92 to

84 dB. However, it is only suitable when one of the excitation harmonic frequencies of the speed is near or coincident with the natural frequency of stator vibration, and it has no benefit at low speed.

2.1 Control Techniques for Vibration and Acoustic Noise Reduction

To study the main sources of vibration, two experimental tests to observe the sources of vibration were proposed by Wu and Pollock [10, 15]. Based on the results of these tests, it was concluded that the main sources of vibration come from the turn-off angle of the phase current. Three methods were demonstrated: I) a two-stage turn-off method, II) a voltage smoothing method, and III) a three-stage turn-off method to reduce vibration during the turn-off excitation. Regarding these methods, the turn-off period is performed by zero or negative voltage stage, resulting in vibration cancellation in each stage and hence low noise. Fig. 2.1(a), 2.1(b),

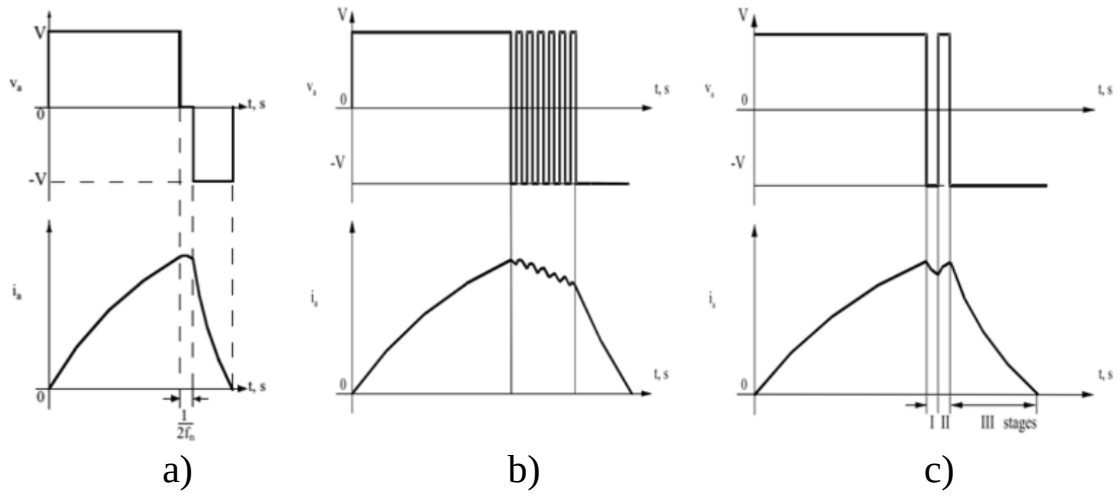

Figure 2.1: Vibration reduction methods by using Wu and Pollock's technique: (a) two-step turn-off, (b) voltage smoothing, and (c) three-stage turn-off [10, 15]

and 2.1(c) show the current and voltage waveform of an SRM by using two-stage turn-off, voltage smoothing and three-stage turn-off method, respectively. These active vibration cancellation methods effectively cancel the vibration in the current

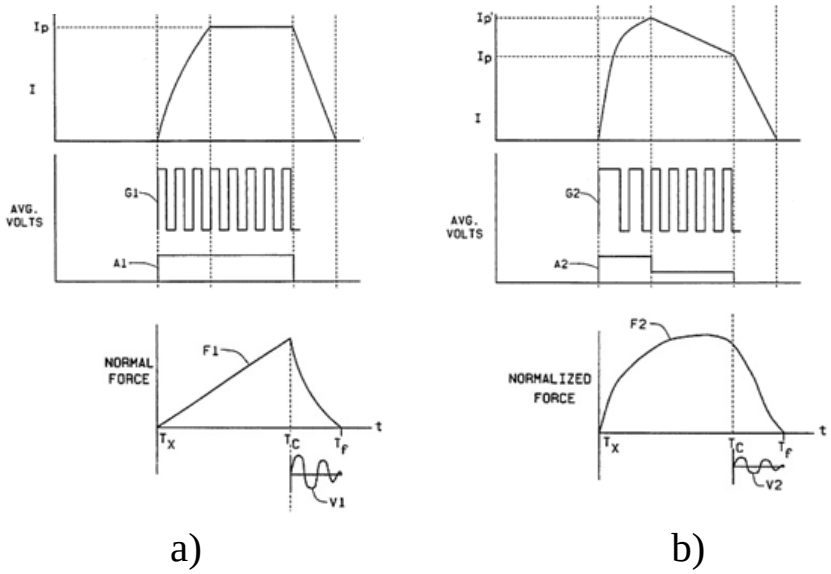

Figure 2.2: Current, voltage, and normal flux waveform of (a) conventional PWM current control and (b) proposed PWM current control [16]

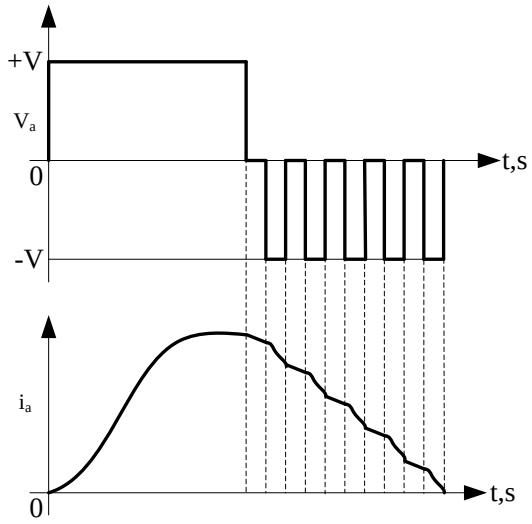

Figure 2.3: PWM current control by using Horst's technique [17]

chopping region at the operating speed up to the base speed of the motor, but they are weak at low speed [18]. Two patents [16, 17] were presented for active vibration cancellation techniques, using current pulse-width modulation (PWM) control. These techniques try to shape the quasi triangular radial forces, as shown in Fig. 2.2(a), to the sinusoidal radial forces, as shown in Fig. 2.2(b), by voltage chopping after the current reaches the high reference current. The result is that the

current decays linearly to low current value.

In [17], Horst used similar techniques to Wu and Pollock. However, whilst Wu and Pollock's second technique chops the current many times at the turn-off angle region with hard chopping (positive to negative voltage), the latter one chops the current with soft chopping (zero to negative voltage). As a result, the phase current slowly decays over the many steps of chopping, so this method is effective only for low speed operation. Control of current and voltage waveform by using Horst's technique is shown in Fig. 2.3.

The investigation of PWM strategies in [19] showed that the PWM strategies affect vibration and noise in SRMs. To study the PWM control method in SRMs further, this study used a three-phase full bridge inverter for sinusoidal bipolar excitation, and the windings of the SRM were connected in a star configuration, as shown in Fig. 2.4. The results demonstrated that sinusoidal bipolar excitation by space vector pulse-width modulation (SVPWM), as shown in Fig. 2.5(a), can reduce the vibration and acoustic noises compared with sinusoidal bipolar excitation by hysteresis current control (HCC), as shown in Fig. 2.5(b), and compared with conventional PWM unipolar excitation, as shown in Fig. 2.5(c). However, SVPWM is very sensitive to vibration and noise when the speed varies.

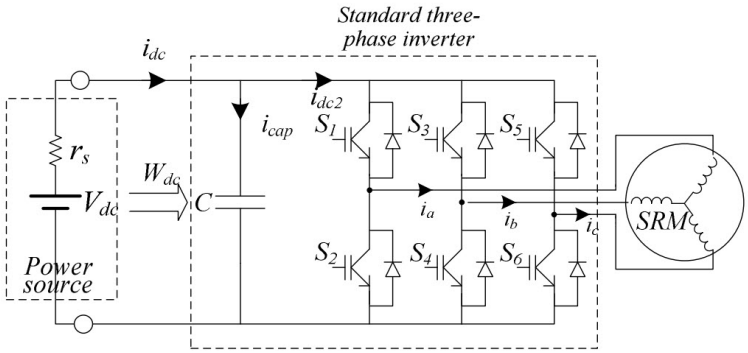

Figure 2.4: SRM drive with standard three-phase full bridge inverter [19]

Another active vibration cancellation technique has been presented in [20]. This technique requires auxiliary winding on the stator poles (Fig. 2.6(a)) and a modified converter to supply a source for these windings. Moreover, it requires installation of an accelerometer that can feed-back the vibration signal for control implementation

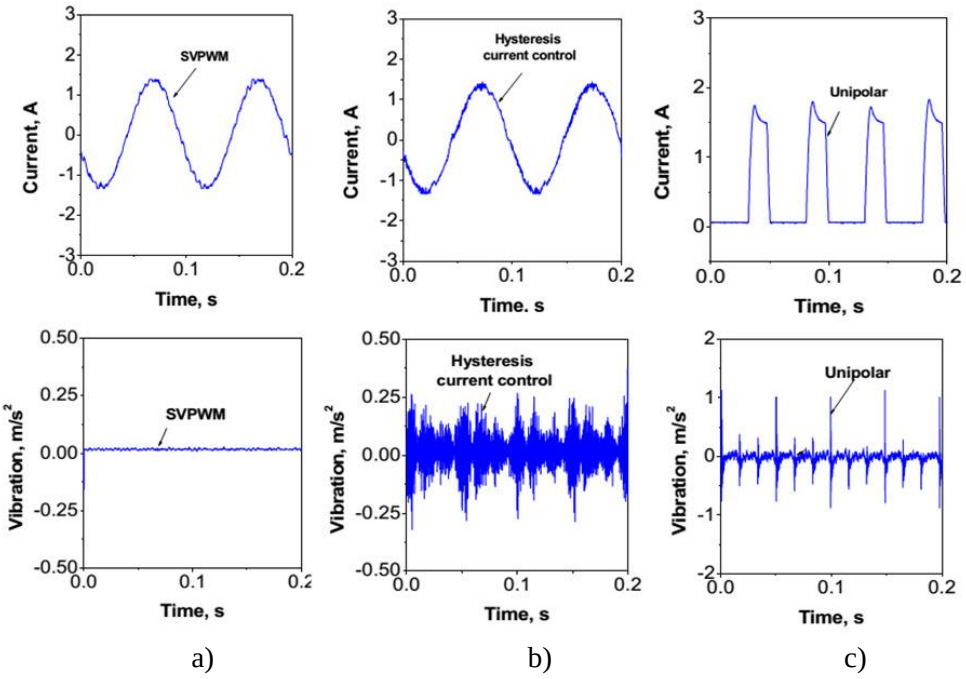

Figure 2.5: Current and vibration waveform: (a) SVPWM sinusoidal bipolar excitation with standard three-phase full bridge inverter, (b) HCC sinusoidal bipolar excitation with standard three-phase full bridge inverter, and (c) conventional PWM unipolar excitation with asymmetric bridge converter [19]

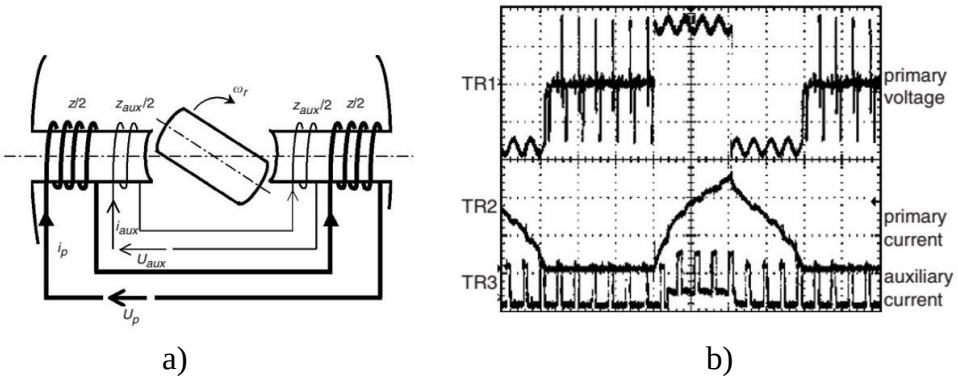

Figure 2.6: Active vibration cancellation technique using auxiliary winding: (a) principle and auxiliary winding and (b) voltage, current, and auxiliary current waveform [20]

by injecting a small pulse current into the auxiliary windings to generate a suppression force, as shown in Fig. 2.6(b). Furthermore, a modified converter topology for reducing noise in SRMs by varying the DC bus voltage has been presented in [21].

Several methods aim to control the radial force which is a main source of noise in SRMs. Hofmann et al. [22] presented a control technique to reduce acoustic noise by controlling the instantaneous force which is created by magnetic flux in the air gap of the machine. The block diagram of direct instantaneous force control (DIFC) is shown in Fig. 2.7.

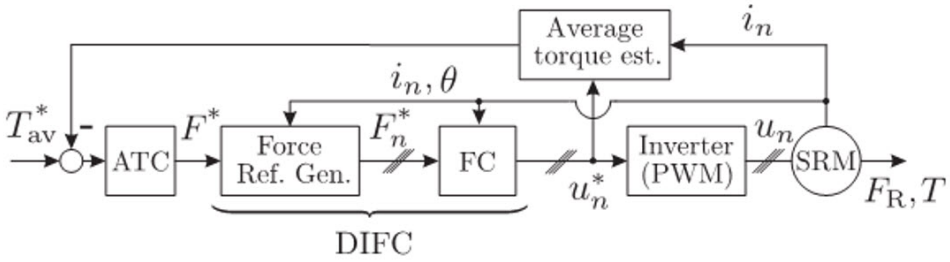

Figure 2.7: Control structure of DIFC [22]

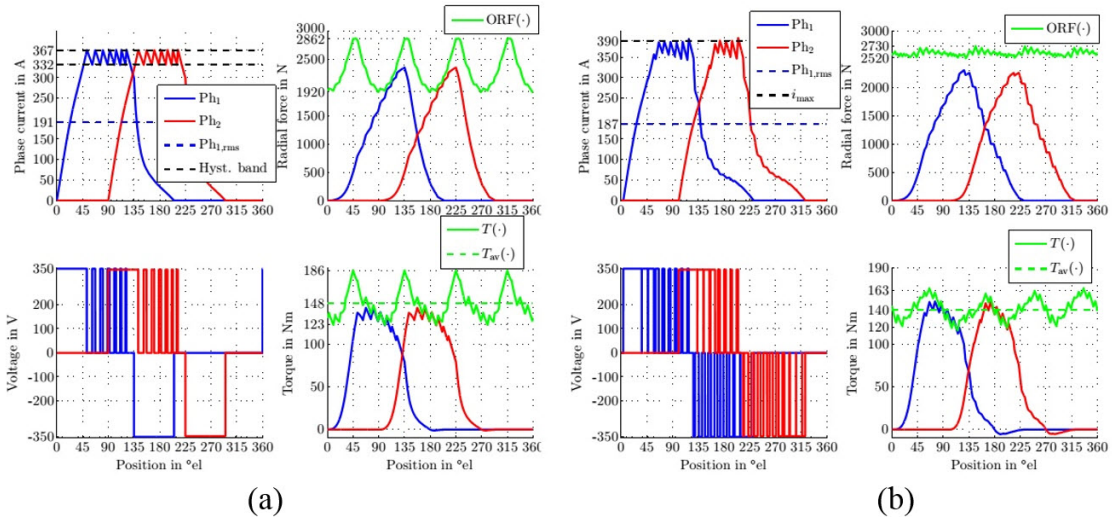

Figure 2.8: Current, radial force, voltage, and torque waveform: (a) conventional hysteresis current control and (b) direct instantaneous force control [22]

This technique controls the sum of the radial force and reduces the ripple of the radial force summation leading to reduced vibration and thereby decreasing acoustic noise in the SRM. However, this technique is only suitable for zeroth-order or uniform mode, as shown in Fig. 2.21(c), of the machine vibration modes. It is also effective only for a high number of SRM phases, and it has negative effects on torque ripple in a low number of SRM phases. The comparison between the results of

conventional control and direct force control are shown in Fig. 2.8. In addition, Lin et al. [23] proposed the technique to control radial force in a 12/8 pole SRM, as shown in Fig. 2.9(a), by exciting the ascending-inductance phase to produce the desired torque and exciting the descending-inductance phase to produce the radial force in order to control the radial force of the SRM, as shown in Fig. 2.9(b). Nevertheless, two disadvantages of this technique have been found: I) a high number of power switches is required, and II) it is lower in efficiency compared to conventional SRM drives.

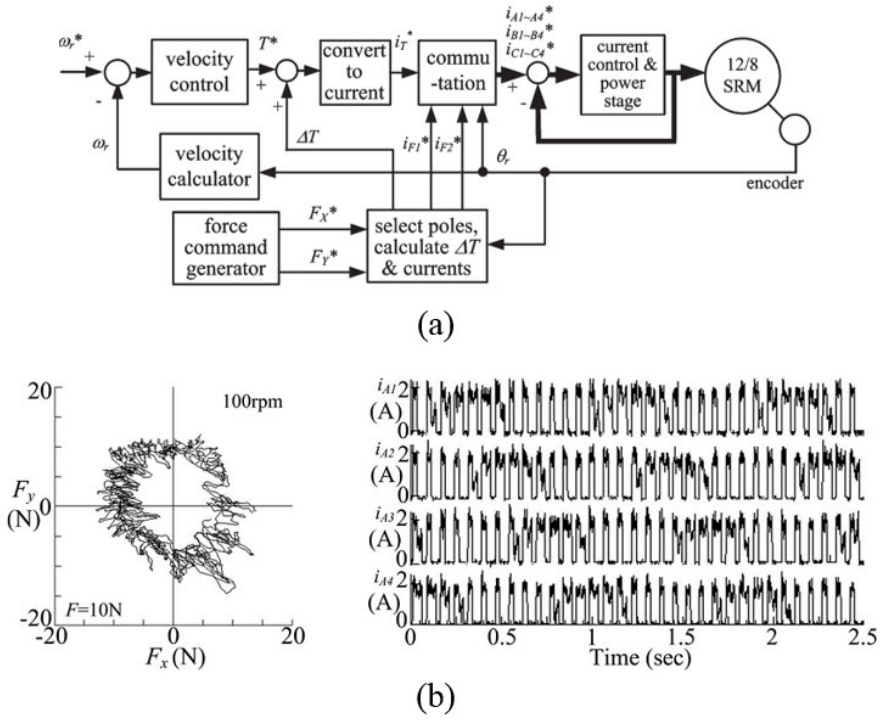

Figure 2.9: Radial force control by using Lin et al.'s technique: (a) block diagram of radial force control and (b) radial force vector and current waveform [23]

2.2 Structural Design Techniques for Vibration and Acoustic Noise Reduction

The structure of the SRM is one of the key factors in creating vibration and acoustic noise in an SRM, as the primary cause of vibration in an SRM is the radial magnetic attraction force between the stator and rotor. Modifying the shape of

SRM structures such as the stator/rotor pole and stator yoke, as well as adding special material in the stator/rotor slot, can have a significant impact on an SRM in terms of vibration and acoustic noise generation. Published articles about SRMs using structural machine design techniques to reduce vibration and acoustic noise have increased since the 1990s. Prior to that, articles were focused instead on the improvement of machine efficiency and on reducing the torque ripple.

2.2.1 Rotor Design

Although the deformation of the stator, which occurs due to radial magnetic forces, is the main cause of the vibration generation in the SRM, optimization of rotor shape design can also decrease the vibration. Making a hole in the rotor structure [24] can reduce the radial magnetic force acting on the stator pole because the main path of flux linkage is obstructed by the hole, deflecting the flow of flux linkage. Therefore, radial magnetic forces, which relate to flux linkage are decreased as shown in Fig. 2.10. Creating the hole in the rotor not only reduces the radial magnetic forces but also decreases the instantaneous torque.

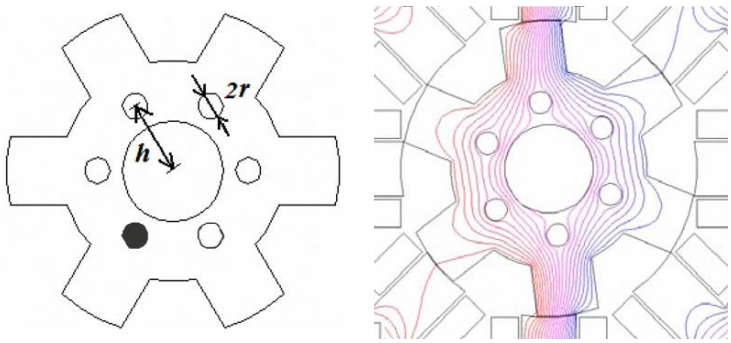

Figure 2.10: Creating a hole in the rotor yoke (left) and flux path on the rotor (right) [24]

Another technique defined in [25] for modifying rotor structure also uses the same concept of making a hole in the rotor. Instead of creating a hole in the rotor yoke, this technique makes a square hole in the rotor pole. Fig. 2.11 shows the square hole in the rotor pole. However, this technique has the same drawback as the previous method.

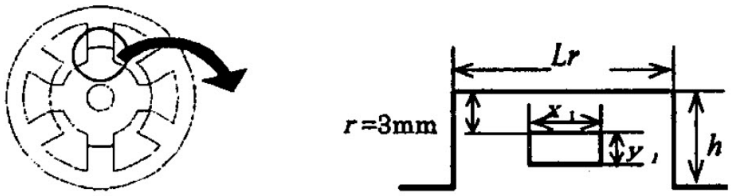

Figure 2.11: Square hole in the rotor pole [25]

Other variations of the rotor structural design method to reduce acoustic noise in SRMs when operating at high speed have been suggested. For instance, another technique proposes reducing aerodynamic sources of noise in the SRM by using a new structure of rotor that fills the rotor slot with non-magnetic materials [26]. The LG vacuum-cleaner is an existing commercial product for SRMs that applies this technique by filling the rotor with plastic materials, as shown in Fig. 2.12. The major disadvantage of this design is the heat removal on the rotor structure.

Figure 2.12: SRM rotor with filled rotor slot of LG vacuum-cleaner [26]

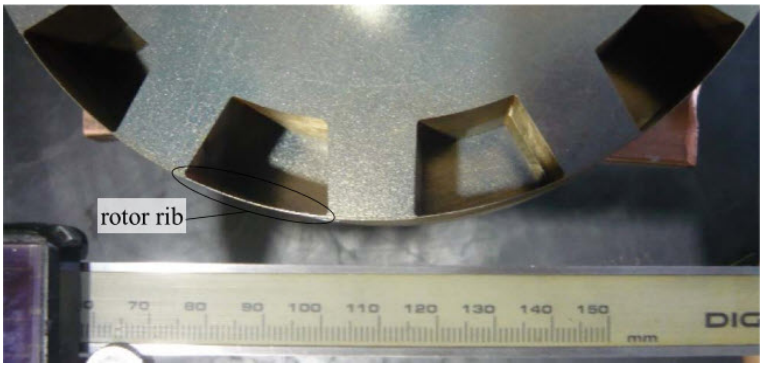

Figure 2.13: Modified rotor core by making thin ribs between salient poles [27]

To eliminate the heat problem, Kiyota [27] designed as new SRM rotor structure with thin ribs that cover the rotor slot as shown in Fig. 2.13. This rotor design has been implemented with an 18/12 SRM. At 7050 r/min of running speed, 11.4 dB

of acoustic noise is reduced compared with the conventional rotor. Windage loss is also decreased with this rotor design. However, the rotor rib may expand at high speed due to centrifugal forces. This is a mechanical restriction of this design.

2.2.2 Stator Design

The main source of vibration in the SRM is the stator core. There are many publications on how to design an SRM stator for vibration reduction. The SRM stator design has four main parameters: the fillet radius of the stator pole corner, the stator pole taper, the stator pole tip, and the stator yoke. In Fig. 2.14 [28], different stator pole and stator yoke shapes have been investigated, and the results reveal that the stator pole shape with a fillet radius and the tapering pole (trapezoidal shape) have better results in reducing displacement of the stator. For the stator yoke structure, the hexagon-round stator yoke shape gives a low deflection of the stator structure compared with other yoke designs. The best stator structures in terms of vibration reduction are shown in Fig. 2.14 inside the dashed line boxes.

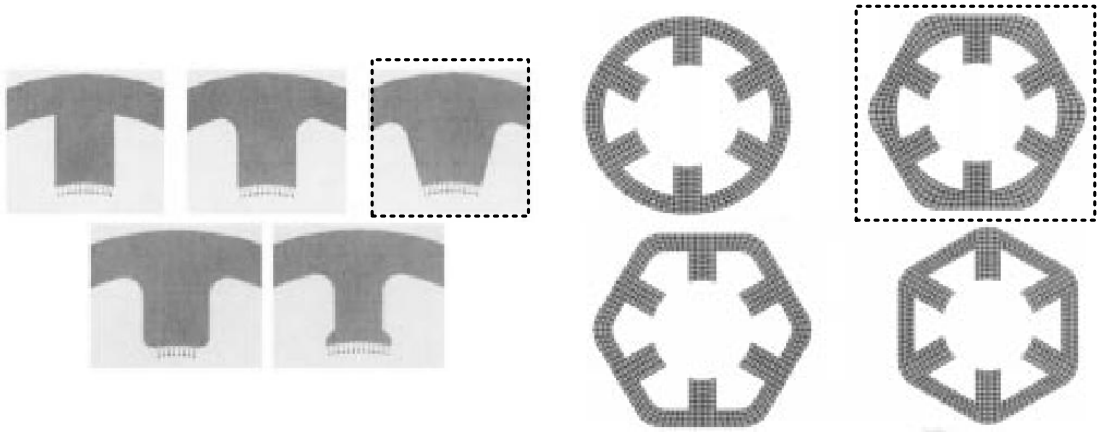

Figure 2.14: Different stator pole shapes (left) and stator yokes (right) [28]

Anwar and Husain [29] presented guidelines for acoustic noise reduction that identify the configuration, geometry and modified stator pole shape of the machines. It has been shown that increased thickness of the stator yoke is a simple approach to reduce noise. Increasing the stator yoke thickness shifts the stator natural frequency to higher frequencies and also improves the stiffness of the stator. However, this

method increases the weight and the thermal diffusion for heat removal of the SRM as well. Increasing the number of stator and rotor poles from 18/12 to 24/16 was also shown to decrease the amplitude of displacement by 21 % in [30] at load 30 Nm and running condition at 2768 r/min.

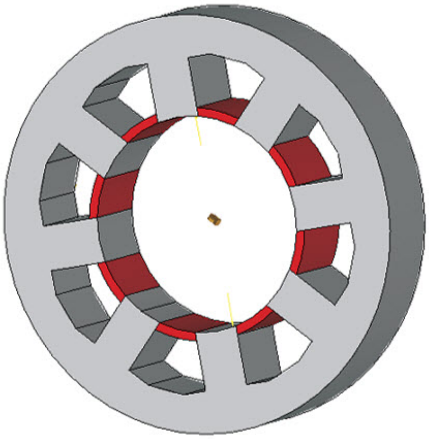

Figure 2.15: Principal idea with structural stator spacers [31]

The installation of structural stator spacers [31] which are made from non-magnetic materials in the stator slot, as shown in Fig. 2.15, is one of the structural design techniques to reduce the noise from aerodynamic sources. This technique also increases the stiffness of the stator structure. However, spacers not only have additional manufacturing costs but also have negative effects such as centrifugal force effects at high-speed operation and heat removal. The centrifugal forces from the SRM rotor, which is a salient pole structure, push the accumulating air outwards in the radial direction, which can blow the spacer piece out the slot wedges of the stator slot especially at high speed.

Takayama [32] presented a new SRM structure design by modifying both the stator and rotor. The new rotor was designed in the shape of a rotor pole with a sharp tip. The aim of this rotor is to change the magnetic flux flow from a radial to tangential direction and thereby to reduce the radial forces acting on the stator pole as illustrated in Fig. 2.16(right). The stator design modified the stator using the hexagon-round stator yoke structure, and the shape of the stator slot was tapered to increase the stator stiffness as shown in Fig. 2.16(left). It has been claimed that this design can reduce the maximum of the radial forces by 69 % and the maximum

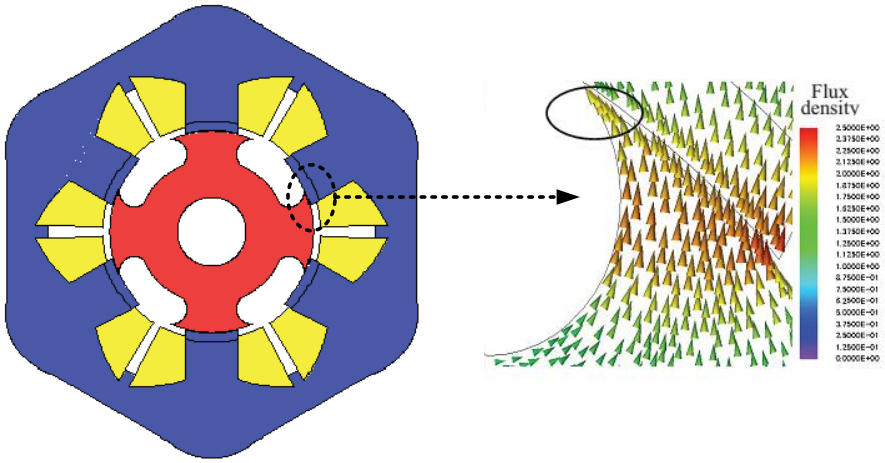

Figure 2.16: Modified structures of SRM in both stator and rotor [32]

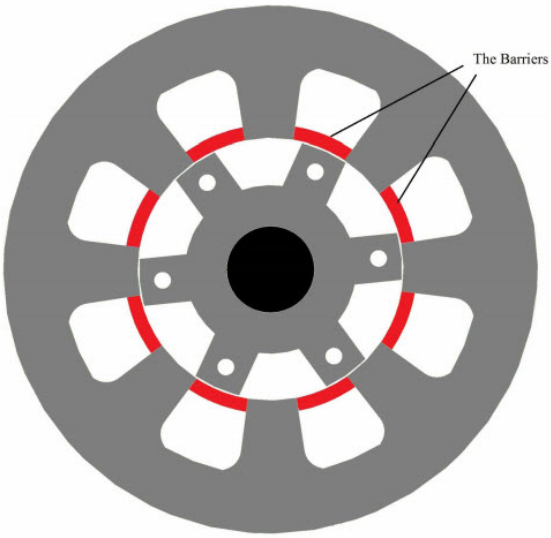

Figure 2.17: Structure design of SRM for noise reduction including stator spacer [33]

of the displacement by 51% compared with a basic SRM structure. The efficiency remains the same as the SRM conventional design.

Naderi [33] presented a new design of 8/6 SRM for noise reduction as shown in Fig. 2.17 by modifying the stator pole shape to a trapezoidal shape, adding a fillet on the corner of the stator pole, and using the stator spacers or barriers on the stator slot to increase the stiffness of the stator structure. Holes were also created in each rotor pole to reduce the magnetic radial forces. This design can decrease the maximum acceleration by 15.6 m/s^2 and sound pressure level by 16 dB compared

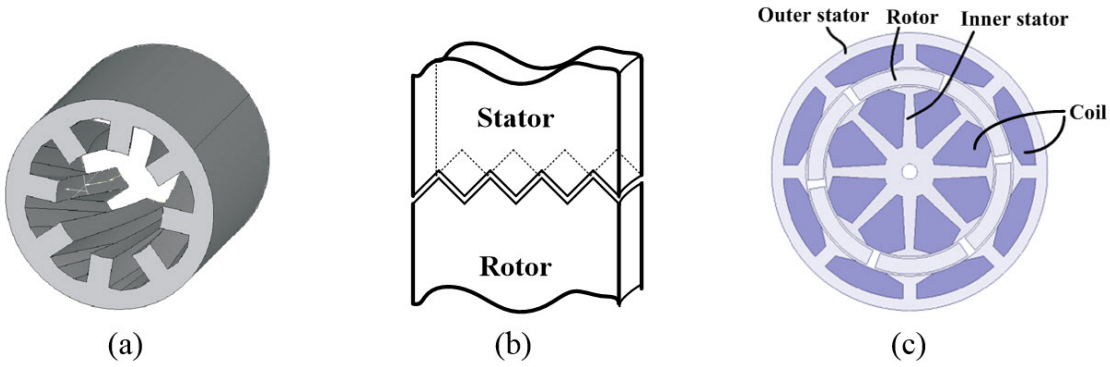

Figure 2.18: Example structural designs of the SRM: (a) skewed stator [34, 35], (b) saw-tooth shaped air gap [36], and (c) double-stator [37]

with the conventional 8/6 SRM. However, using stator spacers will decrease the winding area, and making a hole in the rotor will reduce the magnetic flux linkage and torque production.

Other structural design methods to eliminate noise and vibration in the SRM have been proposed. For example, skewing the rotor and stator, as shown in Fig. 2.18(a), was found in [34, 35] to reduce radial forces in the SRM. While the skewing technique is very effective to reduce noise in induction machines, a skewing technique for SRMs is suitable only for small machines. In large machines, a skewing technique in the SRM produces torsional [38] force, which increases acoustic noise. The skewing technique can give a better performance in terms of reducing radial forces when the stator or both the rotor and stator are skewed compared with only skewing rotor.

Switched reluctance 'shark' machines in [36] have been presented by Rasmussen et al. This method utilizes a saw-tooth air gap, as shown in Fig. 2.18(b), producing positive or negative axial direction of the flux path crossing the air gap, resulting in cancellation of the axial force on both sides to reduce acoustic noise in the switched reluctance shark machines. The skewing and shark air gap techniques, however, require more manufacturing effort. The shark air gap method in particular has very small tolerances. Both techniques also remove the advantage of manufacturing simplicity from an SRM. Another structural design of SRM for reducing noise has been proposed by Abbasin et al. [37]. This design shows a new SRM with a

double-stator configuration which can produce low radial force levels compared with conventional SRM, but the double-stator SRM has more complex structure components. As a result, it requires a more complex manufacturing method, leading to high production cost. It also has a problem with heat removal in the inner stator of the machine. A double-stator structure of SRM is illustrated in Fig. 2.18(c). Many published articles [39–44] investigated the radial force, the natural frequency of vibration modes, and the sound pressure level of the SRM by using analytical models and finite element software tools. The results of these investigations can help the machine designer to avoid resonance frequency.

2.3 Initial Study

From the previous section, it has been found that the electromagnetic force is the main source of vibration and acoustic noise in SRMs. The electromagnetic forces [37, 45–48] in the electrical machine can be divided into the radial and tangential components of the flux density. In the rotary machine, both radial force and tangential force induce vibration and acoustic noise. However, only tangential force contributes to motion. To observe the force distribution in an SRM, the magnetic field distribution in an SRM is calculated by finite element analysis. The radial and tangential components of force density in the air gap can be expressed as Equation (2.1) and (2.2) using the Maxwell Stress Tensor (MST) method.

$$f_n = \frac{1}{2\mu_0}(B_n^2 - B_t^2) \tag{2.1}$$

$$f_t = \frac{1}{\mu_0}(B_n B_t) \tag{2.2}$$

where f_n, f_t, B_n, B_t, and μ_0 denote the radial and tangential component of force density, the radial and tangential component of flux density in the air gap and absolute permeability, respectively. Then, the radial and tangential force are given by

$$F_n = \int_0^{2\pi} RL_z f_n(\theta_{sm}) d\theta_{sm} \tag{2.3}$$

$$F_t = \int_0^{2\pi} RL_z f_t(\theta_{sm}) d\theta_{sm} \tag{2.4}$$

where F_n, F_t, R, L_z, and θ_{sm} denote the radial and tangential force, contour radius, stack length and angular position relative to stator axis, respectively.

The radial and tangential forces can be calculated by 2D/3D magnetic FE simulation, whilst also taking into account the control technique and load condition. The force densities are used as input to the 3D structural FE simulation to predict the frequency of the natural vibration mode and deformation of the SRM structure. The vibration data results obtained by 3D structural analysis are used to calculate the acoustic noise emission in the SRM using the 3D boundary element method (BEM), with analysis undertaken in the frequency domain to reduce computational time. In the BEM, acoustic power is calculated on a field point mesh (acoustic mesh) at a boundary, and this surface performs as several microphones located on each field mesh node. The exterior faces of the SRM are selected to generate structural mesh. Acoustic mesh is then created to cover the machine for acoustic analysis. The direct mapping procedure is used to transfer vibration data from structural mesh to acoustic mesh. Acoustic noise prediction is a multiphysics analysis [43, 49, 50] that

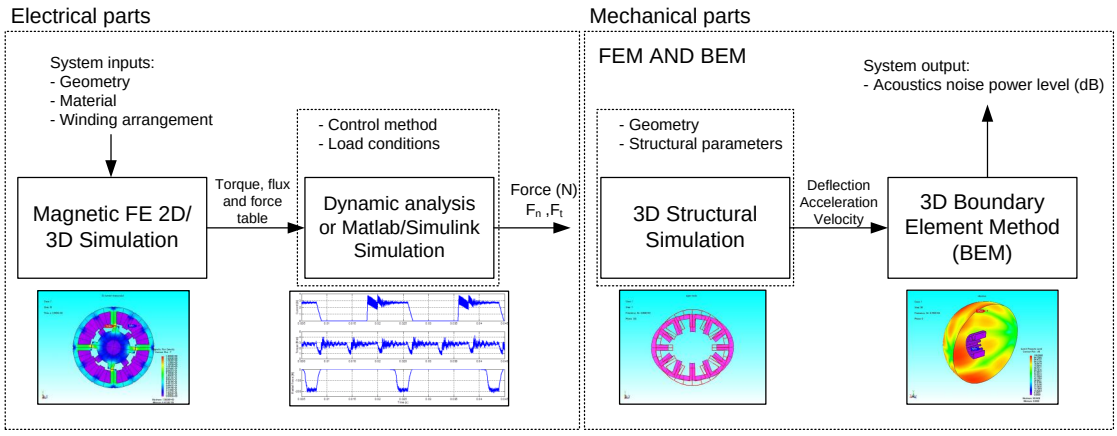

Figure 2.19: Block diagram of vibration and acoustic noise prediction

combines together both electromagnetic analysis and structural analysis to calculate acoustic noise. This analysis can be divided into two parts as shown in the block diagram of acoustic noise prediction in Fig. 2.19. The two parts are the following:

- Electrical parts for calculation of the electromagnetic force in the SRM stator

- Mechanical parts for calculation of the natural vibration mode in the SRM, the acceleration, and the noise generation

2.3.1 Simulation Results and Analysis

Vibration and acoustic noise analysis have been done using the JMAG software which is multiphysics simulation software. In this analysis, a 12/8 conventional SRM is used for vibration and acoustic simulation to understand the behaviour of acoustic noise emitted in SRMs. The effects of electromagnetic force, the commutation angle, the current shape and the thickness of stator yoke, all of which influence the vibration and acoustic noise in SRMs have been discussed. The machine geometry of a 12/8 conventional SRM is listed in Table 2.1 and shown in Fig. 2.20. The mechanical properties of the stack material are as follows: mass density $\rho = 7850$ kg/m^3, Young's modulus $E = 152$ GPa and Poisson′s ratio $\nu = 0.3$; the aluminium frame and end bells have $\rho = 2770$ kg/m^3, $E = 71$ GPa and $\nu = 0.33$. The sound pressure level probe is fixed at one side of the stator at 100 mm distance. The details of the magnetic and structural FE simulation are shown in Appendix A.1.

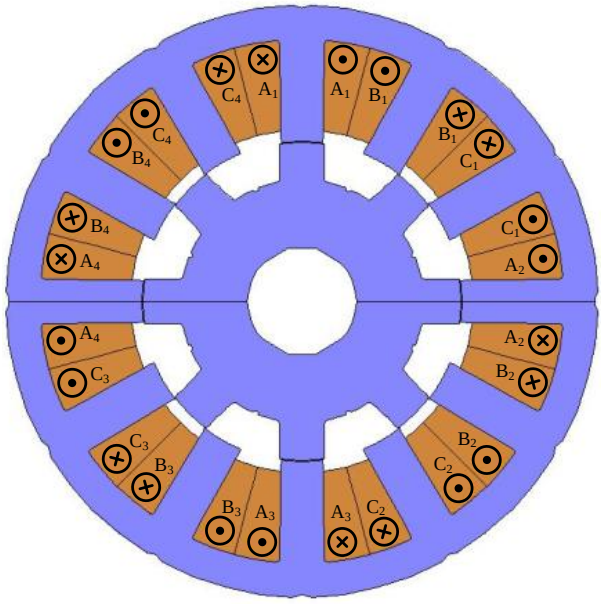

Figure 2.20: 12/8 conventional SRM

Table 2.1: Dimensions of 12/8 SRM.

Parameter	12/8 SRM
No. of stator/rotor poles	12/8
Stator outer diameter [mm]	190
Stator inner diameter [mm]	168
Rotor outer diameter [mm]	102
Shaft diameter [mm]	35
Air gap [mm]	0.25
Stack length [mm]	120
Number of turns per phase	400
Number of coils per phase	4
Coil span	1 slot
Phase resistance [Ω]	1.9 Ω

The maximum acoustic noise occurs when the frequency of the radial magnetic force coincides with one of the natural vibration modes of the stator due to resonance. The natural vibration mode of the stator can be calculated by Eigenfrequency analysis in the JMAG software. The vibration modes of the 12/8 conventional SRM are presented in Fig. 2.21.

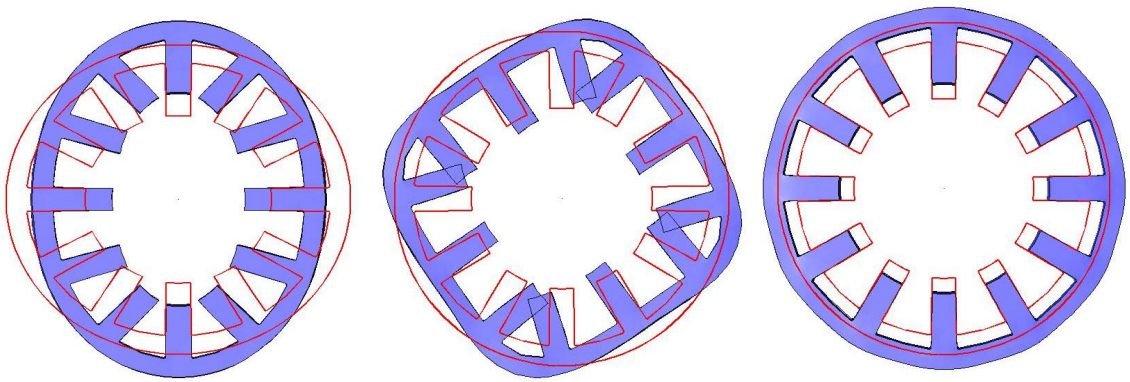

Figure 2.21: Vibration modes of 12/8 conventional SRM: (a) second-order mode shape, (b) fourth-order mode shape, and (c) zeroth-order or uniform mode shape

The dominant vibration mode shapes of a 12/8 SRM are fourth- and zeroth-order mode. Fourth-order mode shape is the most influential vibration mode shape of a 12/8 SRM due to its phase winding arrangement, which generates radial forces at

four stator poles when each phase winding is excited as shown in Fig. 3.1(a). Sum of phase radial force acting on the stator excites the stator to vibrate in zeroth-order mode shape.

2.3.1.1 Influence of Yoke Thickness and Frame

In this analysis, the yoke thickness of a 12/8 conventional SRM has been increased by 5 mm and compared with the original geometry. Moreover, the frame of the SRM has also been considered, and comparison results between an SRM with and without frame are discussed. Dimensions of an SRM with different yoke thicknesses

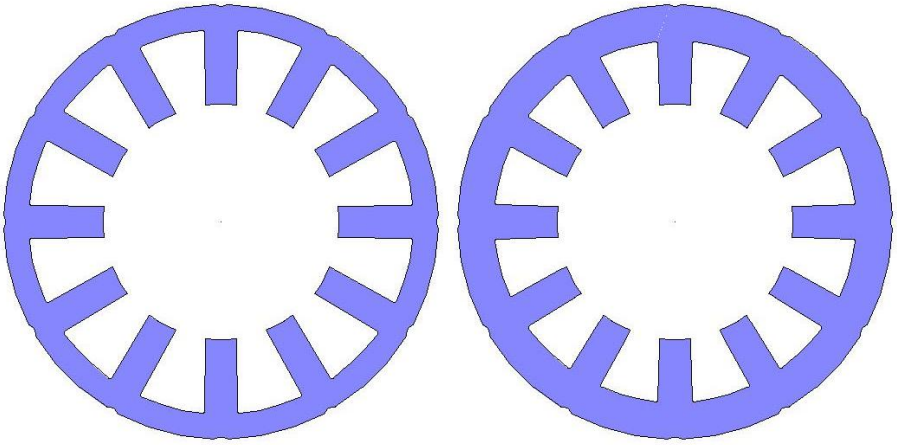

Figure 2.22: Increased yoke thickness: yoke thickness = 11 mm (left) and yoke thickness = 16 mm (right)

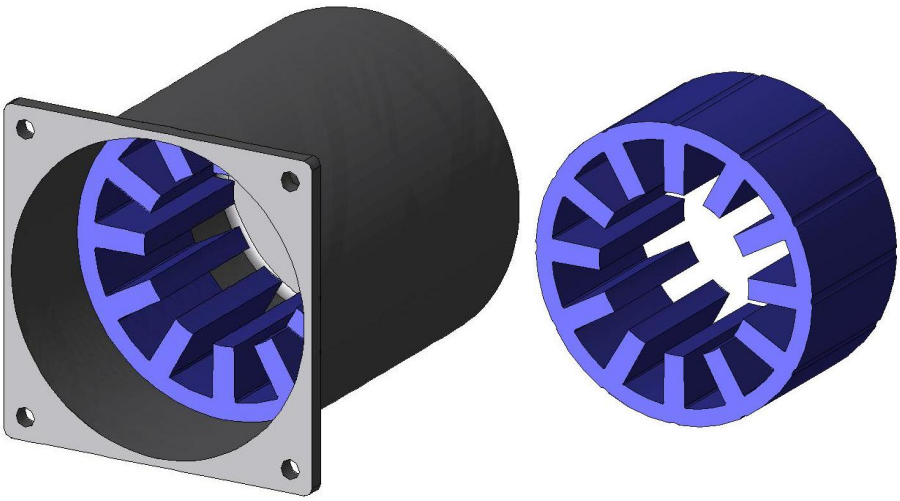

Figure 2.23: Frame effect: SRM with frame (left) and SRM without frame (right)

are illustrated in Fig. 2.22. Fig. 2.23 shows the geometry of an SRM with and without a frame.

Table 2.2: Modal frequency comparison

Parameter	2^{nd} order mode	4^{th} order mode	0^{th} order mode
12/8 SRM with frame	1062 Hz	3346 Hz	6009 Hz
12/8 SRM without frame	569 Hz	2507 Hz	5676 Hz
12/8 SRM without frame and increased yoke thickness by 5 mm	961 Hz	4280 Hz	6506 Hz

Table 2.2 reveals the frequency of the vibration mode at different cases. It is clear that the frequencies of the vibration modes of the machine increase as the yoke thickness increases or with the addition of the frame.

2.3.1.2 Influence of Electromagnetic Force

In this section, the electromagnetic forces, which are a primary cause of vibration in SRM, are discussed. There are three major ways that the electromagnetic forces can act on the stator. Firstly, the radial component of magnetic force, which is the main cause of vibration in SRM as discussed in the previous section, acts on the stator pole tips in a radial direction. Secondly, the tangential component of magnetic force, which mainly contributes to motion, acts on the stator pole tips in a circumferential direction. Finally, a magnetostrictive force [51–53], which results from changing the dimension of a magnetic material (whether by increasing or decreasing the dimension) by subjecting the material to a magnetic field, mostly acts along the pole and core back of the stator. The relationship graph between mechanical strain (ε) and magnetic flux density (B) of the magnetic material for magnetostrictive effect analysis in this thesis is shown in Fig. 2.24.

In this analysis, each component of magnetic and magnetostrictive forces is compared in terms of force distribution in FE magnetic analysis and acceleration, velocity, displacement and sound pressure level in FE structural analysis. Single pulse testing is used in this analysis by applying a short voltage pulse with a frequency of 100 Hz in one phase of the SRM at an aligned position. This position has a high magnetic flux density and high electromagnetic forces. The maximum current level

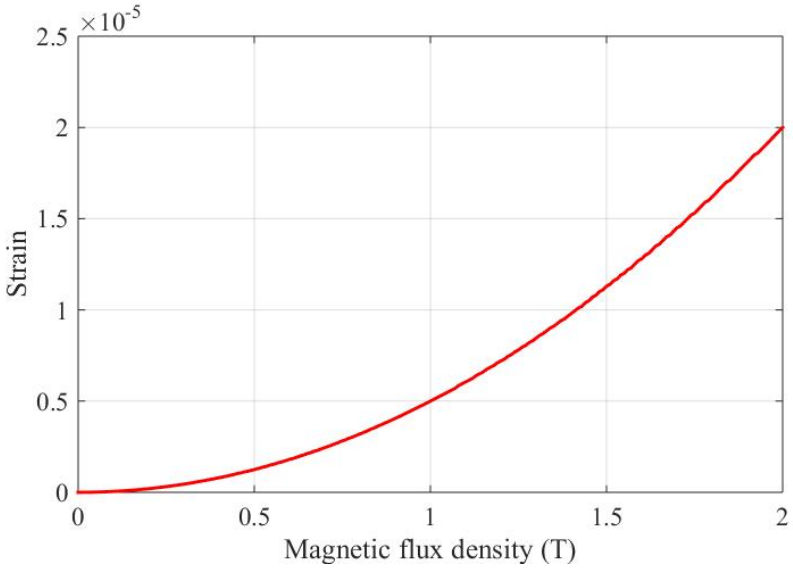

Figure 2.24: B-ε curve

of applying a short voltage pulse is 2.4 A, and the maximum voltage level is 540 Vdc as shown in Fig. 2.28. Magnetic flux density, magnetic force, and magnetostrictive force distribution acting on the stator are shown in Fig. 2.25-2.27, respectively. The magnetic and magnetostrictive force distribution shows that the magnetostrictive force is larger than the magnetic force. An amplitude of an absolute value of magnetic and magnetostrictive force is illustrated in Fig. 2.29. The distribution also confirms that the magnetostrictive force (5613 N) is higher than the magnetic force (479.20 N). Comparison between the radial and tangential components of the magnetic and magnetostrictive forces can be seen in Fig. 2.30 and 2.31. The radial component of magnetic force has a high value compared with the other force components of magnetic and magnetostrictive forces. Moreover, the direction of the radial and tangential components of the magnetic force is the opposite direction to the radial and tangential components of the magnetostrictive force. In the tangential component which can cause vibration of the stator pole, the magnetostrictive force has a high value comparing with the magnetic force. The details of the dynamic characteristic of the magnetic and magnetostrictive forces are summarised in Table 2.4.

After FE magnetic analysis, the electromagnetic force distribution in the stator can be divided into two main forces, namely the magnetic and magnetostrictive force.

These forces are transferred from FE magnetic analysis to FE structural analysis for vibration prediction in the SRM. In the structural analysis, three model cases of a mechanical simulation are performed: I) a model that applies only magnetic force, II) a model that applies only magnetostrictive force, and III) a model that applies both magnetic and magnetostrictive force. In a real rotating machine, both forces should be considered following the third simulation model. However, the simulation model of each force is suitable for investigation and comparison of the vibration of the stator in each force. These simulation models can also show which force is the main source of generating vibration in SRM. The magnetic forces relate to producing torque and to generating unpleasant vibration in the SRM. The magnetostrictive forces generally create vibration in the lamination core [51, 54–57] of the stator, especially in a large stator and stacked core of a transformer. Fig. 2.32-2.35 show an acceleration, displacement, velocity, and sound pressure level of the stator of three different force excitation models.

The dominant mode of vibration of a 12/8 conventional SRM is a fourth-order mode shape of the stator at frequency 3346 Hz. At fourth-order mode shape, the magnetic force excitation gives a high amplitude of acceleration, displacement, velocity, and sound pressure level compared with magnetostrictive force excitation, and it produces results similar to those of the third simulation model that applied both magnetic and magnetostrictive force excitation. The magnetic force has an influence on stator vibration in fourth-order mode shape and zeroth-order mode shape. The magnetostrictive force gives the stator vibrating only in zeroth-order mode shape. In the simulation model of a combination of magnetic and magnetostrictive force, it seems that a high amplitude of vibration appears in the fourth-order mode shape due to magnetic force. In comparison, in the zeroth-order mode shape, the level of magnitude of vibration is decreased as a result of the vibration level of the stator. The vibration level of the magnetic force and the vibration level of magnetostrictive force cancel each other out. In the zeroth-order mode shape, the magnetic force tends to contract the stator frame, while the magnetostrictive force tends to expand the stator frame. The numerical results of vibration are summarised in Table 2.3.

Although the level of magnetostrictive forces is many times larger than that of

the magnetic forces, the effect of the magnetostrictive forces on stator vibration is less significant compared with the effect of the magnetic force, except at some frequencies. The magnetic forces act on an elastic structure, which has low stiffness, of the stator core as shown in Fig. 2.26, while the magnetostrictive forces mainly act on the material itself, which has high stiffness as shown in Fig. 2.27. In the components of magnetic force, the force in the radial component is higher than that in the tangential component. From this analysis, it can be concluded that the main source of the vibration in SRMs is caused by the radial component of magnetic force or radial force.

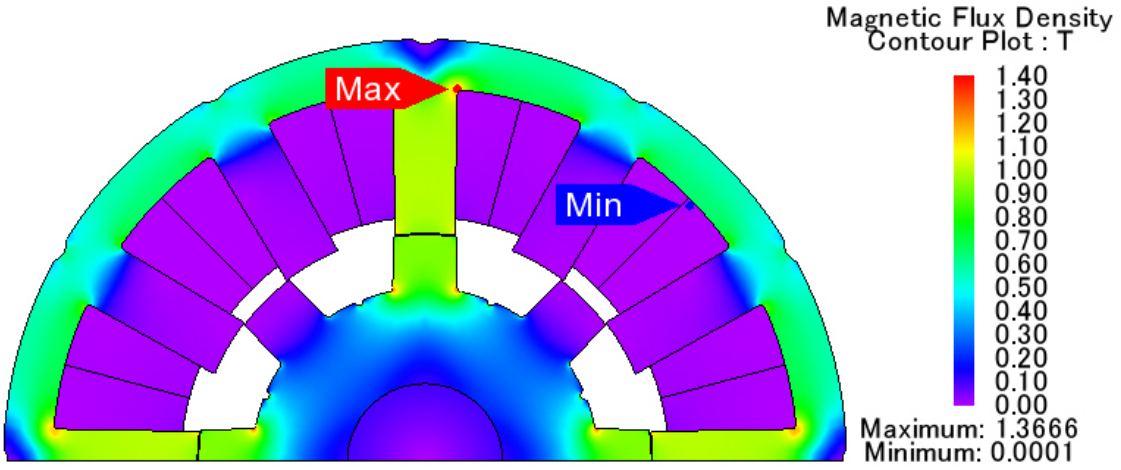

Figure 2.25: Magnetic flux density at aligned position

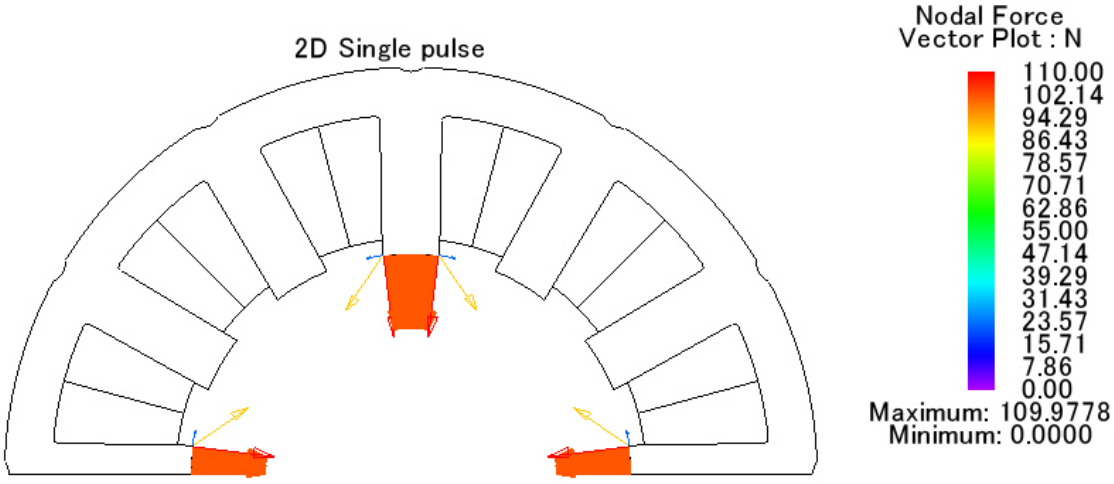

Figure 2.26: Vector plot of magnetic force (radial and tangential component)

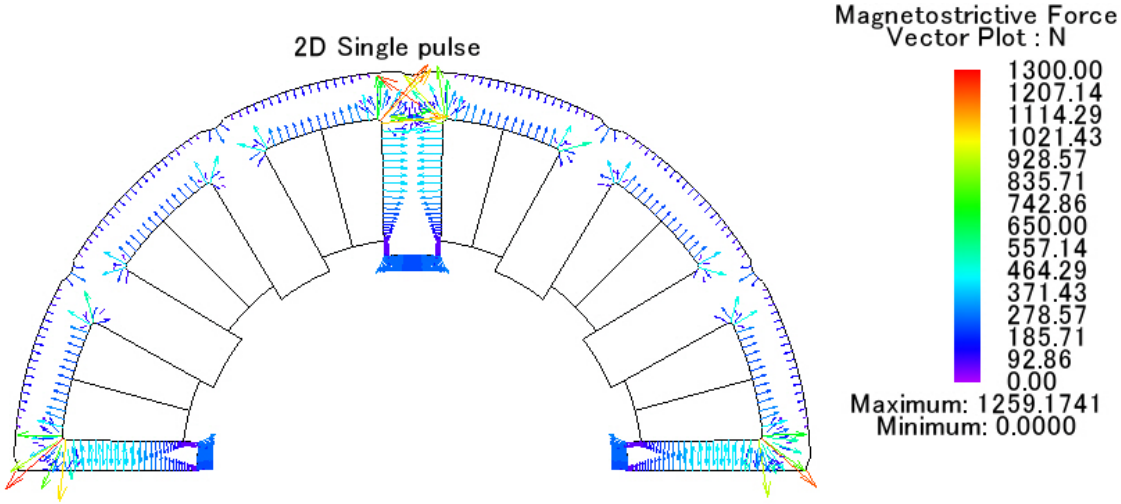

Figure 2.27: Vector plot of magnetostrictive force (radial and tangential component)

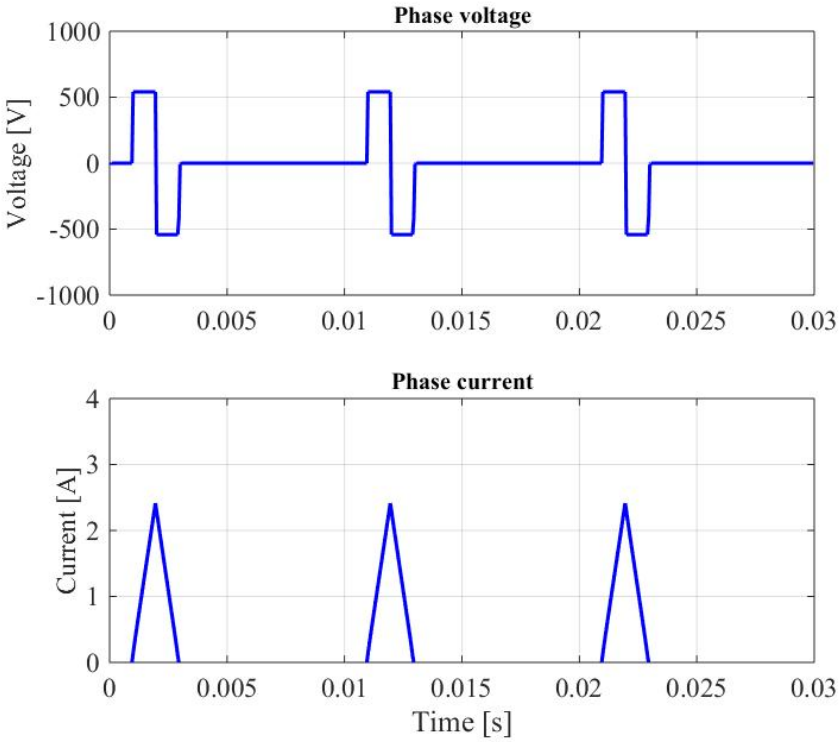

Figure 2.28: Voltage and current of short voltage pulse test

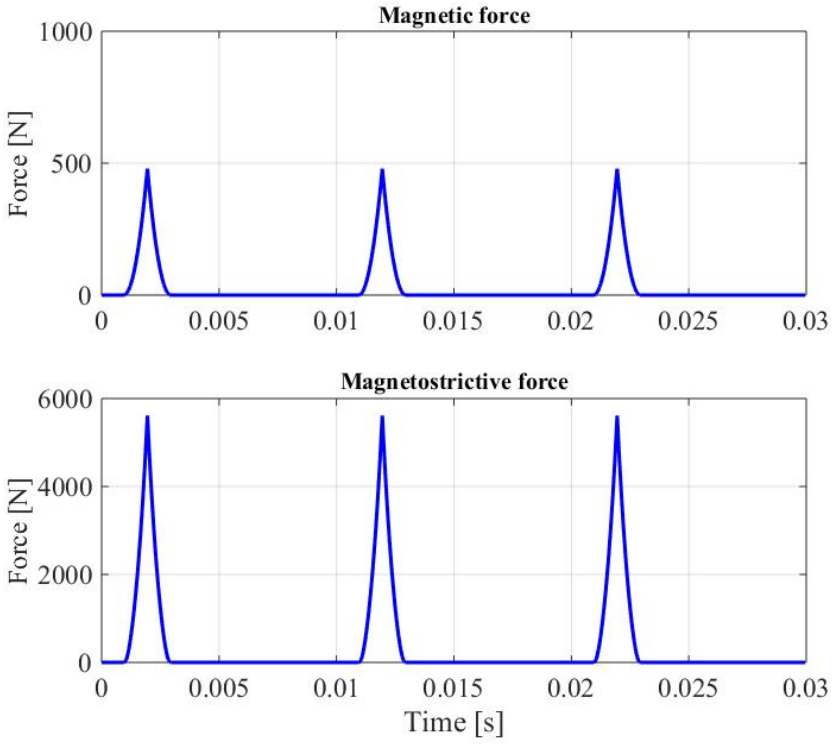

Figure 2.29: Magnetic and magnetostrictive force

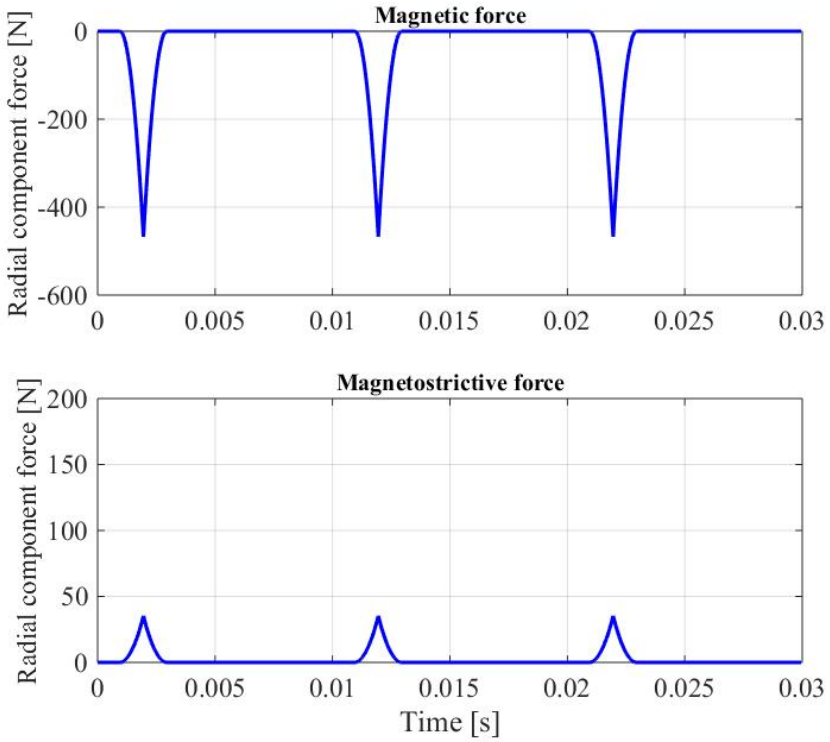

Figure 2.30: Radial component of magnetic and magnetostrictive force

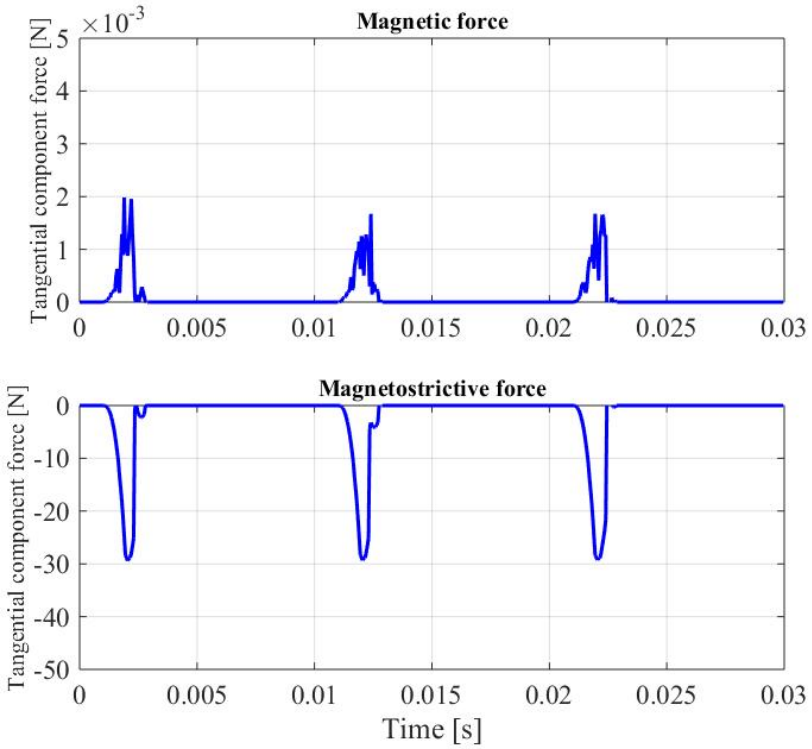

Figure 2.31: Tangential component of magnetic and magnetostrictive force

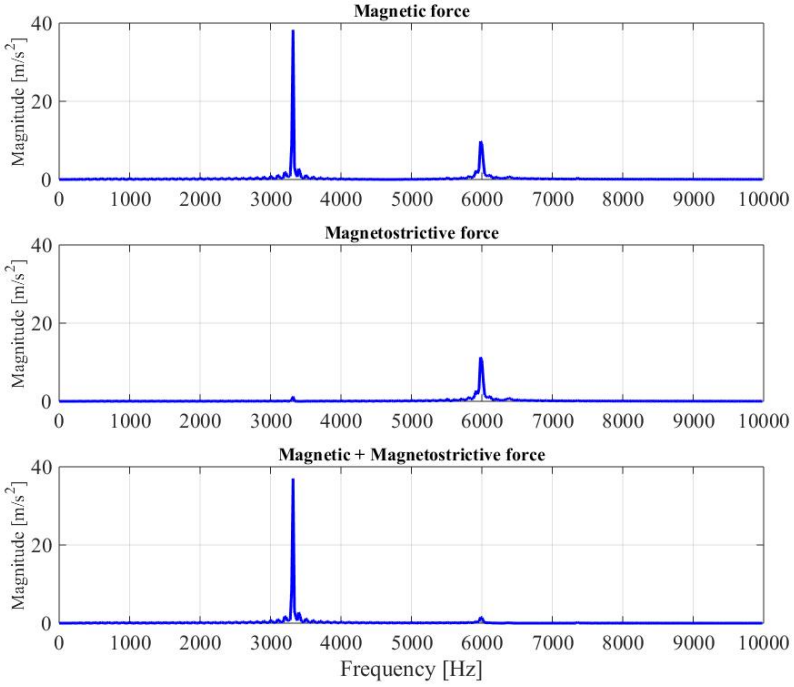

Figure 2.32: Magnitude of acceleration of magnetic, magnetostrictive and magnetic + magnetostrictive force

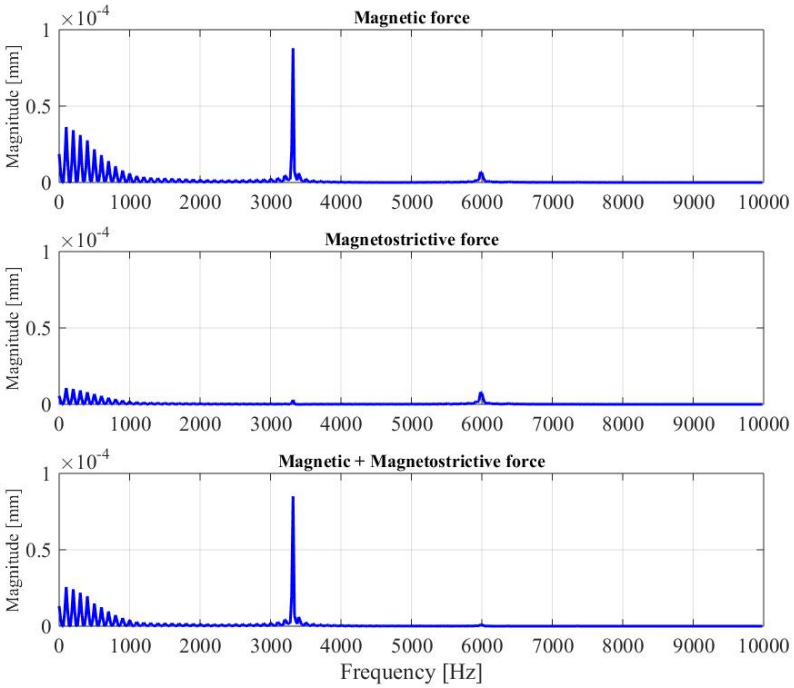

Figure 2.33: Magnitude of displacement of magnetic, magnetostrictive, and magnetic + magnetostrictive force

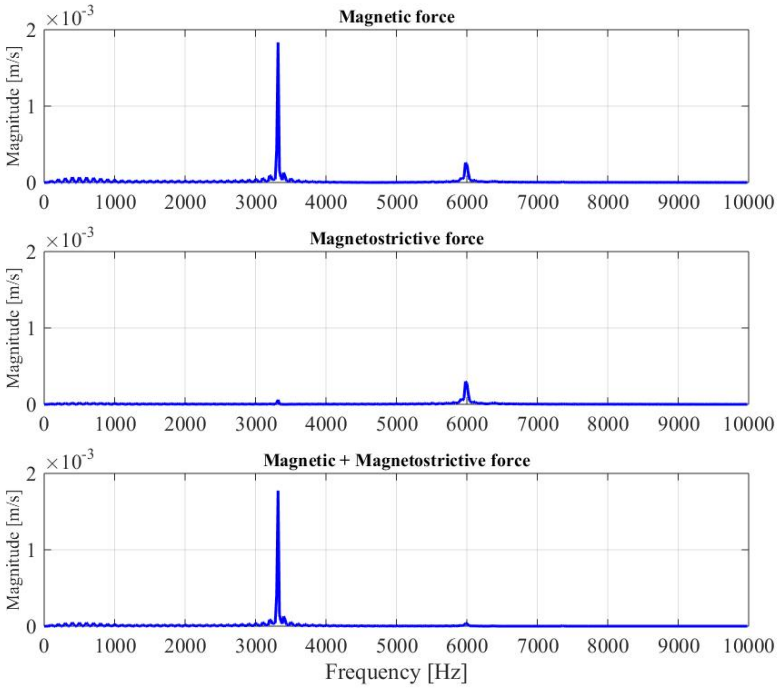

Figure 2.34: Magnitude of velocity of magnetic, magnetostrictive, and magnetic + magnetostrictive force

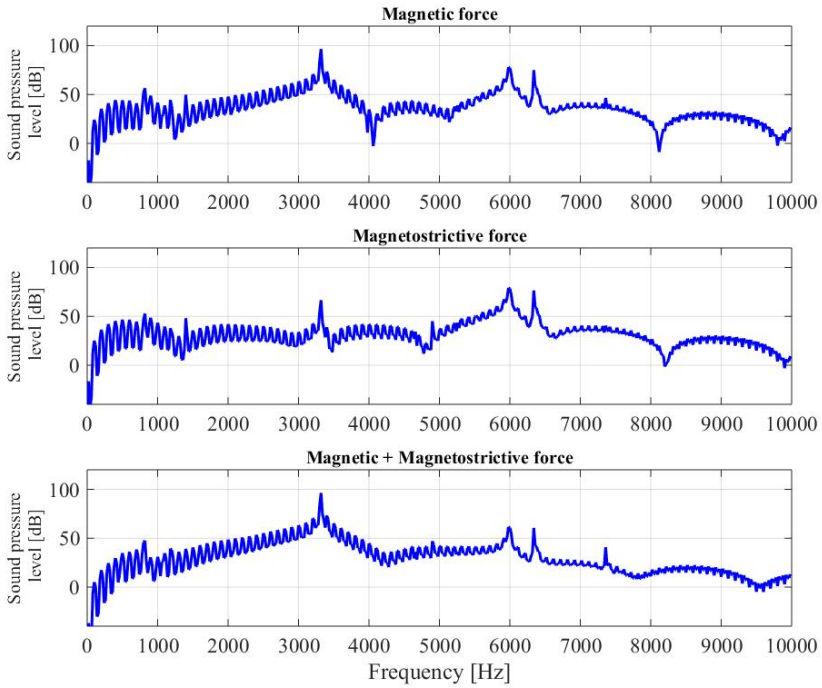

Figure 2.35: Sound level pressure of magnetic, magnetostrictive, and magnetic + magnetostrictive force

Table 2.3: Vibration characteristics of magnetic and magnetostrictive force

Magnetic	2^{nd} order mode	4^{th} order mode	0^{th} order mode
Acceleration [m/s^2]	0.06	38.27	9.77
Velocity [μm/s]	9.32	1835	260
Displacement [nm]	1.37	87.96	6.92
Sound pressure level [dB]	29.76	96.64	77.97
Magnetostrictive	2^{nd} order mode	4^{th} order mode	0^{th} order mode
Acceleration [m/s^2]	0.02	1.25	11.28
Velocity [μm/s]	3.42	60.13	300.2
Displacement [nm]	0.50	2.88	7.99
Sound pressure level [dB]	30.42	66.66	79.20
Magnetic + Magnetostrictive	2^{nd} order mode	4^{th} order mode	0^{th} order mode
Acceleration [m/s^2]	0.04	37.02	1.51
Velocity [μm/s]	5.91	1775	35.67
Displacement [nm]	0.87	85.07	0.95
Sound pressure level [dB]	26.57	96.36	61.61

Table 2.4: Dynamic characteristics of magnetic and magnetostrictive force

	Magnetic	Magnetostrictive
Radial component force [N]	467.30	35.29
Tangential component force [N]	0.002	29.41
Absolute force [N]	479.20	5613.00

2.3.1.3 Influence of Commutation Angle

To understand the effect of commutation angle, three turn-on and turn-off angles are selected to observe the level of vibration generation at 418 and 1000 r/min, with load torque at 2.5 Nm. The current, the radial force on the stator pole, and the sum of radial force waveform at different speeds are shown in Fig. 2.36-2.41, respectively. The torque waveforms are shown in Fig. A.11-A.12 of Appendix A.2. The amplitude of all harmonic components can be observed with the spectrum of radial force on the stator pole and sum of radial force as illustrated in Fig. A.13-A.16 of Appendix A.2. As in the above section, this section explains that severe vibration will appear when the high amplitude of a harmonic component of radial forces coincides with natural frequency of the stator structure.

The simulation results of vibration at different commutation angles are illustrated in Fig. 2.42-2.45, and vibration and dynamic characteristics of each commutation angle are summarised in Table 2.5 and 2.6 for 418 r/min and Table 2.7 and 2.8 for 1000 r/min, respectively. In the vibration and acoustic noise characteristics, it is clear that the dominant vibration modes of a 12/8 conventional SRM are fourth-order mode and uniform or zeroth-order mode due to the high magnitude of the acceleration, velocity, displacement and sound pressure level occurring at these modes. In 0-22.5 degrees of turn-on and turn-off angle, the acceleration level at the fourth-order mode has a high amplitude compared with other cases at both speeds. The other waveforms in the frequency domain, such as displacement and velocity, are shown in Fig. A.17-A.20 of Appendix A.2, respectively.

The maximum magnitude of sound pressure level occurs at the fourth-order mode for all cases at 418 r/min, while at 1000 r/min it appears at the zeroth-order mode in a commutation angle of 0-22.5 degrees. The highest sound level pressure appears at turn-on and turn-off angles of 0-22.5 degrees at 111.2 dB under operation at 1000 r/min and 96.29 dB at 418 r/min. The lowest level of sound pressure can be seen in the turn-on and turn-off angle at 7.5-22.5 degrees at 418 r/min and at the turn-on and turn-off angle at 0-15 degrees at 1000 r/min. Adjustment of the turn-off angle can reduce the maximum of the sound pressure level, while adjustment of the turn-on angle cannot.

In terms of electrical characteristics, the turn-on and turn-off angle at 0-15 degrees give the highest rate of torque ripple at 2.08 and 2.03 at 418 and 1000 r/min, respectively. At 0-22.5 degrees, the turn-on and turn-off angle can reduce the torque ripple rate to 1.06 and 1.23 at 418 and 1000 r/min, respectively. The turn-on and turn-off angle at 0-15 degrees can reduce the maximum of radial forces of both speeds due to the high radial forces occurring at the aligned position (22.5 degrees). Therefore, the high radial forces can be decreased by early turn-off of the conduction of the phase current before the rotor moves to the aligned position. However, by doing this, the total torque will reduce. To obtain the same level of total torque, the RMS current must increase, but higher RMS current causes an increase in copper losses in the SRM.

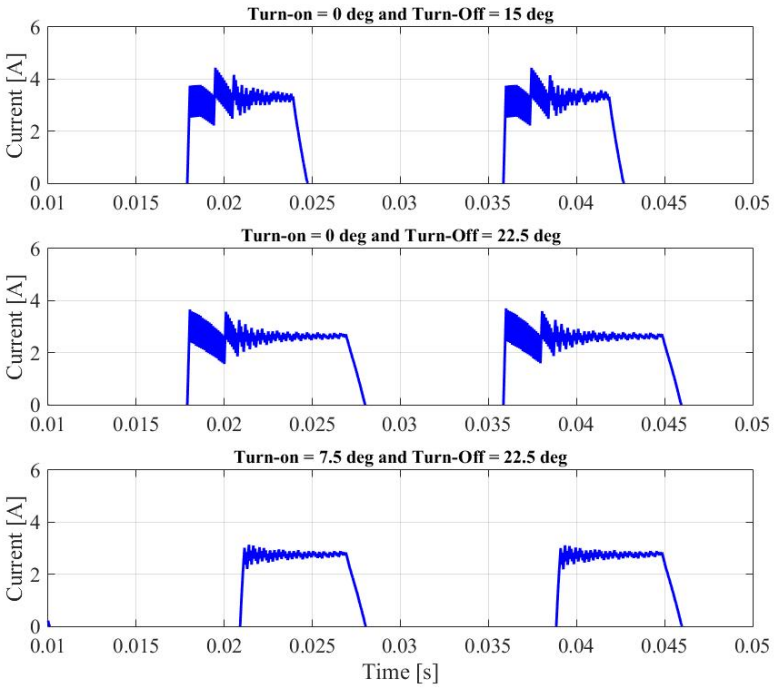

Figure 2.36: Current waveform of three different turn-on and turn-off angles at 418 r/min

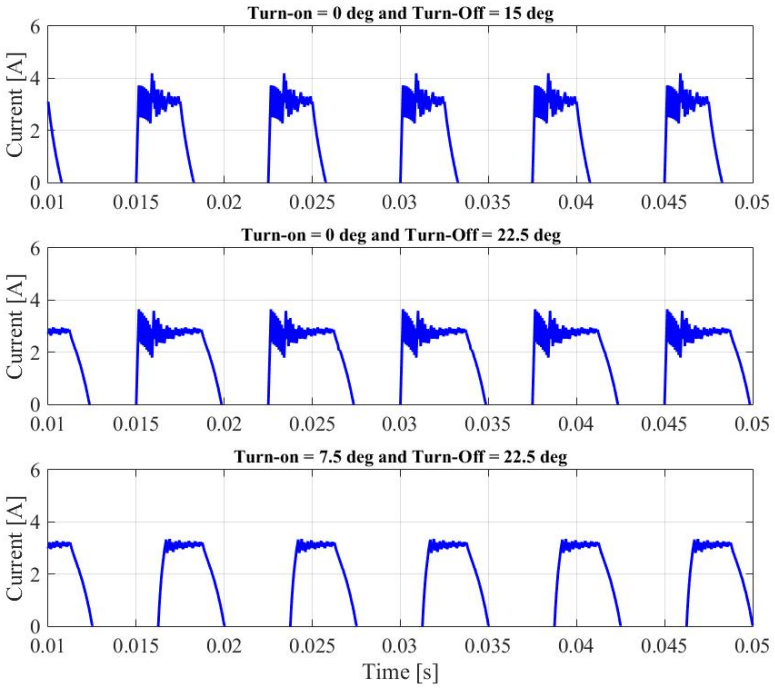

Figure 2.37: Current waveform of three different turn-on and turn-off angles at 1000 r/min

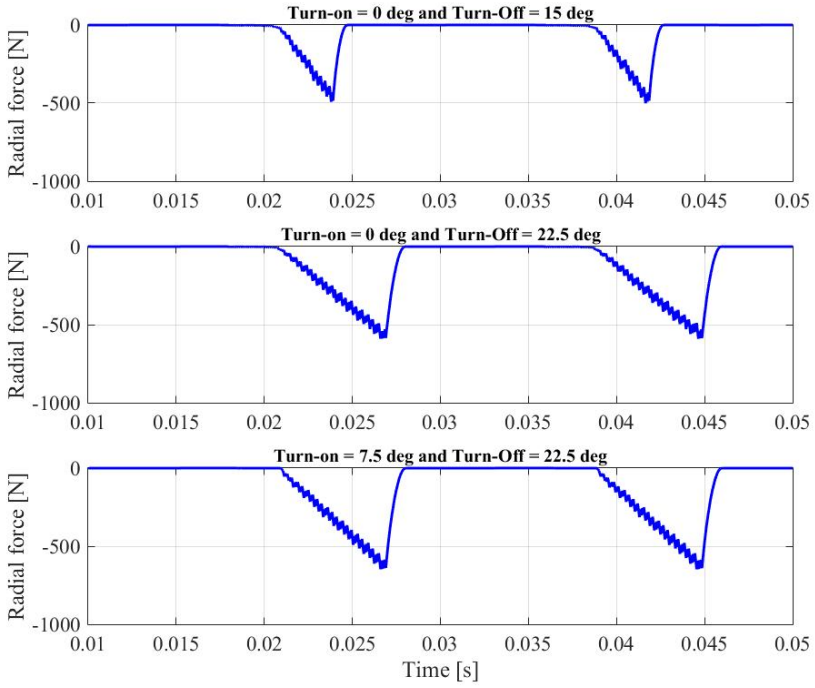

Figure 2.38: Radial forces acting on the single stator pole of three different turn-on and turn-off angles at 418 r/min

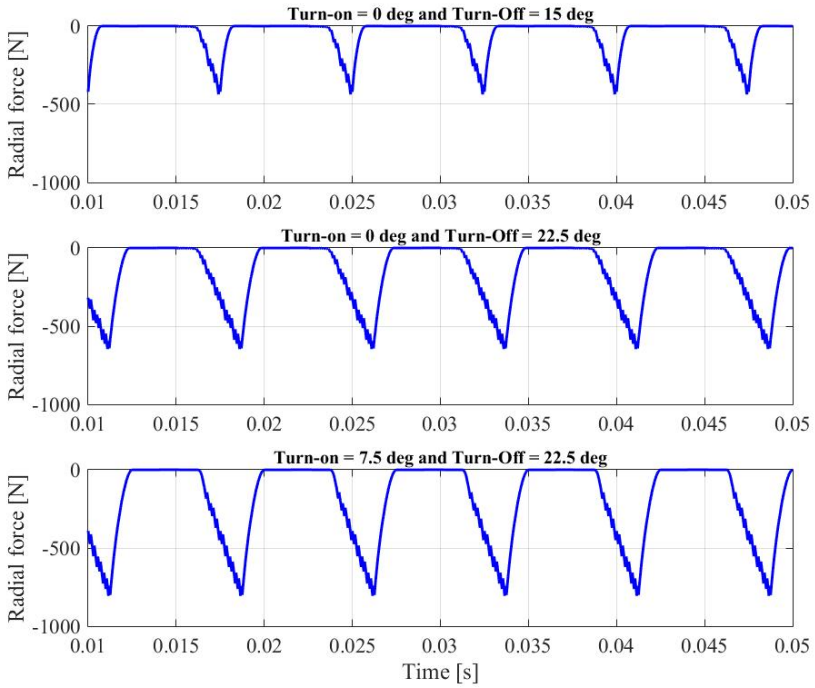

Figure 2.39: Radial forces acting on the single stator pole of three different turn-on and turn-off angles at 1000 r/min

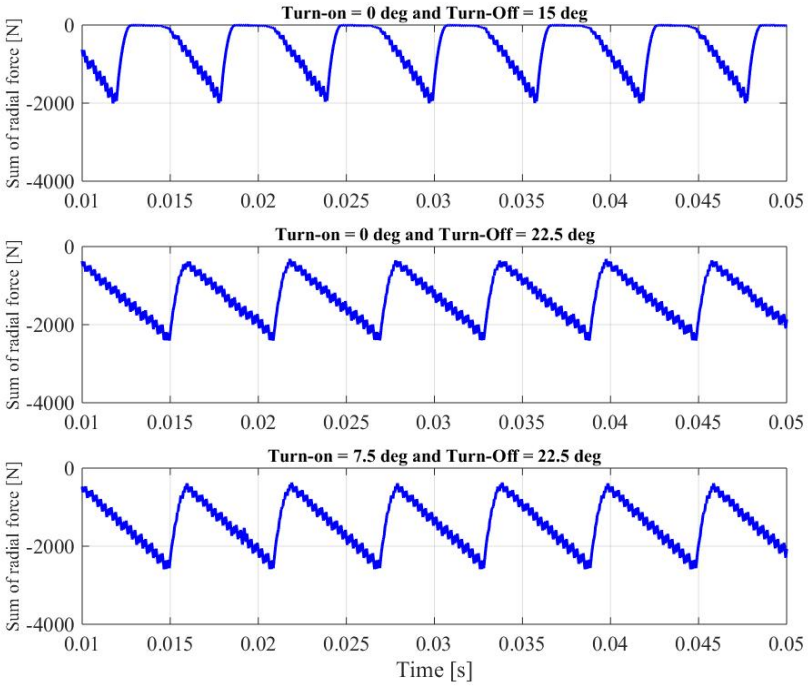

Figure 2.40: Sum of radial forces on the stator of three different turn-on and turn-off angles at 418 r/min

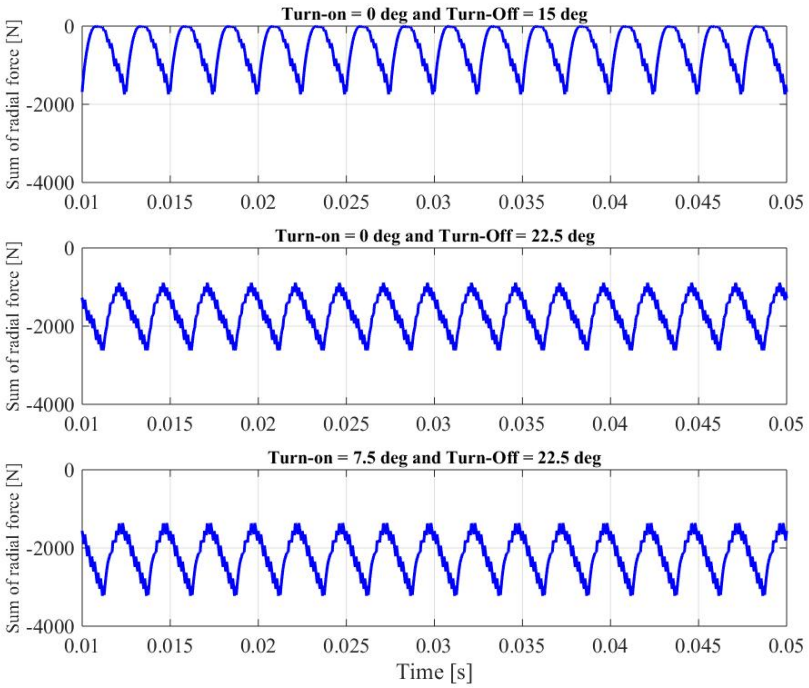

Figure 2.41: Sum of radial forces on the stator of three different turn-on and turn-off angles at 1000 r/min

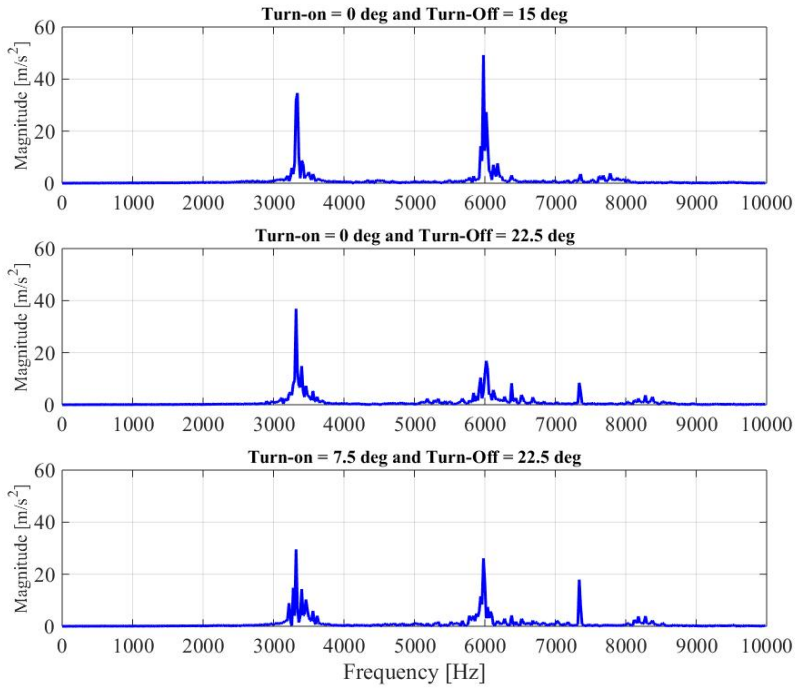

Figure 2.42: Magnitude of acceleration of three different turn-on and turn-off angles at 418 r/min

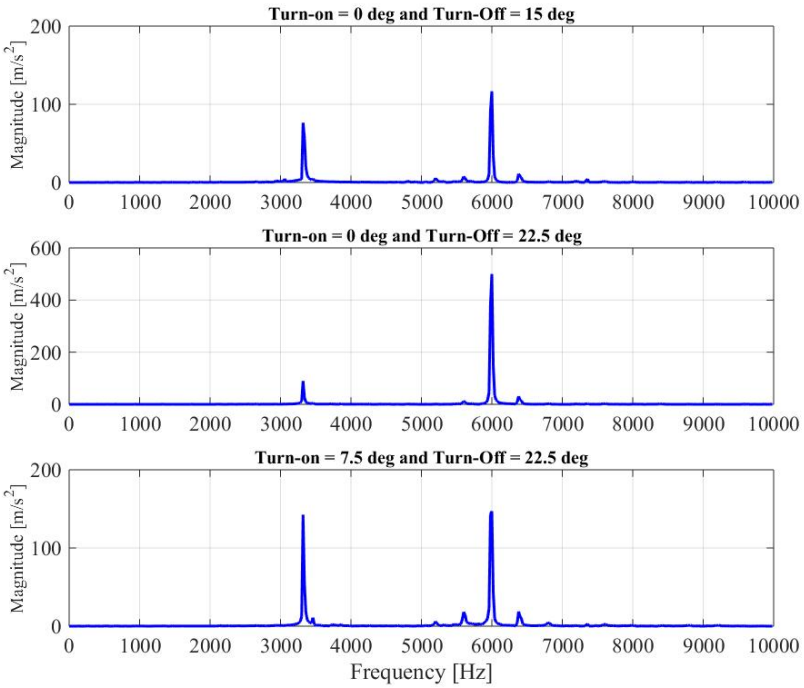

Figure 2.43: Magnitude of acceleration of three different turn-on and turn-off angles at 1000 r/min

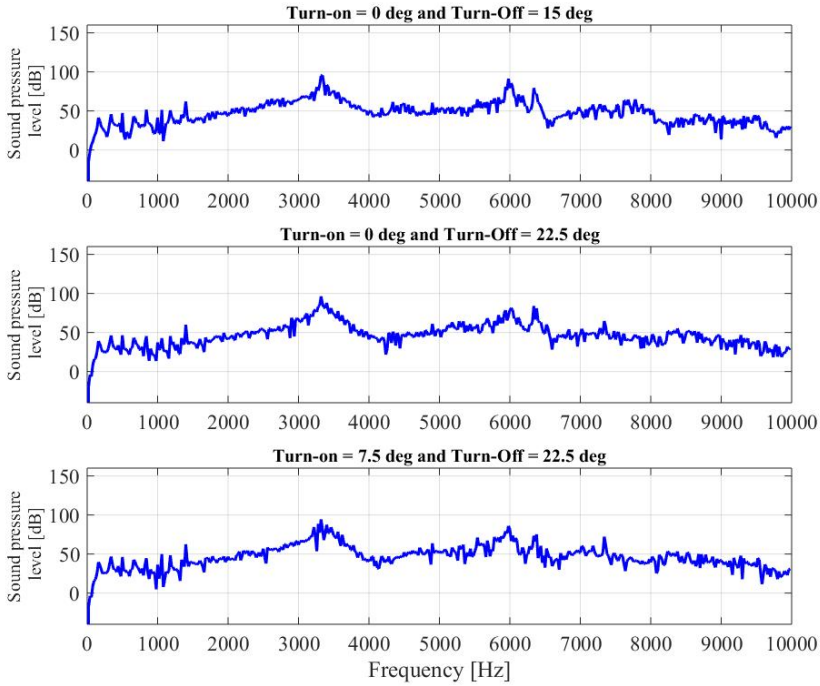

Figure 2.44: Sound pressure level of three different turn-on and turn-off angles at 418 r/min

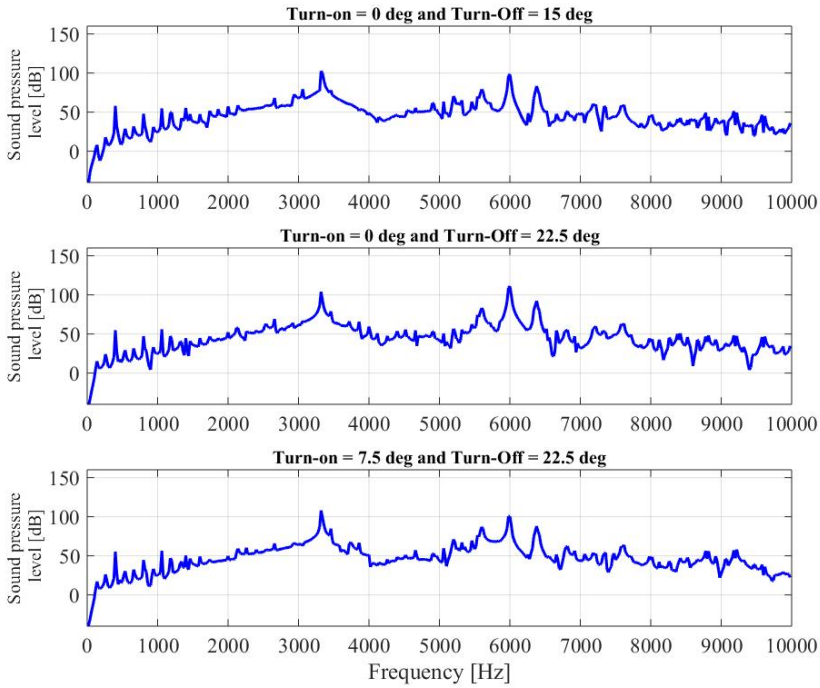

Figure 2.45: Sound pressure level of three different turn-on and turn-off angles at 1000 r/min

Table 2.5: Vibration characteristics of different turn-on and turn-off angles at 418 r/min

Turn-on = 0 deg Turn-off = 15 deg	2^{nd} order mode	4^{th} order mode	0^{th} order mode
Acceleration [m/s^2]	0.07	34.65	49.22
Velocity [μm/s]	10.6	1651	131
Displacement [nm]	1.59	78.7	34.9
Sound pressure level [dB]	51.34	95.0	91.36
Turn-on = 0 deg Turn-off = 22.5 deg	2^{nd} order mode	4^{th} order mode	0^{th} order mode
Acceleration [m/s^2]	0.16	36.88	16.88
Velocity [μm/s]	23.57	1768	446.2
Displacement [nm]	3.54	84.75	11.8
Sound pressure level [dB]	42.75	96.29	81.38
Turn-on = 7.5 deg Turn-off = 22.5 deg	2^{nd} order mode	4^{th} order mode	0^{th} order mode
Acceleration [m/s^2]	0.08	29.57	26.13
Velocity [μm/s]	11.54	1418	695.4
Displacement [nm]	1.73	67.96	18.51
Sound pressure level [dB]	49.88	94.39	85.84

Table 2.6: Dynamic characteristics of different turn-on and turn-off angles at 418 r/min

Parameter	0-15 deg	0-22.5 deg	7.5-22.5 deg
Average torque [Nm]	2.55	2.51	2.47
Torque ripple rate	2.08	1.06	1.46
RMS phase current [A]	1.99	1.86	1.53
Maximum radial force on the pole [N]	501.9	590.7	648.3
Maximum sum of radial force [N]	2045.8	2463.8	2654.2
Ripple rate of sum of radial force	3.32	1.65	1.6

Table 2.7: Vibration characteristics of different turn-on and turn-off angles at 1000 r/min

Turn-on = 0 deg Turn-off = 15 deg	2^{nd} order mode	4^{th} order mode	0^{th} order mode
Acceleration [m/s^2]	0.06	76.39	116.7
Velocity [μm/s]	8.8	3662	3094
Displacement [nm]	1.32	175.5	82.1
Sound pressure level [dB]	54.81	102.6	98.53
Turn-on = 0 deg Turn-off = 22.5 deg	2^{nd} order mode	4^{th} order mode	0^{th} order mode
Acceleration [m/s^2]	0.12	89.69	500.2
Velocity [μm/s]	17.78	4300	13270
Displacement [nm]	2.67	206.1	351.9
Sound pressure level [dB]	56.03	104	111.2
Turn-on = 7.5 deg Turn-off = 22.5 deg	2^{nd} order mode	4^{th} order mode	0^{th} order mode
Acceleration [m/s^2]	0.14	142.6	147.1
Velocity [μm/s]	20.35	6836	3903
Displacement [nm]	3.1	327.7	100.1
Sound pressure level [dB]	56.48	108.0	100.5

Table 2.8: Dynamic characteristics of different turn-on and turn-off angles at 1000 r/min

Parameter	0-15 deg	0-22.5 deg	7.5-22.5 deg
Average torque [Nm]	2.45	2.56	2.47
Torque ripple rate	2.03	1.23	1.99
RMS phase current [A]	1.78	2.02	1.9
Maximum radial force on the pole [N]	437.0	646.6	806.8
Maximum sum of radial force [N]	1771.8	2668.0	3284.2
Ripple rate of sum of radial force	2.93	1.05	0.88

2.3.1.4 Influence of Current Shape

In this analysis, five different current shapes are excited in the phase winding of the machine, and the vibration behaviours in each shape at the two speeds (418 and 1000 r/min) and with torque = 2.5 Nm are observed. The five shapes of the current waveforms are a half sinusoidal (HS) shape, a modified half sinusoidal (MHS) shape, a modified sinusoidal (MS) shape, a square (S) shape and a trapezoidal (TZ) shape. The conduction angle is 0-22.5 degrees in all cases. The current and radial force waveform at different current shapes are presented in Fig. 2.46-2.51, and the vibration and electrical characteristics at different current shapes are concluded in Table 2.9-2.12. The torque waveforms are shown in Fig. A.21-A.22 of Appendix A.2.

Table 2.10 and 2.12 suggest that the HS current shape produces the highest rate of torque ripple. In contrast, the lowest rate of torque ripple is generated by the S current shape. The S current shape has a low rate of the torque ripple, but it gives a high magnitude of the radial force and RMS current. Fig. 2.52-2.55 reveal the comparison results at different current shapes of acceleration and sound level pressure in the frequency domain at all speeds. The results of different current shapes in the frequency domain are summarised in Table 2.9 and 2.11. The radial force, displacement, and velocity waveforms are shown in Fig. A.23-A.30 of Appendix A.2, respectively.

Overall, it is clear that the S current shape creates the highest magnitude of sound pressure level in the fourth-order vibration mode. The lowest magnitude of sound pressure level can be seen in the MS current shape. As a result of the low magnitude of the harmonic contents, the MS current shape coincides with fourth-order and zeroth-order vibration mode. In contrast, the vibration mode at the second-order mode of a 12/8 conventional SRM is hit by the high magnitude of harmonic contents of TZ and S current shape. For this reason, acoustic noise in the second-order mode, when excited by TZ and S current shape, has a higher magnitude than with the other current shapes. The ripple rate of the sum of radial forces is one factor of vibration reduction. The MS current has a low ripple rate of the sum of radial forces, leading to low vibration compared with other current shapes.

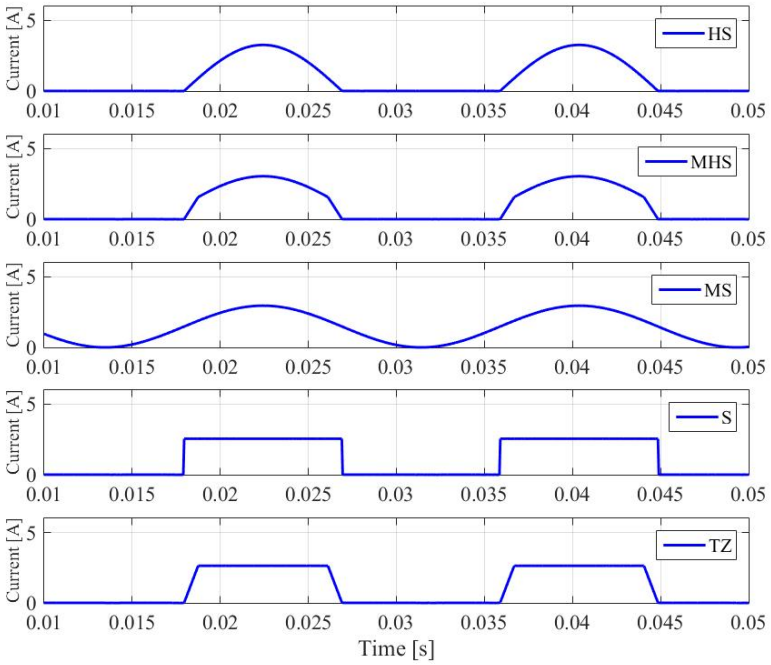

Figure 2.46: Current waveform of different current shapes at 418 r/min

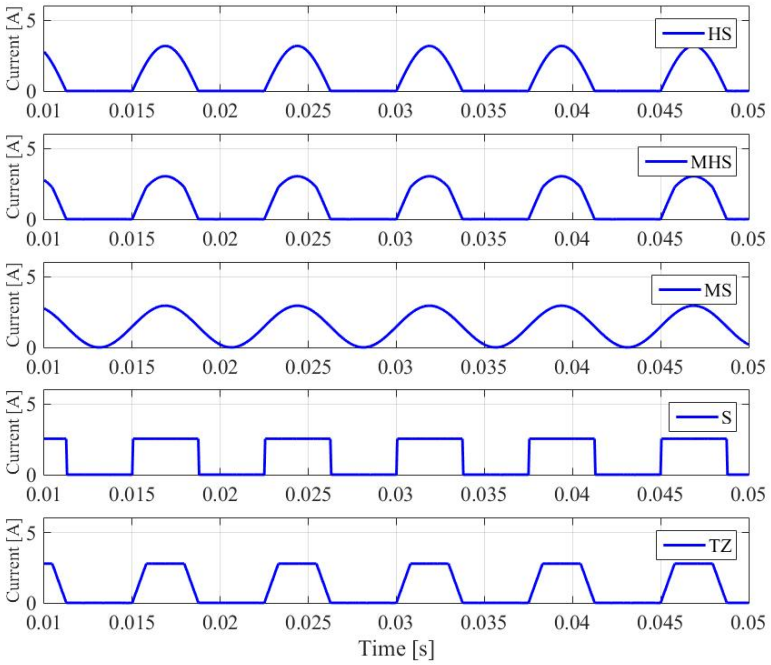

Figure 2.47: Current waveform of different current shapes at 1000 r/min

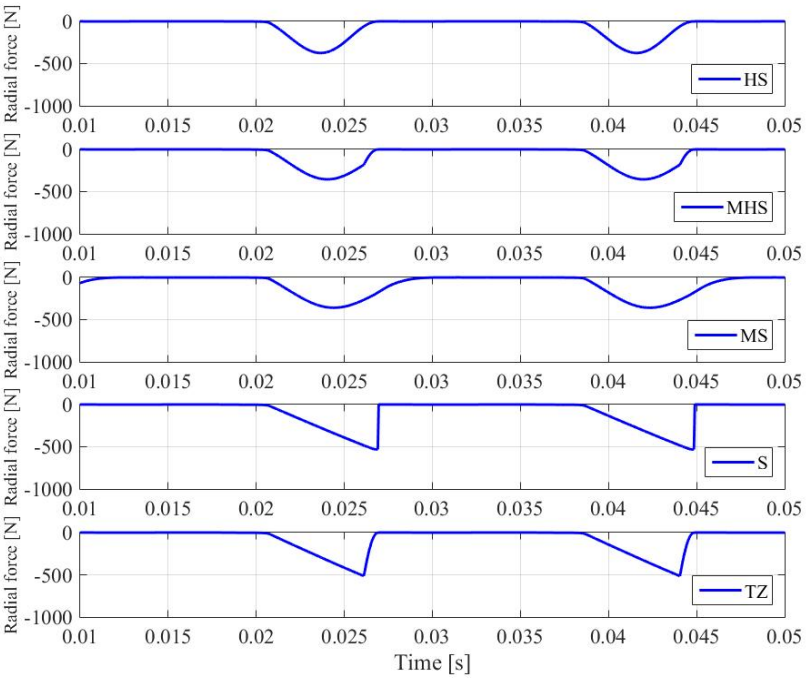

Figure 2.48: Radial forces acting on the single stator pole of different current shapes at 418 r/min

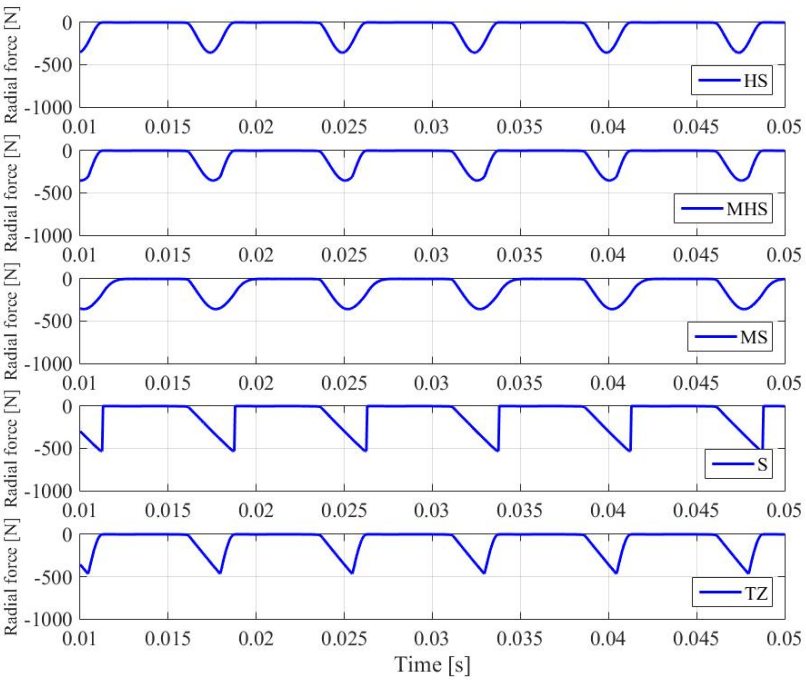

Figure 2.49: Radial forces acting on the single stator pole of different current shapes at 1000 r/min

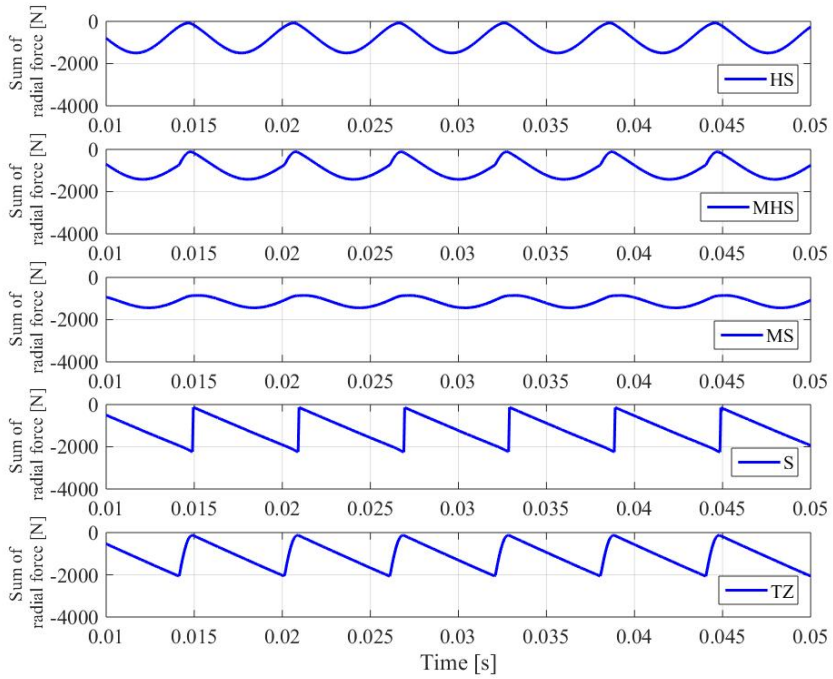

Figure 2.50: Sum of radial forces on the stator of different current shapes at 418 r/min

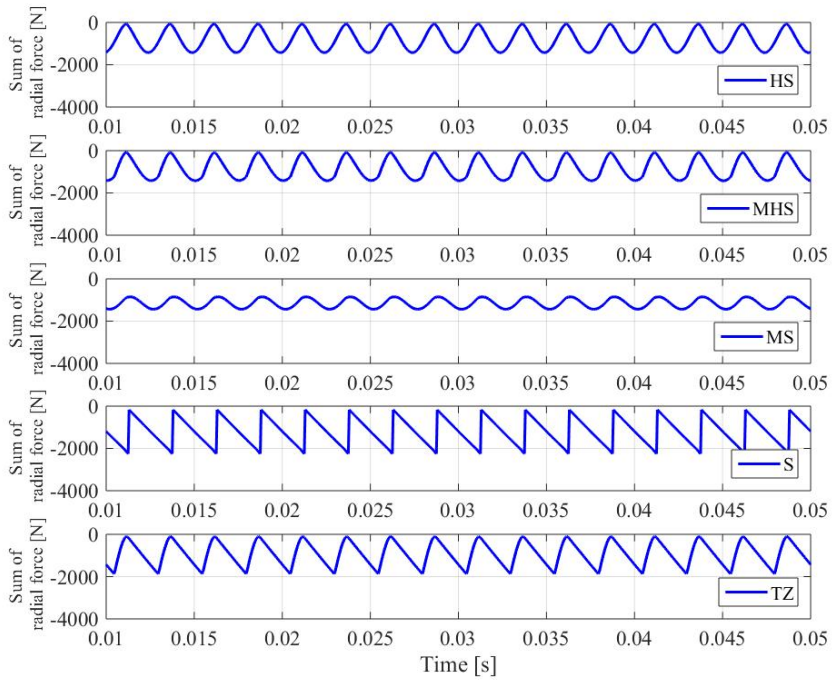

Figure 2.51: Sum of radial forces on the stator of different current shapes at 1000 r/min

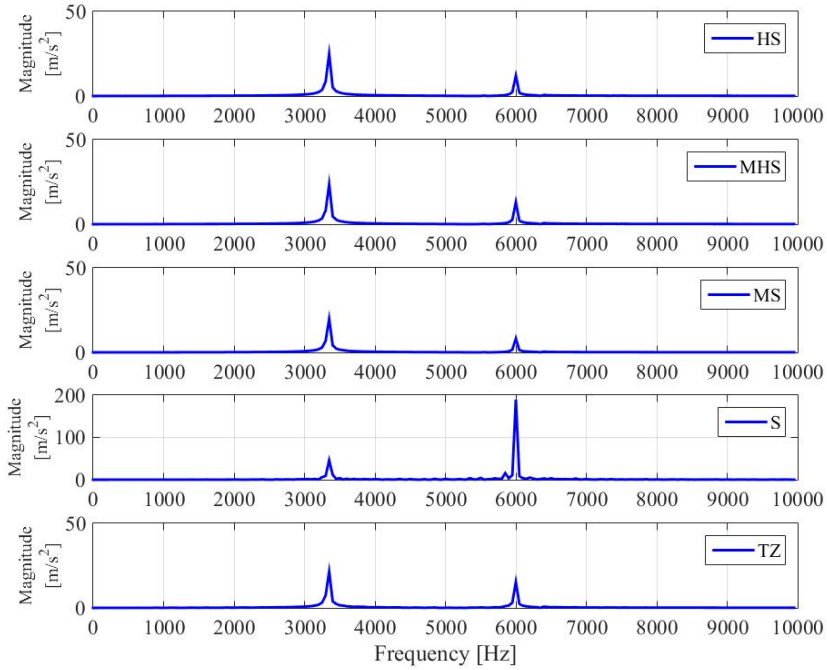

Figure 2.52: Magnitude of acceleration of different current shapes at 418 r/min

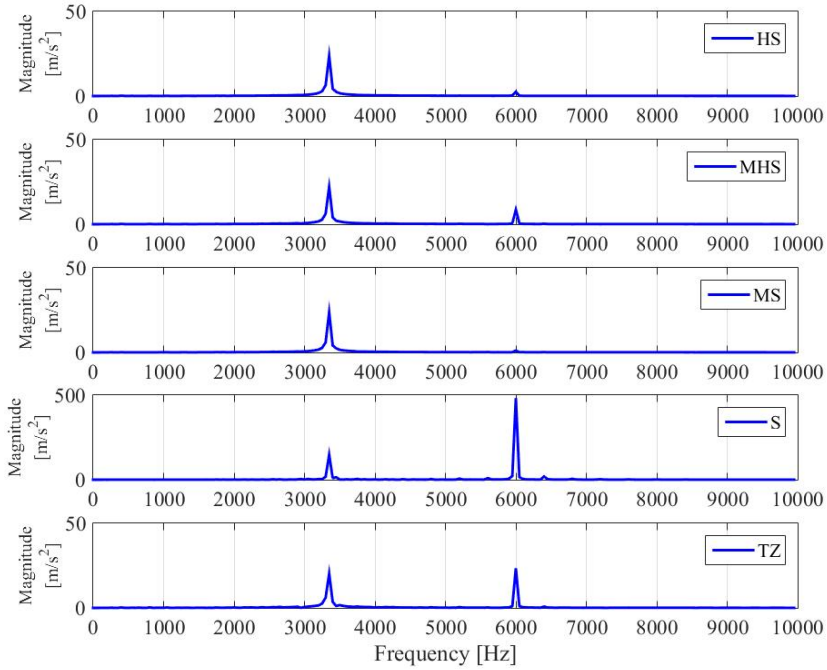

Figure 2.53: Magnitude of acceleration of different current shapes at 1000 r/min

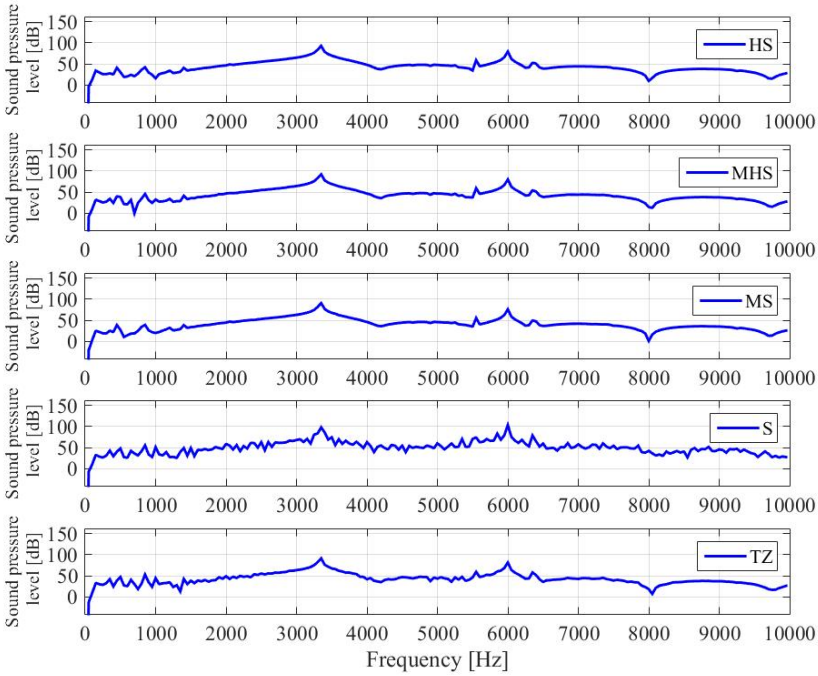

Figure 2.54: Sound pressure level of different current shapes at 418 r/min

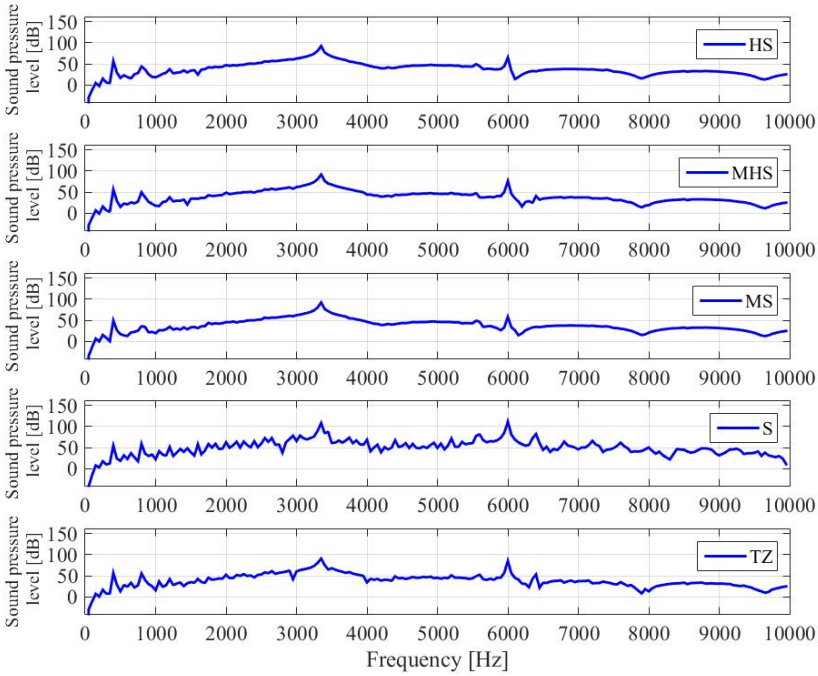

Figure 2.55: Sound pressure level of different current shapes at 1000 r/min

Table 2.9: Vibration characteristics of different current shapes at 418 r/min

HS	2^{nd} order mode	4^{th} order mode	0^{th} order mode
Acceleration [m/s^2]	0.09	24.92	11.98
Velocity [μm/s]	13.5	1184	317.9
Displacement [nm]	2.04	56.2	8.43
Sound pressure level [dB]	25.95	92.72	79.3
MHS	2^{nd} order mode	4^{th} order mode	0^{th} order mode
Acceleration [m/s^2]	0.09	23.65	13
Velocity [μm/s]	13.69	1124	344.9
Displacement [nm]	2.1	53.4	9.14
Sound pressure level [dB]	27.63	92.27	80.02
MS	2^{nd} order mode	4^{th} order mode	0^{th} order mode
Acceleration [m/s^2]	0.08	19.85	8.2
Velocity [μm/s]	11.41	942.8	218.2
Displacement [nm]	1.73	44.79	5.8
Sound pressure level [dB]	22.49	90.75	76.02
S	2^{nd} order mode	4^{th} order mode	0^{th} order mode
Acceleration [m/s^2]	0.12	46.05	189,3
Velocity [μm/s]	17.69	2188	5021
Displacement [nm]	2.68	103.9	133.2
Sound pressure level [dB]	34.14	98.03	103.4
TZ	2^{nd} order mode	4^{th} order mode	0^{th} order mode
Acceleration [m/s^2]	0.06	21.4	15.33
Velocity [μm/s]	9.81	1017	406.5
Displacement [nm]	1.49	48.3	10.8
Sound pressure level [dB]	30.15	91.39	81.48

Table 2.10: Dynamic characteristics of different current shapes at 418 r/min

Parameter	HS	MHS	MS	S	TZ
Average torque [Nm]	2.67	2.62	2.61	2.52	2.56
Torque ripple rate	1.25	0.89	0.52	0.3	0.44
RMS phase current [A]	1.03	1.67	1.8	1.77	1.72
Maximum radial force on the pole [N]	374.5	355.0	359.1	531.6	514.4
Maximum sum of radial force [N]	1507	1434.2	1465.6	2269.4	2082.2
Ripple rate of sum of radial force	1.63	1.42	0.53	1.82	1.85

Table 2.11: Vibration characteristics of different current shapes at 1000 r/min

HS	2^{nd} order mode	4^{th} order mode	0^{th} order mode
Acceleration [m/s^2]	0.09	23.73	2.48
Velocity [μm/s]	14.0	1128	65.7
Displacement [nm]	2.13	53.6	1.74
Sound pressure level [dB]	21.99	92.28	65.34
MHS	2^{nd} order mode	4^{th} order mode	0^{th} order mode
Acceleration [m/s^2]	0.12	22.07	8.61
Velocity [μm/s]	18.93	1048	228.4
Displacement [nm]	2.87	49.8	6.06
Sound pressure level [dB]	17.23	91.64	76.43
MS	2^{nd} order mode	4^{th} order mode	0^{th} order mode
Acceleration [m/s^2]	0.09	23.74	1.1
Velocity [μm/s]	14.13	1128	29.28
Displacement [nm]	2.14	53.57	0.78
Sound pressure level [dB]	26.98	92.28	57.91
S	2^{nd} order mode	4^{th} order mode	0^{th} order mode
Acceleration [m/s^2]	0.47	147.4	482.1
Velocity [μm/s]	71.61	7002	12790
Displacement [nm]	10.86	332.6	339.2
Sound pressure level [dB]	41.58	108.2	111.5
TZ	2^{nd} order mode	4^{th} order mode	0^{th} order mode
Acceleration [m/s^2]	0.24	20.3	23.42
Velocity [μm/s]	36.36	964.3	621.2
Displacement [nm]	5.51	45.81	16.48
Sound pressure level [dB]	36.91	90.92	85.18

Table 2.12: Dynamic characteristics of different current shapes at 1000 r/min

Parameter	HS	MHS	MS	S	TZ
Average torque [Nm]	2.52	2.51	2.59	2.53	2.55
Torque ripple rate	1.28	1.08	0.56	0.3	0.75
RMS phase current [A]	1.54	1.57	1.77	1.76	1.62
Maximum radial force on the pole [N]	357.3	353.8	358.5	532.0	467.0
Maximum sum of radial force [N]	1444.6	1437.4	1458.0	2275.2	1892.6
Ripple rate of sum of radial force	1.68	1.6	0.52	1.74	1.92

2.4 Conclusion

This literature review has indicated that the techniques of acoustic noise reduction of the SRM have been divided into two main techniques: I) active vibration cancellation technique which is a noise reduction method using modified control algorithm techniques and II) passive vibration cancellation technique which is a procedure to decrease noise level by structural machine design techniques. These two techniques of vibration cancellation are designed based on the variables that influence vibration and acoustic noise in the other technique. The two techniques have never been investigated together in any study aiming to identify the variables influencing vibration and acoustic noise. Furthermore, the relationship between the machine dimensions and excitation conditions is not explicit and must be investigated in-depth.

The simulation results of acoustic noise generation enabled the investigation of the original source of vibration generation in SRMs that has done in this thesis. The effects of magnetic and magnetostrictive forces on the vibration of the SRM stator core have observed and compared. Although the level of the magnetostrictive forces is many times higher than that of the magnetic forces, the effect of the magnetostrictive forces on stator vibration is less significant compared with the effect of the magnetic force, except at some specific frequencies. The magnetic forces act on an elastic structure, which has low stiffness, of the stator core, while the magnetostrictive forces mainly act on the material itself, which has high stiffness. In the components of magnetic force, the force in the radial component is higher than that in the tangential component. From this analysis, it can be concluded that the main source of the vibration in an SRM is caused by the radial component of the magnetic force, or the radial force.

Changing the turn-off angle leads to a much higher vibration and acoustic noise in a 12/8 SRM more than does adjusting the turn-on angle. The harmonic content of the radial force in an SRM is a severe problem, and it is difficult to avoid coincidence between the natural frequencies of the vibration mode and the harmonic contents of the radial force frequencies in a wide speed range operation. Different shapes of the excitation current of a 12/8 SRM can create different harmonic contents of radial

force frequency, and that can prevent the harmonic contents from coinciding with the frequency of the vibration mode of the SRM. The modified sinusoidal current shape gives a low amplitude of harmonic contents of radial force frequency at a dominant vibration mode of 12/8 SRM.

Increasing the stiffness of the SRM structure by increasing the stator yoke thickness can shift the frequency of a vibration mode to a higher value. SRMs should be designed such that the frequency of each vibration mode is as high as possible. In addition, it is reported that the acoustic noise in an SRM can be reduced by choosing a suitable control method (i.e. a suitable commutation angle and current shape). However, some choices of control method has negative effects on the machine such as generating high torque ripple and high copper losses and reducing performance of the machine. The frame of the machine also has a significant impact on the dominant mode of the vibration, as the frame can increase the level of natural frequency of the stator.

Chapter 3.
Comparison of Vibration and Magnetic Force Behaviours

Previous research into vibration and acoustic noise in SRMs [2,13,14,58] shows that the main source of the vibration and acoustic noise is the radial magnetic force. To understand the magnetic force characteristics generated in SRMs and how these relate to vibration and acoustic noise, various techniques for vibration and acoustic noise prediction have been presented. In [44] and [40], modal analysis techniques were presented to calculate the radial forces, natural modes of vibration, and acoustic noise in SRMs. In addition, in [59] and [60], an analytical model for vibration and acoustic noise prediction, based on the mechanical impulse response of the SRM, was developed. A multiphysics analysis, which combines both electromagnetic analysis and structural analysis to calculate acoustic noise, was proposed for noise prediction in [43,49,50]. This technique is widely used for the study of vibration and magnetic force behaviours in electrical machines.

In this chapter, multiphysics analysis was used to make compare the vibration behaviours of different SRM topologies. SRM topologies which have different winding arrangements and different structures were chosen. For comparison of winding arrangements, conventional short-pitched and fully-pitched windings were selected. The fully-pitched winding arrangement for SRMs was invented by Mecrow [61] and it showed that with this winding technique, the torque capacity of SRMs can be increased by 30 % compared with the conventional short-pitched winding. For comparison of different structures, a 12/8 conventional SRM and a segmental rotor SRM are chosen. Segmental rotor SRMs have also been investigated and demonstrated in [12,62,63]. SRM with segmental rotor construction improves torque capability per

volume by over 65 %, compared to a conventional SRM. Most of the publications on segmental rotor SRMs focus on optimization design for high torque density, winding arrangement investigation, and control method, while few published articles about vibration and acoustic noise emitted by this machine have been reported. In [64], the results of vibration and acoustic noise of a 12/8 segmental rotor SRM were presented, demonstrating that its noise emission is low compared to conventional SRMs of the same dimensions, but this work was done with different output powers. Load conditions should be consistent because vibration and noise emission depend on applied load.

The different SRM topologies for study in this chapter are listed below:

1) A 12/8 conventional SRM with short-pitched winding (12/8 CON SP)
2) A 12/8 conventional SRM with fully-pitched winding (12/8 CON FP)
3) A 12/8 segmental rotor SRM (12/8 SSRM)
4) A 12/10 single-tooth wound segmental rotor SRM (12/10 SSRM)

For each topology, the same cross-section, stator yoke thickness, and output power condition are considered. Geometries and dimensions of each SRM topology are illustrated in Fig. 3.1, Fig. 3.2, and Table 3.1. Firstly, both static and dynamic magnetic force densities are calculated using the 2D FE method based on hysteresis current control at the same output power. Then force density results are transferred into a 3D structural analysis to predict acceleration, frequency, and natural modes of stator structure. Finally, acoustic noise calculation is performed using 3D BEM. The simulation results for the SRM topologies are compared and discussed. The details of magnetic and structural FE simulation are shown in Appendix B.

3.1 Magnetic Radial Force Generation

The winding configuration of 12/8 CON FP and 12/8 SSRM is fully-pitched, where each coil spans three adjacent stator poles. The winding arrangements for 12/8 CON SP and 12/10 SSRM are short-pitched, where each coil is wound around a single

Table 3.1: Dimensions of different SRM topologies

Parameter	12/8 CON SP	12/8 CON FP	12/8 SSRM	12/10 SSRM
No. of stator/rotor poles	12/8	12/8	12/8	12/10
Stator outer diameter [mm]	150	150	150	150
Stator inner diameter [mm]	130	130	130	130
Rotor outer diameter [mm]	90.8	90.8	90.8	90.8
Shaft diameter [mm]	40	40	32	32
Air gap [mm]	0.3	0.3	0.3	0.3
Stack length [mm]	150	150	150	150
Number of turns per phase	204	204	300	270
Number of coils per phase	4	2	2	2
Coil span	1 slot	3 slots	3 slots	1 wide tooth
Phase resistance [Ω]	0.9 Ω	1.8 Ω	3.58 Ω	2.56 Ω

stator pole, as shown in Fig. 3.1(left). In the segmental rotor machine, this provides a short magnetic flux path which does not flow through the whole stator like in a conventional SRM. Fig. 3.1(right) shows the maximum magnetic forces acting on stator poles in each SRM topology at the aligned position. Eight stator poles in the 12/8 SSRM and six stator poles in the 12/10 SSRM are excited by magnetic radial forces, whereas these forces in 12/8 CON SP and 12/8 CON FP act on four stator poles. Magnetic radial forces are the major cause of the high vibration generation in SRMs and the maximum radial forces appear in SRMs at the aligned position.

To observe the force distribution in SRM topologies, a simplified and linear analytical model analysis from [65,66] proceeds under the assumption that magnetic saturation is neglected and therefore, flux linkage and co-energy can be roughly expressed as Equation (3.1) and (3.2), respectively.

$$\lambda \approx Li = \frac{\mu_0 N_\mathrm{p}^2 r_\mathrm{gap} l_\mathrm{stk} \beta_\mathrm{ovl} i}{g} \tag{3.1}$$

$$W' = \frac{1}{2} L i^2 = \frac{\mu_0 (N_\mathrm{p} i)^2 r_\mathrm{gap} l_\mathrm{stk} \beta_\mathrm{ovl}}{2g} \tag{3.2}$$

where N_p, g, r_gap, l_stk, and β_ovl are the number of turns, air gap length, rotor radius to the air gap, the stack length and the poles overlapping angle between stator and rotor pole, respectively.

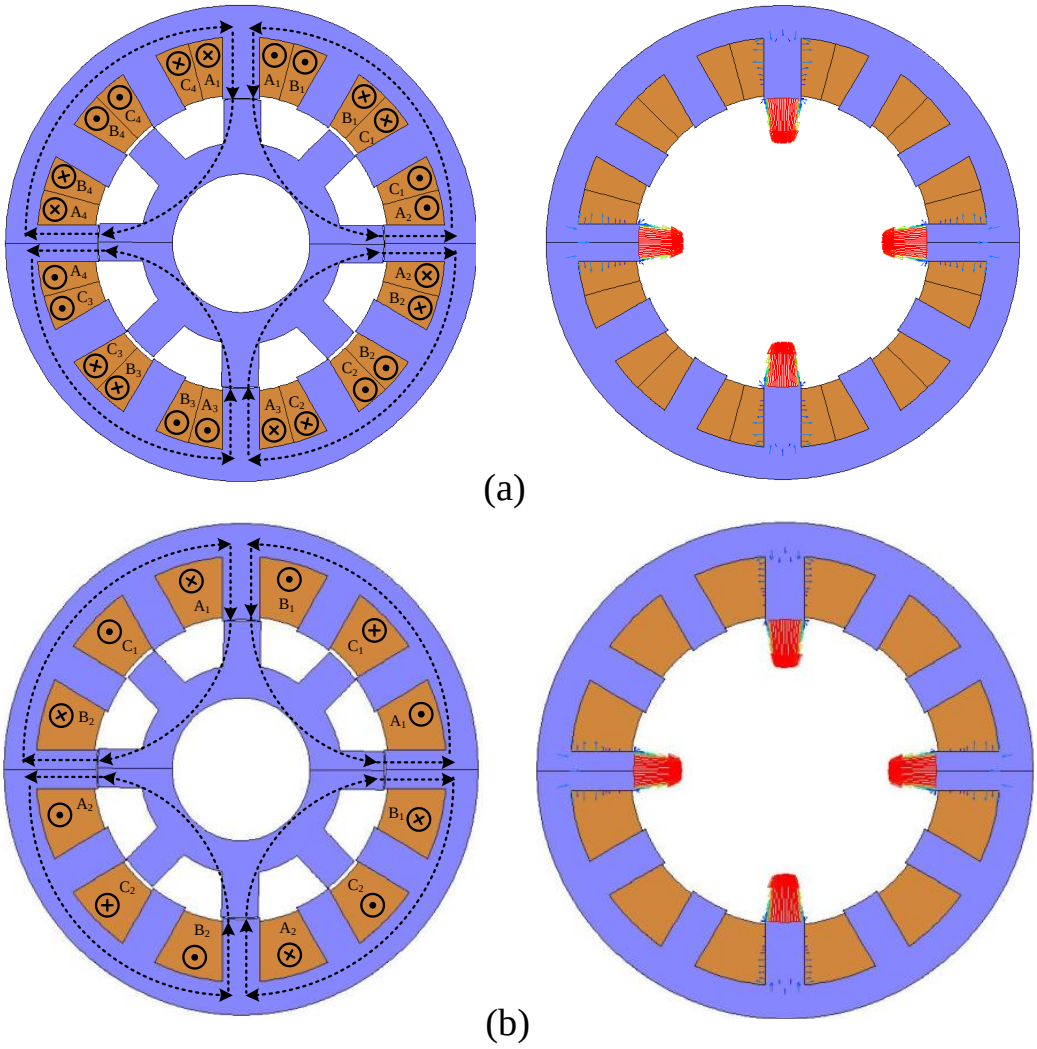

Figure 3.1: Magnetic flux paths (left) and magnetic force (right) acting on stator poles at aligned position: (a) 12/8 conventional SRM with short-pitched winding with phase A excitation and (b) 12/8 conventional SRM with fully-pitched winding with phase A and B excitation

Thus, the radial force acting on each stator pole can be calculated by

$$F_{\mathrm{rad}} = \frac{\partial W'}{\partial g} = -\frac{\mu_0 (N_{\mathrm{p}} i)^2 r_{\mathrm{gap}} l_{\mathrm{stk}} \beta_{\mathrm{ovl}}}{2g^2} \tag{3.3}$$

The torque which is produced in each stator pole can be calculated in the same manner by

$$T = \frac{\partial W'}{\partial \theta} = \frac{\mu_0 (N_{\mathrm{p}} i)^2 r_{\mathrm{gap}} l_{\mathrm{stk}}}{2g} \tag{3.4}$$

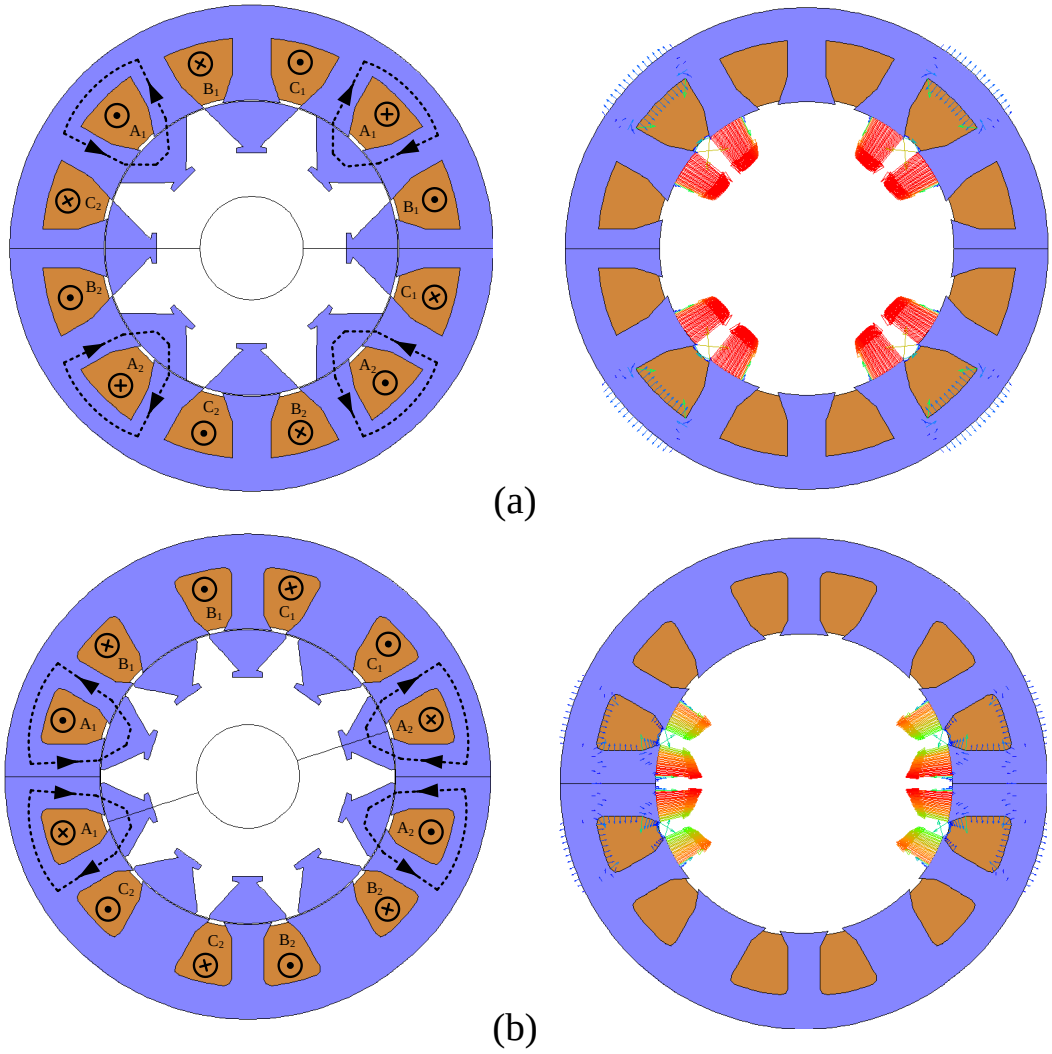

Figure 3.2: Magnetic flux paths (left) and magnetic force (right) acting on stator poles at aligned position: (a) 12/8 segmental rotor SRM with phase A excitation and (b) 12/10 single-tooth wound segmental SRM with phase A excitation

From Equation (3.3) and (3.4), the relationship between torque and radial force is approximately given by

$$F_{\text{rad}} \approx -\frac{T\beta_{\text{ovl}}}{g} \tag{3.5}$$

In this chapter, magnetic radial forces of each SRM topology are investigated in term of static and dynamic radial force generation.

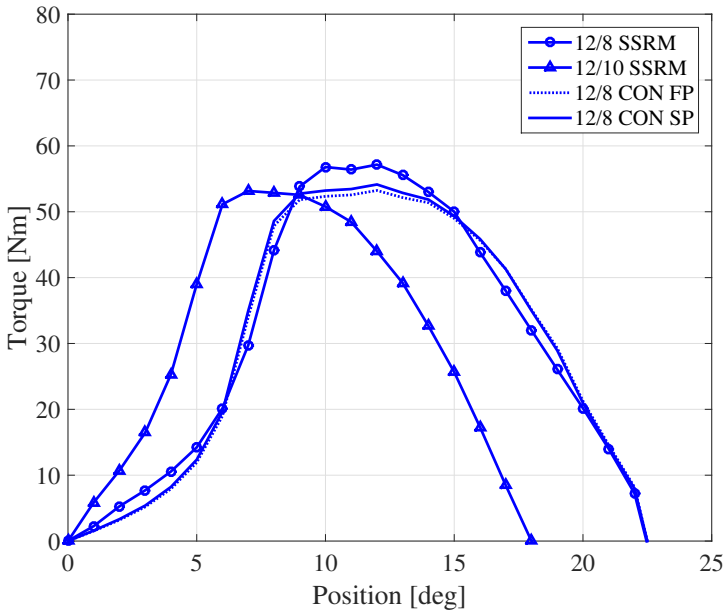

Figure 3.3: Phase torque of different SRM topologies

3.1.1 Static Radial Force

In this analysis, a comparison of radial force in each SRM topology can be observed with the Equation (3.5). This comparison shows that radial forces in each SRM topology only depend on the area of pole overlap, when operating with equal torque output and with air gap length. Fig. 3.1(left) shows the overlapping area between stator and rotor poles at aligned position in each SRM topology. Total pole overlap area is large in the segmental rotor SRM due to magnetic forces acting on eight stator poles in the 12/8 SSRM and six stator poles in the 12/10 SSRM, while the whole area of pole overlapp in both 12/8 conventional SRMs is small. These results in the segmental rotor SRM give high total radial forces compared with the conventional SRM.

On the other hand, the overlapping region of the single stator pole in the 12/8 SSRM is very similar to that in the 12/8 conventional SRM. The geometry of the 12/10 SSRM topology is different from the other topologies as it has two sizes of stator poles: a large (L) pole and a small (S) pole. The large stator pole provides a large area of pole overlap compared with the 12/8 conventional SRM structures, while there is a small area of overlap in the small stator pole of the 12/10 SSRM.

For this reason, two different magnitudes of the radial force are applied on the stator of the 12/10 SSRM. From the above discussion, the overlap area of single stator pole can be roughly expressed as

$$\beta_{\substack{\text{ovl,L pole}\\ \text{12/10 SSRM}}} \approx 2\beta_{\substack{\text{ovl,pole}\\ \text{12/8 CON SP}}} \approx 2\beta_{\substack{\text{ovl,pole}\\ \text{12/8 CON FP}}} \approx 2\beta_{\substack{\text{ovl,pole}\\ \text{12/8 SSRM}}} \approx 2\beta_{\substack{\text{ovl,S pole}\\ \text{12/10 SSRM}}} \tag{3.6}$$

Thus, the radial force exciting the single stator pole and total stator can be shown in the same manner in Equation (3.7) and (3.8), respectively.

$$F_{\substack{\text{rad,L pole}\\ \text{12/10 SSRM}}} \approx 2F_{\substack{\text{rad,pole}\\ \text{12/8 CON SP}}} \approx 2F_{\substack{\text{rad,pole}\\ \text{12/8 CON FP}}} \approx 2F_{\substack{\text{rad,pole}\\ \text{12/8 SSRM}}} \approx 2F_{\substack{\text{rad,S pole}\\ \text{12/10 SSRM}}} \tag{3.7}$$

The total radial forces in the 12/8 SSRM can be computed by summation of the radial forces acting on eight stator poles. In the 12/8 CON SP and 12/8 CON FP, the sum of radial force applied on four stator poles equals the total radial forces. Finally, the sum of the radial forces exciting the two large stator poles and four small stator poles is the total radial force in the 12/10 SSRM.

$$F_{\substack{\text{rad,total}\\ \text{12/10 SSRM}}} \approx F_{\substack{\text{rad,total}\\ \text{12/8 SSRM}}} \approx 2F_{\substack{\text{rad,total}\\ \text{12/8 CON SP}}} \approx 2F_{\substack{\text{rad,total}\\ \text{12/8 CON FP}}} \tag{3.8}$$

To provide an estimation of radial force in each case, 2D magnetic FE analysis is used for radial force calculation. Phase A of each machine is excited by constant current to obtain the same average torque at 30 Nm at the aligned position except that the SRM with fully-pitched winding is subjected to two phases (phase A and B) at the same time. The phase torque output of each SRM topology is shown in Fig. 3.3. The results are shown in Table 3.2. This table shows that the 12/8 SSRM produces a low magnitude of radial force acting on a stator pole, while a high magnitude of radial force is generated by the large pole of the 12/10 SSRM. In addition, the results also confirm that two different magnitudes of radial force are applied on the stator pole (large and small pole) of the 12/10 SSRM. A low magnitude of total radial force is generated by 12/8 CON SP and 2/8 CON FP, while the 12/8 SSRM and the 12/10 SSRM produce a higher magnitude of these forces.

Fig. 3.4 and 3.5 present the radial forces on a single stator pole and the total radial force when the rotor is moved from the unaligned position to the aligned

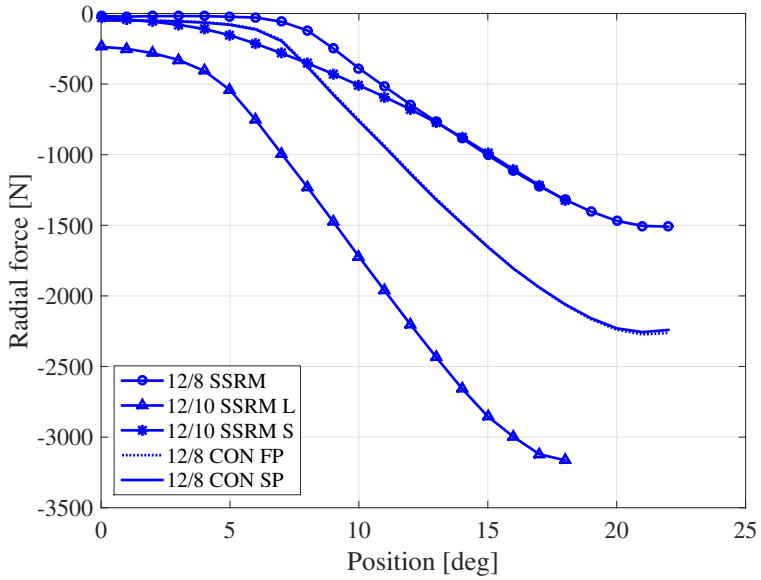

Figure 3.4: Static radial forces acting on a single stator pole in different SRM topologies

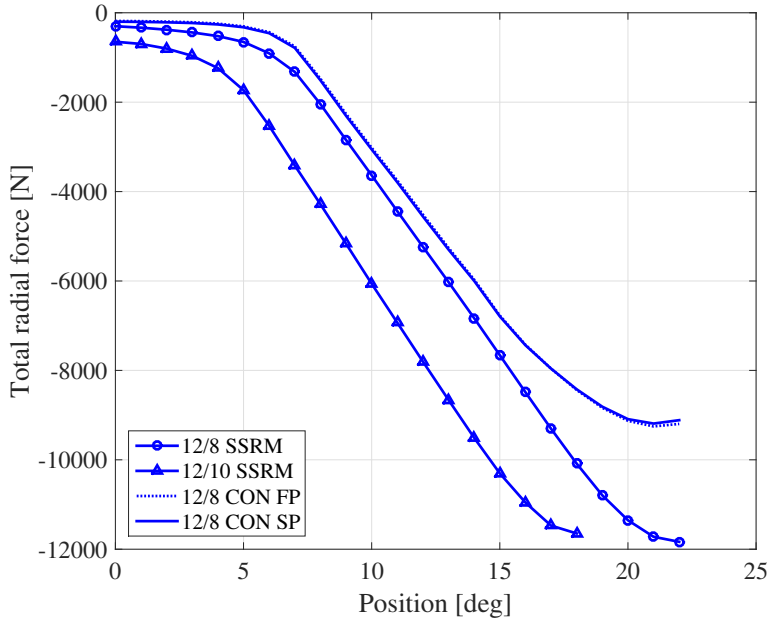

Figure 3.5: Total radial forces on the stator in different SRM topologies

position. The results also confirm the above discussion. Both results of radial forces on a single stator and total radial forces on the whole stator of 12/8 conventional structure with short-pitched and fully-pitched winding are very similar. This result

Table 3.2: Radial force at aligned position of different SRM topologies

SRM topology	Radial force acting on single stator pole [N]	Total radial force acting on stator [N]
12/8 CON SP	2256.20	9189.37
12/8 CON FP	2272.69	9252.75
12/8 SSRM	1509.36	11834.57
12/10 SSRM	3163.94 (Large pole) 1381.27 (Small pole)	11647.56

confirms that the effect of winding arrangement on the same SRM conventional structure does not have significant impact on the static radial force. On the other hand, modifying the SRM geometries as a 12/8 segmental rotor SRM can reduce the radial forces on the stator pole by sharing the total radial forces among eight stator poles rather than the four stator poles in a 12/8 conventional SRM.

3.1.2 Dynamic Radial Force

This section shows the radial force behaviours in each case when the motors are operated at the same output power (1.6 kW) at different speeds of 500 r/min with load torque 30 Nm and 1000 r/min with load torque 15 Nm. Both are operated under hysteresis current control with the same hysteresis band and a 580 Vdc link voltage selected for this analysis. It is known that the turn-off angle has a significant impact on vibration and acoustic noise generation in SRMs. This is due to the maximum magnitude of radial force, being apparent at this stage. Therefore, the turn-off angles of each topology at any speed are assigned at the same condition.

The control parameters in each case are as follows:

1) 500 r/min: Advance turn-on angle = 0 degrees, conduction period = 22.5 degree in 12/8 CON SP and 12/8 SSRM, conduction period = 30 in 12/8 CON FP and conduction period = 18 degrees in 12/10 SSRM.

2) 1000 r/min: Advance turn-on angle = 0 degrees, conduction period = 22.5 degree in 12/8 CON SP and 12/8 SSRM, conduction period = 30 in 12/8 CON FP and conduction period = 18 degrees in 12/10 SSRM.

A 12/8 CON FP is operated under unipolar currents, then each winding is turned on for 2/3 of a cycle. For this reason, the conduction period of this topology is longer than that of 12/8 CON SP.

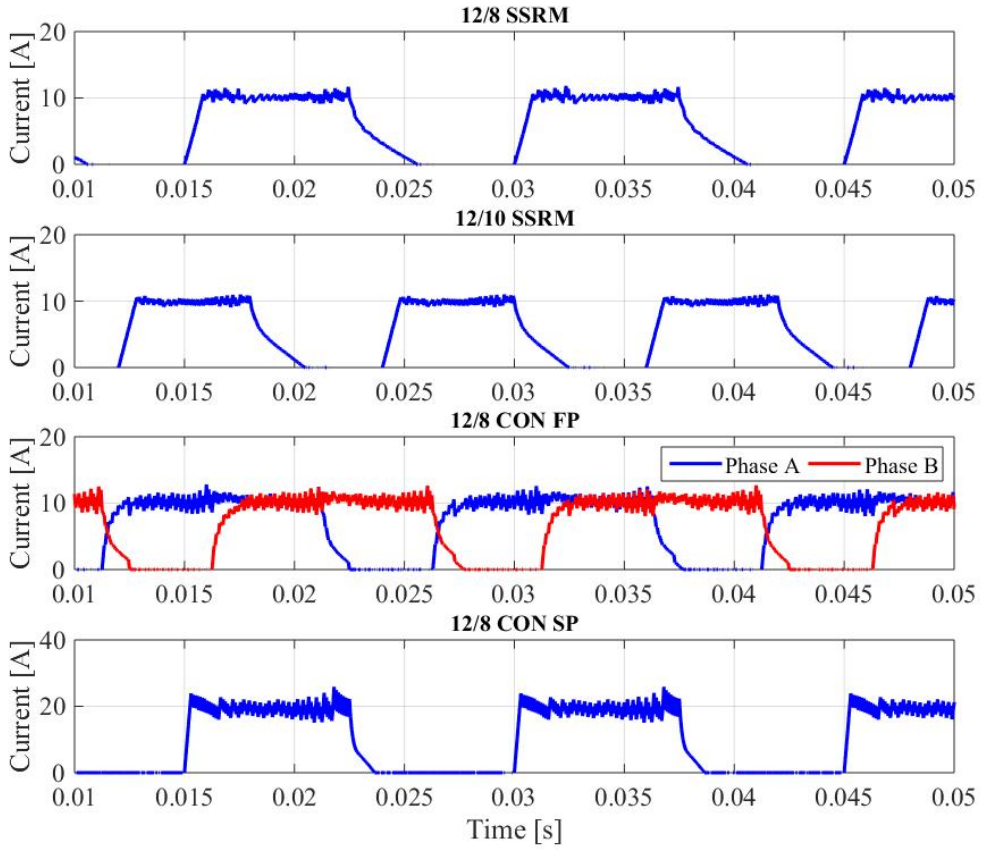

Figure 3.6: Phase current of different SRM topologies at 500 r/min

Fig. 3.6 and 3.7 show the phase current waveform of all SRM topologies under different operating speeds. For the 12/8 CON FP, a pair of phase current (Phase A and B of 12/8 CON FP in Fig. 3.6 and 3.7) are energised related to the rising of the mutual inductance of both phases. The torque waveforms at different speeds of each SRM topology is illustrated in Fig. 3.8 and 3.9.

For study of vibration in each SRM, the simulation of vibration and the acoustic noise is analysed using the multiphysics structural analysis as described in the previous chapter. The force densities are used as input to the 3D structural FE simulation to predict the frequency of the natural vibration mode and deformation

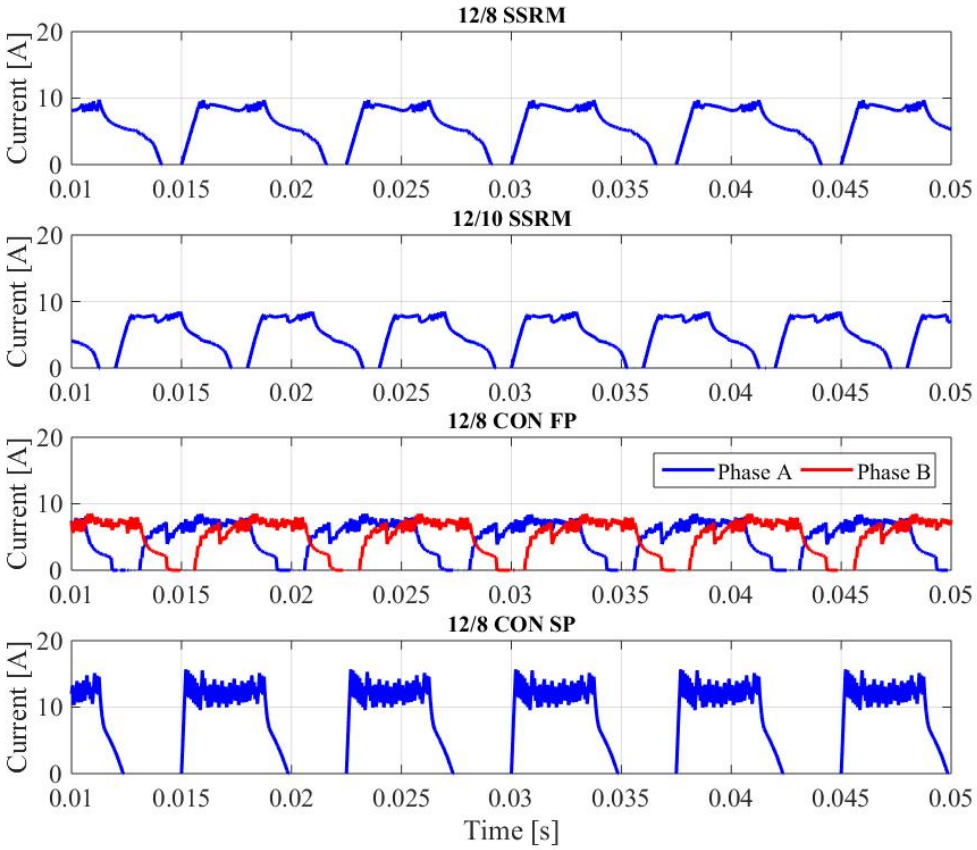

Figure 3.7: Phase current of different SRM topologies at 1000 r/min

of the SRM structures. In the next step, the vibration data obtained from the 3D structural analysis are used to calculate the noise emission in each SRM topology.

The mechanical properties of the stack material are: mass density $\rho = 7850$ kg/m^3, Young's modulus $E = 152$ GPa, and Poisson′s ratio $\nu = 0.3$; the aluminium frame and end bells have $\rho = 2770$ kg/m^3, $E = 71$ GPa and $\nu = 0.33$. The probe of acceleration, velocity, and displacement is on the casing behind the stator pole. The sound pressure level probe is fixed at one side of the stator at 300 mm distance. The vibration and acoustic noise simulation is discussed in next section.

3.2 Comparative Results

The radial force on a single stator and the sums of radial forces at different rotor speeds are illustrated in Fig. 3.10-3.13, respectively. Fig. 3.14 and 3.15 show the

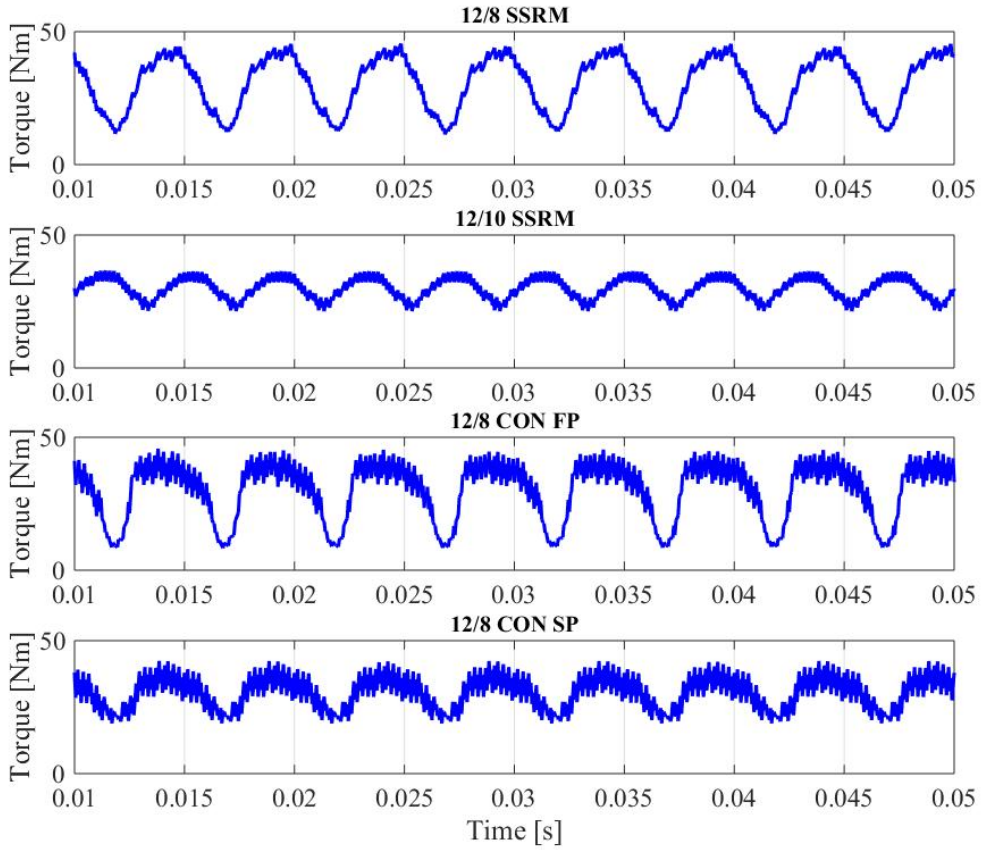

Figure 3.8: Total torque of different SRM topologies at 500 r/min

radial force amplitudes exciting on a single stator pole in the frequency domain. The sum of radial forces are also presented in Fig. 3.16 and 3.17.

At a running condition of 500 r/min, the maximum radial forces exciting each pole of both machines (12/8 CON SP and 12/8 CON FP) are 2208 and 2077 N, respectively with discontinuous radial force waveforms. The minimum amplitude of these forces can be seen in the 12/8 SSRM at 1594 N and a small pole of the 12/10 SSRM at 1430 N with continuous radial force waveform. The high level of radial force on the stator pole generated by 12/10 SSRM is 2710 N. Furthermore, both segmental rotor SRMs produce high amplitudes of the sum of radial forces close to 12000 N compared with the conventional SRM with fully-pitched winding, which are approximately 8309 N and 9288 N in short-pitched windings. However, the ripple rate of the sum of radial forces of conventional SRMs is higher than that of segmental

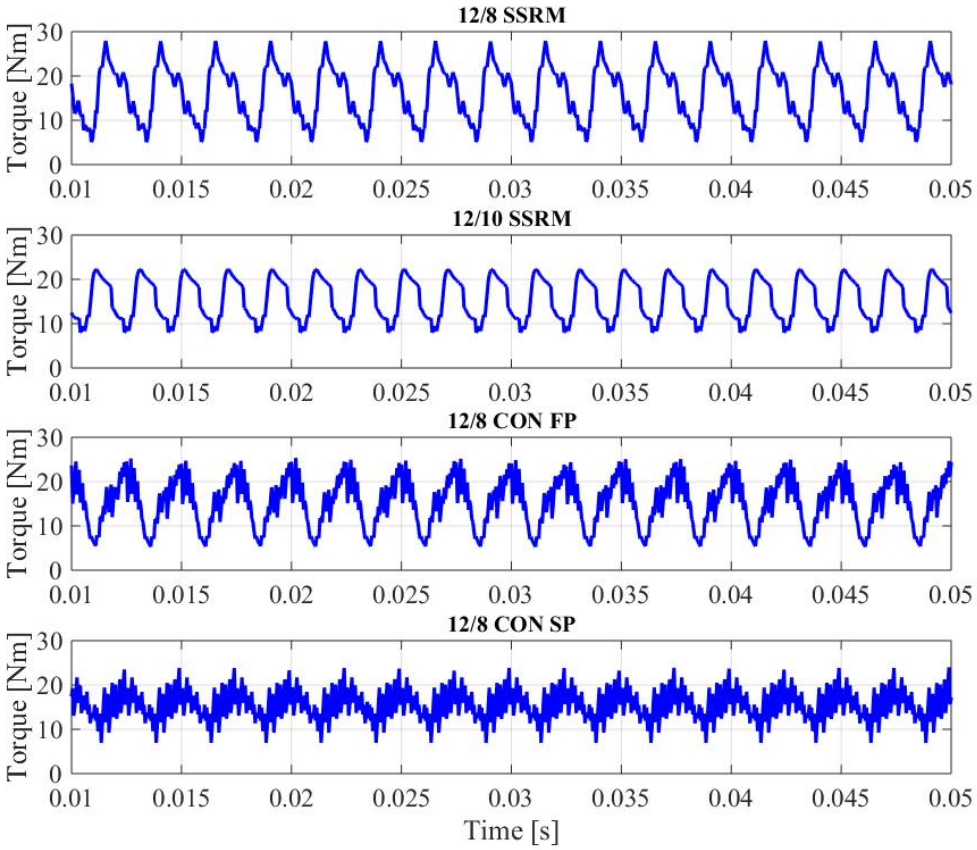

Figure 3.9: Total torque of different SRM topologies at 1000 r/min

rotor SRMs. The ripple rate of the sum of radial forces is high in 12/8 conventional SRMs using fully-pitched winding type at 1.74, whereas the short-pitched winding type has a ripple rate of 1.02. In segmental rotor SRMs, the ripple rate is low at 0.57 in both the 12/10 SSRM and the 12/8 SSRM. The ripple rate of the sum of the radial force waveform can be calculated as

$$Ripple\ rate = \frac{Maximum\ value - Minimum\ value}{Average\ value} \tag{3.9}$$

In a running condition at 1000 r/min, the maximum radial force on a single stator pole of all topologies decreases. Excluding the 12/8 SSRM, the radial forces are similar to those observed when operating at 500 r/min at approximately 1590 N. The 12/10 SSRM also gives a high amplitude of radial force on the stator pole, nevertheless, it shows a low ripple rate of the sum of radial forces at 0.24. The 12/8 conventional SRMs still create a high ripple rate of the sum of radial forces at 1.29

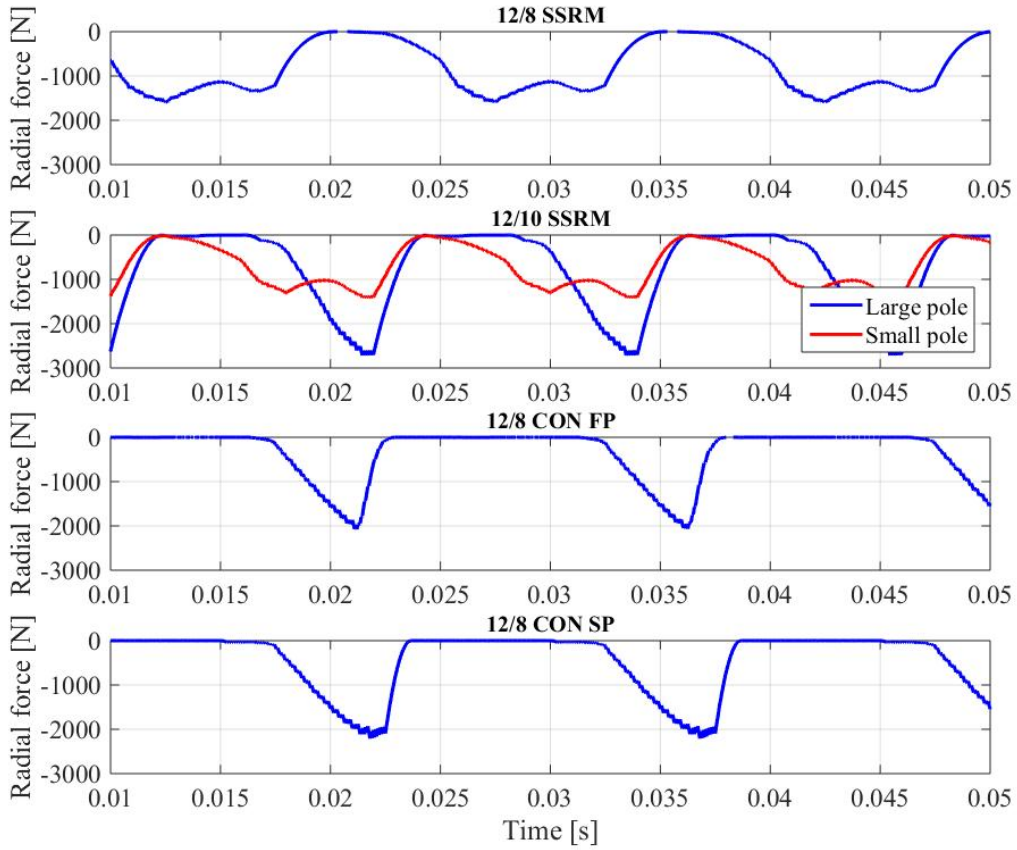

Figure 3.10: Radial forces acting on the single stator pole in different SRM topologies at 500 r/min with load torque = 30 Nm

in the fully-pitched and 0.73 in the short-pitched winding arrangements. The SRMs with segmental rotor structures can decrease the ripple rate of the sum of radial force as shown at both operating speeds. At both speeds, the 12/10 SSRM produces higher frequency of radial force, this is a result of the higher number of rotor poles than the other topologies. The waveforms in Fig. 3.14-3.17 show that 12/8 CON SP and 12/8 CON FP have a high amplitude of high order harmonics, compared with the 12/8 SSRM and the 12/10 SSRM at all speeds, whereas a high amplitude of low order harmonics appears in the 12/10 SSRM. Moreover, the third-harmonic content of the sum of radial forces which is generally created by three-phase SRMs has significant effect, generating high vibration levels on the SRM when corresponding with the natural frequency modes of the stator.

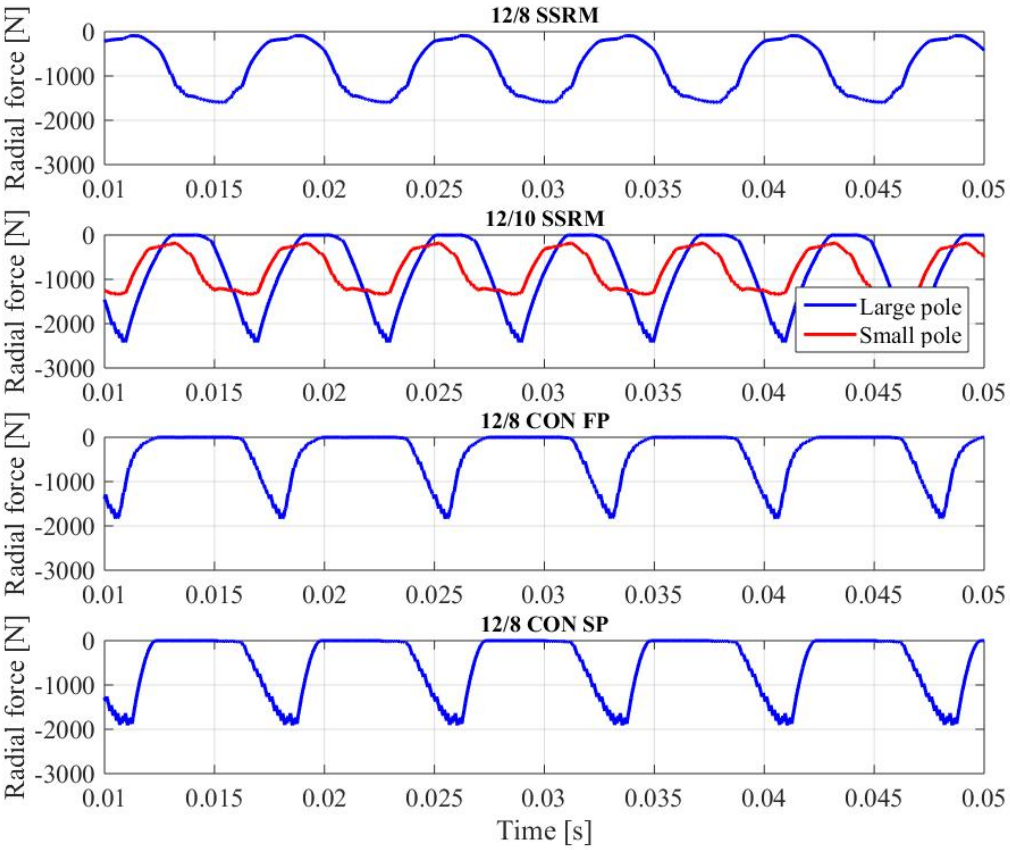

Figure 3.11: Radial forces acting on the single stator pole in different SRM topologies at 1000 r/min with load torque = 15 Nm

This effect is a result of a high ripple rate of the sum of radial forces produced in SRMs. Most of the previous research on noise reduction in SRMs has proposed eliminating the third-harmonic content [67] by modifying the current shape to reduce the sum of radial force ripple. The frequency of the third-harmonic component ($3^{rd}F_n$) which varies with rotational speed of three-phase SRMs can be given by

$$3^{rd}F_n = Number\ of\ phases \times \left[\frac{Speed\ [r/min]\ \times\ Number\ of\ rotor\ poles}{60}\right] \quad (3.10)$$

A high amplitude of high order harmonics is generated by 12/8 conventional SRMs. This is caused by discontinuous waveforms and high ripple rates of the radial forces generated in this topology. In the electrical machine, where the high harmonic radial forces coincide with the natural frequency modes of the stator, this results in the production of high vibration and acoustic noise.

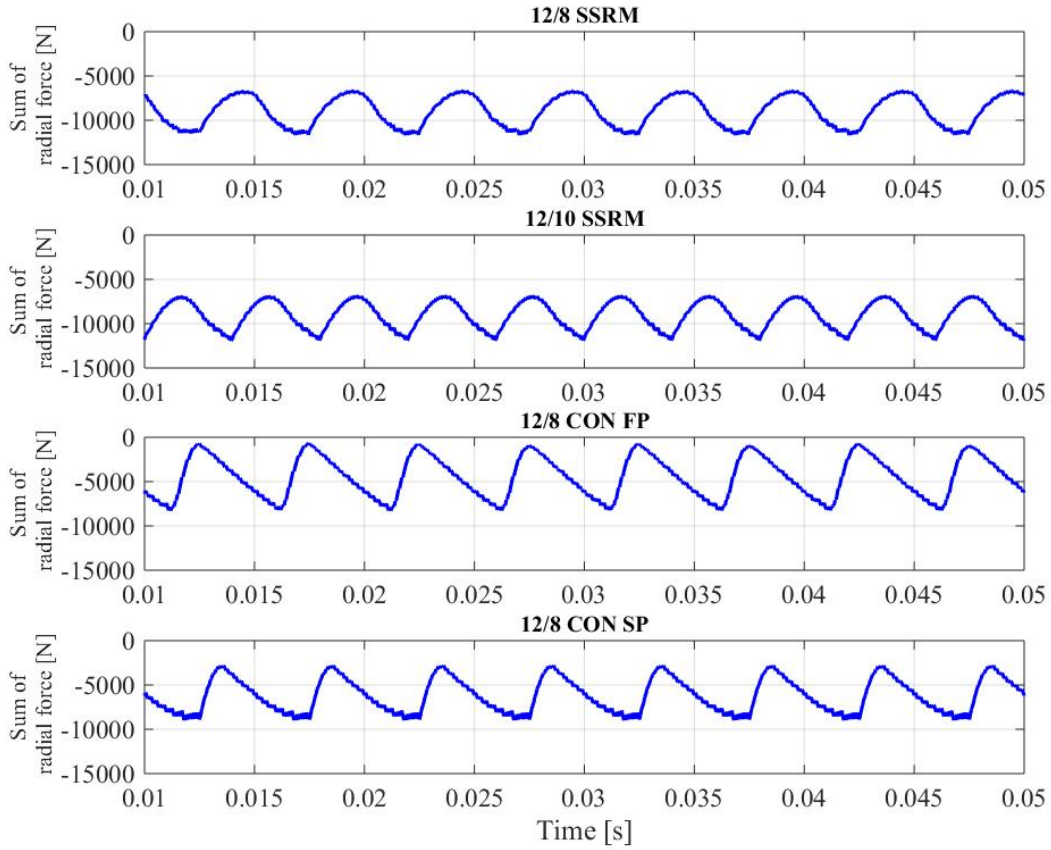

Figure 3.12: Sum of radial forces acting on the stator in different SRM topologies at 500 r/min with load torque = 30 Nm

Fig. 3.20 and 3.22 show the acceleration and sound pressure levels in the frequency domain at 500 r/min. The comparisons of results of each SRM topology are summarised in Table 3.3 and 3.4, including velocity and deformation. The dominant modes of vibration in different SRM topologies are 7602 Hz and 8609 Hz in 12/8 CON SP and FP; 7215 Hz and 8371 Hz in 12/8 SSRM; and 2916 Hz, 7683 Hz, 8384 Hz, 8794, and 9272 Hz in 12/10 SSRM as shown in Fig. 3.18 and 3.19.

High magnitude of acceleration levels in 12/8 CON SP, 12/8 CON FP, and 12/8 SSRM occur in the fourth-order mode of stator natural frequency at 7602 Hz and 7215 Hz, whereas the 12/10 SSRMs have a high magnitude of acceleration in the second-order mode at 2916 Hz. In the 12/10 SSRM, the stator pole structures consist of two different pole shapes (large pole and small pole). The magnetic radial force

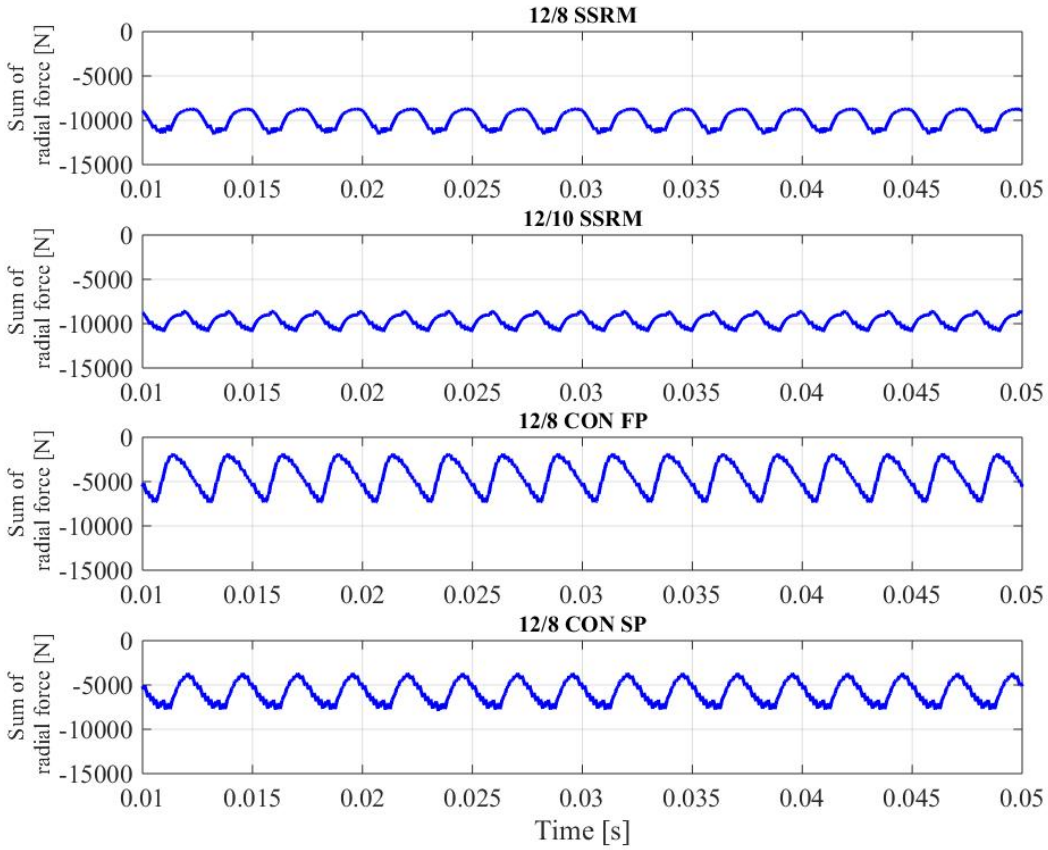

Figure 3.13: Sum of radial forces acting on the stator in different SRM topologies at 1000 r/min with load torque = 15 Nm

acting on the large poles of 12/10 SSRMs has a higher magnitude than that acting on the small ones. Moreover, the waveforms of magnetic radial force in the large and small poles are also different, resulting in the various harmonic content productions. The bending of the small pole to large pole during operation tends to generate a high level of vibration due to the 12/10 SSRMs having different pole shapes and different levels of radial forces acting on each stator pole. From the vibration mode shape in Fig. 3.19 of the 12/10 SSRM, the major mode shape is second-order mode which corresponds to the magnetic flux path through its structures. However, other order modes conform to the movement of the stator pole when they attract each other. The comparisons of results in the frequency domain at 1000 r/min are summarised in Table 3.5 and 3.6. Fig. 3.21 and 3.23 show the acceleration and sound pressure

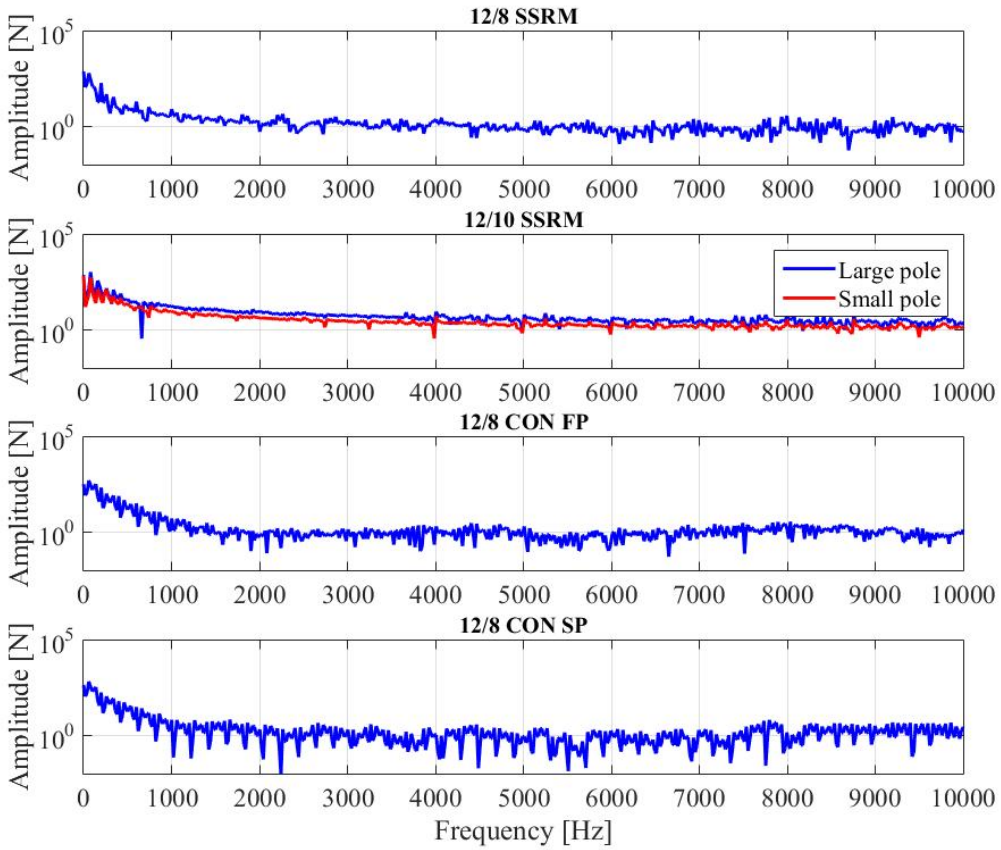

Figure 3.14: Radial force acting on the single stator pole in frequency domain at 500 r/min with load torque = 30 Nm

levels at 1000 r/min. The acceleration and sound pressure levels decrease in the segmental SRM topologies. Conversely, an increased magnitude of acceleration can be seen in the 12/8 conventional SRM, leading to the high sound pressure levels emitted. Especially in the 12/8 CON FP, the magnitude of sound pressure levels at the fourth-order mode slightly increases from 100.6 dB in low speed operation to 107.9 dB in high speed operation.

As a result, the fourth-order vibration mode of 12/8 conventional SRMs coincides with the high order harmonics of the radial force. Moreover, the spectrum of radial force in 12/8 CON confirms that the fourth-order mode is excited by the high amplitudes of the harmonic contents at 1000 r/min. It appears that the 12/10 SSRM shows lower magnitudes of sound pressure levels at 500 r/min and at 1000 r/min,

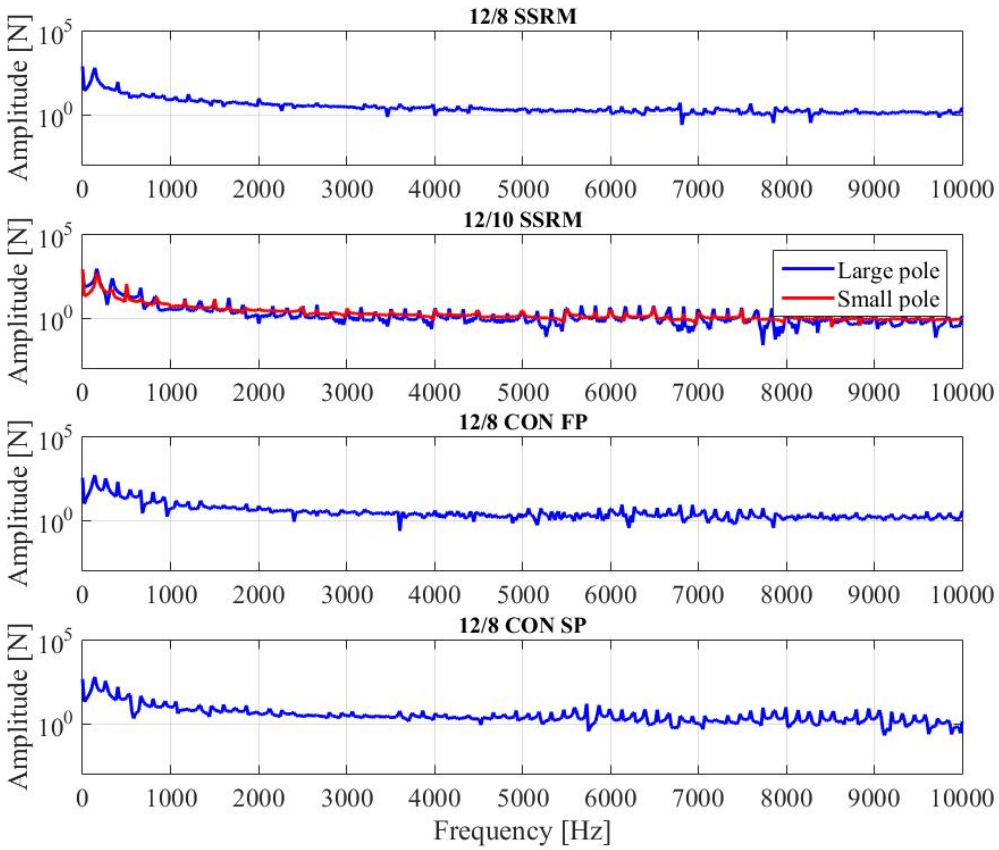

Figure 3.15: Radial force acting on the single stator pole in frequency domain at 1000 r/min with load torque = 15 Nm

and the 12/8 SSRM emits lower levels of sound pressure. As a result segmental rotor SRM topology produces a continuous radial force waveform which has the low amplitude of the high harmonic content and the low ripple rate of the sum of magnetic radial forces compared with the other topologies.

The characteristics of torque, RMS current, and magnetic radial forces at different rotor speeds of all SRM topologies are illustrated in Table 3.7 and 3.8. The high torque ripple rate produced by 12/8 CON FP and 12/8 SSRM due to these topologies have a strong magnetic flux density, while the other segmental rotor SRM has a low ripple rate of torque. In terms of the RMS current consumption, the 12/10 SSRM was applied with low RMS current compared with other SRM topologies and lower copper losses, which are a proportion to the power of RMS current squared.

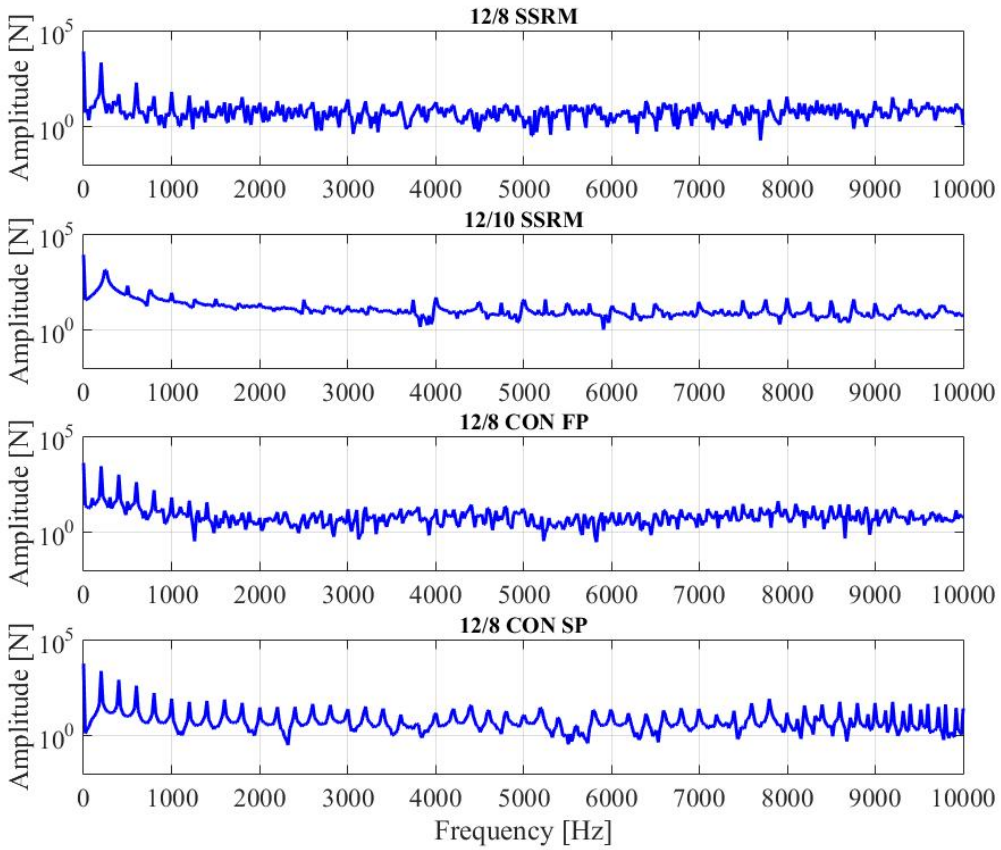

Figure 3.16: Sum of radial force acting on the stator in frequency domain at 500 r/min with load torque = 30 Nm

3.3 Conclusion

The comparison of radial magnetic force and vibration characteristics between conventional SRMs and segmental rotor configuration SRMs have been considered in this chapter. The segmental rotor SRM gives a low level of acoustic noise as it generates continuous radial forces exciting the stator pole and a low ripple rate of the sum of radial forces . The segmental rotor and fully-pitched winding arrangement leads to the generation of continuous radial force waveforms which have low amplitudes of the high order harmonic content, compared with the conventional 12/8 SRM (SP and FP), which have the same vibration mode at the fourth-order mode shape.

The 12/10 SSRM has the dominant vibration mode at low frequency. This is a

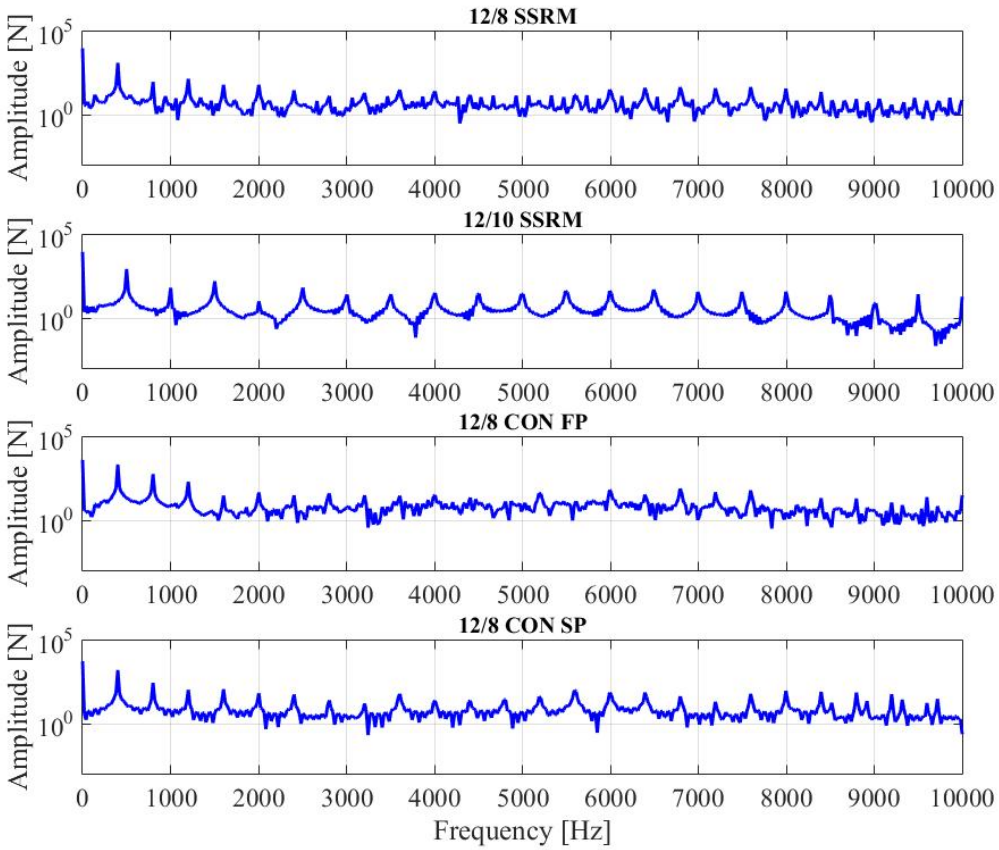

Figure 3.17: Sum of radial force acting on the stator in frequency domain at 1000 r/min with load torque = 15 Nm

second-order mode shape, which can cause high acoustic noise due to coincidence with a lower harmonic order of radial force, which has high amplitude at low harmonic order. This suggests that, to reduce acoustic noise, SRMs should be designed so that the frequency of vibration modes of the stator structure are as high as possible. The radial force waveform should be continuous waveform and a low ripple rate of the sum of radial forces should be achieved by modifying the stator/rotor configuration, winding arrangement or control method. The performance of the SRM should be considered a trade-off between acoustic noise and efficiency.

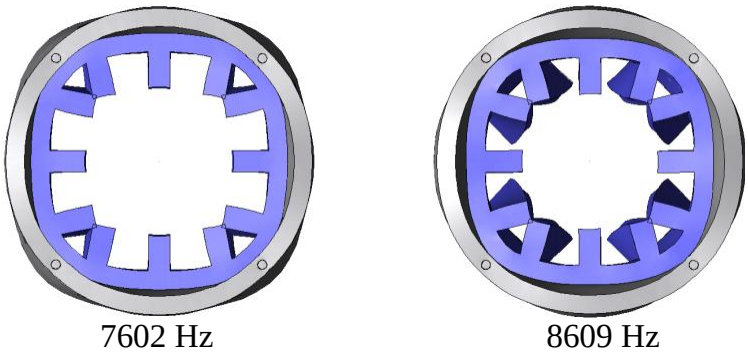

(a)

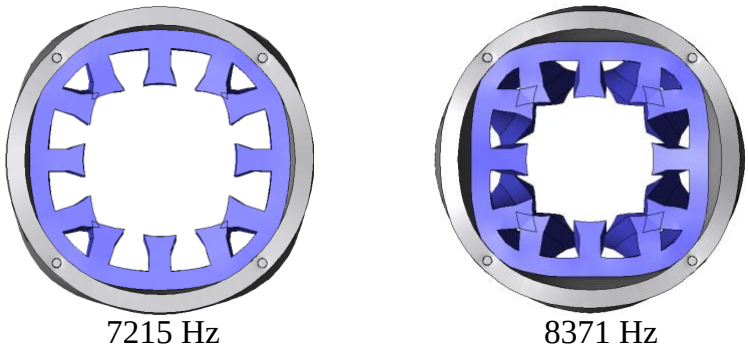

(b)

Figure 3.18: Dominant vibration mode shapes in each SRM topology: (a) 12/8 conventional SRM (12/8 CON SP and FP) and (b) 12/8 segmental rotor SRM

Table 3.3: Vibration characteristics of the 12/8 conventional SRM with short-pitched and fully-pitched windings at 500 r/min

Item	12/8 CON SP		12/8 CON FP	
Dominant natural frequency mode [Hz]	7602	8609	7602	8609
Acceleration [m/s^2]	125	161	388	124
Velocity [mm/s]	2.6	3.0	8.1	2.3
Displacement [nm]	170	42	55	55
Sound pressure level [dB]	90.77	96.08	100.6	93.81

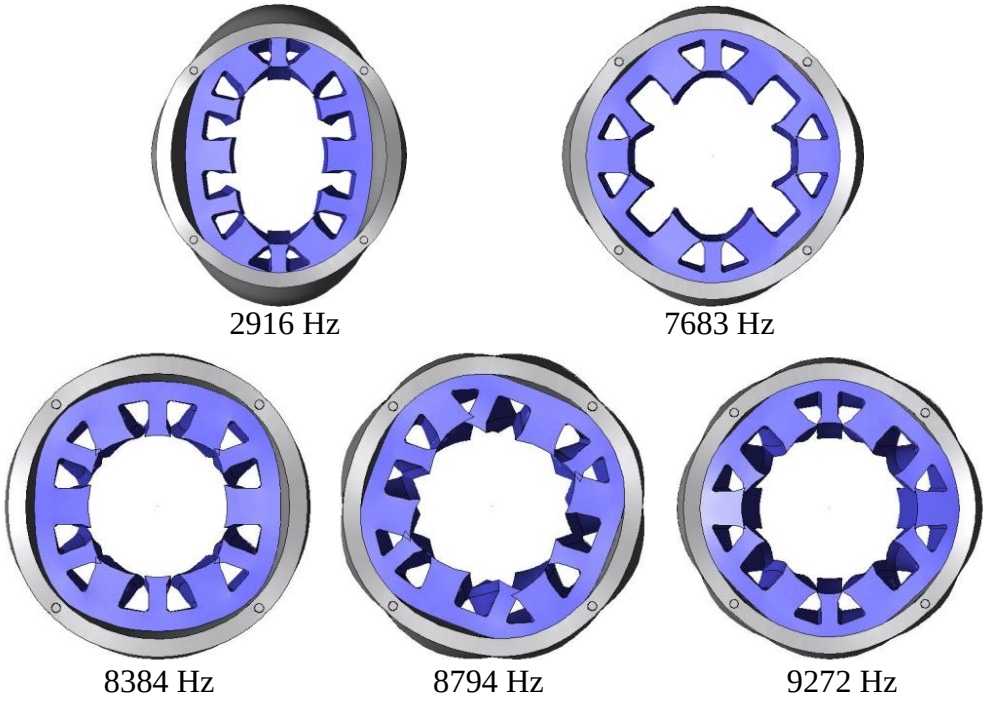

Figure 3.19: Dominant vibration mode shapes of the 12/10 single-tooth wound segmental rotor SRM

Table 3.4: Vibration characteristics of segmental rotor SRM at 500 r/min

Item	12/8 SSRM		12/10 SSRM				
Dominant natural frequency mode [Hz]	7215	8371	2916	7683	8384	8794	9272
Acceleration [m/s^2]	13	56	30	15	63	27	56
Velocity [mm/s]	0.28	1.1	1.6	0.3	1.2	0.5	1.0
Displacement [nm]	6.4	20	89.8	6.4	22.6	8.9	17
Sound pressure level [dB]	55	87.25	82.31	73.3	87.06	79.93	70.67

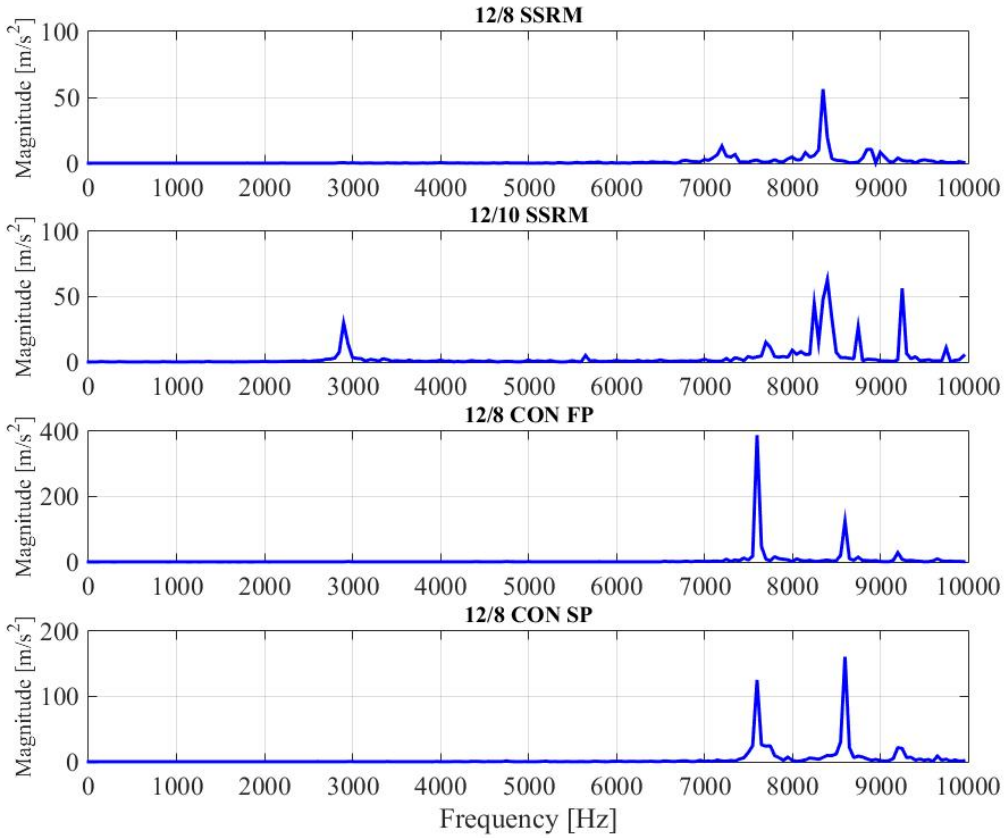

Figure 3.20: Magnitude of acceleration at 500 r/min with load torque = 30 Nm

Table 3.5: Vibration characteristics of the 12/8 conventional SRM with short-pitched and fully-pitched windings at 1000 r/min

Item	12/8 CON SP		12/8 CON FP	
Dominant natural frequency mode [Hz]	7602	8609	7602	8609
Acceleration [m/s^2]	1080	114	907	120
Velocity [mm/s]	22.6	2.1	19	2.2
Displacement [nm]	473.5	39.2	397.8	41
Sound pressure level [dB]	109.5	93.13	107.9	93.54

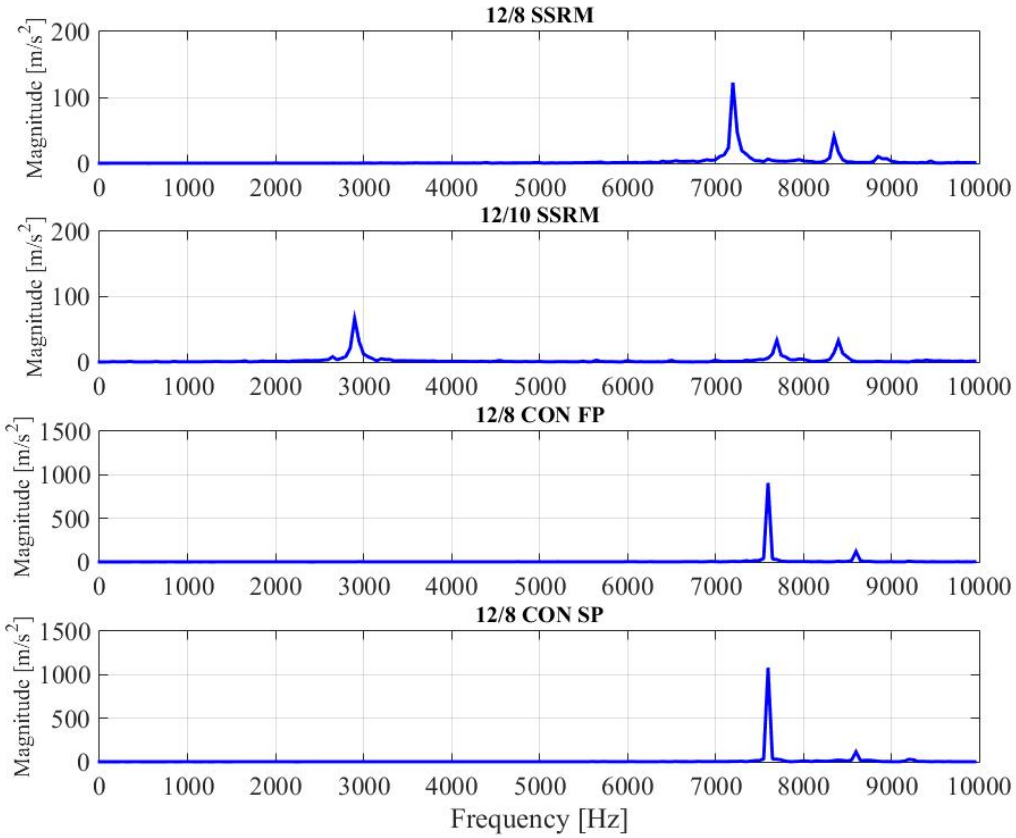

Figure 3.21: Magnitude of acceleration at 1000 r/min with load torque = 15 Nm

Table 3.6: Vibration characteristics of segmental rotor SRM at 1000 r/min

Item	12/8 SSRM		12/10 SSRM				
Dominant natural frequency mode [Hz]	7215	8371	2916	7683	8384	8794	9272
Acceleration [m/s^2]	122.5	41	66	33	33	0.6	1.4
Velocity [mm/s]	2.7	0.8	3.6	0.68	0.62	0.01	0.02
Displacement [nm]	59.8	14.8	199.6	14	11.7	0.2	0.4
Sound pressure level [dB]	73.13	84.41	88.29	70.5	69.2	53.1	48.26

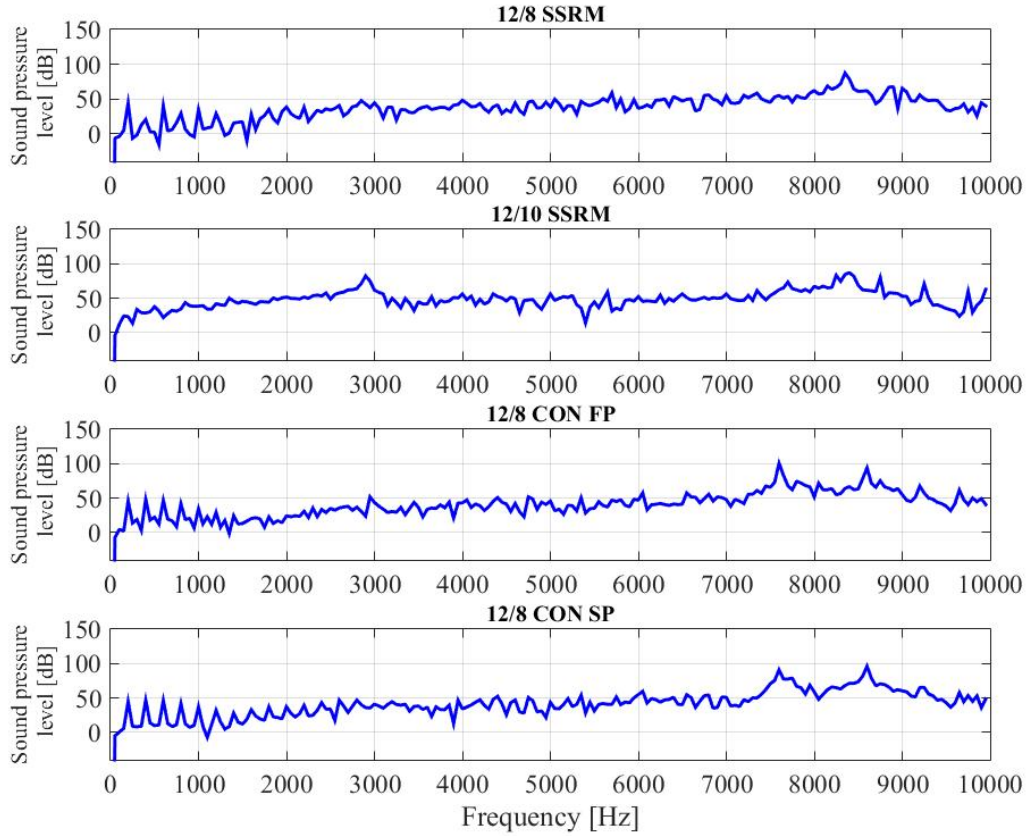

Figure 3.22: Sound pressure level at 500 r/min with load torque = 30 Nm

Table 3.7: Dynamic characteristics of different SRM topologies at 500 r/min

Item	12/8 CON SP	12/8 CON FP	12/8 SSRM	12/10 SSRM
Average torque [Nm]	30.29	30.02	30.29	30.1
Torque ripple rate	0.78	1.25	1.13	0.5
RMS phase current [A]	13.2	8.26	6.84	6.81
Maximum radial force on the pole [N]	2208	2077	1594	2737 (L) 1430 (S)
Maximum sum of radial force [N]	9288	8309	11689	11989
Ripple rate of sum of radial force	1.02	1.74	0.57	0.57

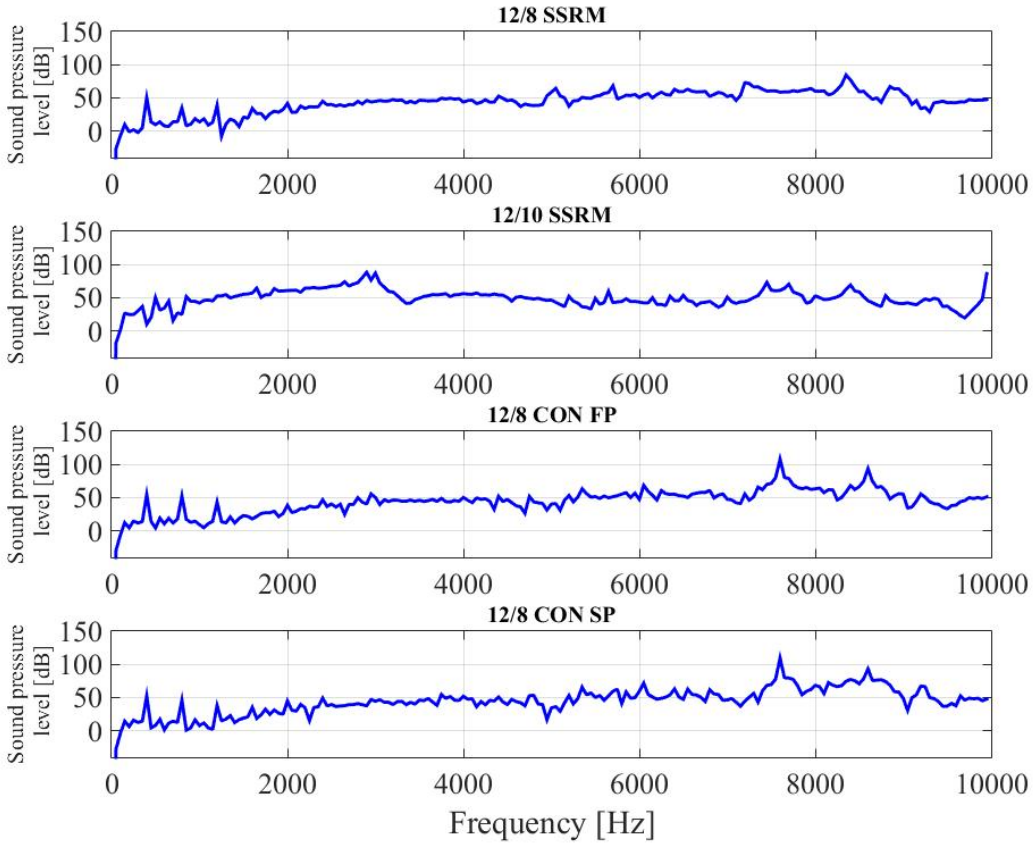

Figure 3.23: Sound pressure level at 1000 r/min with load torque = 15 Nm

Table 3.8: Dynamic characteristics of different SRM topologies at 1000 r/min

Item	12/8 CON SP	12/8 CON FP	12/8 SSRM	12/10 SSRM
Average torque [Nm]	15.42	15.23	16.26	15.4
Torque ripple rate	1.11	1.32	1.41	0.93
RMS phase current [A]	8.8	5.4	6.5	5.6
Maximum radial force on the pole [N]	1920	1841	1596	2424 (L) 1381 (S)
Maximum sum of radial force [N]	7931	7374	11583	11054
Ripple rate of sum of radial force	0.73	1.29	0.3	0.24

Chapter 4.
Mechanical Properties for Structural Simulation Model

Vibration and acoustic noise is becoming an interesting topic in electrical machines due to the high demand for electrical machines and the motivation for development in automotive applications such as electric vehicles, hybrid electric vehicles and electric motorcycles etc. The characteristics of noise, vibration and harshness (NVH) of a vehicle are among the major criteria that determines the quality of the vehicle. Many candidates for electrical machines have been selected for this application, such as the permanent magnet synchronous machine (PMSM), the induction machine (IDM), and the switched reluctance machine (SRM). The SRM is especially widely acknowledged to have high vibration and acoustic noise problems compared with other electrical machine types. However, SRMs have many advantages. For instance, they are magnet free, have no rotor windings, have robust and simple structures, and are cost effective to manufacture, making SRMs attractive in automotive applications.

The major challenge of SRMs in this application is how to reduce any unpleasant and annoying noise in the passenger cabin caused by vibration and acoustic noise from the SRM. The amplitude of vibration and acoustic noise in electrical machines is highest when harmonic amplitudes of excitation force coincide with the resonant frequency of the stator. Therefore, the two main techniques to decrease vibration can be described as I) design of the stator structure to have a resonant frequency as high as possible and II) control of the excitation force to reduce the amplitude of force harmonics.

The resonant frequency is the major factor that determines the vibration in

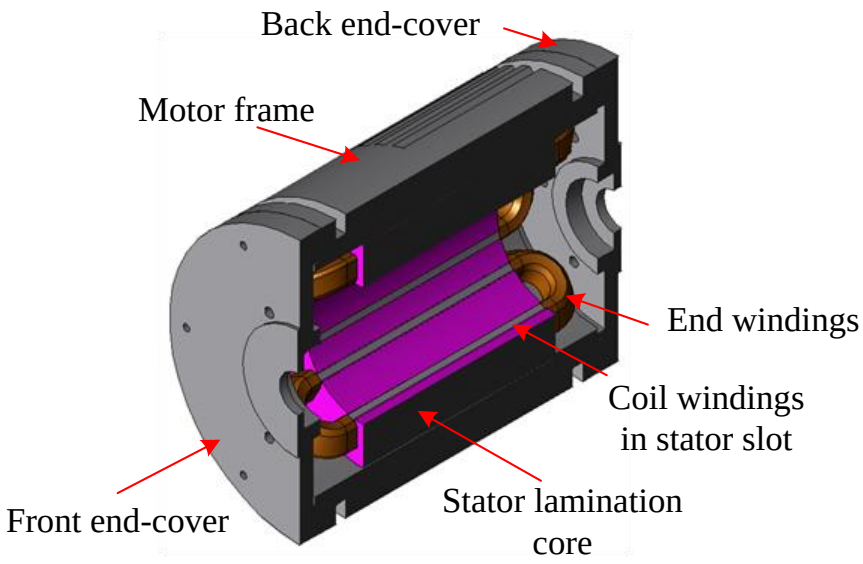

Figure 4.1: Cross-section of structural simulation model of 12/10 single-tooth wound segmental rotor SRM

machine structure and it can be found by using experimental tests and structural simulation model techniques. In the structural simulation model, material property parameters such as mass density, Poisson's ratio, and Young's modulus, are necessary for the simulation model in addition to the dimension and shape of the structure. The relationship between the resonant frequency, stiffness coefficient, and mass density of the stator is roughly given in

$$f_r \propto \sqrt{\frac{k}{m}} \tag{4.1}$$

where f_r, k, and m are resonant frequency, stiffness coefficient, and mass density, respectively. The stiffness can be defined as Young's modulus of the material (E). Fig. 4.1 shows the structural simulation model of a 12/10 single-tooth wound segmental rotor SRM. This model includes the motor frame, end-covers, stator lamination stack, and coil windings (end windings and slot windings). Owing to the changing properties of material during the manufacturing processes of the stator lamination core and varnished windings, the Young's modulus of the stator lamination core and coil winding is difficult to estimate.

Previous studies of SRM coil winding in the structural simulation [68–70] have reported that coil winding can be treated simply as additional mass added to the

stator poles and have also investigated the impact of coil winding on the resonant frequency [71]. On the other hand, some published articles [72, 73] argued that the coil winding cannot be treated as adding mass through the stator poles but it should be complete wound stator poles (slot winding) with end winding. The Young's modulus of the slot and end winding is approximately 1 % of the value of solid copper. The equivalent of Young's modulus on the slot and end winding was determined by experimental investigation on an induction machine [74].

In the stator lamination core, Young's modulus is the most important parameter and plays an important role in the resonant frequency of electrical machines. Tang [68] proposed the technique of measuring the Young's modulus in the stator lamination core by using ultrasonic transducers. This method measures the sound speed of the ultrasonic signal, which travels through the test specimen via an ultrasonic transmitter and receiver, to calculate the Young's modulus of material. This can be approximated as an isotropic material type. In [75], development of the Young's modulus calculation was presented. The results of the experimental modal testing and modal analysis by finite element method were combined using the parameter-fitting technique to find the Young's modulus. This method found that the property of the lamination core is an orthotropic material type. In this chapter, the techniques for the Young's modulus estimation of the stator lamination core and coil winding are presented, and a Semi-Finite Element Method technique is also developed for calculation of the Young's modulus in the lamination core.

4.1 Coil Winding

The Young's modulus of coil windings, which consist of enamelled wires, insulation sheets, and epoxy resin, can be calculated using an equivalent equation which was obtained from experimental investigation in [74]. The Young's modulus of the coil windings is different between the coil windings in the stator slot and the end windings. This practical testing was investigated based on a distributed coil winding type of an induction motor which had long overhang and coil overlapping on the end windings so that it made the end windings stiffer than the slot windings. This

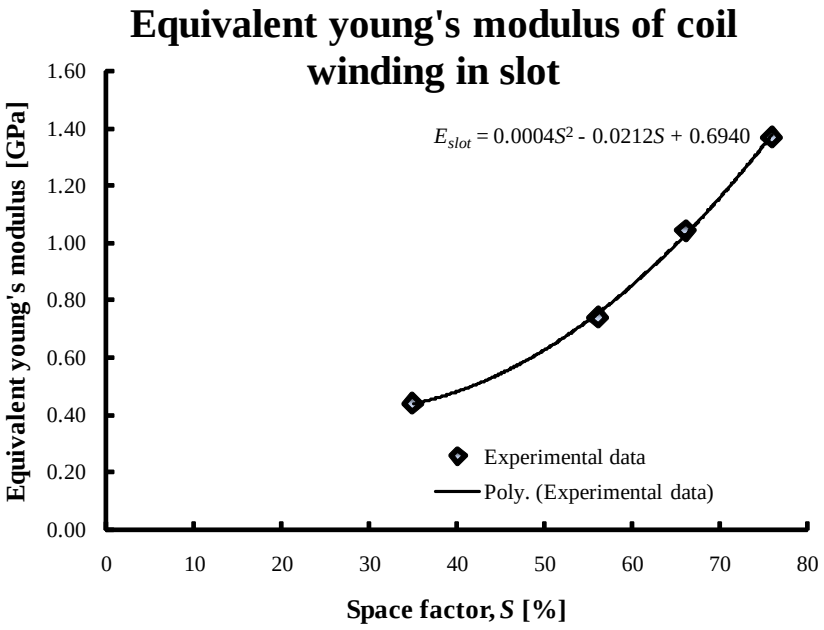

Figure 4.2: Equivalent Young's modulus of coil winding in slot

is significantly different from the SRM, which is a concentrated coil winding type having a short end-turn and non-overlapping end windings. Therefore, it can be assumed that the Young's modulus of the end windings is the same as that of the slot windings for this concentrated coil winding configuration. Fig. 4.2 shows the equivalent of Young's modulus of the coil winding in the stator slot [74]. The Young's modulus equivalent equation of coil winding in the slot was obtained from experimental data using a polynomial parameter fitting technique and Young's modulus of the coil windings in the slot can be calculated as

$$E_{slot} = 0.0004S^2 - 0.0212S + 0.694 \qquad \text{[GPa]} \tag{4.2}$$

where S is the percentage of the space factor of coil windings (35-80%).

The space factor of coil windings in the slot, including the insulation sheet, the enamel, and the epoxy resin in the stator slot, can be assumed to be the slot-fill factor (the ratio of actual cross-section of conductor to the total area of slot). The space factors of coil in slot in this chapter is 41%. The mass density of coil windings can be determined as composite material like the stator lamination core and can be calculated using Equation (4.3). The material properties of solid copper are

Young's modulus = 130 GPa, mass density = 8960 kg/m^3, and Poisson's ratio = 0.343. The epoxy resin is Magna E645 which can be applied as a bonding material for the stator lamination core and insulating varnish for impregnated coils. The other materials (insulating sheet and enamel) are neglected. The coil windings are assumed to be an isotropic material type in this chapter and Young's modulus of coil winding can be calculated using Equation (4.2). The Poisson's ratio also uses the same value as solid copper. The mechanical material property details of coil windings in SRMs are shown in Table 4.4. The percentage of the space factor is very difficult to estimate exactly. There are some studies [76, 77] of compressed coil windings for increasing the fill factor in the motor slots. The fill factor can be increased over 70 % using compressed coil techniques. The Young's modulus of compressed coil can be assumed to be that of solid copper.

4.2 Stator Lamination Core

The resonant frequency is related to the mass density and stiffness coefficient which involves the Young's modulus of the material, as shown in Equation (4.1). The Young's modulus of solid component parts such as motor frames, end-covers, and coil windings can be found in the manufacturing data sheet or material handbook. In contrast, because the material properties change during stator lamination core manufacturing processes, the Young's modulus of the stator lamination core is more complex to predict. The manufacturing data sheet provides only the detail of the Young's modulus of the single lamina and does not give the data for a whole lamination stack. Fig. 4.3 shows the manufacturing material properties (Cogent Electrical Steel Non-Oriented Fully Processed) of non-oriented electrical steel sheet which was used for building the stator lamination core.

In the process of building the stator lamination core, the steel sheets are bonded together with epoxy and assembled as a stack using a hydraulic pressing machine. After that, the lamination stack is baked under pressure for several hours, finally leaving it at room temperature for cooling, as illustrated in Fig. 4.4.

Garvey [78] presented the results of a study of the mechanical properties of a

Grade EN 10106	Conventional density kg/dm³	Resistivity µΩcm	Yield strength N/mm²	Tensile strength N/mm²	Young's Modulus (E) RD N/mm²	TD N/mm²	Hardness HV5 (VPN) –
M235-35A	7,60	59	460	580	185 000	200 000	220
M250-35A	7,60	55	455	575	185 000	200 000	215
M270-35A	7,65	52	450	565	185 000	200 000	215
M300-35A	7,65	50	370	490	185 000	200 000	185
M330-35A	7,65	44	300	430	200 000	220 000	150
M700-35A*	7,80	30	290	405	210 000	220 000	125

Figure 4.3: Material properties of non-oriented electrical steel sheet from the manufacturing

Figure 4.4: Stator lamination core processes

laminated core compared with a solid core. The experimental results show that both Young's modulus and the Shear modulus of lamination cores are smaller than that of solid cores. Damping factors of lamination cores are higher than normally found for solid cores by 1.5 % to 10 %. Increasing stacking factor (high clamping pressure) results in increased values of Young's modulus and Shear modulus and reduced values of damping factors of lamination cores. Furthermore, the interfaces between laminations have a significant effect on the flexibility of the lamination stack both Young's modulus and Shear modulus.

Forming lamination stacks with a vacuum-pressure impregnation process can increase both Young's and Shear modulus by factor of 1.9 and 3.2, respectively. This implies that values of Young's and Shear modulus of lamination cores are obtainable depending on clamping pressures and surface treatments of the individual laminations.

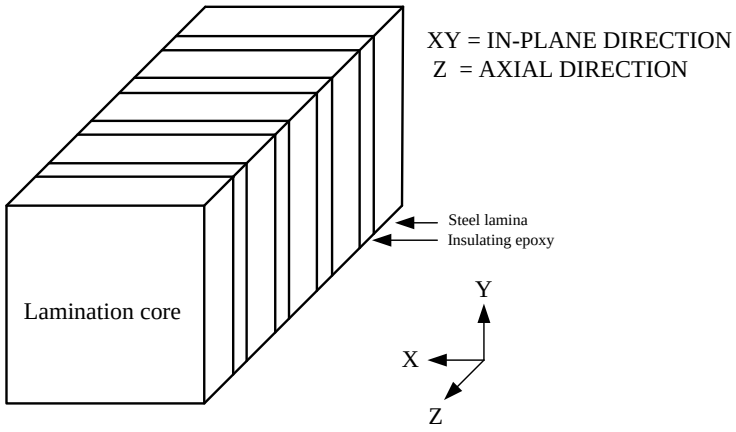

Figure 4.5: Simple lamination core

4.2.1 Analytical Modelling

The equivalent of material properties of the stator lamination core can be calculated with an analytical model [75] using the classical lamination theory [79, 80]. The laminate sheets can be considered as a composite material which consists of electrical steel sheets (subscript f) and the insulating epoxy resin (subscript m) as shown in Fig. 4.5.

The steel volume fraction ϕ is the volume ratio of steel to the total volume of the lamination core. Analytical modelling proceeds under the assumption that steel sheet and insulating epoxy materials are isotropic. After that, ideal bonding exists between the steel sheets and insulating epoxy and pressure loads are only applied to the relevant layer. The mass density of the lamination core can be calculated by

$$\rho = \rho_f \phi + \rho_m (1 - \phi) \tag{4.3}$$

In-plane Young's modulus (xy direction)

$$E_p = E_f \phi + E_m (1 - \phi) \tag{4.4}$$

Through-thickness Young's modulus (axial direction)

$$E_z = \left(\frac{\phi}{E_f} + \frac{1 - \phi}{E_m} \right)^{-1} \tag{4.5}$$

In-plane Poisson's ratio (xy direction)

$$\nu_p = \nu_f \phi + \nu_m (1 - \phi) \tag{4.6}$$

Through-thickness Poisson's ratio (axial direction)

$$\nu_{zp} = \nu_p \frac{E_z}{E_p} \tag{4.7}$$

Shear modulus of the steel sheet

$$G_f = \frac{E_f}{2(1+\nu_f)} \tag{4.8}$$

Shear modulus of the insulating epoxy

$$G_m = \frac{E_m}{2(1+\nu_m)} \tag{4.9}$$

The effective shear modulus in the in-plane direction

$$G_p = \frac{E_p}{2(1+\nu_p)} \tag{4.10}$$

The effective shear modulus in the axial direction

$$G_{zp} = \frac{G_m G_f}{G_m \phi + G_f(1-\phi)} \tag{4.11}$$

In this analytical model, the 0.35 mm thickness M270-35A steel sheet, which was used for making the stator lamination core of 12/10 single-tooth wound segmental rotor SRM (12/10 SSRM), was considered. The material properties are known from the manufacturer's data sheet. Young's modulus of the steel sheet is 192.5 GPa which is obtained from the average volume between the Young's modulus in rolling and transverse directions. The mass density of the steel sheet is 7650 kg/m^3. Poisson's ratio of both steel sheet and insulating epoxy is approximately the same at 0.3. The estimated values of Young's modulus and the mass density of the insulating epoxy (Magna E645) are 3.447 GPa and 1186 kg/m^3, respectively. The steel sheet thickness is 0.35 mm and the insulating epoxy layer thickness is approximately 0.0105 mm. The thickness of the epoxy resin can be calculated from the actual stator stack length compared with its length in the motor design sheet. The steel volume fraction is 0.9709.

Using Equation (4.3)-(4.11), the material property results for the stator lamination core are: ρ = 7461.9 kg/m^3, E_p = 186.99 GPa, E_z = 74.15 GPa, ν_p = 0.3, ν_{zp} = 0.119, G_f = 74.04 GPa, G_m = 1.326 GPa, G_p = 71.923 GPa and G_{zp} = 28.52 GPa.

4.2.2 Semi-Finite Element Method (Semi-FEM) Technique

To prove the results of the material properties in the analytical model and to develop the technique for Young's modulus calculation, ANSYS 3D finite element software was used for Young's modulus calculations. The material properties used are the same as those for the analytical model. The ideal surface connection between two materials was also considered. Young's modulus of material in each direction was calculated using the equivalent Young's modulus formula, and some results from finite element were applied as an input to the equivalent Young's modulus formula. The fundamental formula of Young's modulus is given by

$$E = \frac{\text{Tensile stress}}{\text{Extension strain}} = \frac{\sigma}{\varepsilon} = \frac{F/A_0}{\triangle L/L_0} \tag{4.12}$$

where F is the force acting on an object under tension, A_0 is the area to which force is applied, $\triangle L$ is the length of the object changes, and L_0 is original length of the object.

4.2.2.1 Young's Modulus in Axial Direction (Z Direction)

Fig. 4.6 shows the diagram of the Young's modulus calculation in the axial direction. The force was applied to both ends of the lamination stack. As mentioned above, ideal surface connection between steel sheet and insulating epoxy was considered as the 'no separation' type of the contacting surface in ANSYS software. The tensile stress in each object (steel and epoxy layer) is the same and constant. To calculate the total extension strain in the object, Equation (4.13) was used. The individual extension strain of each object can be found from the finite element software, and it can be used to compute the total extension strain.

$$\varepsilon_{tz} = \frac{\triangle L}{L_0} = \frac{N_f \varepsilon_{fz} L_f + N_m \varepsilon_{mz} L_m}{N_f L_f + N_m L_m} \tag{4.13}$$

where ε_{tz}, ε_{fz}, ε_{mz}, N_f, N_m, L_f, and L_m are the total extension strain, the extension strain of steel layer, the extension strain of epoxy layer in axial direction, the number of steel layers, the number of epoxy layers, the steel layer length, and the epoxy layer

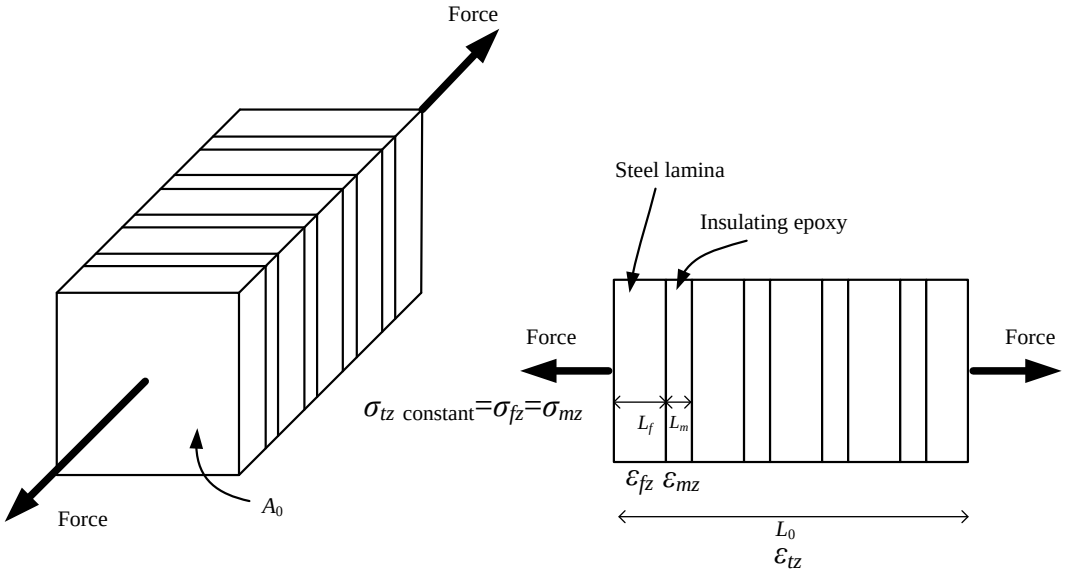

Figure 4.6: Calculation of the Young's modulus in the axial direction (z direction)

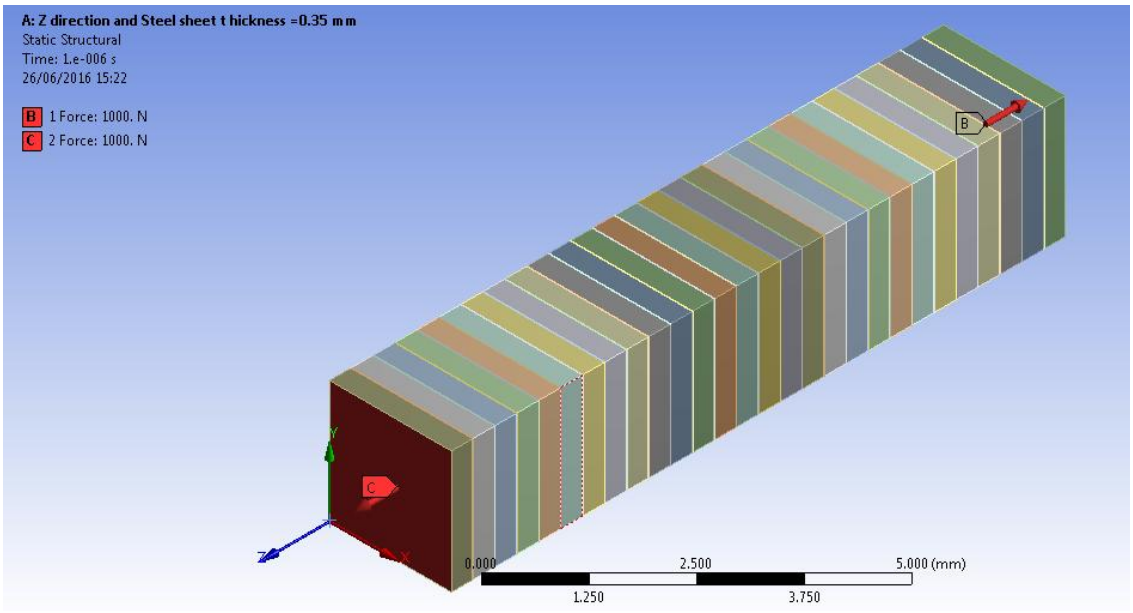

Figure 4.7: Direction of applied force in the lamination stack

length, respectively. The total tensile stress in axial direction, σ_{tz} is given by

$$\sigma_{tz} = \frac{\text{Force}}{A_0} \tag{4.14}$$

Finally, the Young's modulus of the lamination stack in the axial direction can be expressed as

$$E_z = \frac{\sigma_{tz}}{\varepsilon_{tz}} \tag{4.15}$$

The force versus direction, which was applied to the lamination stack, is shown in Fig. 4.7.

4.2.2.2 Young's Modulus in In-plane Direction (XY Direction)

The calculation of Young's modulus in the in-plane direction is illustrates in Fig. 4.8. A constant displacement was applied in perpendicular directions to the lamination stack, and another side was supported by a frictionless support. This meant that the extension strains of all individual objects were the same and constant. A frictionless support is more realistic than a fixed support. In the frictionless support, constraint is applied into the normal direction on the surface, while the fixed support applies the constraint in all degrees of freedom on the surface. Following the same assumption of the Young's modulus in the axial direction calculation, the total tensile stress of the in-plane direction can be expressed as

$$\sigma_{tp} = \frac{\text{Force}}{A_t} = \frac{N_f \sigma_{fp} A_f + N_m \sigma_{mp} A_m}{N_f A_f + N_m A_m} \tag{4.16}$$

where σ_{tp}, σ_{fp}, σ_{mp}, A_f, A_m, and A_t are the total tensile stress, the tensile stress of steel layer, the tensile stress of epoxy layer in the in-plane direction, the area of steel layer, the area of epoxy layer, and the total area of the object to which displacement is applied, respectively.

The extension strain of the object in the in-plane direction, ε_{tp} was considered constant and can also be calculated by

$$\varepsilon_{tp} = \frac{\triangle L}{L_0} \tag{4.17}$$

The Young's modulus of the lamination stack in the in-plane direction can be expressed as

$$E_p = \frac{\sigma_{tp}}{\varepsilon_{tp}} \tag{4.18}$$

The direction of the constant displacement which was applied to the lamination stack is shown in Fig. 4.9. The Young's modulus of the lamination stack can be obtained from the slope of tensile stresses to the extension strain. The slopes of tensile stresses to the extension strain are shown in Fig. 4.10. In addition, the Young's modulus of the lamination stack with different thicknesses (0.35 mm, 0.3

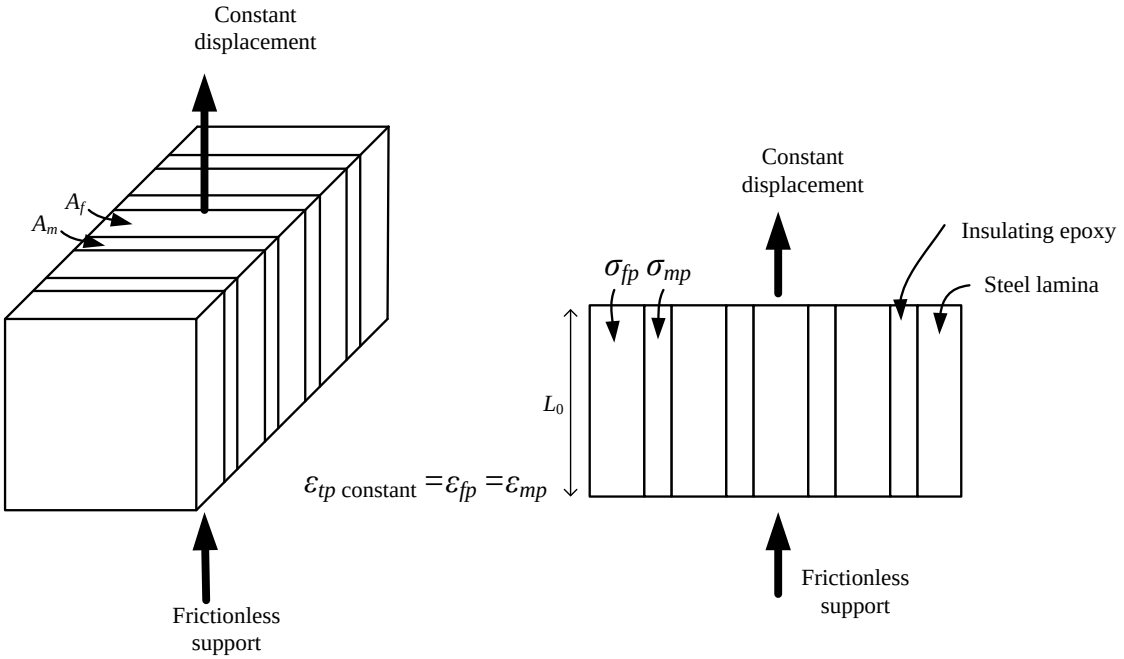

Figure 4.8: Calculation of the Young's modulus on in-plane direction (xy direction)

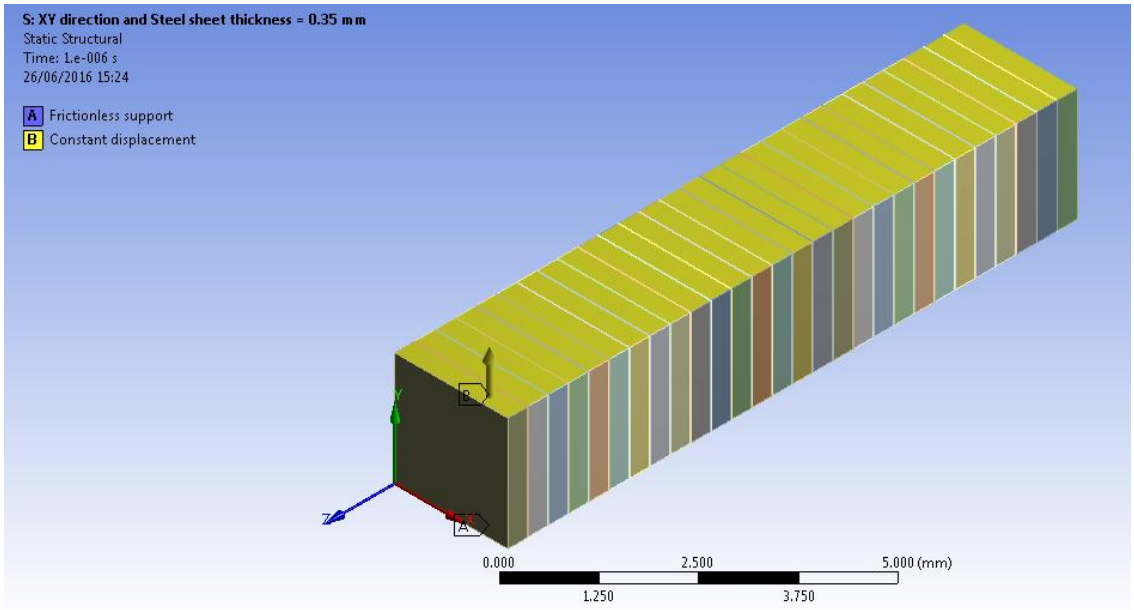

Figure 4.9: Direction of the displacement in the lamination stack

mm, 0.25mm, and 0.2 mm) was simulated and computed using the same thickness of the epoxy layer at 0.0105 mm.

The comparative results of the Young's modulus between the analytical model and the Semi-FEM at different steel sheet thicknesses are summarised in Table 4.3.

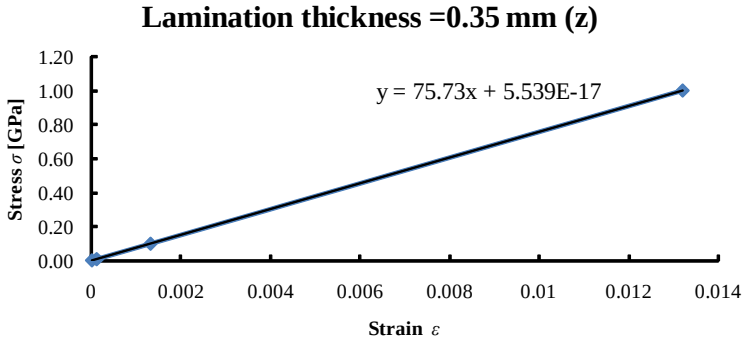

(a)

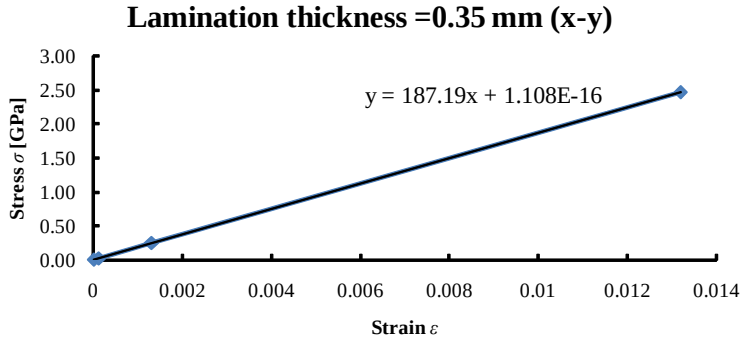

(b)

Figure 4.10: Young's modulus of the lamination stack with steel thickness at 0.35 mm: (a) axial direction and (b) in-plane direction.

Both Young's modulus results in the analytical model and the Semi-FEM are similar, with the percentage of error about 0.11 % in the in-plane direction and about 2-3 % in the axial direction. The Young's modulus of the lamination stack in the axial direction dramatically changes to low values with reduction in the thickness of steel sheet, while its value only slightly decreases in the in-plane direction. The other parameters of material property of the lamination core, such as Shear modulus and Poisson's ratio, can be found by Equation (4.6)-(4.11).

The motor casing and end-covers were built with aluminium alloy. The material properties of the aluminium alloy are Young's modulus E= 71 GPa, Poisson's ratio ν = 0.33, and mass density $\rho = 2770$ kg/m^3. The material properties of the lamination core are shown in Table 4.4.

The material properties from the above discussion are used in the structural simulation model of the 12/10 SSRM for calculation of the resonant frequency.

Figure 4.11: Second-order resonant mode shape of 12/10 single-tooth wound segmental rotor SRM

Table 4.1: Resonant frequency comparison between experimental test and structural simulation model

	Experimental test	Simulation model	Error [%]
Resonant frequency of 2^{nd} mode [Hz]	2210	2282.4	3.28

The material property parameters of the structural simulation model are presented in Table 4.4. The modal damping coefficient of the simulation model is 0.05. The details of the structural FE simulation are shown in Appendix C. The method of the structural simulation model, having material properties of the proposed technique, was implemented according to the experimental testing in [81] and [82] using the excitation method and an elastic rope for support. The procedures and details of the vibration testing are described in the next chapter.

The percentage error between the experimental test and the simulation model is 3.28%. The results are shown in Table 4.1. The second-order mode shape of vibration is a dominant mode shape of the 12/10 SSRM, as shown in Fig. 4.11. In this chapter, the structural simulation model of the 12/10 SSRM was implemented on JMAG software which can couple analysis with the magnetic simulation module.

4.3 Comparative Results

Table 4.5 presents the material parameters of the stator lamination stack using different techniques that have been proposed for Young's modulus estimation. These

Table 4.2: Resonant frequencies with different material property modelling techniques

Young's modulus modelling technique	2^{nd} mode Resonant frequency [Hz]	Error [%]
Experimental test	2210	-
Semi-FEM	2282.4	3.28
Analytical model	2283.3	3.32
Modal analysis and parameter fitting	2254.5	2.01
Ultrasonic	2335	5.66
Solid steel	2360	6.79

Table 4.3: Comparative results of the Young's modulus at different steel sheet thicknesses

E_p Analytical model [GPa]	E_p Semi-FEM [GPa]	Error [%]	E_z Analytical model [GPa]	E_z Semi-FEM [GPa]	Error [%]	Steel thickness [mm]
186.99	187.19	0.11	74.15	75.73	2.14	0.35
186.11	186.29	0.10	67.43	68.74	1.91	0.3
184.88	185.07	0.10	59.96	60.99	1.69	0.25
183.07	183.26	0.10	51.53	53.25	3.23	0.2

Table 4.4: Material properties of the structural simulation model

Parameter	Stator lamination core	Frame and end-covers	Slot windings	End windings
Mass density [kg/m^3]	7461.9	2770	4373	4373
Young's modulus [GPa]	$E_p = 187.19$ $E_z = 75.73$	$E_p = 71$	$E_p = 0.497$	$E_p = 0.497$
Poisson's ratio	$\nu_p = 0.3$ $\nu_z = 0.1214$	$\nu_p = 0.33$	$\nu_p = 0.343$	$\nu_p = 0.343$
Material type	Orthotropy	Isotropy	Isotropy	Isotropy

material properties were applied to the motor structural simulation model, which includes the motor casing, stator lamination stack, coil winding, and the aluminium end-covers. The resonant frequency results were predicted and compared to the simulation models with different material property modelling techniques and experimental tests.

From the comparison of results in Table 4.2, the models have very different steel

Table 4.5: Comparison of material properties of the stator lamination core at different modelling techniques

Parameter	Semi-FEM technique	Analytical model technique [75]	Modal analysis and parameter fitting technique [75]	Ultrasonic technique [68]	Solid steel
Mass density [kg/m^3]	7461.9	7461.9	7279.3	7293	7840
Steel volume fraction	0.97	0.97	0.95	0.935	1
Young's modulus [GPa]	$E_p = 187.19$	$E_p = 186.99$	$E_p = 180$	$E_p = 152.1$	$E_p = 207$
	$E_z = 75.73$	$E_z = 74.15$	$E_z = 110$		
Poisson's ratio	$\nu_p = 0.3$	$\nu_p = 0.3$	$\nu_p = 0.2$	$\nu_p = 0.3$	$\nu_p = 0.3$
	$\nu_z = 0.1214$	$\nu_z = 0.119$	$\nu_z = 0.15$		
Material type	Orthotropy	Orthotropy	Orthotropy	Isotropy	Isotropy

volume fractions, including the ultrasonic method ($\phi = 0.93$) and the solid steel (An alloy steel EN24, $\phi = 1$) give the highest percentage of the error compared to the models (modal analysis and the parameter fitting method (0.35 mm thickness M250-35A steel sheet, $\phi = 0.95$), the analytical model ($\phi = 0.97$), and the Semi-FEM ($\phi = 0.97$)) which have steel volume fractions similar to those of the SRM prototype at 0.97. Three techniques for Young's modulus estimation (Semi-FEM, analytical model, and Modal analysis and parameter fitting) provide good values of the Young's modulus of the stator lamination stack with the percentage error lower than 4%. However, Young's modulus of the stator lamination stack depends on the steel volume fraction and on steel sheet thickness, per the above discussion, and this confirms that the stator lamination core cannot be treated as solid steel. The Semi-FEM and analytical model techniques are useful for early stage machine design for vibration and acoustic noise prediction from structural simulations. This would be useful before building a machine prototype. However, the ultrasonic and modal analysis and parameter fitting techniques are only suitable for ready built machine prototypes.

4.4 Conclusion

The techniques of the material property calculation for electrical machines are presented. It can be assumed that the Young's modulus of the end windings is the same as that of the slot windings in the concentrated coil winding configuration in SRMs. Furthermore, the semi-finite element method is developed for calculation of

the Young's modulus in the stator lamination core. The comparative results of different steel thicknesses show that the steel sheet thickness and steel volume fraction have a significant impact on the Young's modulus in the axial direction.

A comparison of the results of the resonant frequency between the experimental modal test and the structural simulation model, having material properties from the proposed technique, show that the results are similar. The proposed technique for the Young's modulus calculation can be applied initially to determine and investigate the stator lamination core with adhesive bonding without a ready built stator structure. This technique can also be developed to calculate Young's modulus of complex lamination structures or a two-composite material, having highly different Poisson's ratios. In a future study, the proposed technique will be developed to investigate the Young's modulus of the lamination core using a welding method of construction, with comparative results between bonding and welding methods.

Chapter 5.
Vibration Measurement Techniques

A 12/10 single-tooth wound segmental rotor SRM was used for the experimental modal testing procedure. This modal testing aims to identify the dominant modal parameters, such as modal shapes, resonant frequencies, and damping coefficients, of the test machine. The results are compared with the simulation to improve the simulation model used for acoustic noise and vibration prediction. Two basic techniques [81,82] for modal tests were applied for measuring the modal parameters: 1) the excitation method and 2) the impact hammer method. Three main stages of the modal testing procedure are (1) force excitation in the SRM, (2) data acquisition, and (3) signal processing analysis. The equipment for the modal test includes an accelerometer for measuring the acceleration occurring in the SRM, a power drive unit for supplying force excitation in the excitation method, an impact hammer for supplying force excitation in the impact hammer method, an oscilloscope for data acquisition, and a computer for data processing.

The details of the equipment are as follows:
- An accelerometer (Monitran MTN/1130F model, sensitivity = 100 mV/g or 10.2 mV/m/s^2 $\pm$ 10 % and frequency response range 2 kHz - 15 kHz $\pm$5 %) was installed into the motor frame behind the large pole for maximum sensitivity.
- An impact hammer (PCB 203A model, sensitivity = 0.056 mV/N) was used to supply an impulse force signal.

In this experimental modal test, the influence of the mounting arrangement [83] and the impact of end-covers [71] on vibration in the SRM were investigated.

5.1 Excitation Method

This method uses the power drive unit to supply a current to the SRM phase winding, to generate an electromagnetic force excitation in the SRM. The SRM's rotor was held stationary at the aligned position, in which maximum radial force can be generated. One phase of the SRM was excited by short voltage pulses with frequency 10 Hz.

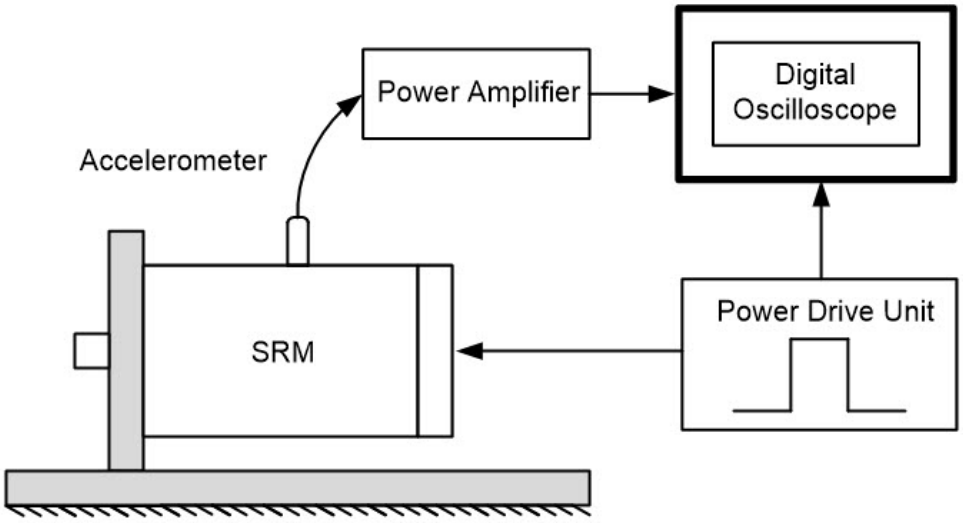

Figure 5.1: The modal testing with excitation method

The pulse duration was adjusted to reach the current level at 2.7 A. The motor was installed on a test bench with flange-mounting as shown in Fig. 5.1. Fig. 5.2 shows the voltage, current, and acceleration waveform of the modal testing with this excitation method. The maximum acceleration is 5.28 m/s^2. To find the machine's resonant frequency, the Fast Fourier transform (FFT) was applied to calculate the resonant frequency from the acceleration signal. The acceleration spectrum result is illustrated in Fig. 5.3. The resonant frequency is 2289 Hz, which matches the second-order mode shape.

Moreover, the acceleration signal can also be used to determine the modal damping ratio parameter, as shown in Fig. 5.4. The modal damping ratio can be found by

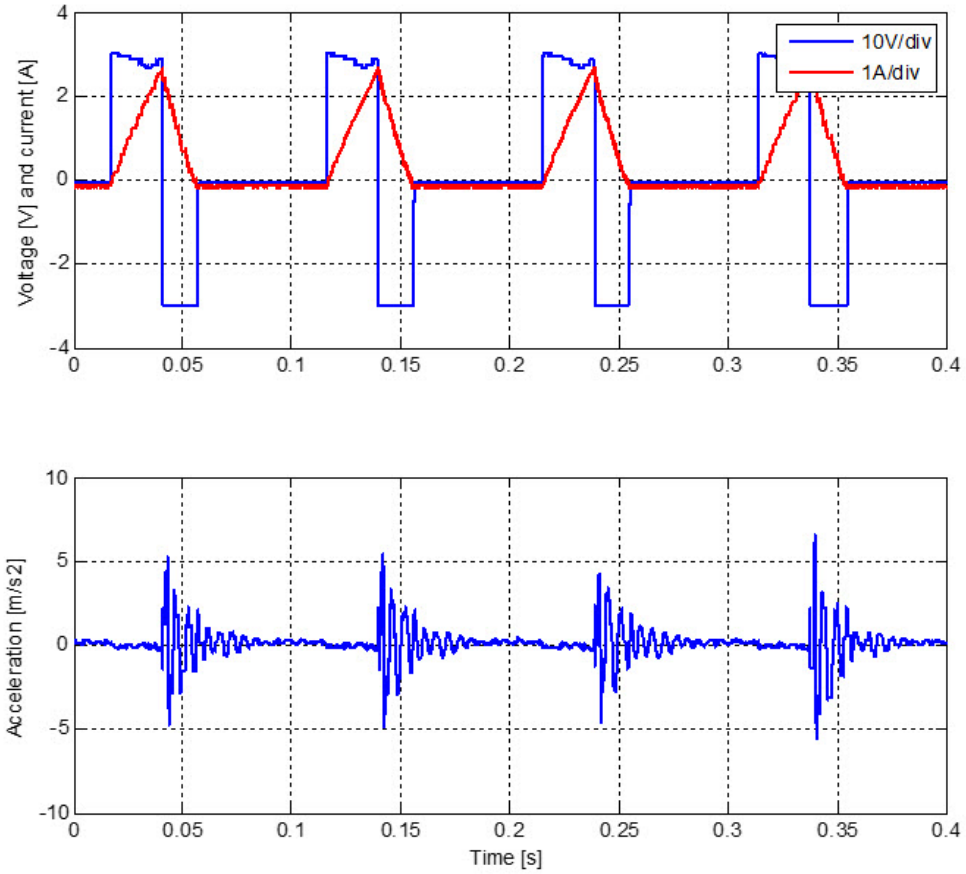

Figure 5.2: Current, voltage pulse, and acceleration signal in excitation method

$$\delta = \frac{1}{N} \ln \frac{a_k}{a_{k+N}} \tag{5.1}$$

$$\zeta = \frac{\delta}{\sqrt{(2\pi)^2 + \delta^2}} \approx \frac{\delta}{2\pi} \quad (\text{if} \quad \delta \ll 1) \tag{5.2}$$

where a_k and a_{k+N} are two acceleration peak amplitudes separated by N which is the number of complete cycles. δ is the logarithmic decrement and ζ is the modal damping ratio. The measured and calculated results are shown in Table 5.1.

5.2 Impact Hammer Method

In this method, impulse force was supplied to the SRM by hitting the motor structure with the impact hammer on the opposite side to the accelerometer with nearly constant force as shown in Fig. 5.5.

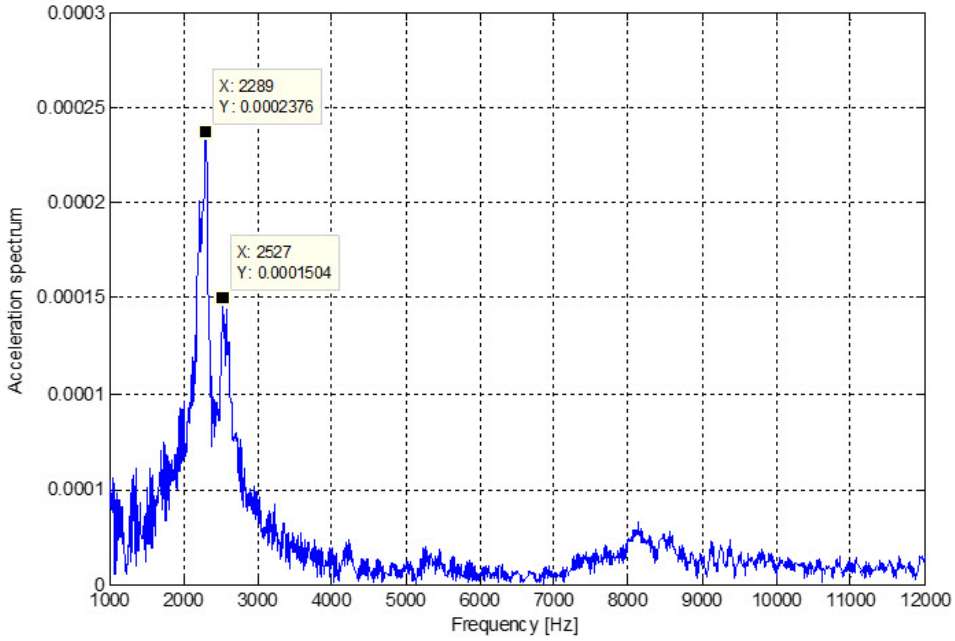

Figure 5.3: Acceleration spectrum signal in frequency domain

Table 5.1: Measured and calculated vibration result in excitation method

Parameter	
Peak No.2 [m/s^2]	3.28
Peak No.9 [m/s^2]	0.40
Number of complete cycles [N]	7
Modal damping ratio [ζ]	0.048
Resonant frequency [Hz]	2289

Impulse force can be measured via an integrated circuit piezoelectric (ICP) force ring transducer which is mounted at the hammer tip. The width of the impulse force and the bandwidth frequency of the hammer tip are determined by the material types of the tip, and can be varied with different tips, as shown in Fig 5.6. For this modal testing, an aluminium tip was used in the impact hammer. The frequency bandwidth of the impulse force should cover the entire frequency range of interest. From the simulation results of the vibration prediction model, the resonant frequency range of the test machine is approximately 2200 Hz. Therefore, the frequency bandwidth range of hammer tip should cover 2200 Hz.

The acceleration and impulse force signals were captured to determine the reso-

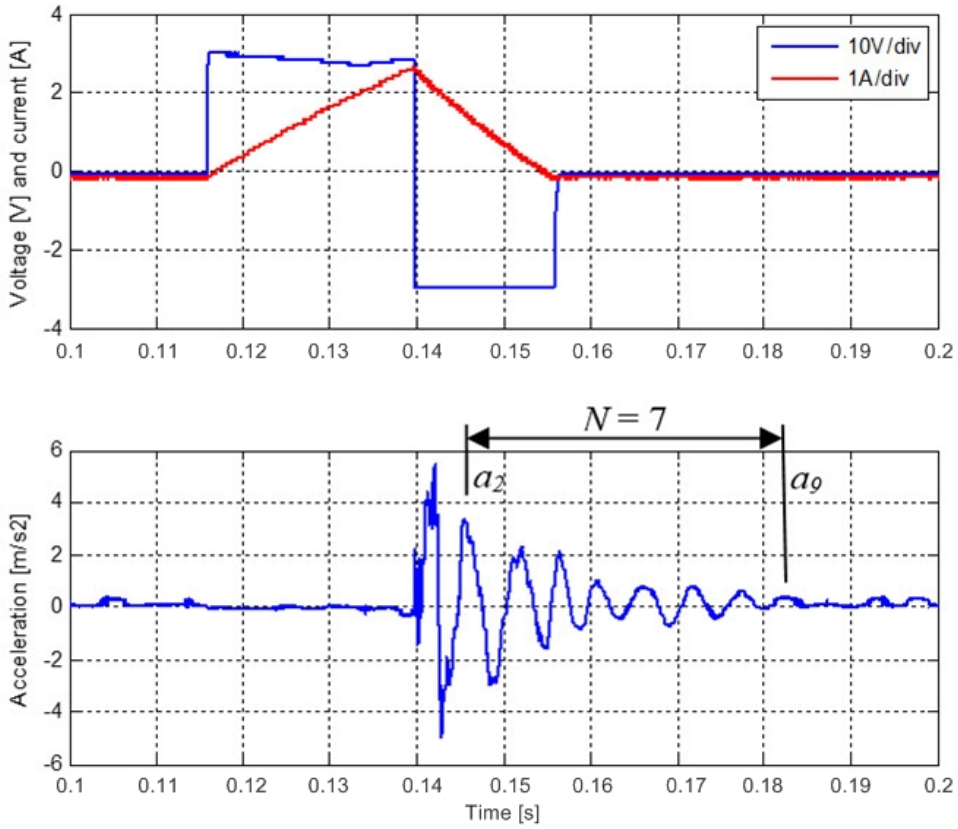

Figure 5.4: Detailed view of the current, voltage pulse, and acceleration signal in the excitation method

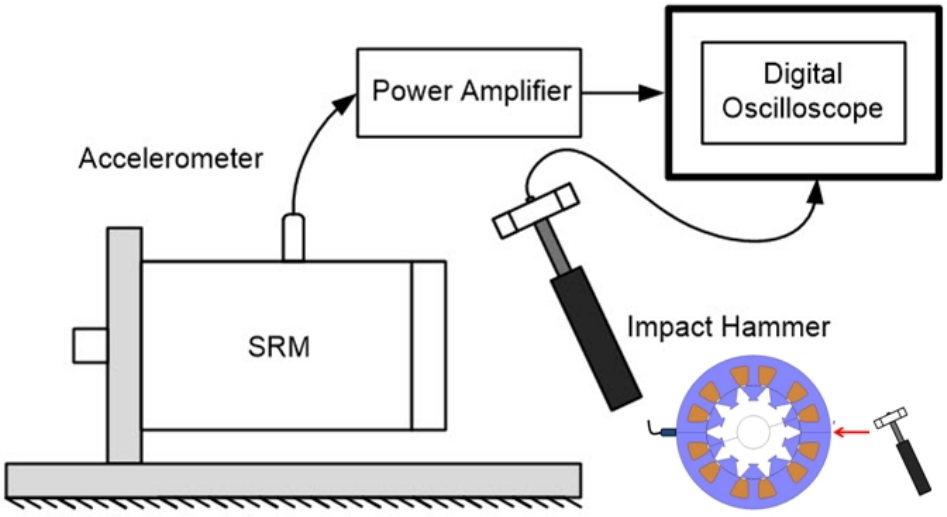

Figure 5.5: The modal testing with impact hammer method

nant frequency and modal damping coefficient. A maximum amplitude of impulse force of 1 N was supplied to machine structure. The maximum amplitude of the

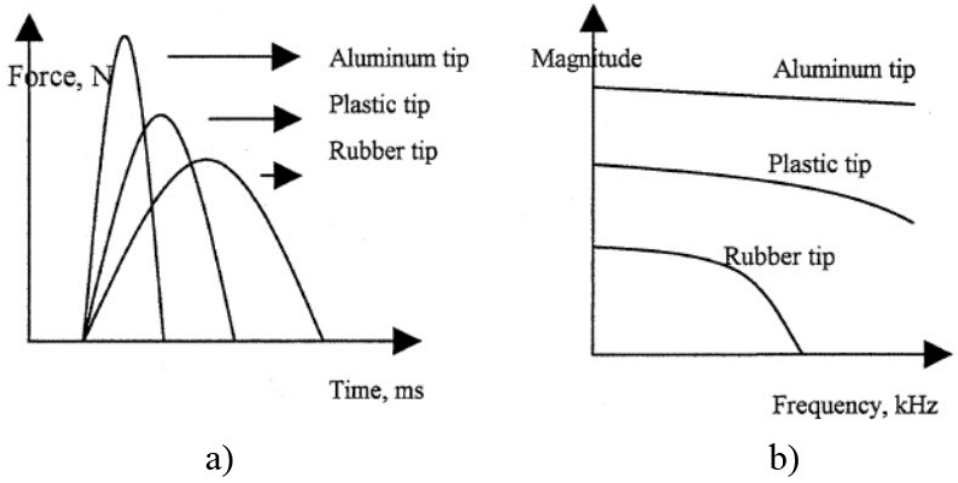

Figure 5.6: Impact hammer force waveform and frequency bandwidth: (a) impulse force and (b) force frequency bandwidth [81]

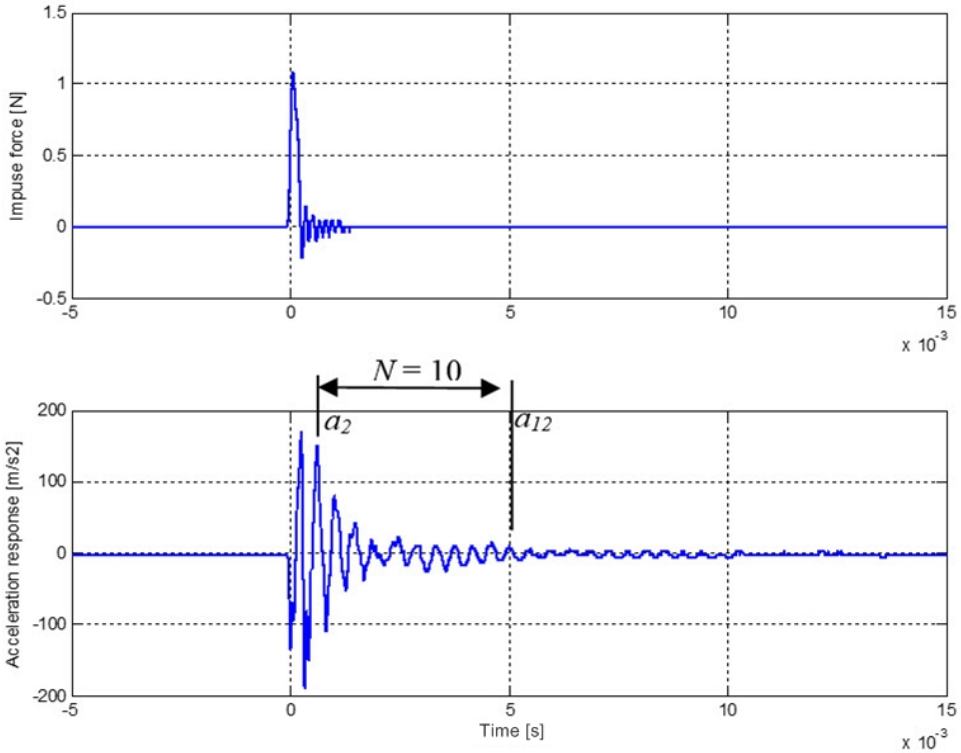

Figure 5.7: Impulse force and acceleration waveform using impact hammer method

acceleration response was 170 m/s^2. The impulse force and acceleration response signal are shown in Fig. 5.7. The resonant frequency and modal damping ratio are calculated as summarised in Table 5.2. Fig. 5.8 and 5.9 present the acceleration response spectrum and impulse force bandwidth, respectively.

The resonant frequency in the impact hammer method is 2267 Hz, close to that in the excitation method, which is 2289 Hz.

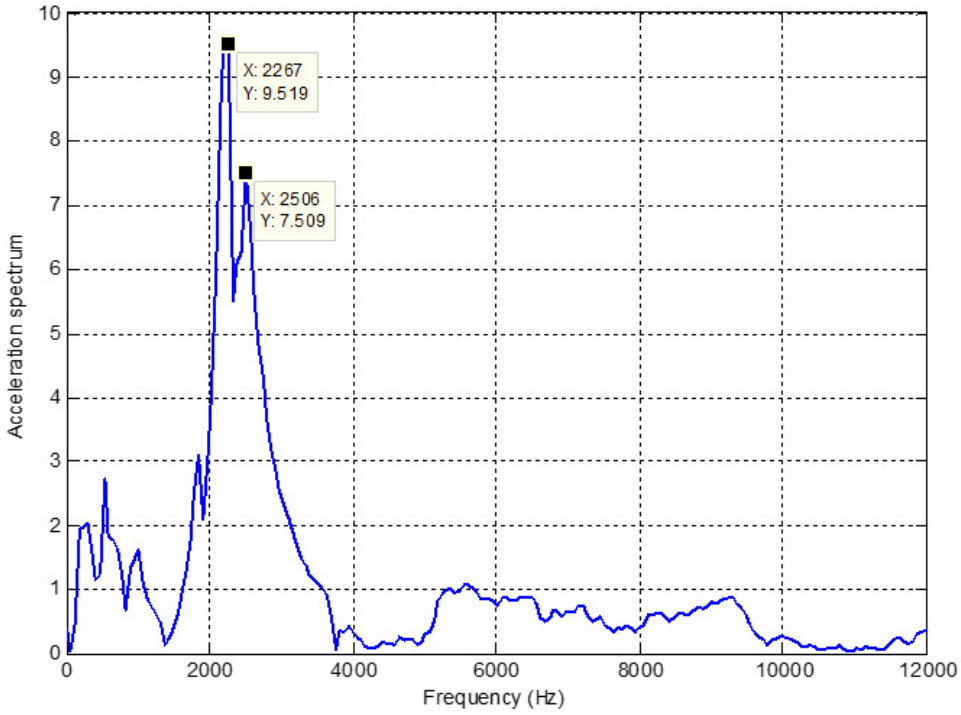

Figure 5.8: Acceleration spectrum using impact hammer method

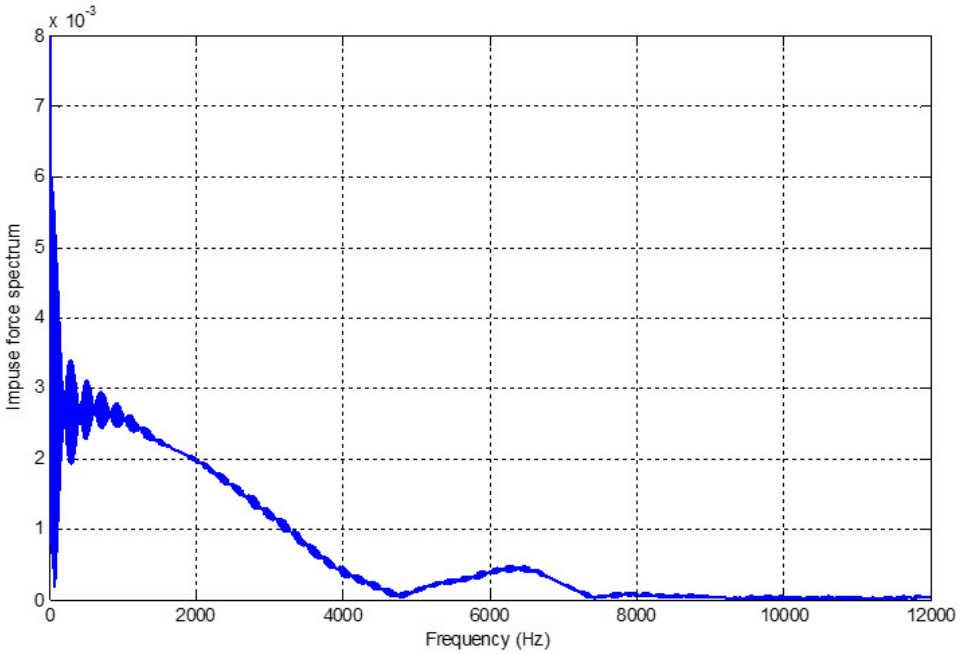

Figure 5.9: Impulse force frequency bandwidth

Table 5.2: Measured and calculated vibration result in impact hammer method

Parameter	
Peak No.2 [m/s^2]	150
Peak No.9 [m/s^2]	60
Number of complete cycles [N]	10
Modal damping ratio [ζ]	0.051
Resonant frequency [Hz]	2267

From both methods of the experimental modal testing, the resonant frequency range of the 12/10 single-tooth wound segmental rotor SRM is 2267-2289 Hz, and the modal damping ratio range is 0.048-0.051.

5.3 Mounting Effect on Vibration in SRM

To investigate the mounting effect on the vibration in the SRM, two mounting support methods were applied in the experimental modal test: 1) a flange-mounted support as shown in Fig. 5.10(a) and 2) an elastic rope support as shown in Fig. 5.10(b).

Figure 5.10: Mounting support: (a) flange-mounted support and (b) elastic rope support

In the first test, the motor was mounted as discussed above. The alternative elastic rope support for both experimental modal test setups is shown in Fig. 5.11 and 5.12.

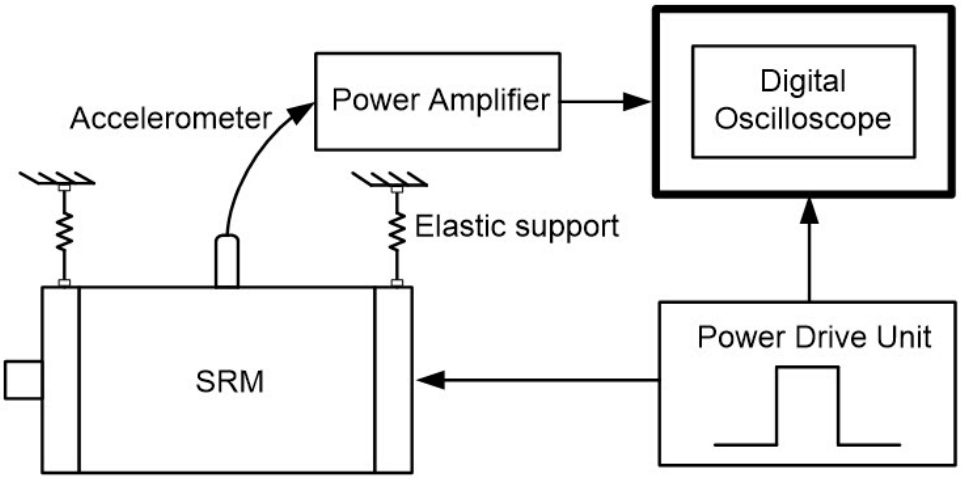

Figure 5.11: The modal testing with excitation method using elastic rope support

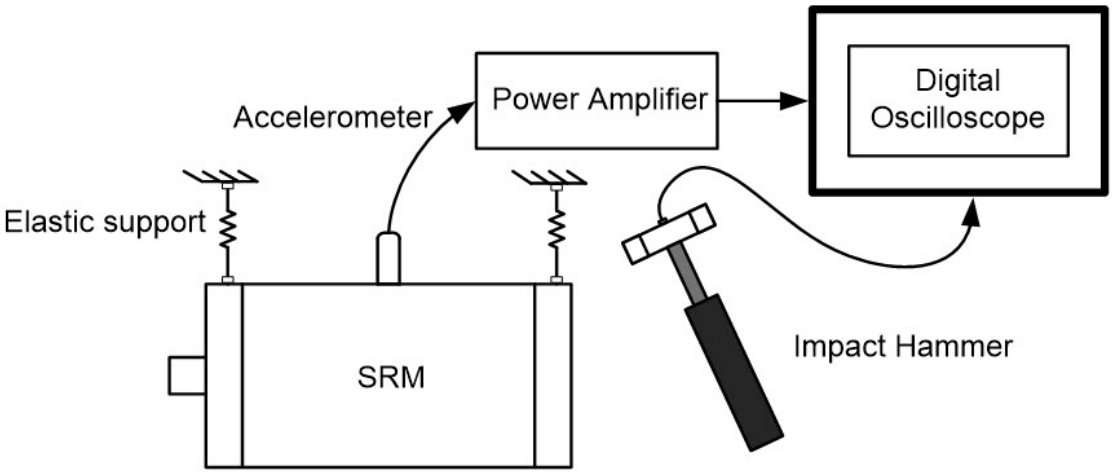

Figure 5.12: The modal testing with impact hammer method using elastic rope support

The implementation testing was done by supplying force to the motor structure which is suspended by an elastic rope. The acceleration signal was acquired by FFT calculation to determine the resonant frequency. The acceleration spectra of the excitation and impact hammer methods are illustrated in Fig. 5.13 and 5.14, respectively. The comparative vibration results with different techniques and supports are shown in Table 5.3. The resonant frequency decreases when using an elastic rope support. From the approximate formula of the stator resonant frequency, the relationship between the resonant frequency, stiffness coefficient, and mass density

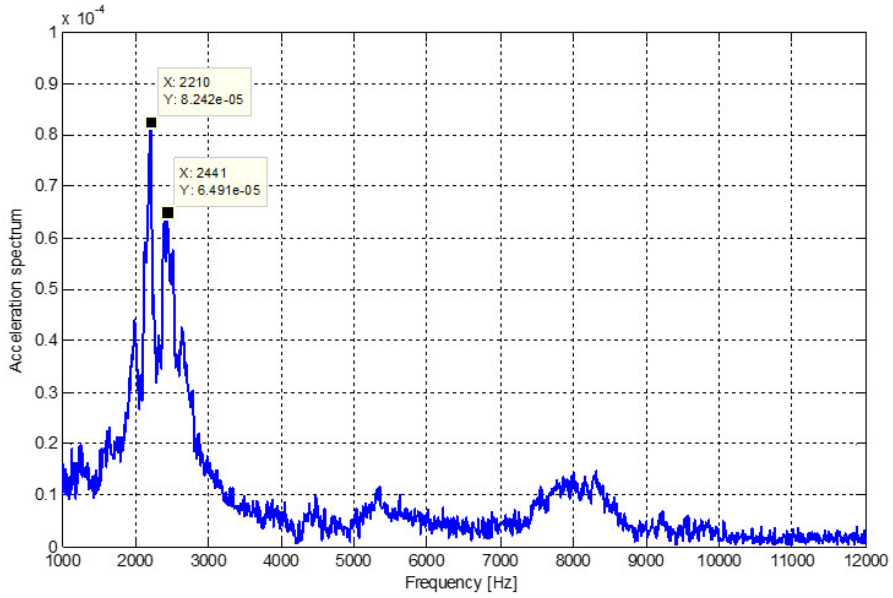

Figure 5.13: Acceleration spectrum for the excitation method using elastic rope support

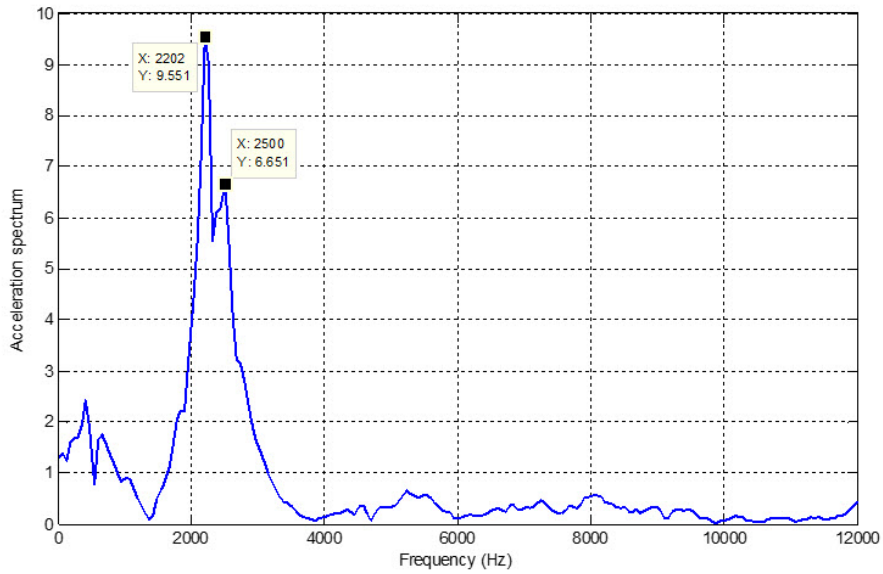

Figure 5.14: Acceleration spectrum for the impact hammer method using an elastic rope support

of the stator is roughly given in Equation (4.1). In the flange-mounted support, the stiffness coefficient of the system is high because the motor structure was mounted on the test bench which increases the stiffness of the system. On the other hand, the stiffness coefficient is low when it is supported by an elastic rope.

Table 5.3: Vibration results with different techniques and supports

Support	Method	Resonant frequency [Hz]	Modal damping ratio
Flange-mounted	Impact hammer	2267	0.051
	Excitation	2289	0.048
Elastic rope	Impact hammer	2202	0.048
	Excitation	2210	0.051

5.4 Effect of End-covers on Vibration in SRM

In this test, the SRM was disassembled. Three main component parts of the SRM were investigated: 1) complete motor (motor frame, end-covers, stator, rotor, and coil windings) 2) motor without rotor (motor frame, end-covers, stator, and coil windings), and 3) Motor with only stator (motor frame, stator, and coil windings). Modal testing, using the impact hammer method with an elastic rope support, was performed to find the resonant frequency. The acceleration spectrum of the

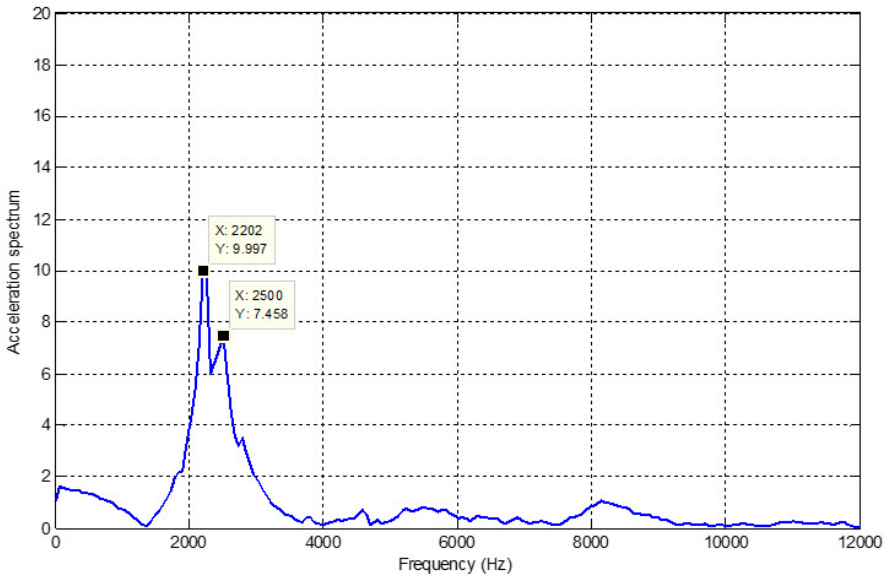

Figure 5.15: Acceleration spectrum of the SRM without rotor with impact hammer method using elastic rope support

complete motor is shown in Fig. 5.14. Fig. 5.15 and 5.16 present the acceleration spectrum of the motor without rotor and with only stator, respectively. The vibration results for different motor assemblies are shown in Table 5.4.

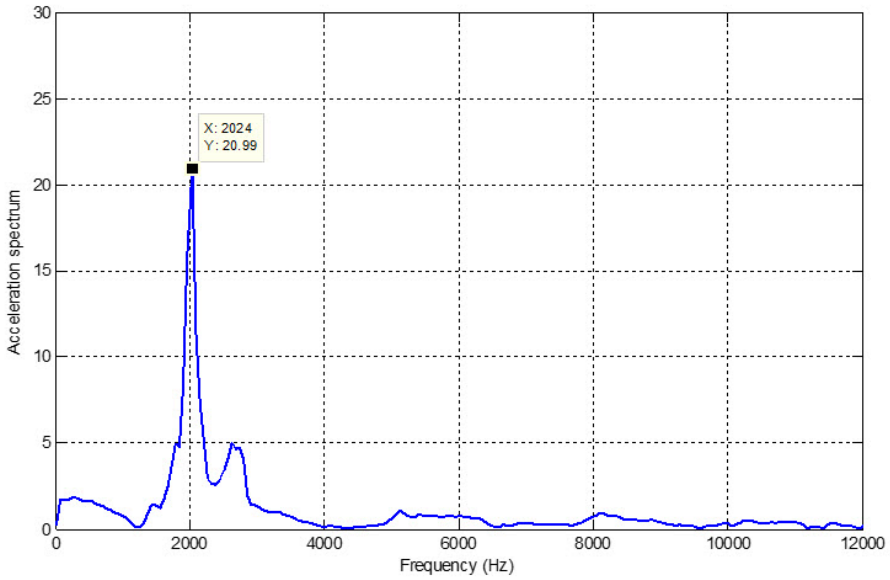

Figure 5.16: Acceleration spectrum of the SRM with only stator with impact hammer method using elastic rope support

Table 5.4: Resonant results with different motor assemblies

Support	Assembly	Method	Resonant frequency [Hz]
Elastic rope	Complete motor	Impact hammer	2202
	Without rotor	Impact hammer	2202
	Only stator	Impact hammer	2024

From the results in Table 5.4, the end-covers significantly affect the resonant frequency, which increases from 2024 Hz in the motor with only a stator, to 2202 Hz when the motor includes end-covers. According to Equation (4.1), the end-covers significantly improve the stiffness of the motor structure rather than increasing mass density. It also clear that rotor structure does not affect the resonant frequency of the stator.

5.5 Conclusion

The experimental modal test of a 12/10 single-tooth wound segmental rotor SRM was done in this chapter using two techniques. The dominant mode shape of the 12/10 SSRM is second-order mode. The results of the excitation and impact ham-

mer methods are close, although the technique of excited phase winding is more similar to the SRM operation. This confirms the effectiveness of both methods for vibration testing in SRMs. From the testing results, the modal damping ratio can be calculated and applied for use as input data for a structural simulation model.

The mounting of the SRM has an effect on the resonant frequency of the motor. Comparing the results, the flange-mounted support has a higher resonant frequency than the elastic rope support. Using the flange-mounted support increases the stiffness of the front cover because the flange-mounting is fixed on the base of the testing platform.

The last section of investigation in the motor assembly found that the front and end covers significantly impact the system vibration by increasing the resonant frequency of the motor. Conversely, the rotor does not have an effect on the resonant frequency of SRMs.

Chapter 6.
Investigation of Stator Deformation in Segmented Core

In the traditional electrical machine manufacturing process, a stack of single-piece lamination is commonly used to form the stator and rotor. Due to high raw material consumption and waste in the conventional process, segmented lamination cores are usually employed for large electrical machines, such as high power transformers, turbine generators, and electric marine propulsion. Segment use is increasingly being developed and applied to a wide range of electrical machines. It is well-known that the advantages of segmented core design mean a lower demand for raw materials, reduced material waste, small stamping dies and punching equipment, high slot fill factor, simple winding, fast production, and low manufacturing costs. However, many publications have reported that making segmented lamination cores causes an increase in stator core losses. Klontz and Li [84] discuss the key factors of core losses in different joint designs of segmented lamination cores and methods of reducing losses. Analytical modelling of eddy current loss calculation in segmented lamination cores was presented in [85]. In terms of vibration and acoustic noise effects, out-of-round lamination core due to the tolerance of machine cutting and imperfect contacts between segmented joints are also a root cause of vibration and acoustic noise generation in synchronous machines, as reported in [86].

Compressive hoop stress is one of the major influences on core losses in the segmented cores resulting from assembly and fabrication of stator and casing. This phenomenon was investigated in [87] and the results showed that increasing of compressive hoop stress on the laminated steel sheet creates high iron losses. To tightly hold each piece of the segmented core together, a shrink fit process is used with an

aluminium casing to cover the stack of the segmented laminated core. Bernard and Daniel [88] offered an analytical model and the effects of stress on hysteresis losses for rotor and stator with shrink fit of an SRM. The thermal modelling of segmented lamination cores in permanent magnet traction motors was also presented in [89] to improve machine output capability. Most research on segmented lamination cores has been performed on the core loss calculation of the segmented laminated cores. The effect of vibration and acoustic noise in segmented laminated cores appears to be largely undocumented. The stiffness and deformation of the stator with segmented laminated cores are difficult to predict in an analytical model. In [90] and [91], a method to calculate the deformation of stator stack, with one-piece lamination, using structural finite element analysis method was revealed and compared the structure of a conventional stator to the new stator design of switched reluctance motor.

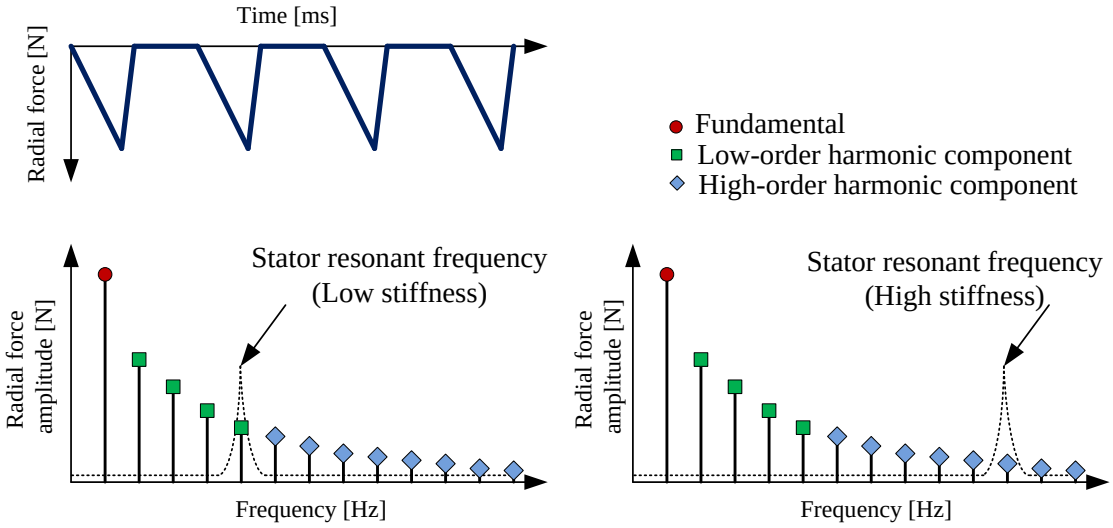

Figure 6.1: The effect of stator stiffness

Fig. 6.1 illustrates that how severe vibration appears and how it relates to radial forces. The harmonic components of the radial forces have a higher amplitude at low-order harmonics compared to those at the high-order harmonics. It is well known that the high amplitude vibration occurs when stator resonant frequency coincides with the high amplitude harmonic component of the radial forces, as shown in Fig. 6.1(left). Therefore, if a motor designer can shift stator resonant frequency to the high-frequency range, the high amplitude vibration generation will be reduced,

as shown in Fig. 6.1(right). This research discusses and compares the stiffness and deformation of six different types of SRM segmented stator cores, under compressive assembly with an aluminium casing. The six types of the different segmented stators are shown in Fig. 6.2. All stator types have the same geometry, though the joint contact of each segmented stator is different.

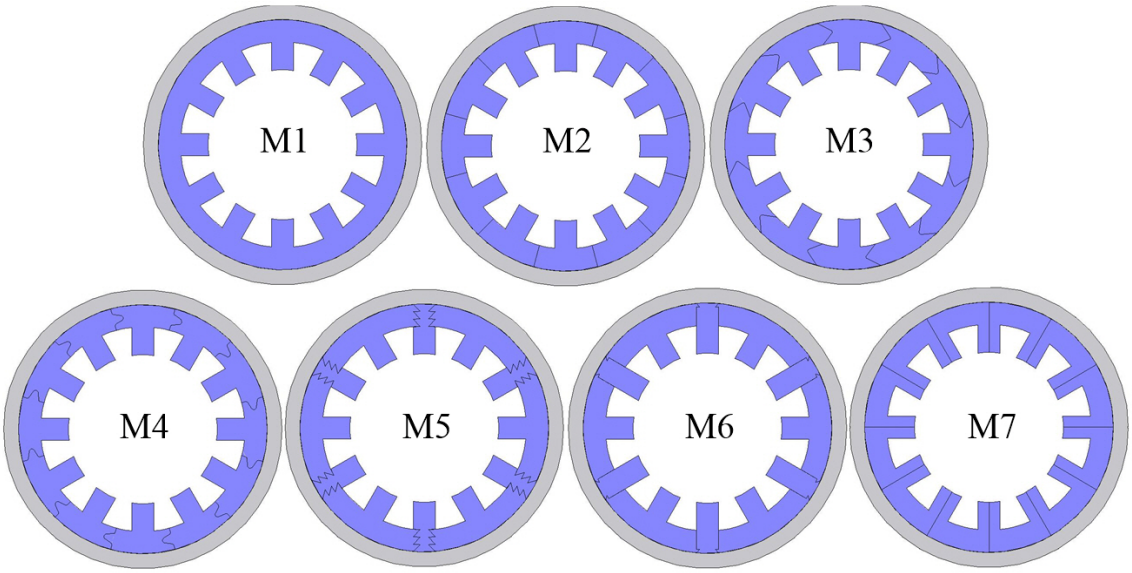

Figure 6.2: Segmented stator models

6.1 Compressive Hoop Stress on Stator

Shrink fit is a common technique in which an interference fit is executed by changing the size of a component before assembly by heating or cooling it before assembly, according to the thermal expansion theory of the material. The component is then left to return to room temperature after assembly. This technique is used in the manufacturing process of electric machines, such as assembling stator cores with casings, rotors, and shafts. The effect of interference fit on a steel sheet is to create a mechanical stress distribution in the steel sheet, which causes high iron losses. The mechanical stress by interference fit was performed using ANSYS software for stress analysis. Most stress appearing in the stator yoke and slots is the compressive hoop stress and is tensile in the stator casing, as indicated in Fig. 6.3.

The compressive hoop stress distribution of all stator models under shrink fitting

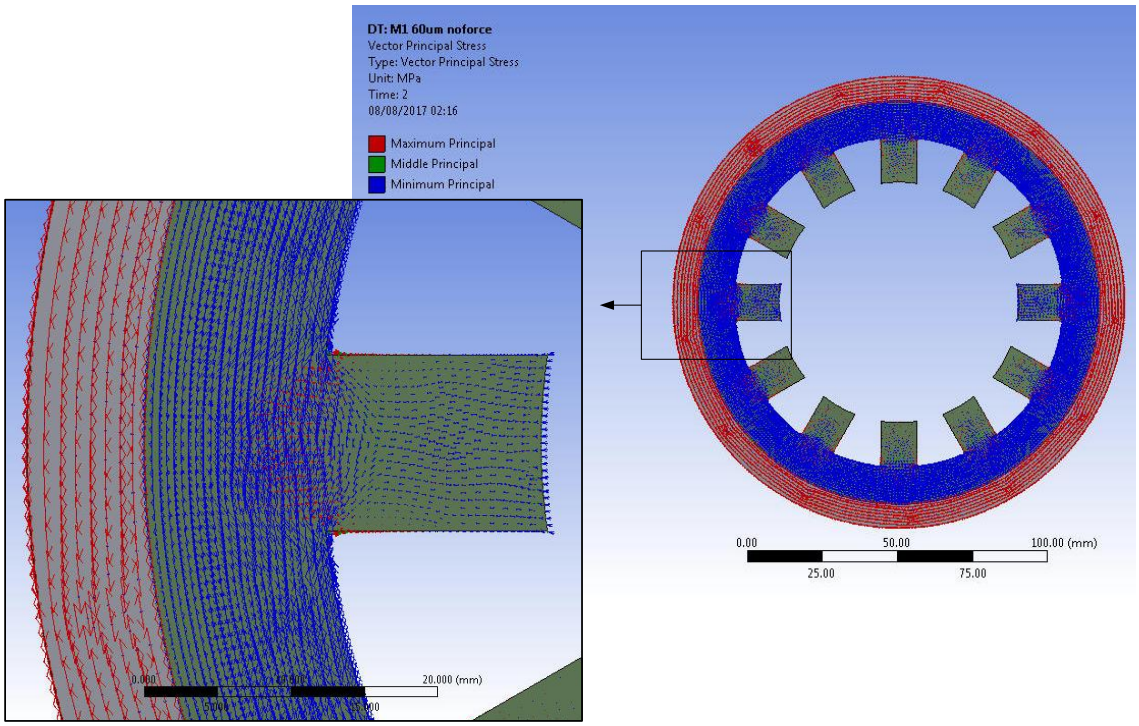

Figure 6.3: Vector principal stress display under interference fit technique, (blue arrow: compressive hoop stress and red arrow: tensile stress)

at 60 μm was calculated and displayed with colour contours, as shown in Fig. 6.4-6.10. Furthermore, the results also show that the minimum value of the stress is the maximum compressive hoop stress. A negative sign of the principal stress can be defined as the compressive hoop stress, whereas the positive sign of the principal stress can be defined as the tensile stress.

Stator M1 is the single piece stator core and the conventional stator design. The strength of the stator M1 model is higher that of the segmented stator core. From Fig. 6.4, the high compressive hoop stress of stator M1 model is located around the stator slots. The segmented stator M2 model, which has a radial line segment joint, also has high compressive hoop stress around the stator slots, similar to the M1 model, as indicated in Fig. 6.5. The large triangle mitre segment joint of the segmented stator M3 model has the high compressive hoop stress at the point of the triangle joint, as indicated in Fig. 6.6. On the other hand, the small triangle mitre with the radial line segment joint of the segmented stator M4 model has the high compressive hoop stress at the bottom of the triangle and the radial line joint, as

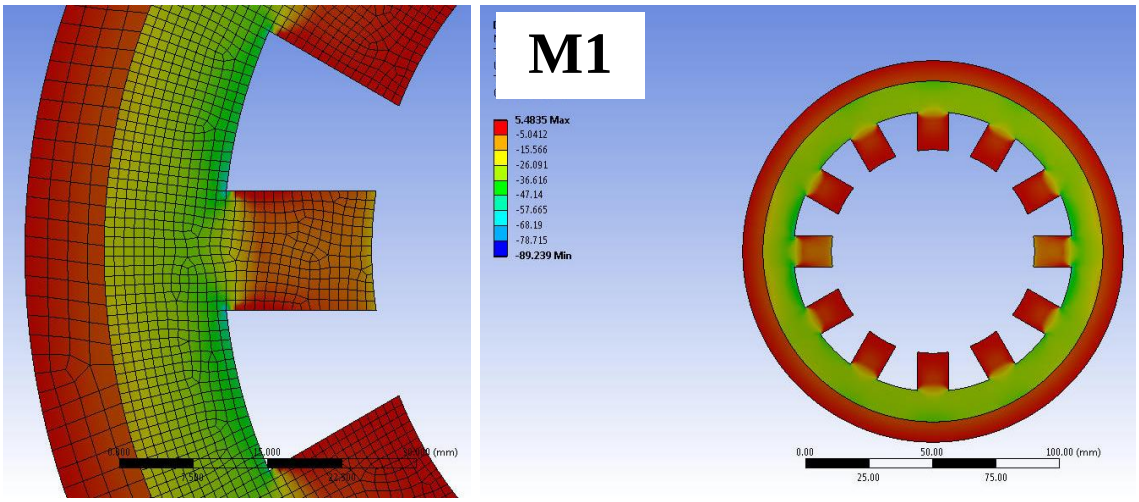

Figure 6.4: Compressive hoop stress distribution on stator M1 model

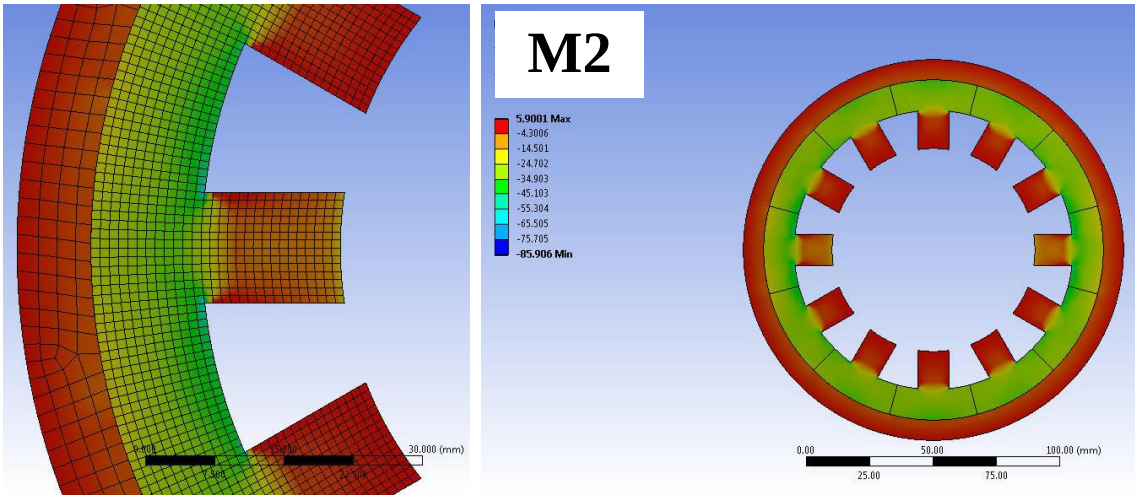

Figure 6.5: Compressive hoop stress distribution on stator M2 model

indicated in Fig. 6.7, and also at the stator slot. The segment joint of the segmented stator M5 model is saw-shaped. High compressive hoop stress occurs at the tip of the saw-shaped, as illustrated in Fig. 6.8. This finding is different from that of the segmented stator M6 model, which is the radial line with single saw-shaped segment joint. The high compressive hoop stress of this model is around the bottom of the saw-shaped, as shown in Fig. 6.9.

The segment joint of the segmented stator M7 model is the radial line that splits the stator poles, whereas, in the other models, the segment joint is made on the stator yoke. The high compressive hoop stress of M7 model appears around the stator slot, as illustrated in Fig. 6.10, similarly to the M1 and M2 model.

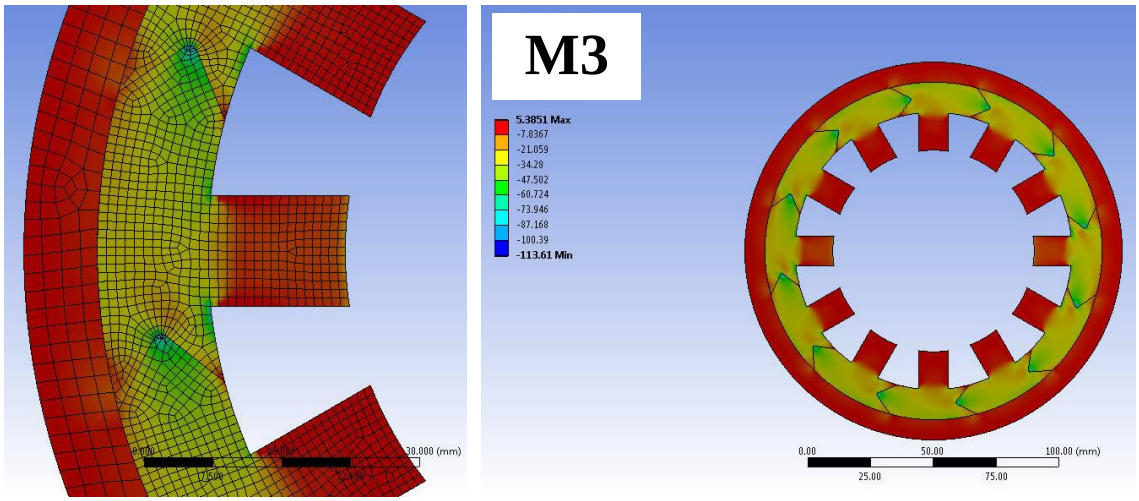

Figure 6.6: Compressive hoop stress distribution on stator M3 model

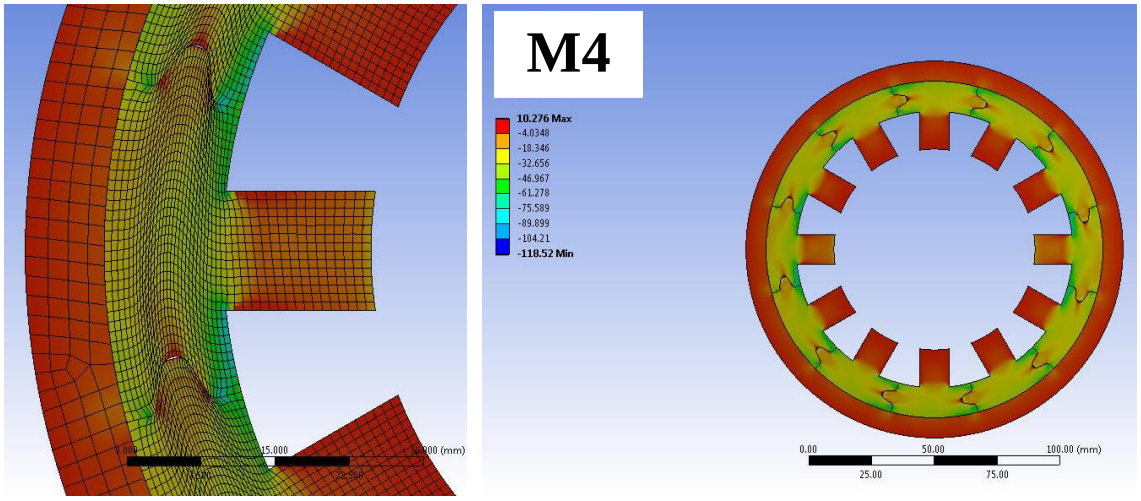

Figure 6.7: Compressive hoop stress distribution on stator M4 model

In addition, the stress distribution on stator model at the different interference fits, from 0 to 100 μm, was calculated in each stator model to investigate the average compressive hoop stress on the stator model and the high compressive hoop stress, as described above in each stator model. The average compressive hoop stress on the stator model is shown in Fig. 6.11 and summarised in Table 6.1.

The single piece stator model M1 has a high value of average compressive hoop stress at all interference fits compared to the other stator model. At 60 μm of interference fit, the segmented stator M5 gives a low value of the average compressive hoop stress compared any other models at -26.92 MPa. Models M2, M7 and M6 have a similar average compressive hoop stress at around -28 MPa. The models M3

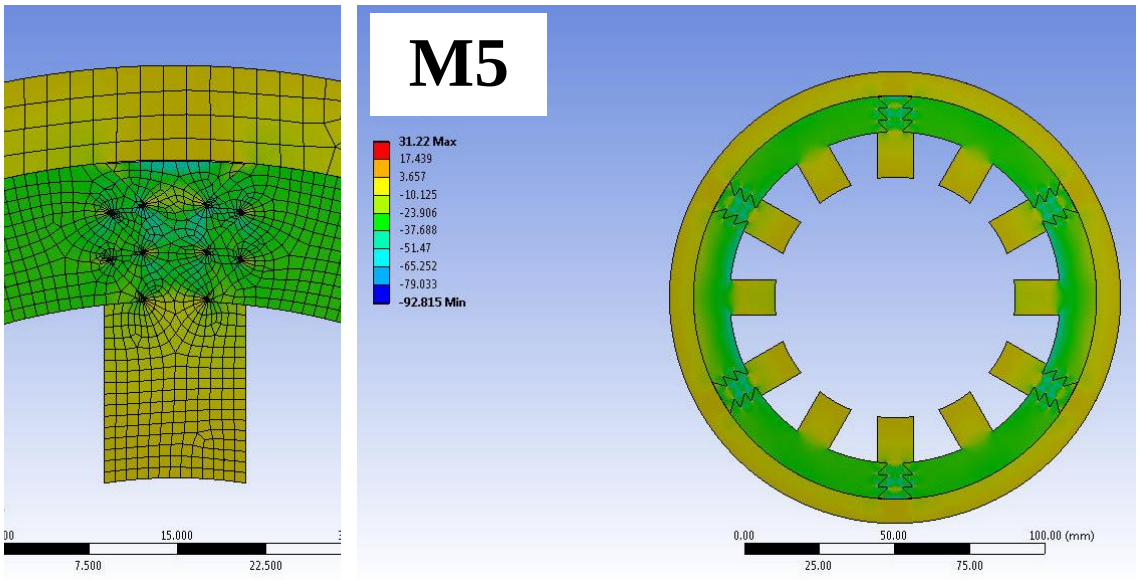

Figure 6.8: Compressive hoop stress distribution on stator M5 model

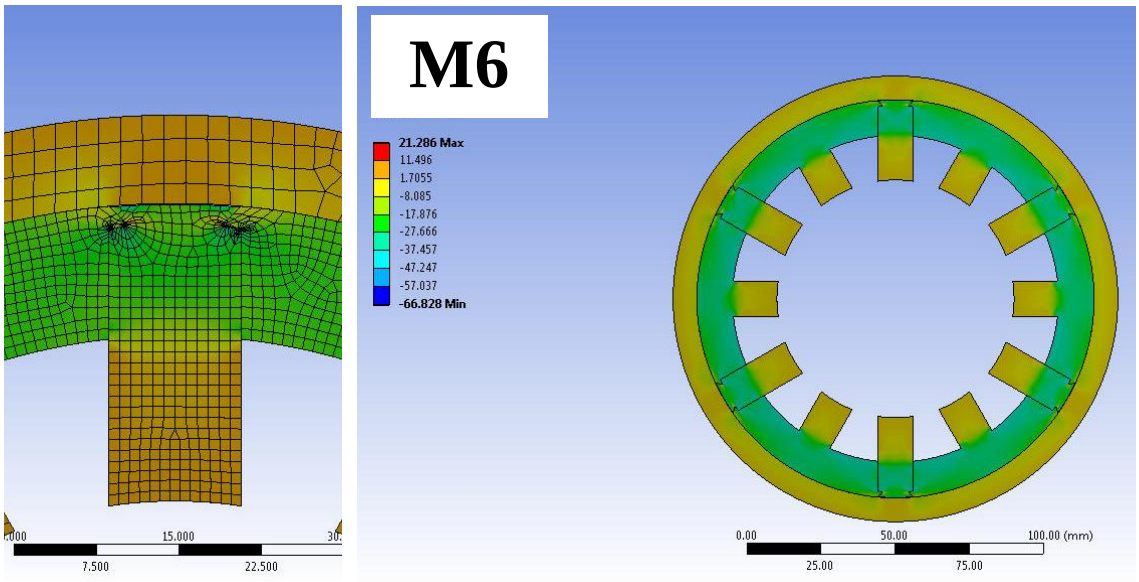

Figure 6.9: Compressive hoop stress distribution on stator M6 model

and M4 also have a similar value at around -27 MPa.

A high average compressive hoop stress on the stator steel sheet has a significant impact on iron loss characteristics. The circumferential or hoop stress is higher than the radial stress when using the shrink fitting technique in assembly processes [92]. An increasing of the iron losses on the steel sheet depends on each material. Some materials have a saturation point of the iron losses, which do not increase after this

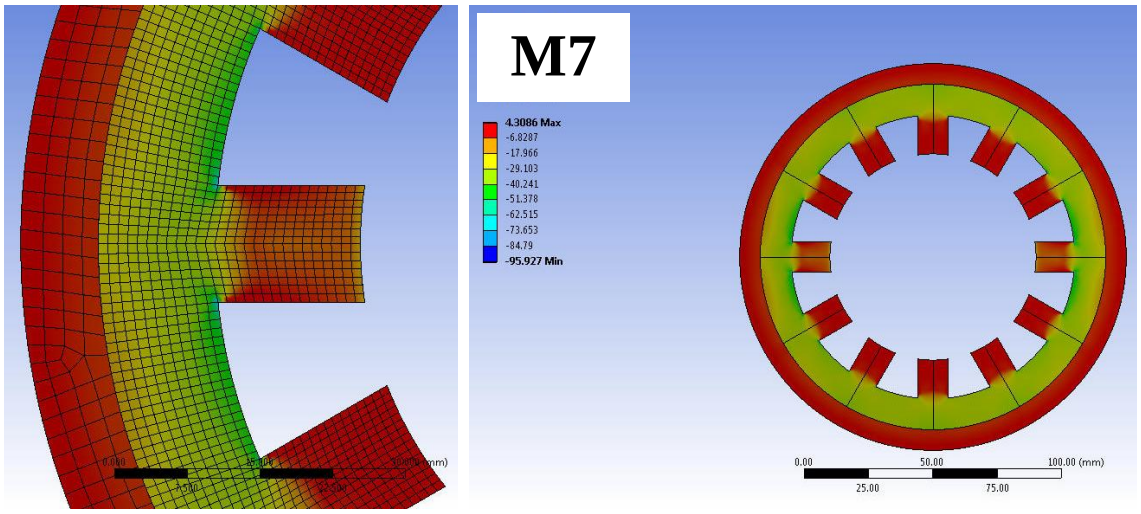

Figure 6.10: Compressive hoop stress distribution on stator M7 model

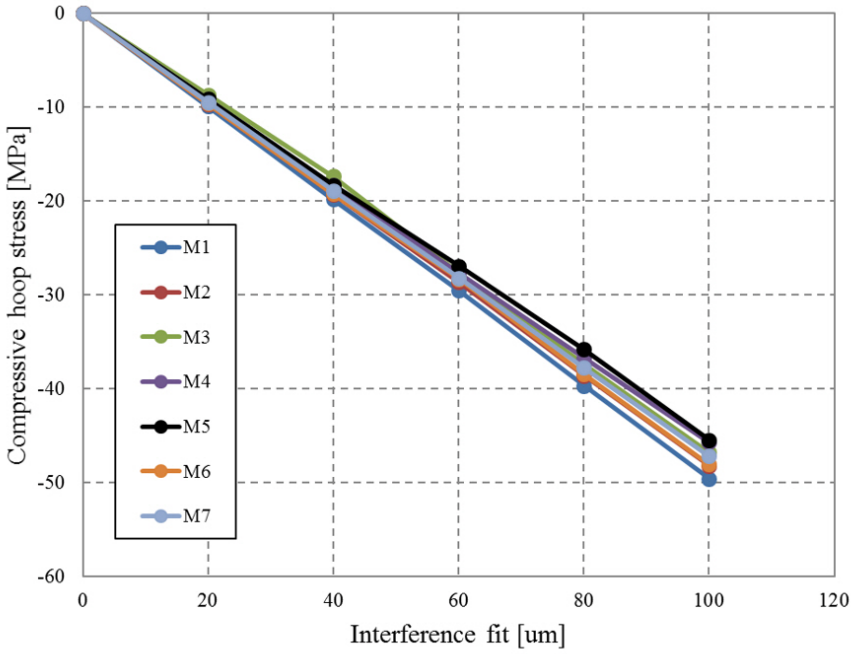

Figure 6.11: Average compressive hoop stress at different interference fits

point. Another parameter that has a major effect on the iron losses, apart from the compressive hoop stress, is flux density. The high iron losses are created in the stator core when it operates at high flux density and with high-stress distribution in the stator core. The motor designer should consider maximum flux density of the motor when using shrink fitting techniques. The stress distribution in the stator core by shrink fitting changes the magnetic flux path in the stator [93, 94]. The magnetic

flux flows to the stator area, which is not under mechanical compression stress. This flow increases the magnetic flux density in the area of non-stress distribution in the stator, causing high iron losses.

Table 6.1: The average compressive hoop stress of all stator model at different interference fits

Interference	Average compressive hoop stress [MPa]						
fit [μm]	M1	M2	M3	M4	M5	M6	M7
0	0.0	0.0	0.0	0.0	0.0	0.0	0.0
20	-9.92	-9.65	-8.69	-9.17	-9.14	-9.62	-9.44
40	-19.84	-19.30	-17.37	-18.35	-18.29	-19.24	-18.88
60	-29.53	-28.66	-27.68	-27.68	-26.92	-28.32	-28.22
80	-39.68	-38.60	-37.44	-36.73	-35.80	-38.47	-37.77
100	-49.60	-48.42	-46.80	-45.70	-45.49	-48.09	-47.21

6.2 Deformation of Stator

To observe the stiffness of segmental stators for 12/10 single-tooth wound segmented rotor SRM (12/10 SSRM), two types of segmented joint model M5 and M6, as shown in Fig. 6.8 and 6.9, were selected due to their suitability for manufacturing and coil winding assembly. The stator of the 12/10 SSRM is cut and separated into 12 segmented parts, as shown in Fig. 6.12(right). The coil winding can be inserted from behind the large poles of the stator which are part number 1, 3, 5, 7, 9, and 11 in the red colour. The other choices of segmented joint model (M2, M3, M4, and M7), which are shown in Fig. 6.2 can also be used to build segmented stators of the 12/10 SSRM, though this process will require more effort in the process of coil winding compared to the segmented joint types M5 and M6. The magnetic flux path and directions of attraction force at the aligned rotor position of the 12/10 SSRM are shown in Fig. 6.12.

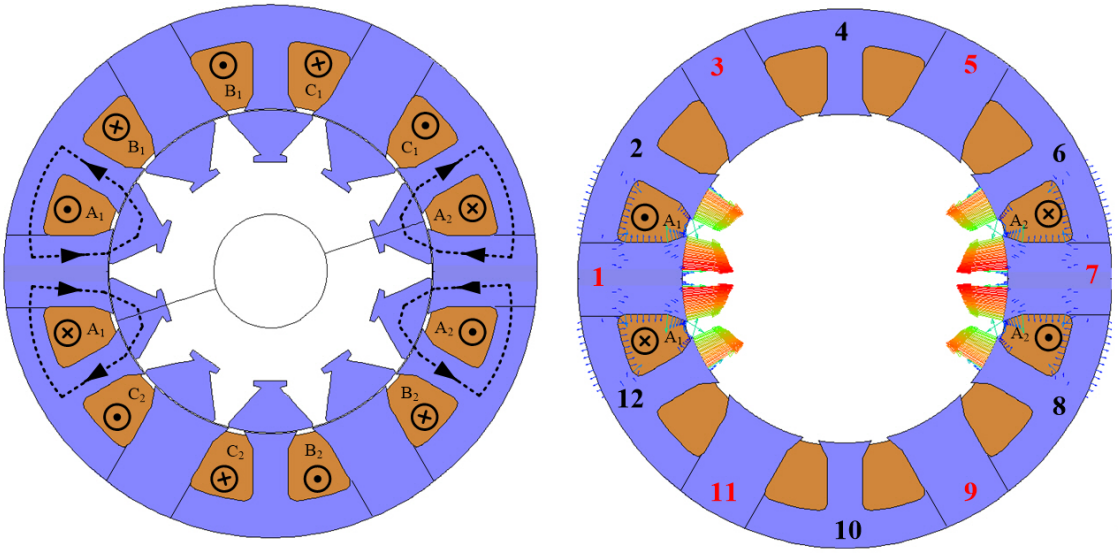

Figure 6.12: Magnetic flux path and magnetic force 12/10 single-tooth wound segmented rotor

The opposing stator poles tend to attract each other resulting from attraction forces of the stator acting to the rotor. The movement direction of the 12/10 SSRM is shown in Fig. 4.11, corresponding with a second-order mode shape of vibration, so this mode shape is a dominant mode shape of the 12/10 SSRM. Stator deformation

is related to a dominant mode shape of the 12/10 SSRM structures.

Fig. 6.2 shows the different joints of segmented stator core investigated in this research. In this investigation, the effects of the motor casing are considered. The modal analysis commonly used to determine the stiffness of stator structure is more complex when the frame is considered with a shrink fitting method.

6.2.1 Simulation Techniques and Analysis Results

The analysis in this research was conducted using an ANSYS structural analysis. There are two ways of applying force into the segmented stator cores: (I) external force and (II) internal force, as presented in Fig. 6.13. The characteristics of radial forces in a switched reluctance motor are maximum at the aligned position, which generates a significant deformation in the stator. This finding is similar to applied internal force into two opposite stator poles with different force directions, as shown in Fig. 6.13(right). In FE simulation, the analysis with applied internal force is suitable, but in the experimental test, it is more difficult to apply internal force to the inside stator structure. Therefore, the analysis method with applied external forces, as shown in Fig. 6.13(left), was developed for the experimental test.

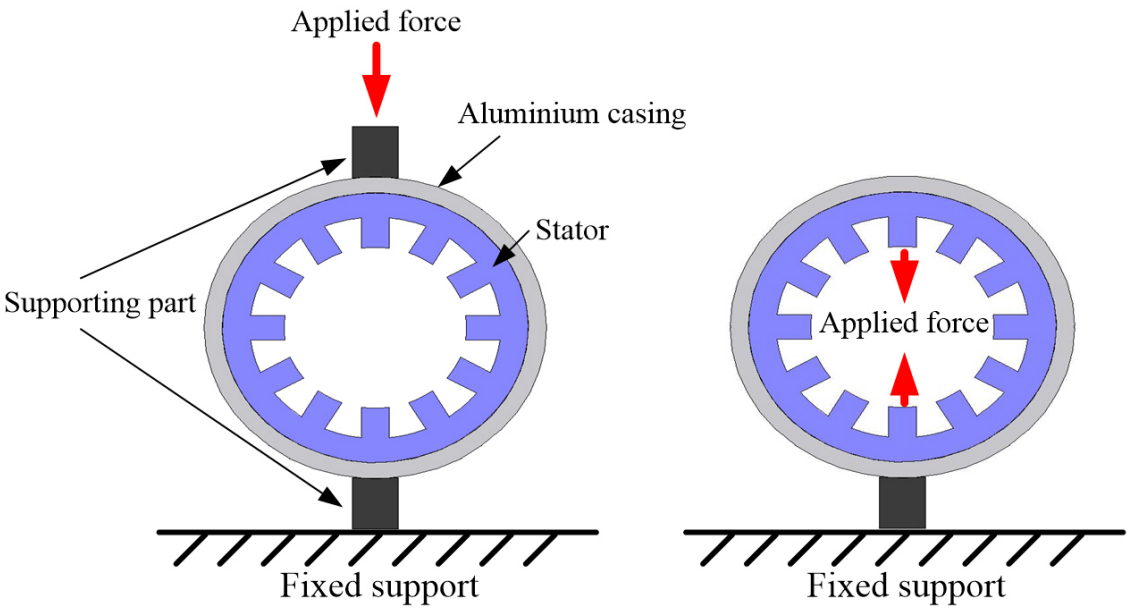

Figure 6.13: Direction of applied force: external force (left) and internal force (right)

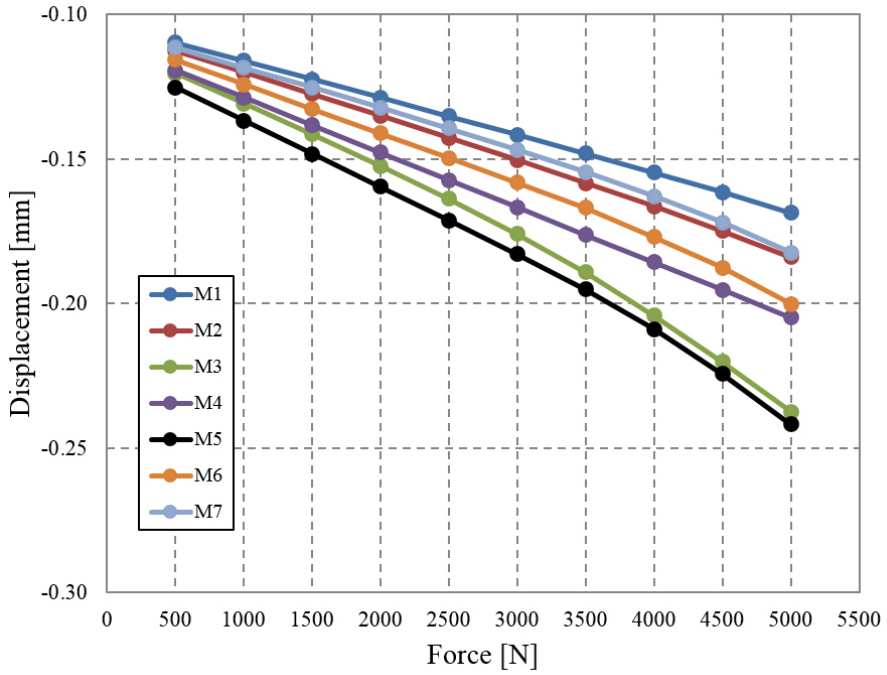

Figure 6.14: Simulation results of displacement vs. force at different joints of segmented stator model with applied internal force

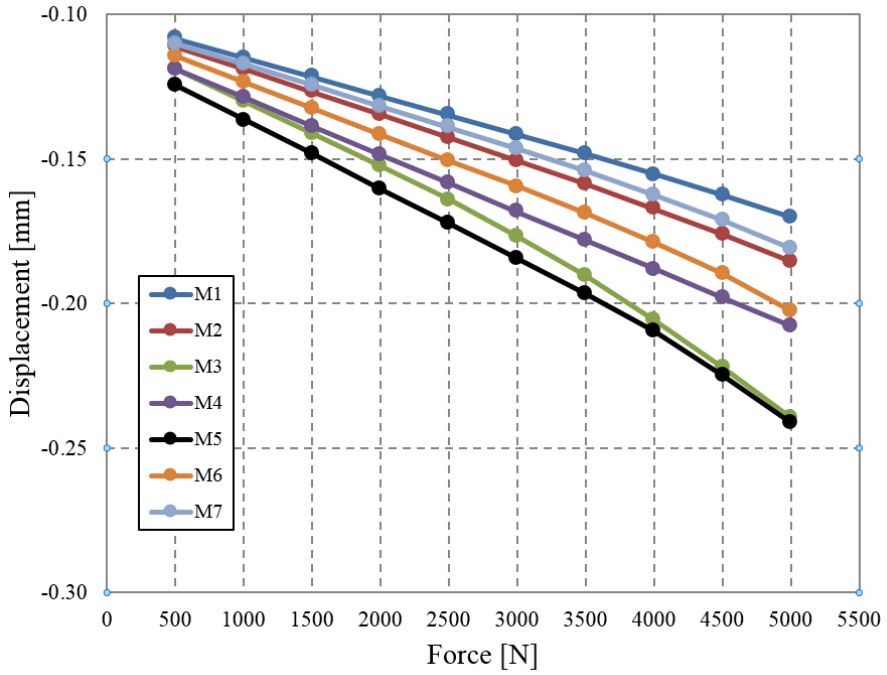

Figure 6.15: Simulation results of displacement vs. force at different joints of segmented stator model with applied external force

To verify both analyses, FE simulation method is used to initially calculate for stator deformation of segmented lamination core with different types of joint. Both results are compared and should be similar. In both analyses, shrink fitting with aluminium casing is considered. The radial interference fit between casing and segmented stator cores is 60 μm (120 μm in diameter). Fig. 6.14 and 6.15 show the graphic representation of comparative results with different types of segmented joint and show the comparative results between applied internal and external forces. The stiffness (k) of the stator model can be calculated by

$$k = \frac{F}{\delta} \tag{6.1}$$

where F and δ are the applying force and the deformation of the body by applying force, respectively. The stiffness of each stator models was calculated and shown in Table 6.2. The stiffness is typically measured in newtons per millimetre.

Table 6.2: Comparison of the stator stiffness between applied external force and applied internal force at 60 μm of the radial interference fit, using FE analysis

Stator model	Stator stiffness with internal force [N/mm]	Stator stiffness with external force [N/mm]	error [%]
M1	77172.4	73847.5	4.3
M2	63749.9	61346.5	3.8
M3	39194.2	38046.8	2.9
M4	52684.9	50666.6	3.8
M5	39994.5	39665.0	0.8
M6	55249.5	52934.1	4.2
M7	65420.6	64884.5	0.8

Constant forces from 500 to 5000 N are applied into stator structures, and deformation of the stator is measured. In this observation, solid steel (EN24T) is used to build the segmented stator rather than lamination core, and the motor casing is aluminium alloy (6082T6). The comparative results show that the minimum deformation of the segmented stator can be seen in segmented stator model M7, whereas the M3 segmented stator model gives a maximum deformation to with any other segmented stator model. The problem of model M7 is that the coil winding may

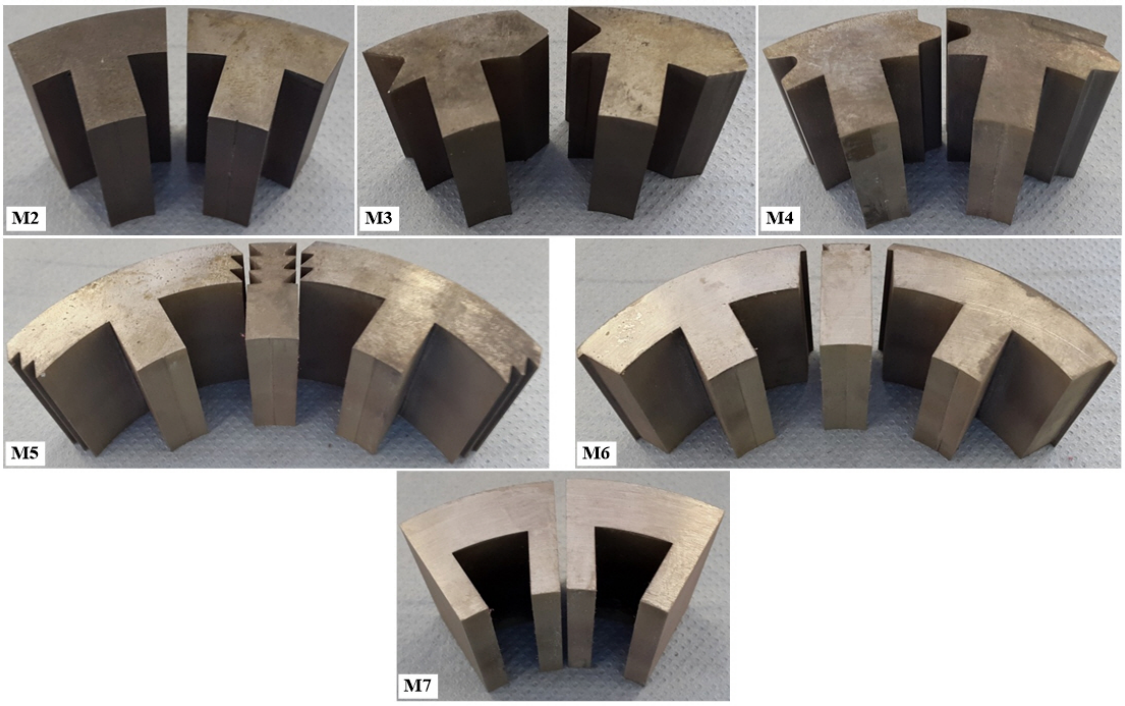

Figure 6.16: Different segment joints of experimental segmented stator

damage coils when the stator poles vibrate in the dominant mode shape. This damage is due to the contact of each segmented joint in the middle of the stator pole holding the coil.

It seems that both the results with applied external and internal force are similar so the analysis method with applied external force can be employed in an experimental test for validation between the simulation and the experimental test. The prototypes of different segmented stators are shown in Fig. 6.16.

The results reveal that the segmented joint model M6 is stiffer than the model M5. However, model M6 has high deformation compared to model M2. To improve the stiffness of model M6, the modified structures at the corner of the stator pole were applied by filling the corner of the stator pole to be a curve shape, as this technique is highly effective in conventional single piece stator cores. Fig. 6.17 shows a new model M6 after modified pole corner. Fig. 6.18 result shows that by using this technique, the stiffness of the stator structure was improved by 0.78 %. However, in Fig. 6.19, the comparison of the average compressive hoop stress between segmented stator M6 model and M6 NEW model shows that two models

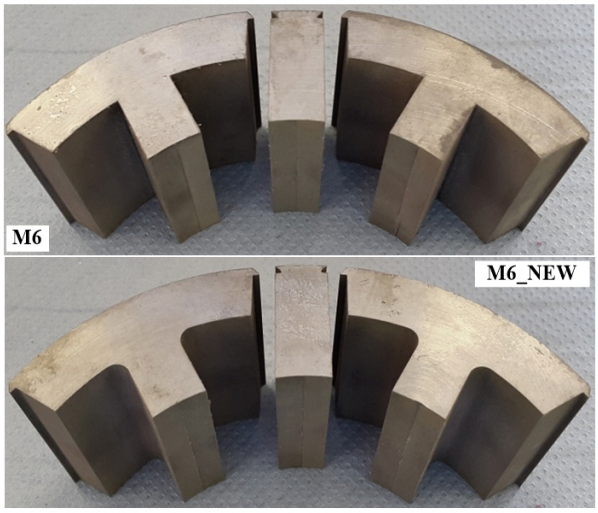

Figure 6.17: Comparison of the pole corner structure between model M6 and model M6 NEW

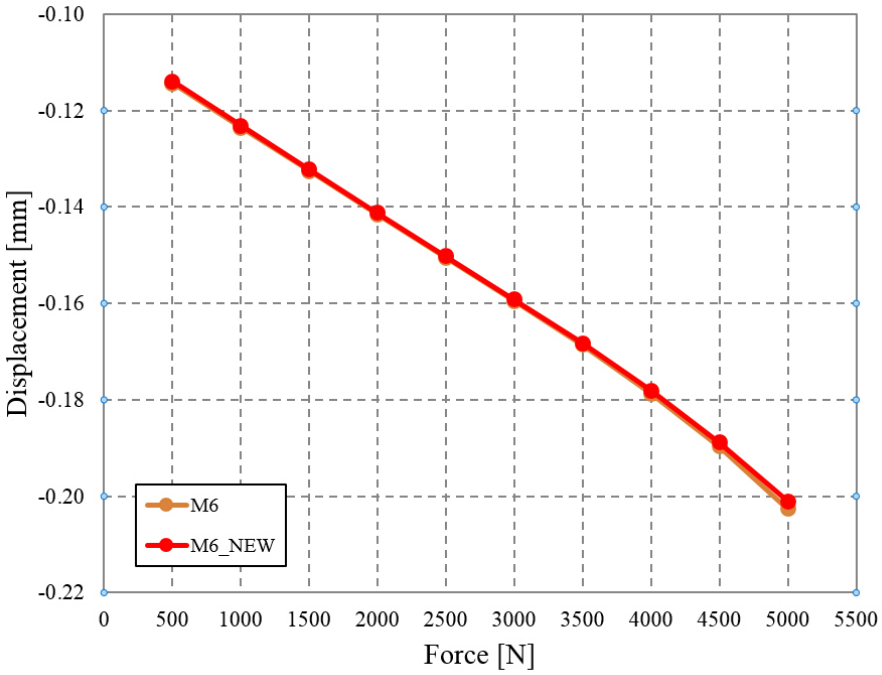

Figure 6.18: Comparison of the stator displacement between model M6 and model M6 NEW

have a similar value of the average compressive hoop stress on the stator model.

In the M6 NEW model, most of the compressive hoop stress spreads around the stator slots compared to that of the stator M6 model, which is located around segment joints. Fig. 6.20 shows the compressive hoop stress distribution on both

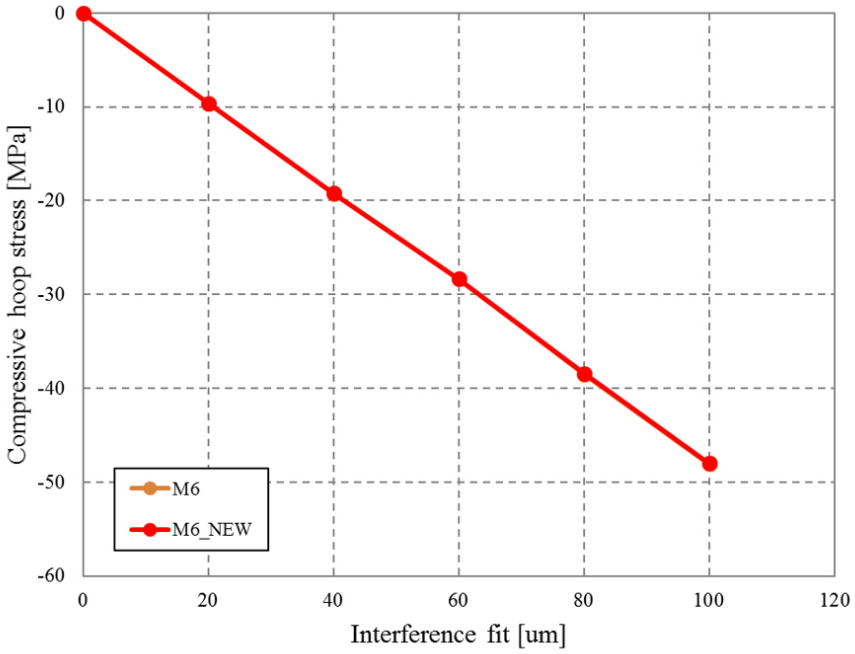

Figure 6.19: Comparison of the average compressive hoop stress between model M6 and model M6 NEW

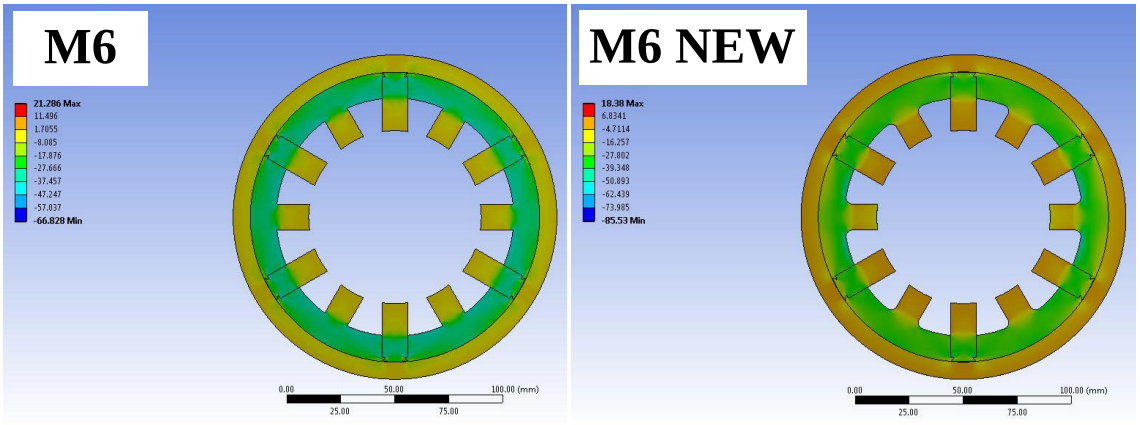

Figure 6.20: Compressive hoop stress distribution on stator M6 model (right) and M6 NEW model (left)

segmented stator model. From the above section, all segmented stator models are simulated with 60 μm radial interference fit under the aluminium casing. To study the effects of interference fit on the stiffness of the segmented stator, various levels of interference fit are applied, from 20 to 100 μm. The inner diameter of the casing is made slightly smaller than the outer diameter of the segmented stator by 20,

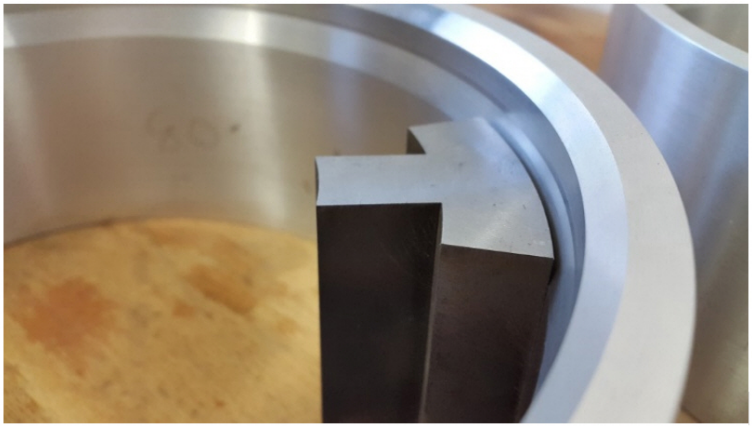

Figure 6.21: Aluminium casing

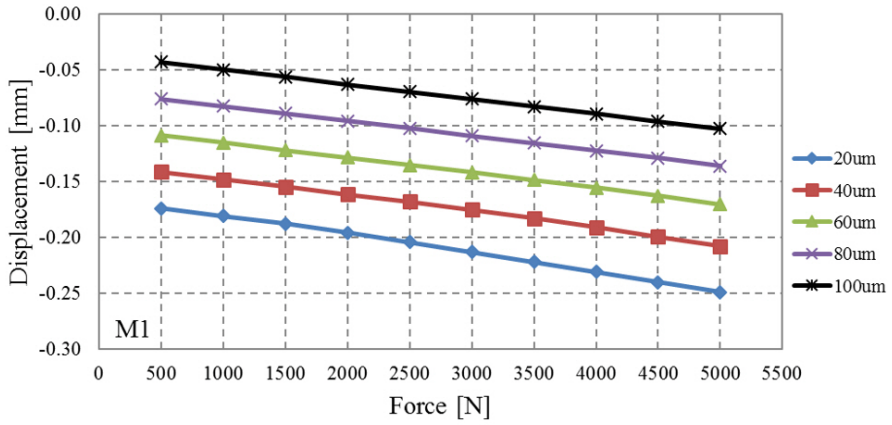

Figure 6.22: The stator deformation of model M1 with different interference fits

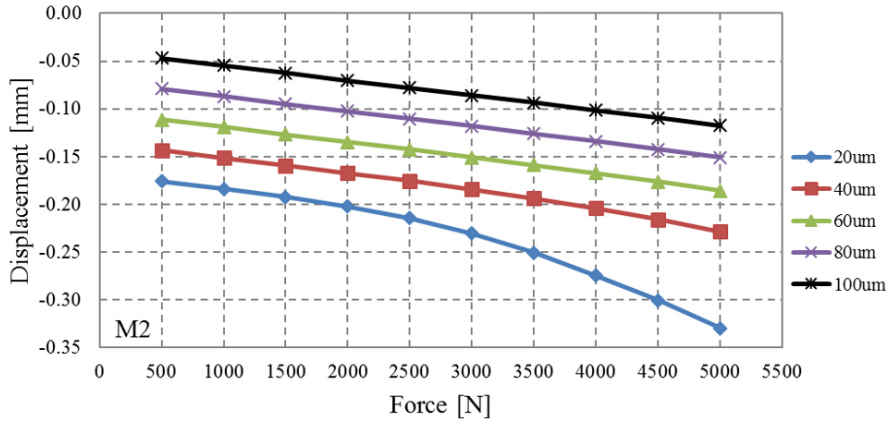

Figure 6.23: The stator deformation of model M2 with different interference fits

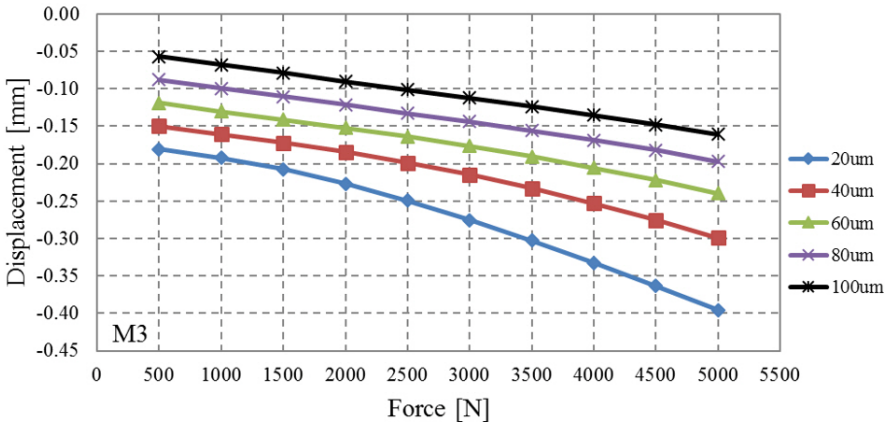

Figure 6.24: The stator deformation of model M3 with different interference fits

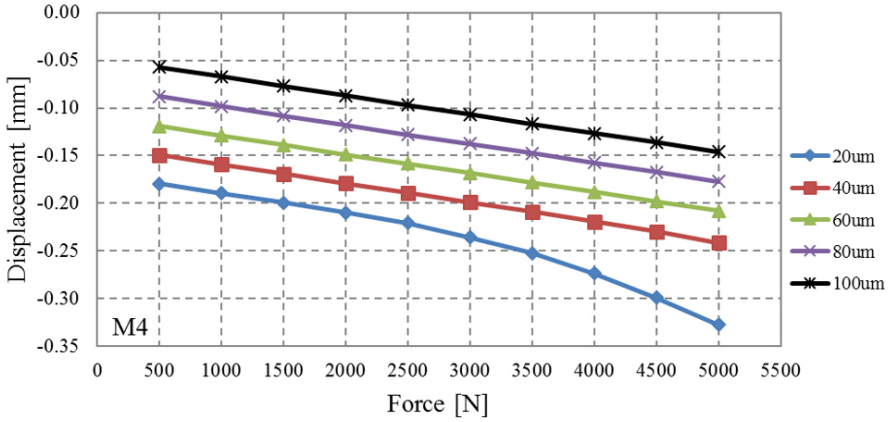

Figure 6.25: The stator deformation of model M4 with different interference fits

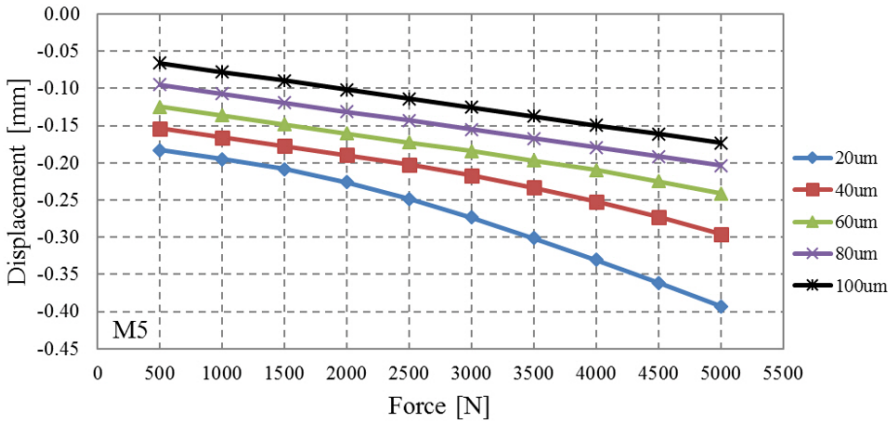

Figure 6.26: The stator deformation of model M5 with different interference fits

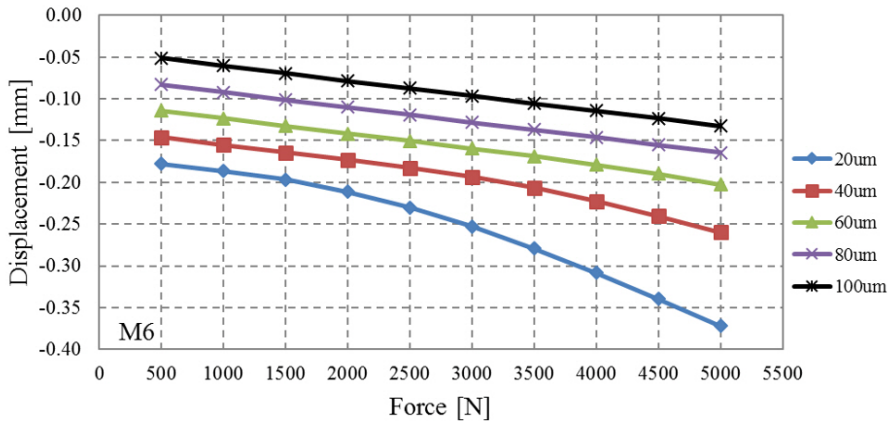

Figure 6.27: The stator deformation of model M6 with different interference fits

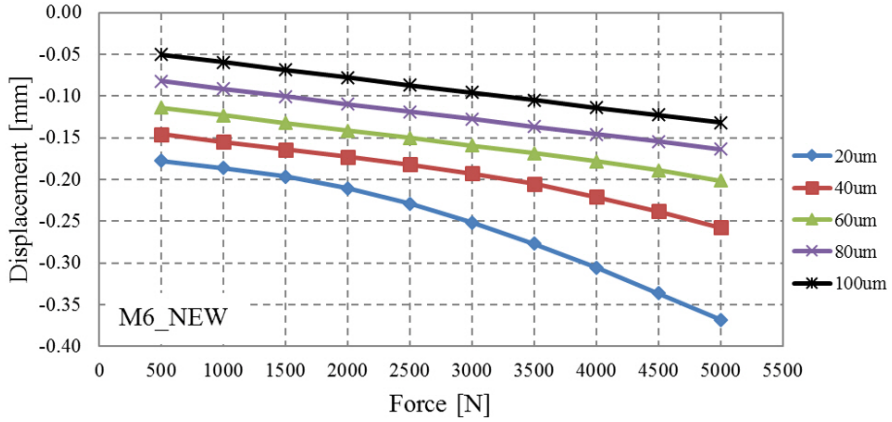

Figure 6.28: The stator deformation of model M6 NEW with different interference fits

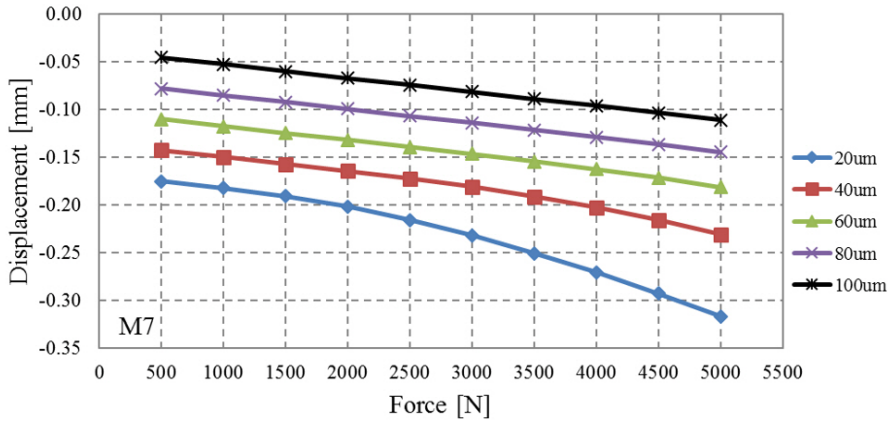

Figure 6.29: The stator deformation of model M7 with different interference fits

Table 6.3: The stiffness of the stator M1, M2, M3, and M4 model at different interference fits

Interference fit [μm]	Stiffness [N/mm]			
	M1	M2	M3	M4
20	59174.6	29968.8	20480.9	31968.4
40	68216.4	54429.8	30614.7	49766.8
60	73847.4	61346.5	38046.8	50666.6
80	75213.8	63111.9	42136.7	50712.9
100	75577.6	63718.6	43850.9	50652.7

Table 6.4: The stiffness of the stator M5, M6, M6 NEW, and M7 model at different interference fits

Interference fits [μm]	Stiffness [N/mm]			
	M5	M6	M6 NEW	M7
20	21042.6	22862.1	23347.9	31780.0
40	32751.9	41144.0	41979.0	52934.9
60	39665.0	52934.1	53347.2	64884.5
80	41683.5	55464.9	55431.5	68161.0
100	41962.4	55447.3	55402.5	69156.3

40, 60, 80, and 100 μm. The aluminium casing is shown in Fig. 6.21. All results of the different interference fits in each segmented stator models are presented in Fig. 6.22-6.29.

The simulation results show that low levels of interference fit, such as 20 and 40 μm, increase the radial deformation in the segmented stator. With low levels of interference fit, deformation dramatically increases when considerable force is applied. It was found that the minimum level of interference fit, for which rate change of deformation with force remains linear was 60 μm. At 80 μm and 100 μm of radial interference fit level, deformation remains linear. However, with high levels of interference fit, the high-stress distribution will occur, generating high core losses in the stator.

Table 6.3 and 6.4 summarise the stiffness of all stator model at different interference fits. These tables show that the stiffness dramatically increases when the

interference fit increases from 20-60 μm. From 60-100 μm of the interference fit, the stiffness increases slightly. Therefore, the radial interference fit at 60 μm is suitable for assembly of the stator core with the stator frame as it is the minimum level of shrink fit, for which the stiffness remains linear. Also, this fit has a lower compressive force, giving a low value of the maximum compressive hoop stress on the stator compared to interference fit at 80 and 100 μm.

6.2.2 Construction of Stator Prototype

In Section 6.2.1, the radial interference fit of 60 μm was selected for stator assembly. The segmented stator core was constructed using the solid steel (EN24T), and the motor casing is an aluminium alloy (6082T6). The segmented stator core was cut using an Electrical Discharge Machining (EDM) wire erosion machine, which has minimum tolerance at $\pm$20 μm, as shown in Fig. 6.30. The aluminium casing was also cut by an EDM machine and then turned into an inner/outer surface by a CNC lathe, which has a minimum tolerance of $\pm$10 μm.

The outer diameter of the segmented stator core is 134 mm, and stator yoke wall thickness is 12 mm. The aluminium stator casing has an inner diameter of 133.88 mm and wall thickness of 8 mm. The stator yoke thickness should be thicker than the wall thickness of the casing to reduce the influence of casing stiffness to the stator core stiffness. This analysis focuses only on the stiffness of the stator core. If the casing wall thickness is thicker than the stator yoke thickness, it will have an effect on the stiffness of the stator core. The lengths of both stator core and aluminium casing are the same, at 50 mm. The stator M1 model is a single core, whereas the stator M2, M3, M4, and M7 models were cut equally in 12 pieces. The large six pieces and small six pieces of the stator segment were made in the stator M5, M6, and M6 NEW models. The prototype of all segmented stator models were cut as shown in Fig. 6.31-6.34.

After finished cutting the stator core, measuring the outer diameter of the stator is the next step in determining the exact value of the outer diameter, according to the EDM machine, which has a high tolerance for error. A clamping ring was made to hold each of the segmented stators tightly for measuring, as shown in Fig. 6.35.

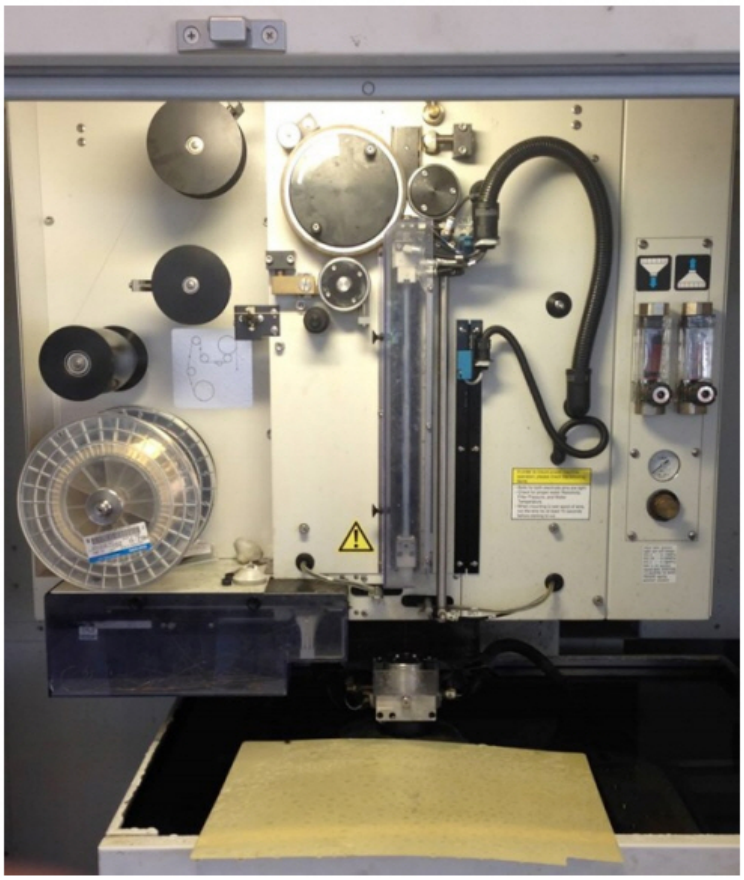

Figure 6.30: EDM machine

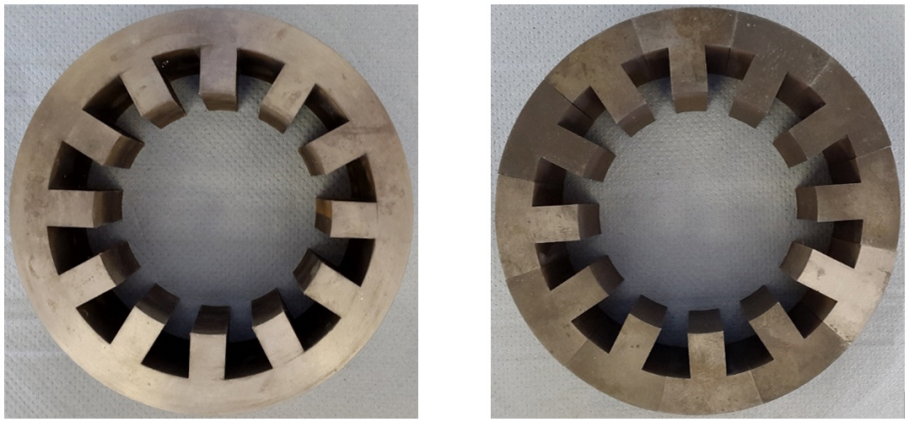

Figure 6.31: The prototype of stator model: M1 (left) and M2 (right)

The turning of the inner and outer surface of aluminium casing was performed after the measuring the outer diameter of the segmented stator core. For this reason, the inner and outer of casing diameter in each stator models are different. The assembly process is illustrated in Fig. 6.36. The parts of assembly process consist

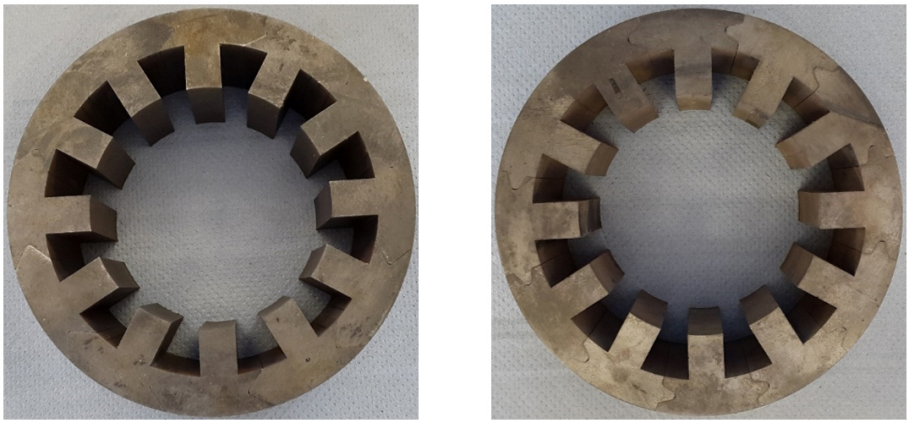

Figure 6.32: The prototype of stator model: M3 (left) and M4 (right)

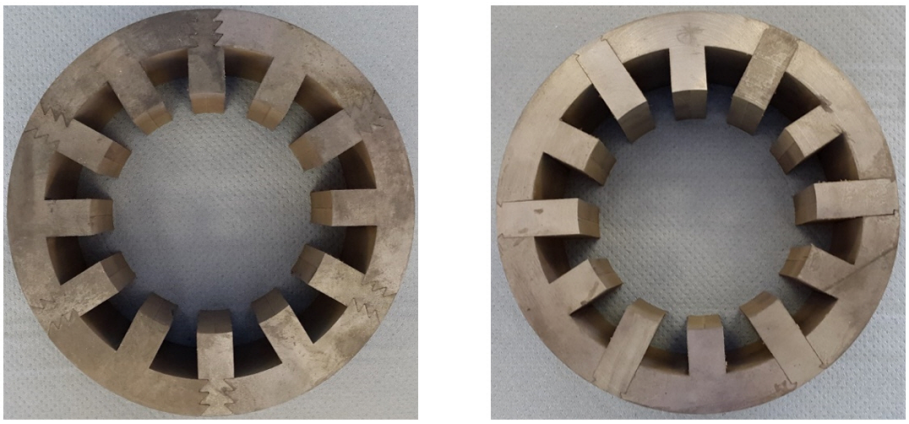

Figure 6.33: The prototype of stator model: M5 (left) and M6 (right)

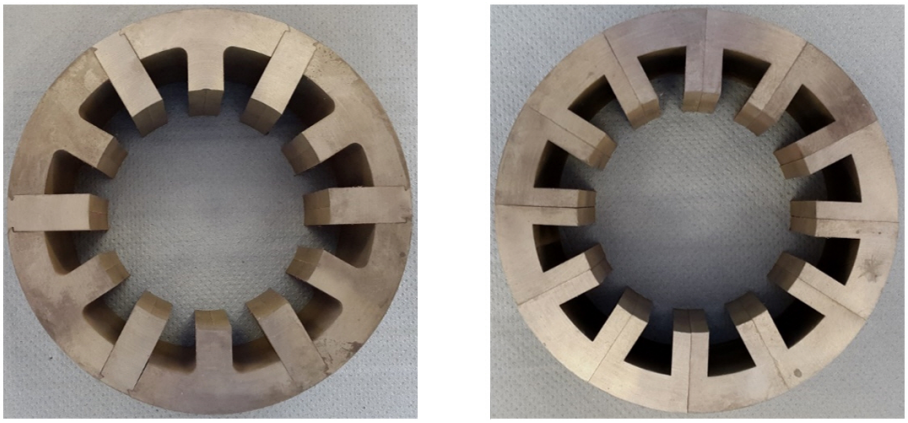

Figure 6.34: The prototype of stator model: M6 NEW (left) and M7 (right)

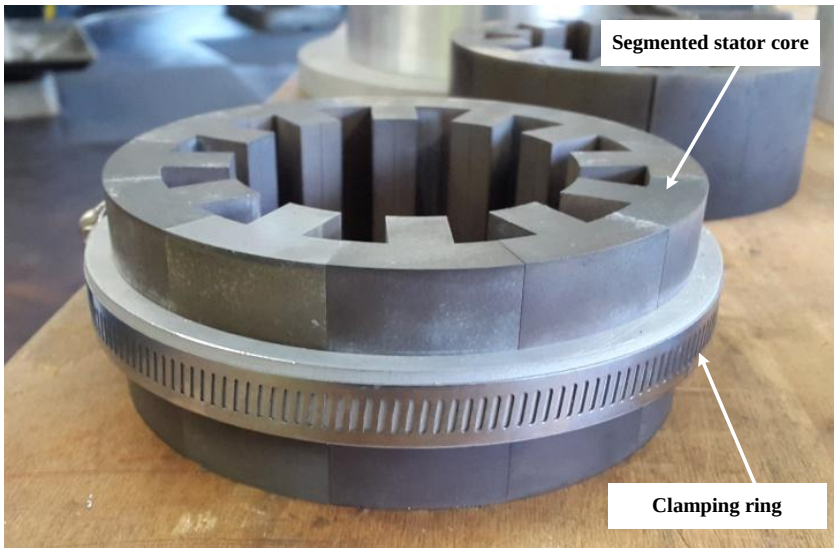

Figure 6.35: Measurement procedure of the prototype of stator model

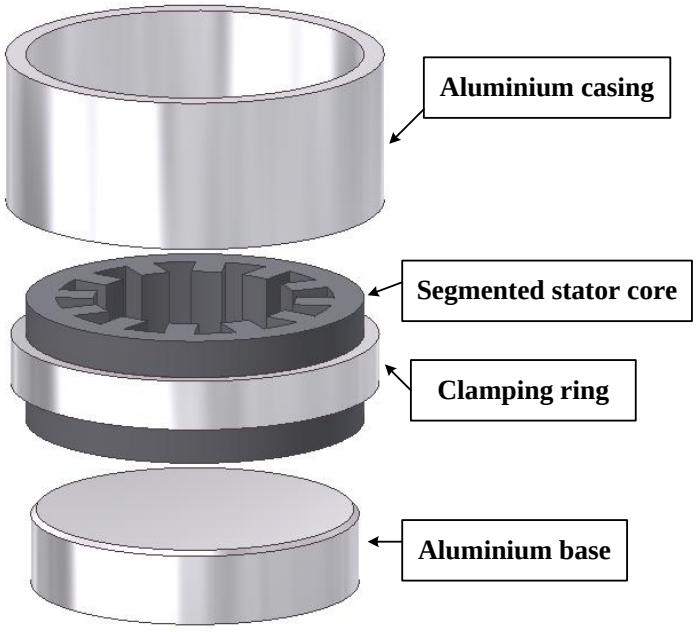

Figure 6.36: The assembly process of the stator core

of aluminium casing, segmented stator core, the clamping ring and aluminium base. The aluminium casing was heated at 80°C which expands the inner diameter up to 134.0656 mm, to achieve a clearance fit between the outer stator core and inner aluminium stator housing. The original inner diameter is 133.88 mm at 20°C of ambient temperature. Aluminium has a linear expansion coefficient of 23.1 m/m.K

x 10^{-6}. A hydraulic pressing machine was used to press the hot aluminium casing on to the stator core and then allows it to return to room temperature. The two supporting parts (top and bottom) were made by using EN24T solid steel material and were used to hold the stator prototype during the experimental testing, as shown in Fig. 6.37. The pressing force was applied on the top supporting part, while another supporting part was fixed on the base of the testing platform.

6.2.3 Experimental Testing

6.2.3.1 Stiffness Test

The experimental stiffness testing of the stator prototype, as described above, was implemented by applying the external force as shown in Fig. 6.13(left). The 10 kN Shimadzu Autograph AGS-X as shown in Fig. 6.38, is an automatic high precision stress/strain material machine testing and was used to apply an external force to the stator prototype. This machine has a load cell with accuracy within ±0.01 N and positional accuracy of ±0.01 mm. The testing machine automatically measures the deformation of the stator prototype and applied force. All stator prototypes were tested three times on three different days to avoid the effect of temperature on the stator prototype. The final results were calculated as average values. The comparative results of the stiffness between simulations and experimental testing are shown Table 6.5.

The stiffness values of both results are quite different due to the tolerance of manufacturing machine (±20 μm for stator core cutting machine and ±10 μm of turning machine for inner/outer surface of aluminium casing) and the error of measuring of segmented stator core surface. Furthermore, aluminium is softer than steel and more easily dents, dings, scratches, and warps under applied high weight or force, compared to steel, as shown in Fig. 6.40. This case usually occurs in real testing, whereas in simulation, alumnium is considered an ideal material. For this reason, the deformation of the structure of the stator prototype in experimental testing is higher than in the simulation. In experimental testing, the supporting parts, which are the middle part linking between the heading part of the testing

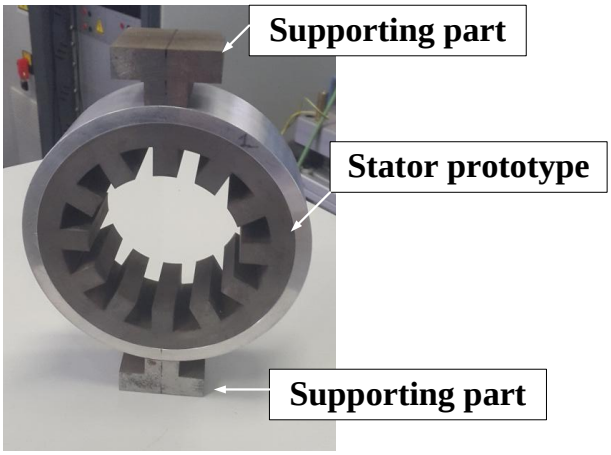

Figure 6.37: Complete stator prototype with supporting part for testing

Figure 6.38: The 10 kN Shimadzu Autograph AGS-X material machine testing

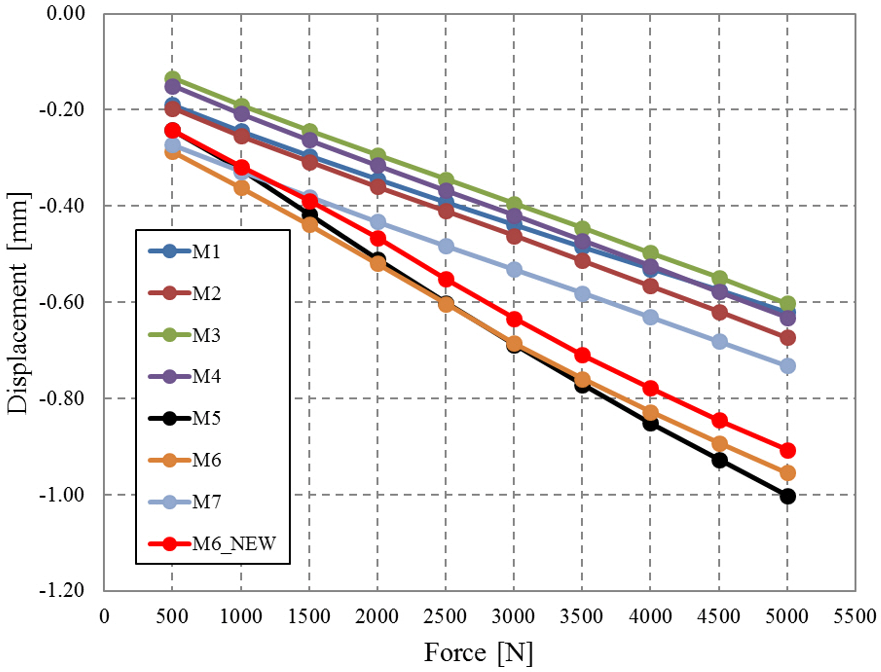

Figure 6.39: Experimental results of displacement vs. force at different stator models

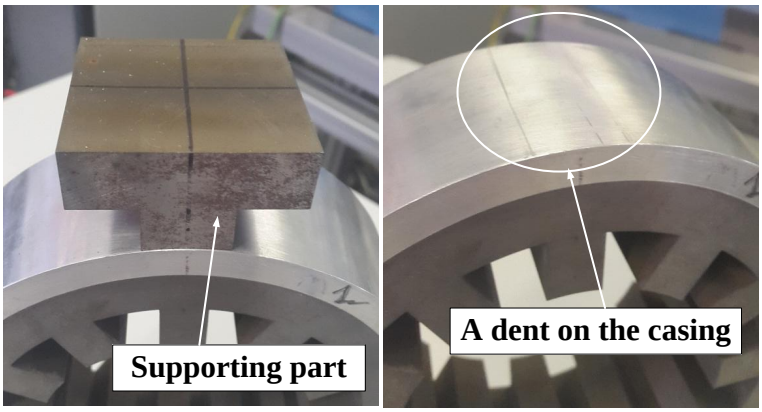

Figure 6.40: A dent on the stator casing after experimental testing

machine for applied force and aluminium casing, are made of steel.

The surface contacts of the simulation model have two contacts. First, it is the contact of aluminium casing to the steel of the stator core and second, it is the contact between each segment of the stator core which is steel contacting to steel. The building of the FE model in the structural simulation of the stator deformation, all surfaces of contact between aluminium and steel are defined as frictional contact with the coefficient of static friction [95] is 0.61 for aluminium to steel (casing and segmented stator core) and 0.74 for steel to steel (segmented

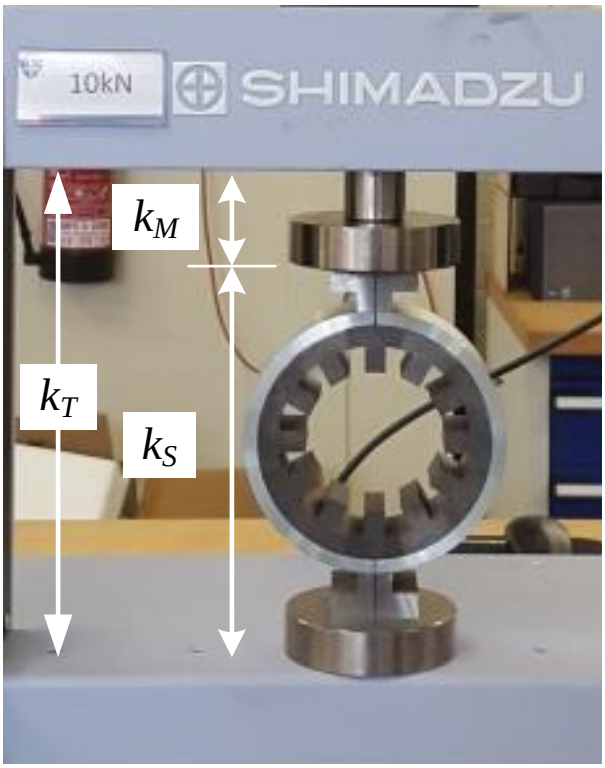

Figure 6.41: Stiffness constant of the system testing

stator core and segmented stator core). In the real experiment of surface contact, it is difficult to determine the exact values. The exact values depend on the cleaning of surface contact and how ideal it is for each surface contact. In the simulation, the contact is assumed as perfect.

The stiffness result calculated using Equation (6.1) of each stator prototype from the experimental test is the total stiffness of the system (k_T). The total stiffness of the system consists of two stiffness constants connecting in series. The first constant is the stiffness constant of the machine testing (k_M) and another one is the stiffness constant of the stator prototype (k_S) as shown in Fig. 6.41.

To determine the stiffness constant of the machine, force was applied without the stator prototype, as shown in Fig. 6.42, and the force levels are the same as the complete testing with the stator prototype. To determine the stiffness constant, the simple spring/mass system as shown in Fig. 6.43 and Hooke's law in is used for calculating each stiffness constant in the system. Equation (6.2) and (6.3) are used

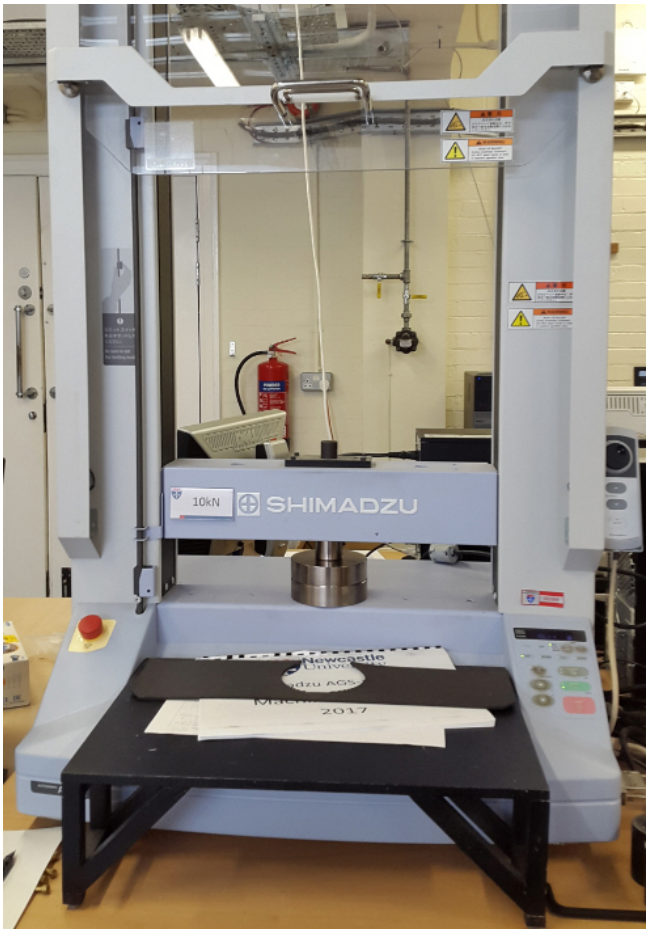

Figure 6.42: Testing set up for finding the stiffness constant of the machine testing

to calculate the total spring constant in parallel and in series, respectively.

$$k_T = k_1 + k_2 \tag{6.2}$$

$$\frac{1}{k_T} = \frac{1}{k_1} + \frac{1}{k_1} \tag{6.3}$$

In this case, Equation (6.3) is applied to calculate the stiffness constant in the experimental testing for series springs as

$$\frac{1}{k_T} = \frac{1}{k_M} + \frac{1}{k_S} \tag{6.4}$$

The calculated results of each stiffness constant in different stator prototypes are summarised in Table 6.5. The stiffness constant of the testing machine is constant

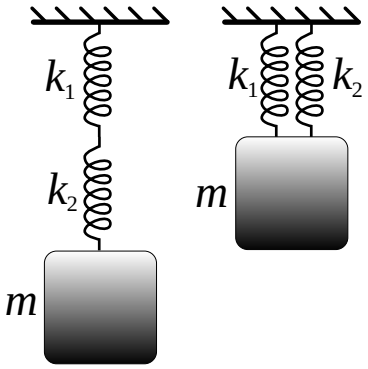

Figure 6.43: The spring constant of the simple spring/mass system in series (left) and in parallel (right)

Table 6.5: The stiffness constants of the experimental test system in each stator prototype

Stator model	k_T [N/mm]	k_M [N/mm]	$k_S = \frac{k_T k_M}{k_M - k_T}$ [N/mm]
M1	10668.08	12532.33	71715.81
M2	9561.10	12532.33	40327.73
M3	9770.95	12532.33	44344.75
M4	9496.12	12532.33	39196.49
M5	5834.07	12532.33	10915.46
M6	6712.27	12532.33	14453.52
M6 NEW	6734.66	12532.33	14557.72
M7	9986.96	12532.33	49171.53

at 12532.33 N/mm, while the other constants, such as k_T and k_S vary depending on the structure of the stator segment joint.

The ranking of the stator stiffness in Table 6.6 shows that the stator M1 and M7 models have a high stiffness as the first and second ranking in both simulation and experimental testing. These stator prototypes had a high tolerance to sensitivity on the error of assembly processes. The stator M3 model has a high sensitivity to the error of assembly processes as it moves from the bottom in simulation to third ranking of the stator stiffness in experimental testing. Moreover, this finding also confirms that making the corner of the stator pole a curve shape can slightly improve

Table 6.6: Comparison of the stator stiffness between simulation and experimental testing results at 60 μm of the radial interference fit

Stator model	Stiffness [N/mm] (Simulation)	Ranking	Stiffness [N/mm] (Experimental test)	Ranking
M1	73847.5	1	71715.81 (err 3.0 %)	1
M2	61346.5	3	40327.73 (err 52.1 %)	4
M3	38046.8	8	44344.75 (err 14.2 %)	3
M4	50666.6	6	39196.49 (err 29.3 %)	5
M5	39665.0	7	10915.46 (err 263.4 %)	8
M6	52934.1	5	14453.52 (err 266.2 %)	7
M6 NEW	53347.2	4	14557.72 (err 266.5 %)	6
M7	64884.5	2	49171.53 (err 32.0 %)	2

the stiffness of the stator structure, as shown in the ranking of the stator stiffness in the stator M6 and M6 NEW model. The stator M6 NEW model is stiffer than the stator M6 model in both results. The experimental result of the stator model M1 has the lowest error by 3 % compared to the simulation result. A high percentage error of the stator stiffness between simulation and experimental testing is revealed in the stator model M5, M6 and M6 NEW. These three types of stator (M5, M6, and M6 NEW) have two different sizes of the stator segment (large and small). Furthermore, the back of the small segments have a small gap between stator and casing. These gaps reduce surface contact between the stator core and casing when compared to any other stator models.

As the interference fit of aluminium casing and the varying interference fit of the simulation model were performed to achieve the low percentage of error (within 5%) when compared to the testing result. Table 6.7 shows a new stiffness result, interference fit, and error within 5% of each stator model. The single core stator model M1 has the same interference fit at 60 μm and does not need to adjust the interference fit. The interference fit of the stator models M5, M6, and M6 NEW are dramatically dropped to 8.9, 14.05, and 14.01 μm, respectively to obtain error rates within 5%. To make these three types of the stator, a high interference fit should be selected to compensate the high error tolerance of the assembly processes. The

Table 6.7: Comparison of the stator stiffness between simulation and experimental testing results by varying the radial interference fit to obtain a percentage of error within 5 %

Stator model	Stiffness [N/mm] (Simulation)	Interference fit [μm]	Stiffness [N/mm] (Experimental test)	Error [%]
M1	73497.5	60	71715.81	2.5
M2	42302.8	28.2	40327.73	4.9
M3	42156.0	79.5	44344.75	4.9
M4	41098.5	26.4	39196.49	4.9
M5	11436.6	8.9	10915.46	4.8
M6	15149.8	14.05	14453.52	4.8
M6 NEW	15258.6	14.01	14557.72	4.8
M7	51555.3	37.9	49171.53	4.8

stator model M3 has high stiffness as a result of the interference fit increased to 79.5 μm. The interference fit of the other stator models, such as M2, M4, and M7 is slightly reduced to 28.2, 26.4, and 37.9 μm, respectively.

6.2.3.2 Modal Test

Modal testing is a vibration testing of a structure. There are three key parameters determined, namely natural frequencies, mass, and modal damping ratio. As mentioned above, stators with a high resonant frequency can avoid coincidence with the high amplitude of the low-order harmonic component of the magnetic radial forces. The second order vibration mode, which relates to phase excitation of 12/10 SSRM, is focused on during testing. The method of modal testing is described in the Chapter 5. The impact hammer technique was used for stator modal testing. Two accelerometers were mounted on the stator casing, as shown in Fig. 6.44.

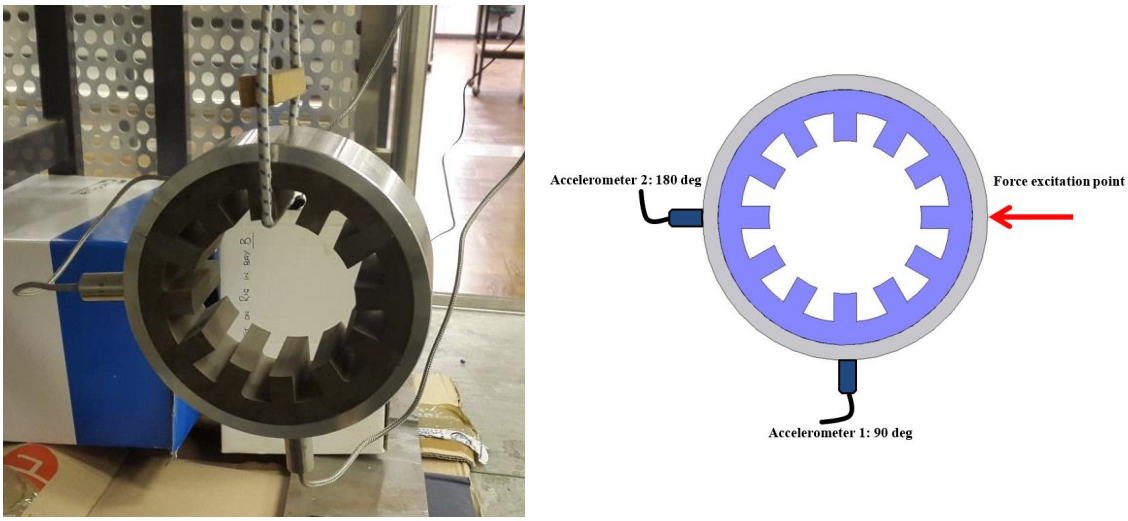

Figure 6.44: Stator modal testing

The force excitation by impact hammer was applied on the opposite side of the accelerometer 2, and two acceleration signals were recorded with data acquisition (DEWE-43 Dewesoft hardware), which calculated the resonant frequency and modal damping ratio. The FFT spectrum of the acceleration signal in each prototype is illustrated in Fig. 6.45-6.48 and the resonant frequency and modal damping ratio are summarised in Table 6.8.

Table 6.8 shows both simulation and experimental modal testing results. The percentage of error is high in stator M4 at 19.3 %. In the stators M5, M6, and M6 NEW, there are two peaks of resonant frequency. The first peak appears due to the movement of the stator pole, which appears on both accelerometers, whereas

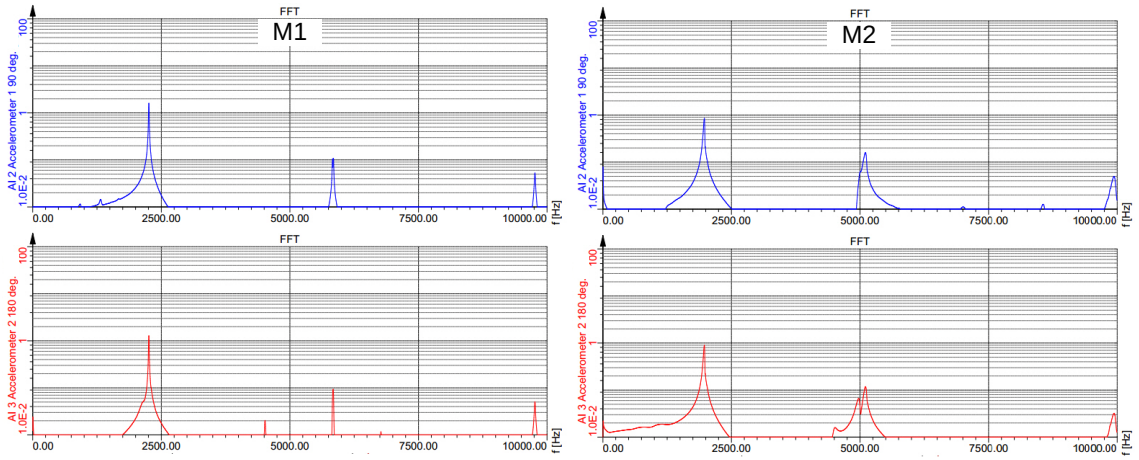

Figure 6.45: Acceleration spectrums of M1 (left) and M2 (right) using modal hammer testing

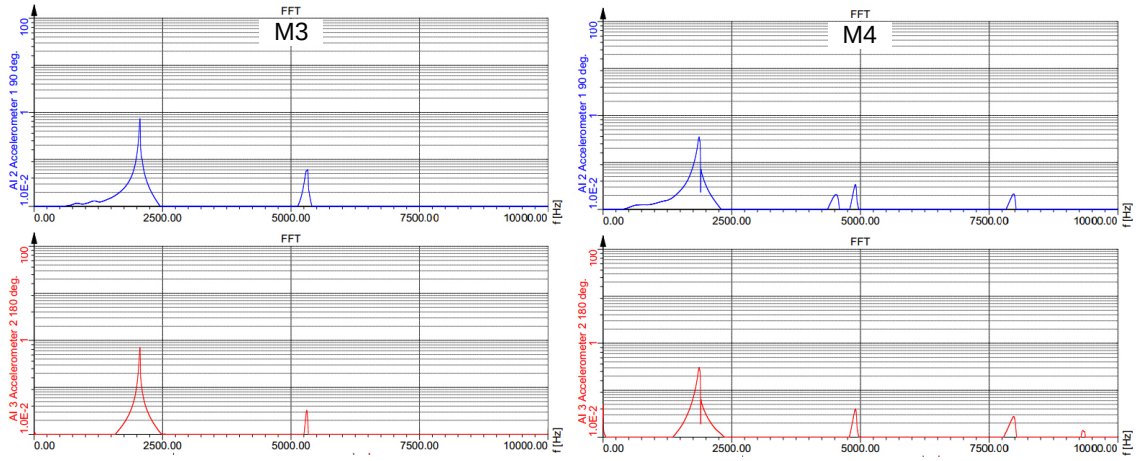

Figure 6.46: Acceleration spectrums of M3 (left) and M4 (right) using modal hammer testing

the second peak of the FFT spectrum only occurs on accelerometer 1 at 90 degrees, which was fixed on the large segment of the stator core. The small segment of stator core was measured by the accelerometer 2 at 180 degrees, as shown in Fig. 6.49, and shows that the pole movement of the small segment becomes the dominant resonant frequency of the stator structure. The small segment of the stator core is easier to vibrate compared to the large segment.

The movement of the small segment of the stator does not show on the FE simulation of modal testing (the first peak of FFT spectrum) as it has a high percentage of error when compared to simulation and experimental modal testing results. The

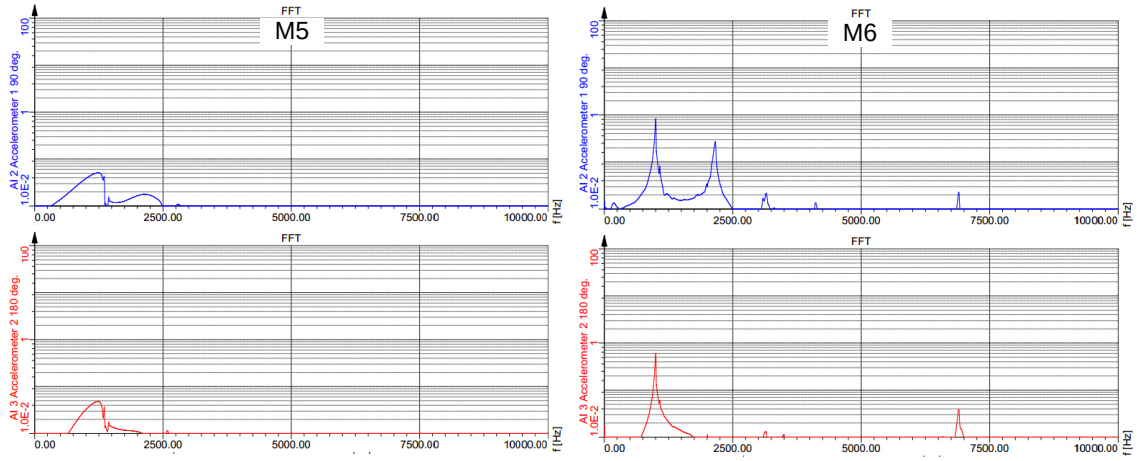

Figure 6.47: Acceleration spectrums of M5 (left) and M6 (right) using modal hammer testing

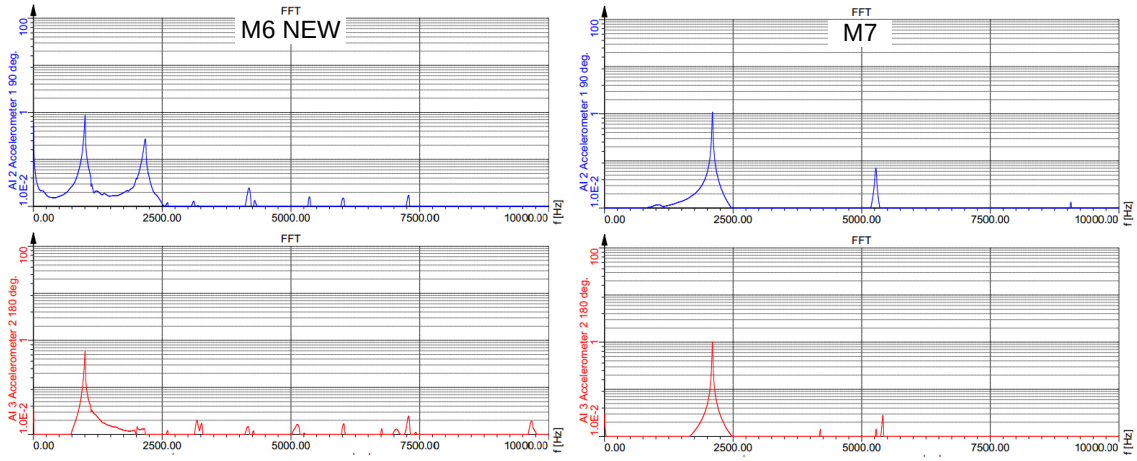

Figure 6.48: Acceleration spectrums of M6 NEW (left) and M7 (right) using modal hammer testing

results also confirm that stators M1 and M7 have high resonant frequency.

The modal damping ratios of stator M5, M6, and M6 NEW are high at around 0.02-0.06, compared to the other stator models, which are around 0.001-0.007. The damping ratio (ζ) is a key parameter in describing how long a system oscillates after a disturbance. Damping ratio can be calculated using a simple spring-mass system. Fig. 6.50 shows the effect of the varying damping ratio on the spring-mass (second-order) system.

The critically damped (ζ=1) is the best damping ratio of the engineering design as it uses minimal time to return the system to the steady state or equilibrium of

Table 6.8: The resonant frequency and modal damping ratio of all stator prototypes

Stator model	Resonant frequency [Hz] (Simulation)	Resonant frequency [Hz] (Experimental test)	Modal damping ratio
M1	2298	2256.7 (err 1.8 %)	0.0013
M2	2263	2018 (err 12.1 %)	0.0047
M3	2240	2057.3 (err 8.9 %)	0.0037
M4	2223	1863.6 (err 19.3 %)	0.0072
M5 1^{st} peak	2166	1268.7 (err 70.7 %)	0.0204
M5 2^{nd} peak	”	2148.4 (err 0.8 %)	”
M6 1^{st} peak	2235	1001 (err 123.3 %)	0.0062
M6 2^{nd} peak	”	2158.2 (err 3.6 %)	”
M6 NEW 1^{st} peak	2266	1005.9 (err 125.3 %)	0.0056
M6 NEW 2^{nd} peak	”	2177.7 (err 4.1 %)	”
M7	2265	2096.4 (err 8.0 %)	0.0018

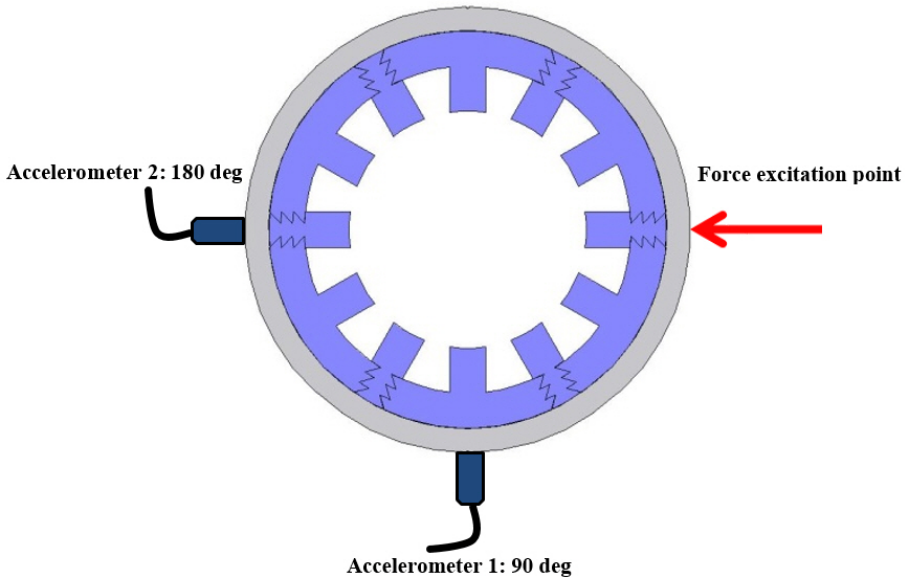

Figure 6.49: Position of accelerometer on stator M5, M6, and M6 NEW model

having less oscillation. The system designer should design the damping ratio of the system close to critical damping ratio.

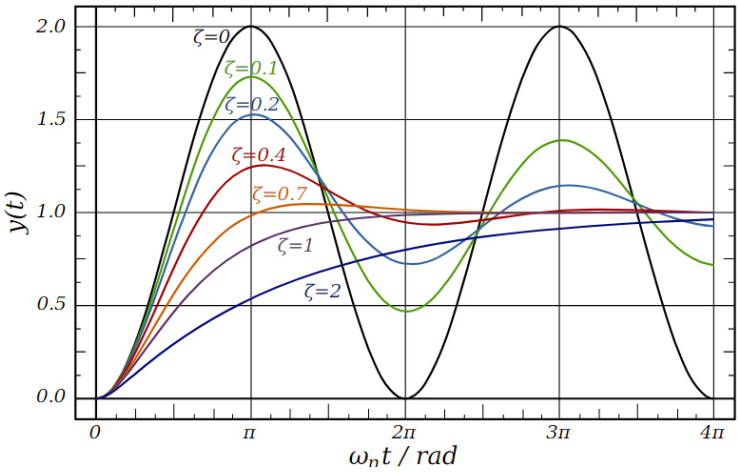

Figure 6.50: The effect of varying damping ratio on the spring-mass system

6.2.3.3 Effect of Temperature on Resonant Frequency

This testing was implemented to study the impact of temperature on the resonant frequency of the assembled stator prototype. The modal testing technique was selected for this testing as it is easy to implement. The temperature was controlled using an oven. All stator prototypes were hung in the oven with elastic rope. Two accelerometers were mounted on the motor casing similar to the previous testing. The temperature sensor was used for controlling the temperature during the testing starting from 20°C to 70°C with increasing every step of 10°C. The stator prototype was hit by the impact hammer and the acceleration signals were captured by data acquisition hardware. The hardware and experimental setup are illustrated in Fig. 6.51. The relationship between varying temperature on the stator resonant frequency is shown in Fig. 6.52.

The dramatically changing resonant frequency can be seen in the stator M4 model by 801.6 Hz from 1863.6 Hz at 20°C to 1062.0 Hz at 70°C and M5 model 895.2 Hz from 1268.7 Hz at 20°C to 373.5 Hz at 70°C, respectively. The stator M6 NEW model may reduce the rate of change of resonant frequency due to the varying temperature and can improve from 456.6 Hz (1000.1 Hz at 20°C to 544.4 Hz at 70°C) of the stator M6 model to 368.7 Hz (1005.9 Hz at 20°C to 637.2 Hz at 70°C) of stator M6 NEW model. In another test, M2 model had the interference fit changed from 60 μm to 100 μm. The resonant frequency of the stator M2 model

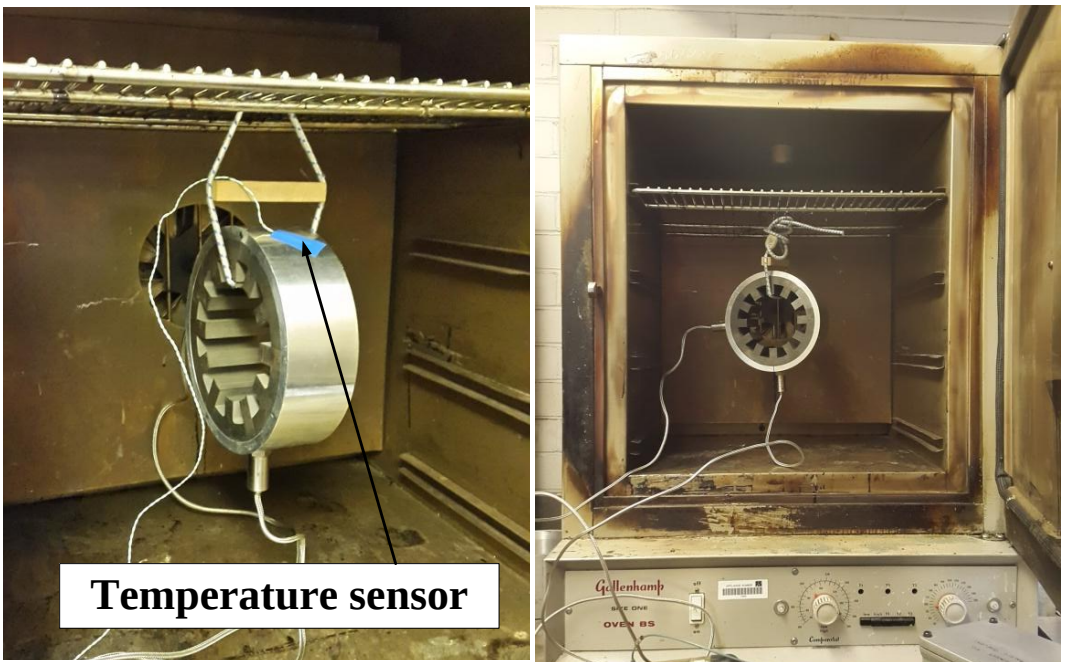

Figure 6.51: The temperature testing of the stator prototype

Table 6.9: The comparative experimental results from modal test of the stator M1 (60 μm), M2 (60 μm), and M2 (100 μm) model at different interference fits at room temperature = 20°C

Stator model	Stiffness [N/mm]	Resonant frequency [Hz]	Damping ratio
M1@60μm	71715.81	2256.7	0.0013
M2@60μm	40327.73	2018	0.0047
M2@100μm	56638.31	2120.3	0.0019

shifted by 102.3 Hz from 2018 Hz at 60 μm to 2120.3 at 100 μm of the interference fit. This finding may confirm that changing the interference fit of the stator casing increased the stiffness of the stator prototype.

Table 6.9 summarises the comparative results between stator M2 model the interference fits at 60 μm and 100 μm. The stiffness was changed and was similar to that of the stator M1 model. Fig. 6.53 shows the effect of the damping ratio on the varying temperature. The stator M5 model also rapidly increases in terms of rate change of damping ratio by 0.0449 from 0.0204 at 20°C to 0.0653 at 70°C. It means that the stator M5 model has low oscillation compared to the other models. Both rate changes of resonant frequency and damping ratio of stator M1 model slightly

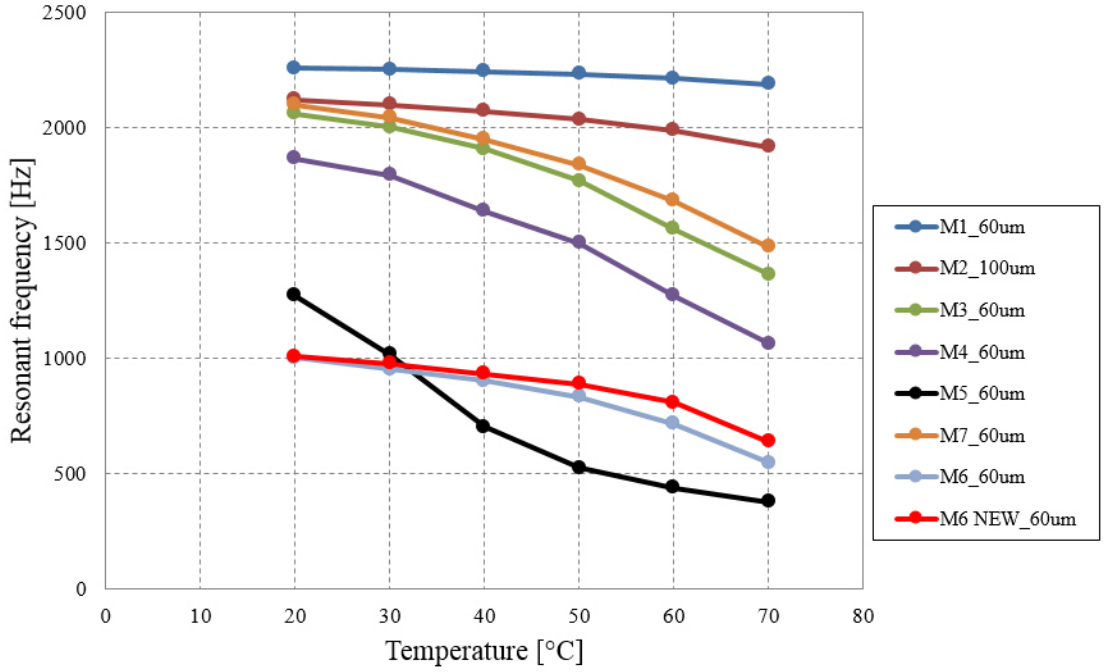

Figure 6.52: The relationship between temperature and resonant frequency

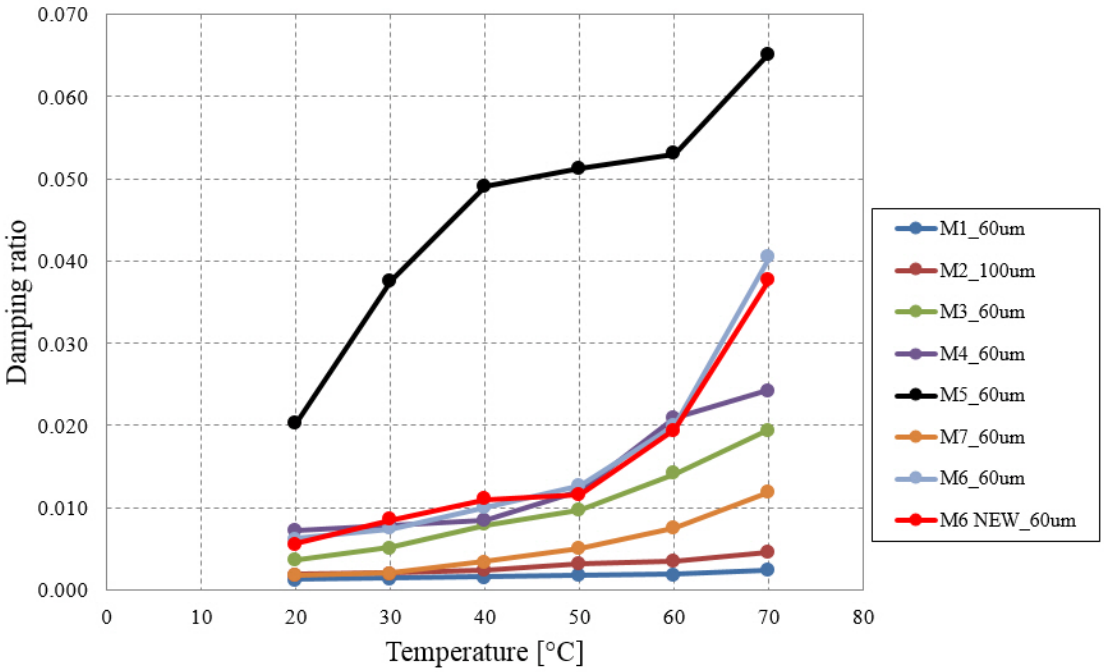

Figure 6.53: The relationship between temperature and modal damping ratio

vary by 70.8 Hz of resonant frequency and 0.0011 of modal damping ratio when increasing the temperature from 20°C to 70°C. The high damping ratio values do

not mean that the vibration of the stator structure will reduce. The reduction also depends on the stiffness of the stator structure. The most optimal values between damping ratio and stiffness of the stator structure should be optimized and considered to have the high stiffness and the damping ratio as close as possible to the critically damped (ζ=1) ideal point. The numerical values of the resonant frequency and modal damping ratio at different temperatures are presented in Table D.1-D.4 of Appendix D.

6.3 Conclusion

In this chapter, stator prototypes with different segment joints of the segmented stator core were investigated (deformation and compressive hoop stress). The simulation of the FE structural model was built to predict the characteristics of the segmented stator core, using an aluminium casing shrink fitting technique, in an assembly process of the stator prototype. Experimental testing also was used to verify the simulation technique. The stiffness of the stator structure can improve the quality of the vibration, which mainly occurs in the stator of the electrical machine, especially in the switched reluctance machine. The compressive hoop stress is one of the main causes of generating iron losses in the stator core when using the shrink fitting method. The compressive hoop stress depends on interference fit. An increase of interference fit causes high compressive hoop stress in the back of the stator core.

Most high compressive hoop stress of the segmented stator core appears in the contact joints of each segmented core. This stress can be reduced by selecting the radial line segment joints, such as the case in the stator M2 and M7 models. These types of segment joint lower and spread compressive hoop stress. The stator slot then becomes an area of higher compressive stress similar to the single piece stator core M1 model. The deformation results of the stator structure also show that the stator M1 and M7 model have high structural stiffness and tolerance to the error sensitivity of the assembly processes compared to the stator M3 model, which is incredibly sensitive. The stiffness values between simulation and experimental

testing are quite different due to the high tolerance of manufacturing machine and the error in the geometrical measurement procedure. Additionally aluminium is softer than steel and, easily dents when applying a high compressive force. The frictional coefficient also has a significant effect on simulation results. The surface contact of segment joints in the assembly processes is not perfect contact like the surface contact in simulation testing.

Adjusting the stator pole corner to be a curve shape can slightly improve the stiffness of the segmented stator core. The effect of the stator pole movement in stator M5, M6, and M6 NEW can drop the resonant frequency and become another dominant frequency. The stiffness testing results confirm that the stiffness of the stator structures is reduced when making a stator core a segmented core by at least 31 % (comparison between model M1 and M7). Moreover, to build a segmented stator using the shrink fitting technique, the high interference fit should be used to compensate the high error tolerance in the segment manufacturing processes.

Changing the interference fit of the stator aluminium housing can increase the stiffness and resonant frequency of the stator prototype. The comparative results show the different stiffness and resonant frequencies between 60 μm and 100 μm of the interference fit.

Varying temperatures have an impact on the resonant frequency and modal damping ratio. The stator M5 model gives a high rate of change in resonant frequency and damping ratio of the varying temperatures. The stiffness and damping ratio should be considered when designing the machine. For many engineering designs, it is desirable to have structural stiffness and a damping ratio that are as high as possible in order to reach the critical damping point.

Chapter 7.
A Control Technique for Vibration Reduction

The control method has a significant impact on the vibration in an SRM. Fig. 7.1 shows the measured waveform of voltage, current and acceleration from an experimental test of an SRM in the aligned rotor position (locked-rotor test). A large acceleration occurs at turn-off stage due to a sudden decrease in the attraction force. The relationship between rate change of voltage with time and vibration [59, 60], as described by Faraday's Law, is given by

$$\lambda = Li \tag{7.1}$$

$$\begin{aligned} v &= Ri + \frac{d\lambda}{dt} = Ri + \frac{d(Li)}{dt} \\ &= Ri + L\frac{di}{dt} + i\frac{dL}{dX}\frac{dX}{dt} \end{aligned} \tag{7.2}$$

$$X = |\vec{X}| = \sqrt{(\vec{r})^2 + (\vec{\theta})^2 + (\vec{z})^2} \tag{7.3}$$

where v is the phase voltage, i is the phase current, λ is the flux linkage per phase, R is the phase resistance, L is the phase inductance, and X is the air gap length, which can change in three directions ((r) radial, (θ) tangential, and (z) axial direction). In this test, the air gap length normally changes in the radial direction. In Equation (7.2), the three terms on the right-hand side represent the resistance voltage drop, the Ldi/dt term, and the back-EMF term. The last two terms of the equation play an important role in balancing both sides of the equation. Their importance is a result of a velocity of geometry variation dX/dt, which moves stator poles along the air gap, and of current gradient di/dt, which has a quick response due to the time response of the electrical system being faster than that of a mechanical system.

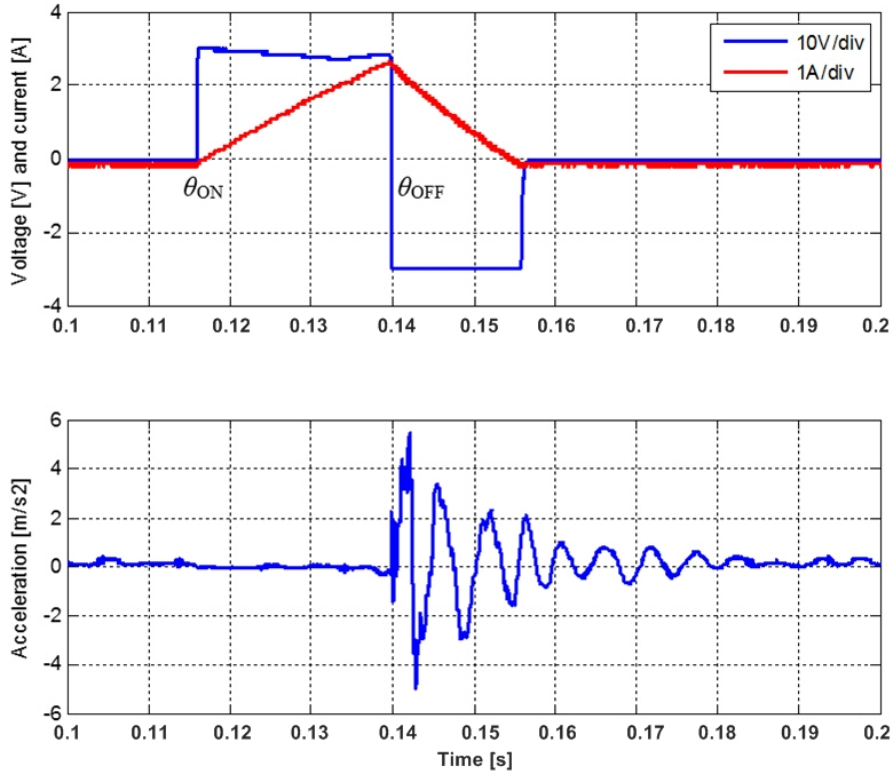

Figure 7.1: Waveform of current, voltage pulse, and acceleration at aligned rotor position

As the experimental waveform shown in Fig. 7.1 demonstrates, when switches are turned on, the terms on the right-hand side of the equation are influenced by Ldi/dt rather than movement of stator poles dX/dt (acceleration of the stator is almost zero). In contrast, when switches are turned off, phase voltage suddenly changes from positive to negative. At this stage, the terms on the right-hand side of the equation are dominated by both the stator pole movement and phase current variation. This change reflects a compensation on both sides of Equation (7.2). As a result, phase current (decreasing) and geometry of stator (sudden motion and vibration) change. At the switching instant of phase voltage, the acceleration term d^2X/dt^2 comes in sight into Equation (7.4) and analytically differentiates both sides of Equation (7.2) with time:

$$\frac{dv}{dt} = R\frac{di}{dt} + 2\frac{dL}{dx}\frac{dx}{dt}\frac{di}{dt} + L\frac{d^2i}{dt^2} + i\frac{dL}{dX}\frac{d^2X}{dt^2} \tag{7.4}$$

To confirm this phenomenon, the simulation model using JMAG software has

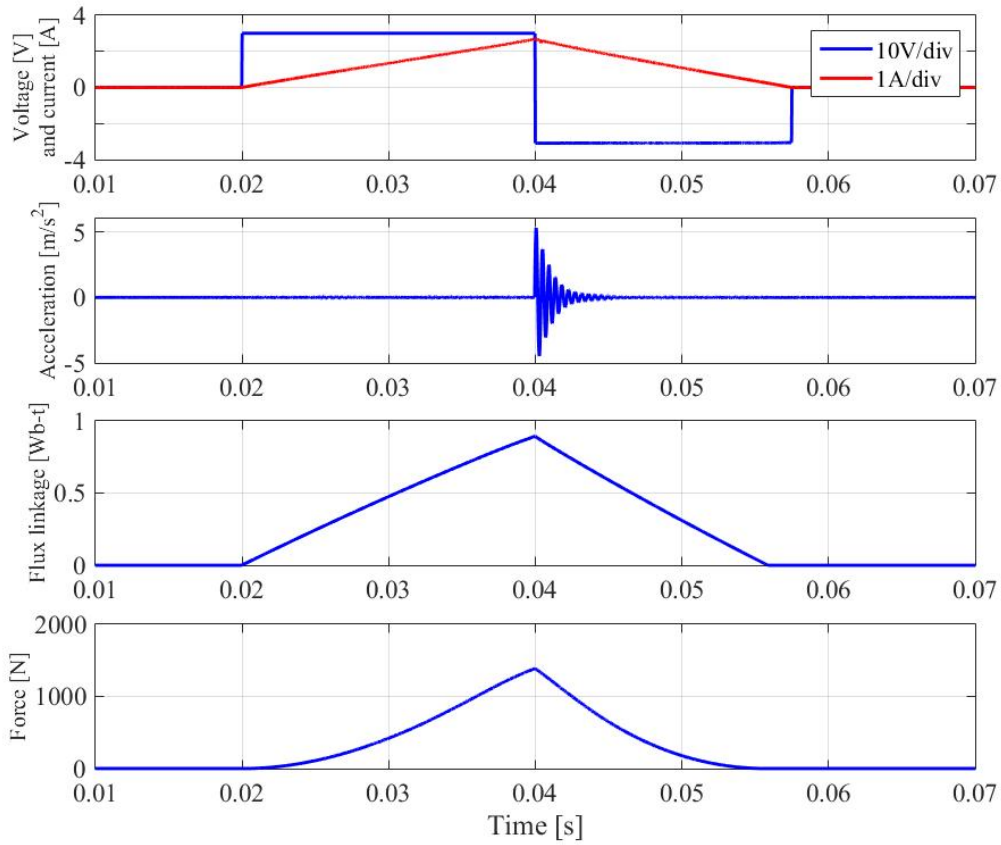

Figure 7.2: Simulation waveform of current, voltage pulse, acceleration, flux linkage and electromagnetic force at aligned rotor position

been done based on the same condition as the experimental test by applying a short voltage pulse to one phase winding of the SRM at an aligned position. Fig. 7.2 shows the voltage, current, acceleration, flux linkage, and electromagnetic force of the simulation model. This simulation model verifies that high acceleration occurs in the SRM during the turn-off stage of the phase voltage. At the turn-on stage of phase voltage, where the current is applied to phase winding, the electromagnetic force will be generated due to the magnetic flux generated by the phase winding. This force is an attractive electromagnetic force which tends to contract the stator frame when the force rapidly increases and to expand the stator frame when it is rapidly transitioned from ascending to descending.

Fig. 7.3 shows the amplitude of the electromagnetic force and the magnitude of the acceleration in the frequency domain. The harmonic components of the

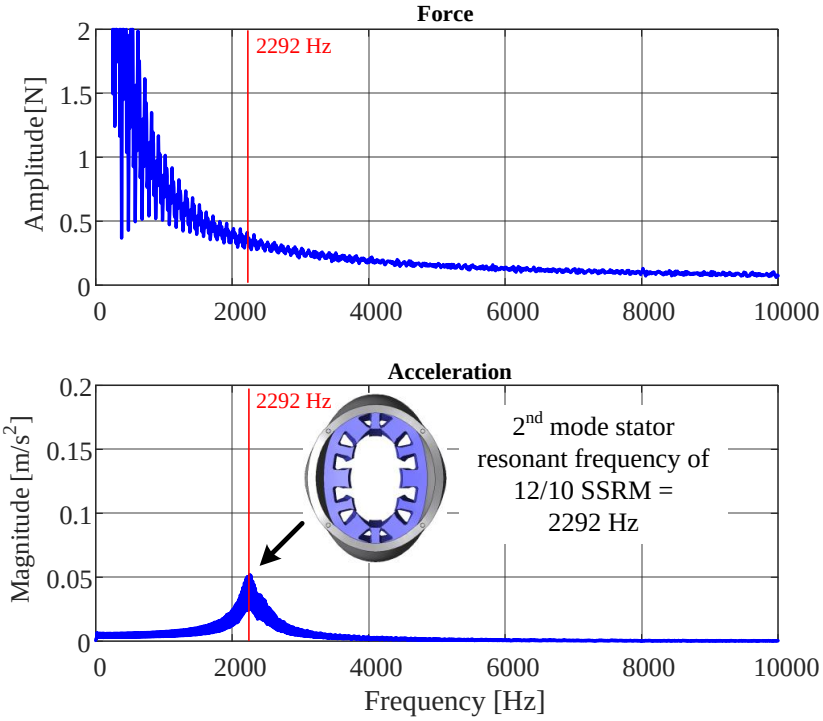

Figure 7.3: Simulation waveform of electromagnetic force and acceleration in frequency domain

electromagnetic force have a higher amplitude at low-order harmonics compared to those at the high-order harmonics, as shown in Fig. 7.3(top). The high magnitude of the acceleration appears when the stator resonant frequency coincides with the high amplitude harmonic component of the electromagnetic force, as shown at 2292 Hz in Fig. 7.3(bottom).

The relationship between electromagnetic force (F_m) and magnetic flux density (B) is described by

$$F_m = \frac{B^2 A}{2\mu_0} \tag{7.5}$$

where A and μ_0 are the effective cross-section area for flux distribution and the permeability of free space, respectively.

From above, it can be seen that vibration is sensitive to the rate of change of voltage with time in the SRM. To minimise this issue, several control techniques have been proposed. Many papers concerning vibration reduction using radial force control have been reported in [22, 67, 96–98]. This technique aims to reduce radial force ripple, which is a major source of vibration generation in an SRM. However, the

accuracy of the radial force model is very important for this control. The radial force model can be obtained by using either the finite element method or an analytical model technique. In [99], it was revealed that a variable dc-link voltage during a single-pulse operation can reduce the noise level by 25-15 dB at low speed. However, the dynamic response of the system is slow and also requires an additional power electronic device to control the dc-link voltage.

An active vibration cancellation (AVC) technique [10,15,100] which applies two-stage voltage control is well-known as a very effective and convenient technique to reduce vibration in an SRM with no need for extra control hardware. An AVC technique with smoothing voltage commutation by PWM was reported in [101]. A cosine function modulated by a high carrier PWM frequency was employed to reduce the rate change of voltage with time during turn-off. This method creates a long tail of current, which increases the copper losses. In this research, an investigation of AVC technique under a current chopping control has been carried out. The simulation of an AVC control algorithm has been improved and simulated using MATLAB/Simulink and the JMAG 2D magnetic/ 3D structural finite element method. A summary of each developing AVC method is presented and discussed.

7.1 AVC Techniques for Drive Control System of SRM

7.1.1 Basic Principle of AVC Techniques

Damped oscillation at the dominant resonant frequency component of large vibration occurs in an SRM during turn-off. As shown in Fig. 7.4(top), it is a conventional excitation. During the turn-off stage the voltage was changed from V_{dc} to $-V_{dc}$, and as a result it induces a high amplitude of the vibration. The AVC with two-stage voltage control can reduce the oscillating vibration by creating two vibrations which cancel each other out. In the first stage, during turn-off, the phase voltage changes from V_{dc} to 0 by utilizing the freewheeling loop, and the first vibration occurs then. A free decay vibration will oscillate corresponding to the resonant frequency. Then,

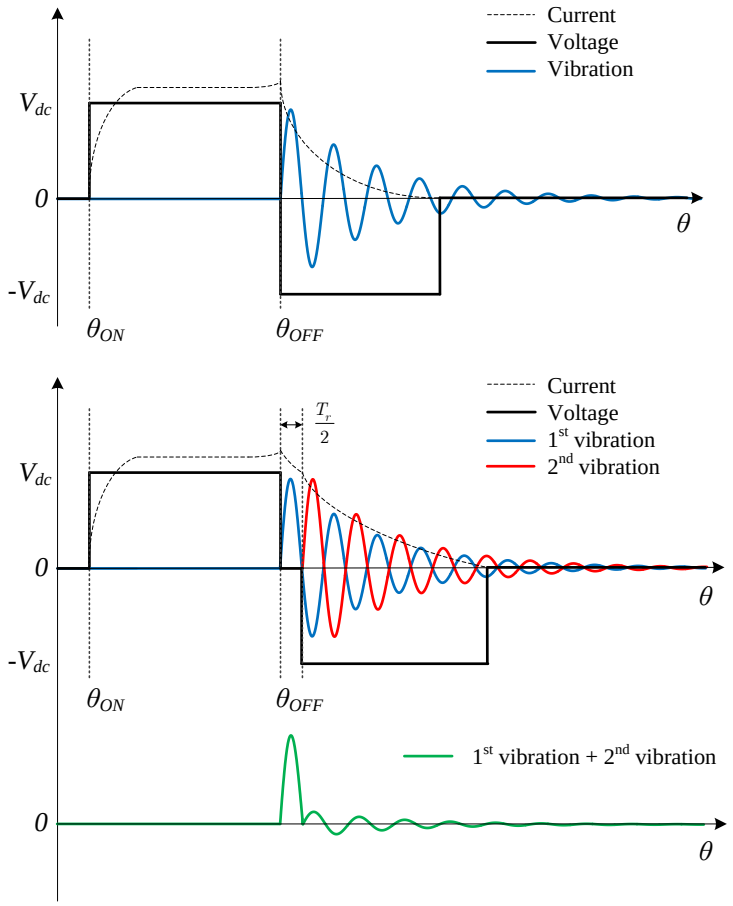

Figure 7.4: Mechanical vibration of conventional excitation (top) and AVC with two-stage voltage control (bottom)

after a half period of a resonant cycle $T_r/2$, the negative voltage $-V_{dc}$ is applied to the phase winding, which generates the second vibration against the first vibration. T_r denotes a resonant cycle. Fig. 7.4(bottom) shows the implementation of the two-stage voltage control.

7.1.2 Simulation and Investigation of AVC Techniques

Previous investigations of AVC techniques have been successful under single-pulse operation. The implementation in [102, 103] of AVC method under a current chopping control has been reported to give significantly less benefit to reducing vibration in the SRM. An AVC technique to employ in current chopping control was presented in [18]. By using an average positive voltage control during current chopping control

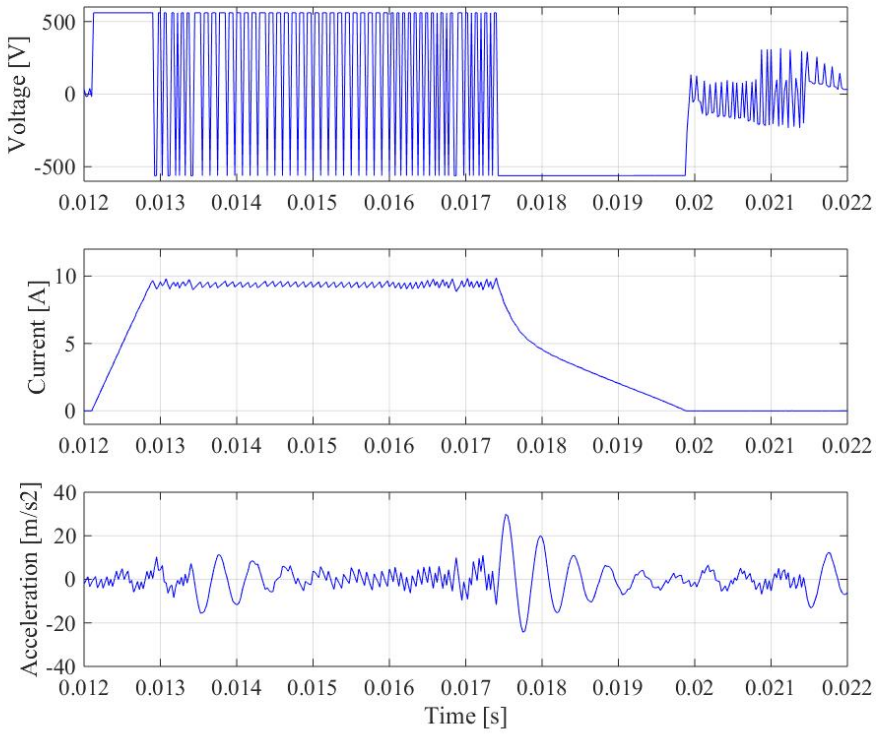

Figure 7.5: Simulation waveforms of hysteresis current chopping control with hard chopping

and applying an average negative voltage during the turn-off stage, this method can generate two opposing vibrations which are equal in amplitude and thus cancel each other out. In theory, it is difficult to create two vibrations of the same magnitude because the behaviour of the vibration is a damped oscillation, and the two sides of amplitude vibration in that damped oscillation are not equal. Furthermore, the amplitude of vibration in an SRM is related to the attraction force, which also depends on the rotor position and turn-off position. To investigate the AVC technique under current chopping control, several techniques have been attempted. One of them has been developed with two-stage voltage control and smooth voltage PWM control during the period of the turn-off.

The simulation of AVC control has been performed under the current chopping control. The conditions of the current control are the same, with speed = 500 r/min, desired average torque = 30 Nm, turn-on = 0 mechanical degrees at the unaligned rotor position, and turn-off = 16 mechanical degrees before the aligned

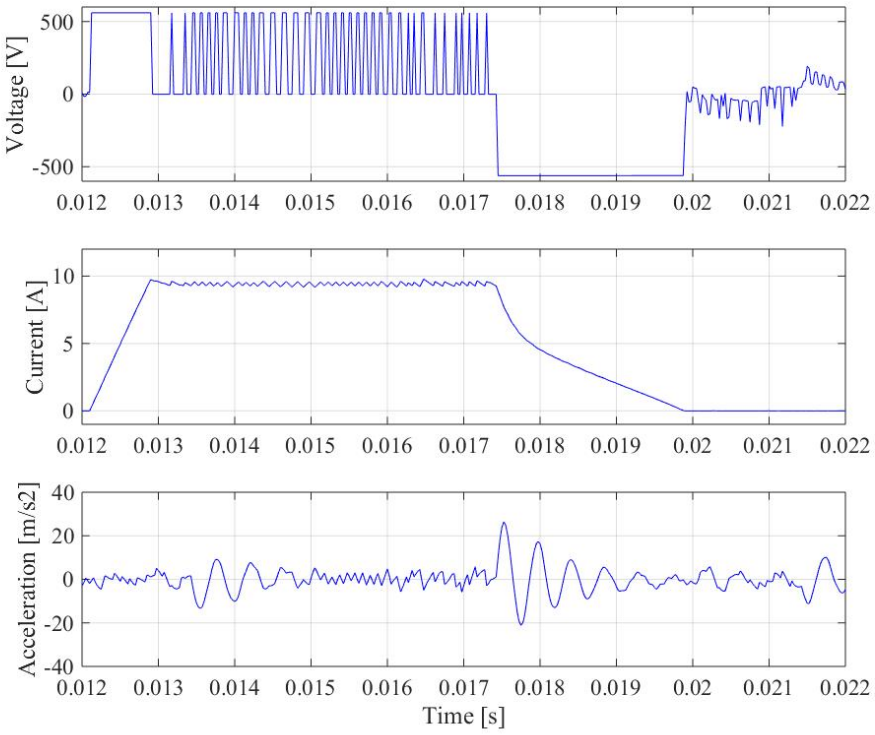

Figure 7.6: Simulation waveforms of hysteresis current chopping control with soft chopping

rotor position at 18 mechanical degrees. The AVC control has been implemented in MATLAB/Simulink, which was directly linked to the 12/10 SSRM model in JMAG magnetic FE, and the acceleration signal of the stator has been observed using JMAG structural FE with the modal damping coefficient of the 12/10 SSRM structures at 0.051. The acceleration signal was probed behind the excited stator pole. The phase current and torque of the 12/10 SSRM have also been monitored to investigate the RMS current, which relates to copper losses in the machine, and the phase torque per RMS current. Current chopping control with hard and soft chopping are two conventional current control options.

Fig. 7.5 and 7.6 show the simulation results of the acceleration signal. With hard chopping, the amplitude of acceleration signal is very high, reaching to 29.89 m/s^2, while the current control with soft chopping produces a lower magnitude of vibration at 26.38 m/s^2. From the simulation results of both current controls, it is clear that reducing the rate of change of voltage with time will decrease the

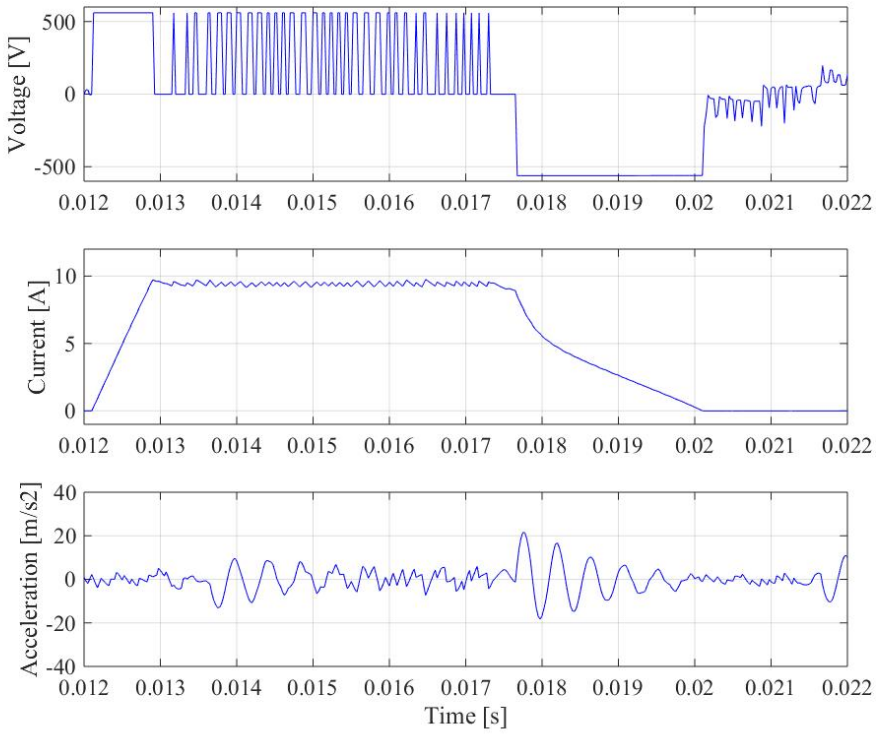

Figure 7.7: Simulation waveforms of hysteresis current chopping control with AVC method using two-stage commutation

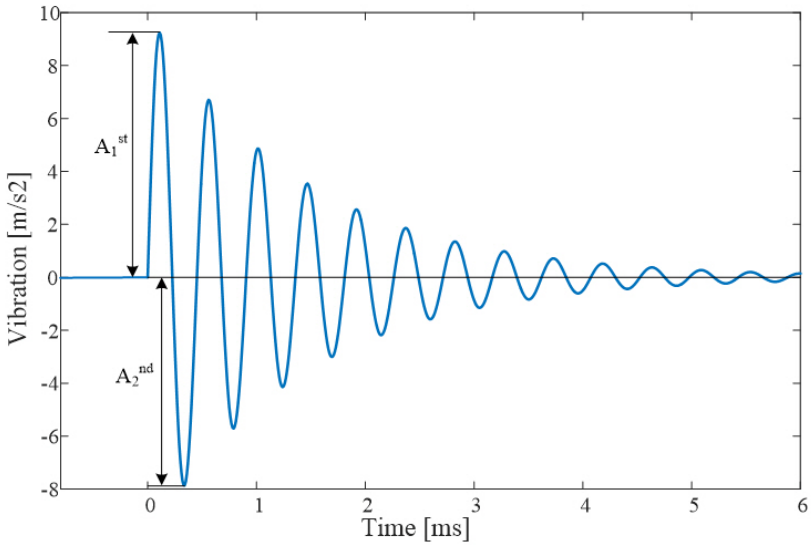

Figure 7.8: Vibration signal

vibration. The effect of reducing the time derivative of voltage can also reduce the vibration during the current chopping period before the turn-off stage. Simulation

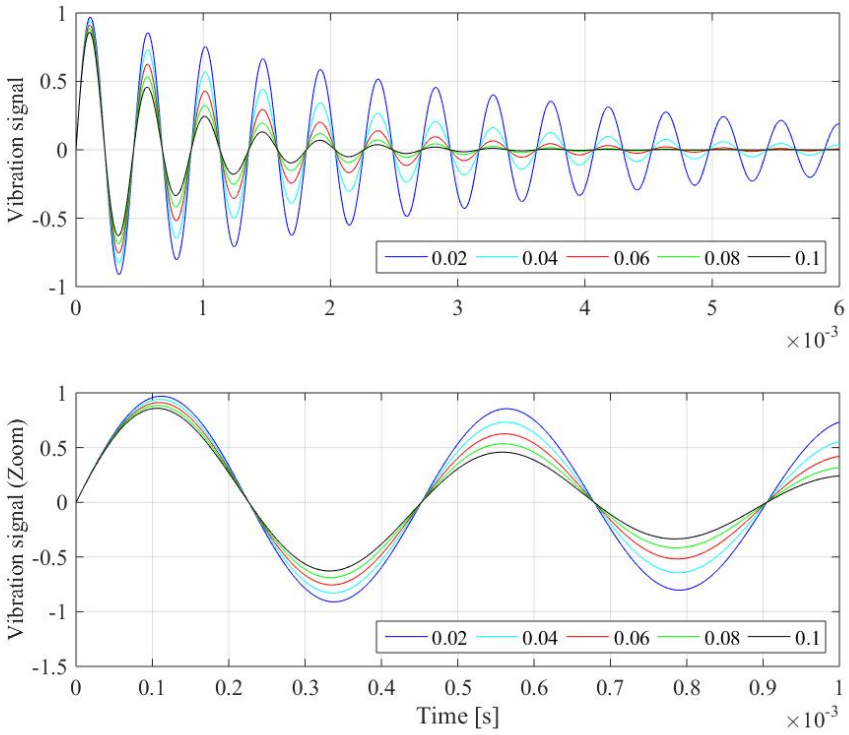

Figure 7.9: Damping ratio effect on the vibration signal

results of the AVC technique with two-stage voltage control, as discussed above, are shown in Fig. 7.7. Using the concept of generating two vibrations that cancel each other out, under the AVC method with two-stage voltage control, the acceleration amplitude is reduced by around 18.23 % from 26.38 m/s^2 with conventional current control and soft chopping to 21.57 m/s^2. In terms of electrical performance, the AVC method with two-stage voltage control increases the RMS phase current by 1.97 % compared with the conventional method.

The vibration waveform is a damped oscillating waveform. The equivalent function of the vibration is a decaying sine function as shown in Equation (7.6):

$$A = ke^{-(\zeta\omega_n t)} \sin(\omega_n t) \tag{7.6}$$

where A is the amplitude of vibration, k is the factor of amplitude, ζ is the modal damping coefficient or modal damping ratio, and ω_n is a natural angular frequency ($\omega_n = 2\pi f_r$, f_r is the resonant frequency)

Fig. 7.8 shows that the amplitudes of positive ($A_{1^{st}}$) and negative ($A_{2^{nd}}$) vibration

signals are not equal due to the damped oscillation. As in the above section, the AVC concept tries to generate the $A_{1^{st}}$ of the second vibration signal to cancel the $A_{2^{nd}}$ of the first vibration signal, as shown in Fig. 7.4(bottom). The amplitude of the vibration signal produced is related to the rate change of applied phase voltage. The $A_{2^{nd}}$ of the first vibration is generated by changing the phase voltage from V_{dc} to 0. The vibration signal then decays according to the damped oscillation, and the $A_{1^{st}}$ of the second vibration which aims to cancel the $A_{2^{nd}}$ of the first vibration is generated by changing the phase voltage from 0 to $-V_{dc}$. The amplitudes of the $A_{2^{nd}}$ of the first vibration and the $A_{1^{st}}$ of the second vibration do not cancel each other out completely because the phase voltage level which is applied to generate the $A_{1^{st}}$ of the second vibration is equal to the voltage that generates the $A_{1^{st}}$ of the first vibration. Therefore, the voltage level of phase excitation for creating the $A_{1^{st}}$ of the second vibration should be reduced accordingly with the damping ratio of the vibration signal. This approach will generate an $A_{1^{st}}$ of the second vibration that is as close as possible to the $A_{2^{nd}}$ of the first vibration.

Fig. 7.9 shows the vibration signal with different damping ratios from 0.02 to 0.1. The difference of amplitudes between $A_{1^{st}}$ and $A_{2^{nd}}$ is very high at the high damping ratio and quite low at the low damping ratio. Table 7.1 reveals the amplitude proportion between the positive and negative sides of the vibration signal at different modal damping ratios, according to Equation (7.6). From Table 7.1, the voltage level for generating the $A_{1^{st}}$ of the second vibration can be excited in the SRM according to the ratio of $A_{1^{st}}$ / $A_{2^{nd}}$ of the vibration signal. The damping ratio of the 12/10 SSRM in this research is around 0.05, so the percentage of the voltage level for generating the $A_{1^{st}}$ of the second vibration should be about 85 % of the voltage of the $A_{1^{st}}$ of the first vibration. Furthermore, for reducing the high vibration amplitude which relates to the rate change of phase voltage, the PWM technique is applied to produce the average voltage for phase voltage excitation. The average phase voltage level can be adjusted by varying the duty ratio of the PWM.

Fig. 7.10 shows the diagram of the AVC technique with two-stage commutation using the PWM technique. There are 6 stages to this method. The full V_{dc} is applied in the first stage to increase the phase current, and the PWM technique is applied

Table 7.1: The ratio of the positive ($A_{1^{st}}$) and negative ($A_{2^{nd}}$) amplitudes of vibration signal with different damping ratios

Damping ratio	$A_{1^{st}}$	$A_{2^{nd}}$	Ratio of $A_{1^{st}}/A_{2^{nd}}$
0.1	8.589	6.274	0.73
0.09	8.717	6.570	0.75
0.08	8.847	6.881	0.78
0.07	8.981	7.208	0.80
0.06	9.117	7.551	0.83
0.05	9.256	7.911	0.85
0.04	9.398	8.288	0.88
0.03	9.544	8.686	0.91
0.02	9.693	9.102	0.94
0.01	9.844	9.540	0.97

in the second stage to reduce the phase voltage. Applying the PWM technique in this order can decrease the amplitude of vibration. In the third stage, which is the freewheeling stage, the phase voltage is zero. The PWM technique is used again in the fourth and fifth stages. The average phase voltage in the fourth stage is around 85 % of the average phase voltage in the second stage. The duty ratio of the PWM is varied to get a smooth average phase voltage before full negative phase voltage is applied in the sixth stage to decrease the phase current to zero. The simulation waveforms for this technique are shown in Fig. 7.11. In this technique, st the same torque output of 30 Nm, the amplitude of the acceleration is reduced by 39.5 % from 21.57 m/s^2 under conventional AVC with two-stage commutation to 12.91 m/s^2. However, the RMS current with this technique is 6.77 A, which is higher than the RMS current of the conventional AVC with two-stage commutation by 8.84 %, due to the long decay of the phase current.

The disadvantages of the AVC method with two-stage commutation and PWM are the long tail of the phase current and the need to know exactly the resonant frequency of the SRM. To decrease the long decay of the phase current and the requirement for the resonant frequency data, the AVC technique with smooth voltage PWM is developed. The AVC technique with smooth voltage PWM diagram is

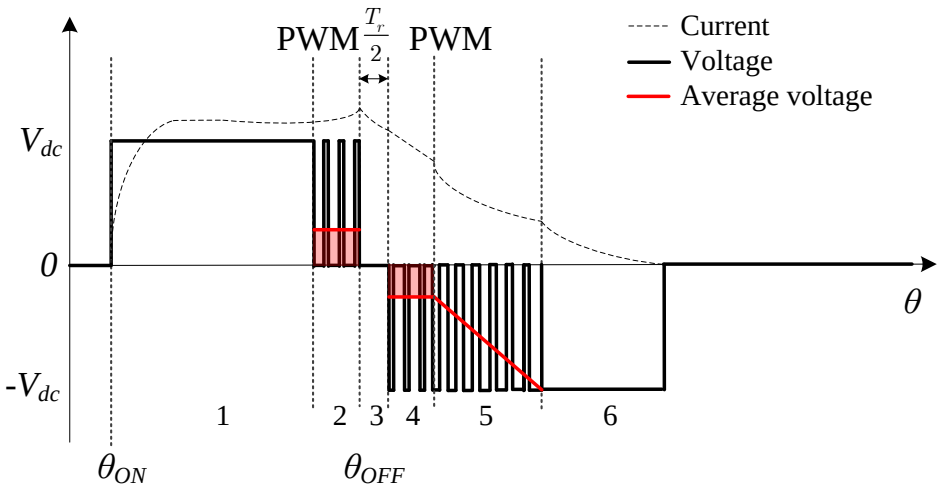

Figure 7.10: The AVC technique with two-stage commutation and PWM method

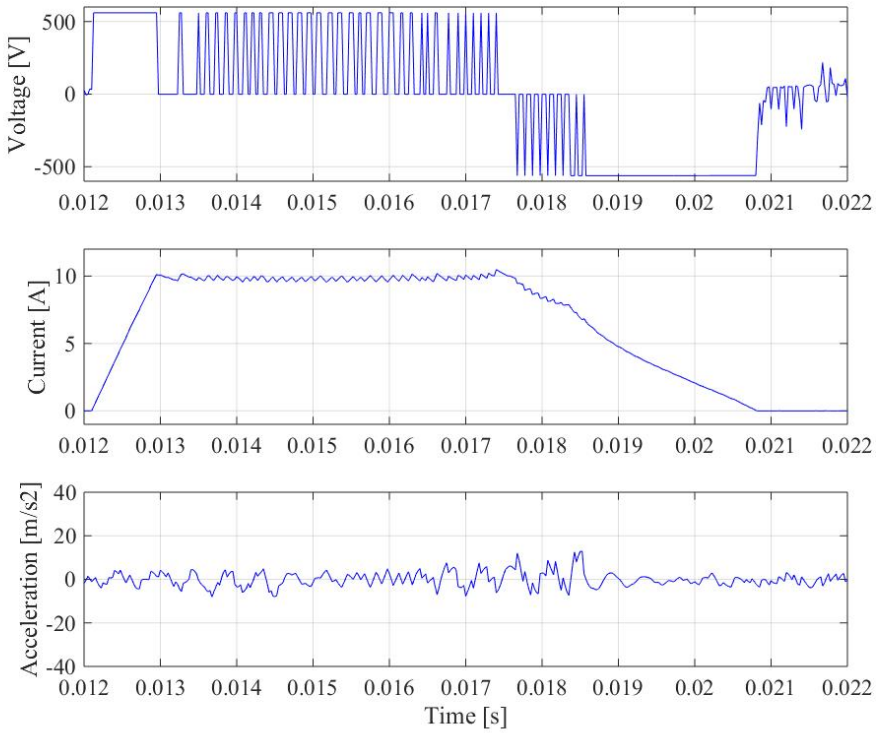

Figure 7.11: Simulation waveforms of hysteresis current chopping control with AVC method using two-stage commutation and PWM method

shown in Fig. 7.12. There are six stages, as with the previous technique. The first and final stages are the same as earlier, while the second and fifth stages smooth the average phase voltage by varying the duty ratio of the PWM technique. The third

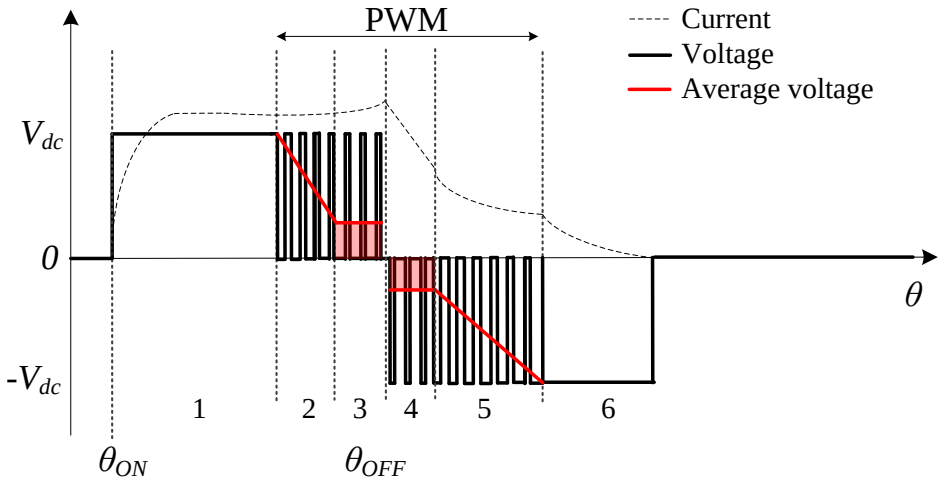

Figure 7.12: The AVC technique with smooth voltage PWM

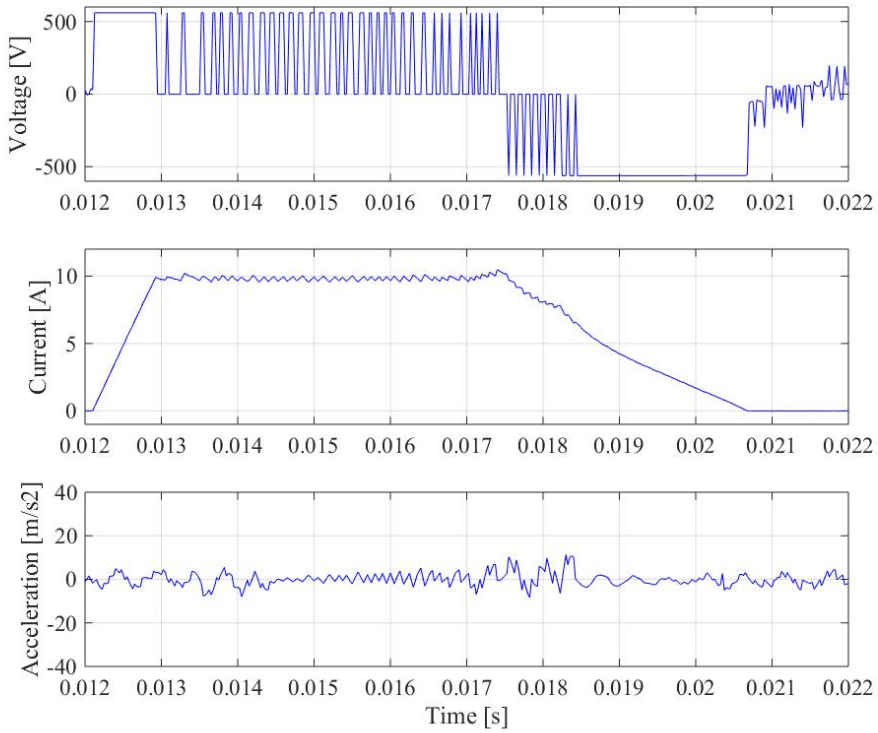

Figure 7.13: Simulation waveforms of hysteresis current chopping control with AVC method using smooth voltage PWM

and fourth stages are the stages where PWM is used to reduce the phase voltage. The ratio of the average voltage between the third and fourth stage is 0.85, according to the damping ratio of the SRM. This technique does not have the freewheeling

Table 7.2: Comparative simulation results of the different control techniques

Current Control technique	Maximum acceleration [m/s^2]	Average phase torque [Nm]	RMS phase current [A]
Hard chopping	29.89	30.21	6.09
Soft chopping	26.38	30.39	6.10
AVC with two-stage commutation	21.57	29.99	6.22
AVC with two-stage commutation and PWM	12.91	29.52	6.77
AVC with smooth voltage PWM	11.33	29.68	6.70

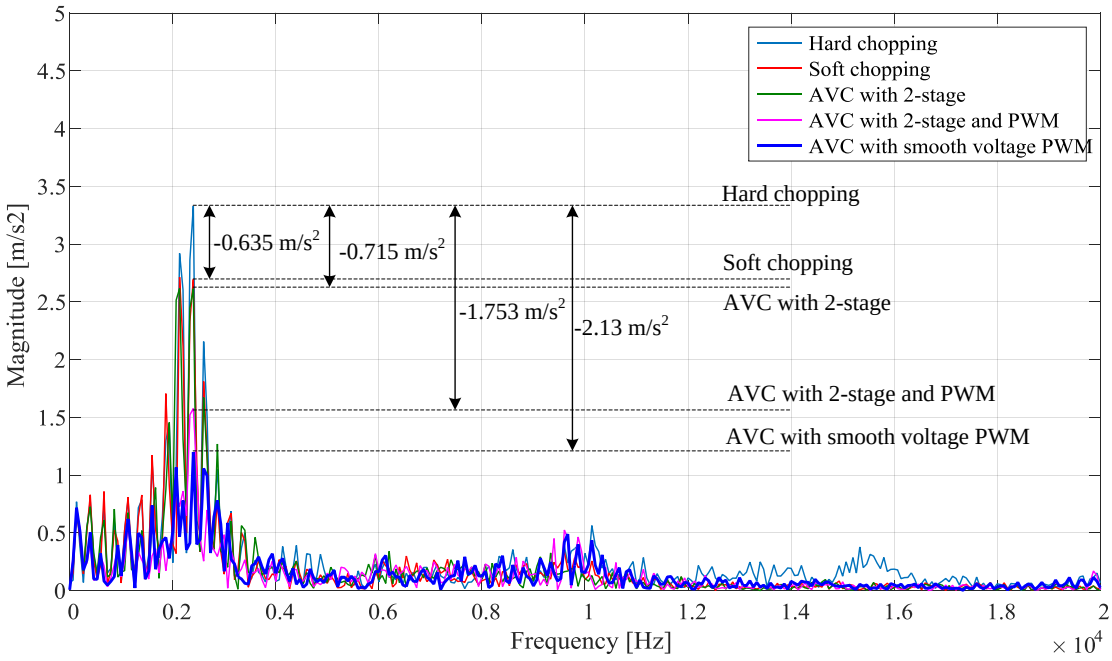

Figure 7.14: Comparison of the magnitude of the acceleration in frequency domain at different control techniques

(zero voltage) stage, so it can reduce the long decay of the phase current. However, during the smooth voltage PWM in the second and fifth stages, the phase current continues to decay. Fig. 7.13 shows the simulation waveforms of the AVC technique with smooth voltage PWM. 47.47 % of the amplitude of the acceleration is reduced by this method, compared with the conventional AVC technique. The amplitude

of the acceleration goes from 21.57 m/s^2 in the two-stage commutation method to 11.33 m/s^2 in the smooth voltage PWM method. It is also decreased by 12.24 % when compared with the AVC technique with two-stage commutation and the PWM method. This method can reduce the RMS phase current by 1.03 % compared to the AVC technique with two-stage commutation and the PWM method from 6.77 to 6.70 A.

The PWM frequency of the simulation is 10 kHz. The magnitude of the acceleration in the frequency domain is shown in Fig. 7.14. The AVC technique with smooth voltage PWM can reduce the magnitude of the acceleration by 2.13 m/s^2 compared with the conventional hard chopping method and it can be seen that the conventional AVC with two-stage commutation in the hysteresis current control has less impact on decreasing the magnitude of acceleration. The reduced magnitude of the soft chopping and the AVC with two-stage commutation method is quite similar at 0.635 and 0.715 m/s^2, respectively. This finding confirms the previous research [102, 103] about the AVC technique with two-stage commutation in the hysteresis current control, indicating that this technique is ineffective compared to single-pulse voltage control when applied in hysteresis current control. Moreover, the PWM frequency of the proposed technique becomes the main factor influencing the magnitude of the acceleration. Both methods utilizing the PWM technique create a high acceleration at the PWM frequency. For this reason, the selected PWM frequency should be as high as possible to avoid coincidence with the frequency of the higher vibration modes of the SRM structure or at least should be above the frequency range that human ear can nominally perceive (from 20 Hz to 20 kHz).

7.2 Experimental Dynamic Test

The experimental system setup is shown in Fig. 7.15. The rotor of three-phase 12/10 SSRM was connected to the rotor of the load machine via a flexible coupling and torque transducer. A permanent magnet AC (PMAC) servo motor was used as a load machine, with a maximum torque output of 41.1 Nm and a maximum rotational speed of 4000 r/min. A high-performance ARM Cortex-M3 MCU, STM32F103RE

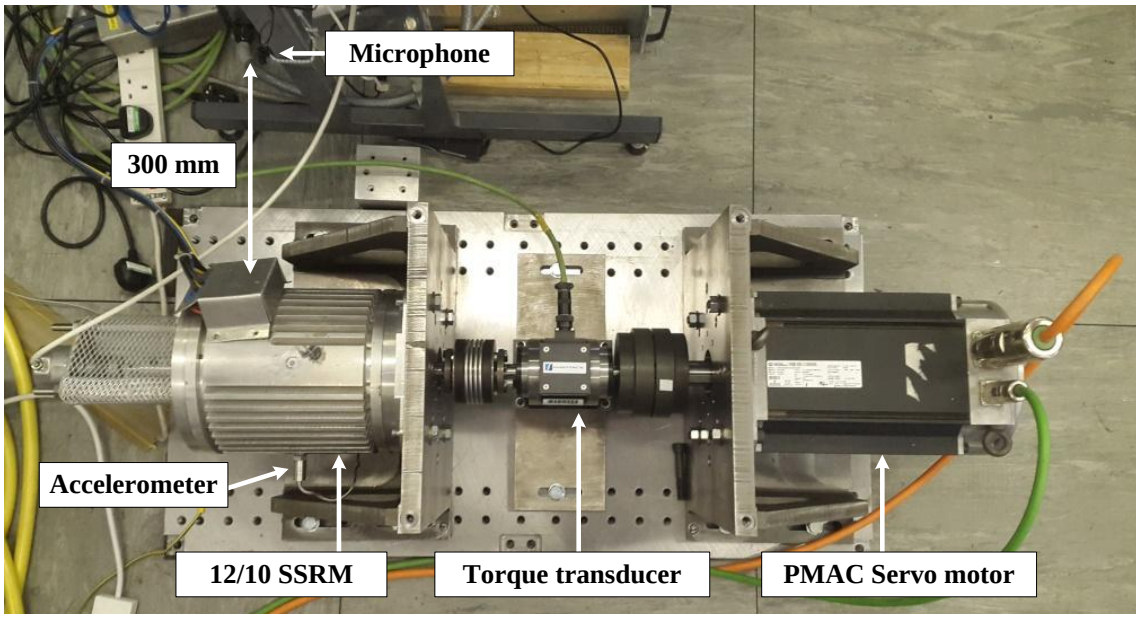

Figure 7.15: Dynamic test rig for acoustic noise and vibration measurement

was selected for the main controller of the control system. The main controller unit generates the PWM gate signal to the asymmetrical half-bridge converter, which uses the dc-bus voltage of 140 V. The six switching power semiconductor devices of the asymmetrical half-bridge converter were power MOSFETs, which are suitable for high switching frequency. The two feedback signals for the control system are the rotor position and the phase current in the SRM. A 12-bit absolute encoder, Hengstler AC 58-I-SSI, was chosen for detecting the rotor position, and three current sensors, ACS770, were used for capturing each phase current of the machine. The two sensors of emitted acoustic noise and vibration are a microphone with a sensitivity of 5.6234 mV/Pa and an accelerometer with a sensitivity of 10.2 mV/m/s^2. A microphone was located on the one side of SSRM at 300 mm distance, whereas the accelerometer was mounted into the motor casing behind a large pole of the SSRM as shown in Fig. 7.15.

To improve the accuracy of the noise measuring equipment, a sound level calibrator, namely Extech model 407744, which generates a 1 kHz sine wave at 94 dB (an accuracy of 5% frequency and ±0.8 dB), was applied to calibrate the microphone before dynamic testing. All signals such as voltage, current, acceleration, and noise were captured and subjected to FFT analysis using the universal data acqui-

Table 7.3: Motor and drive system details

Parameter	
SRM type	12/10 SSRM
Number of phases	3 phases
Dominant vibration mode	Second-order mode
Dominant resonant frequency at 2^{nd} mode	2292 Hz
Damping ratio	0.05
Converter topology	Asymmetrical half-bridge
DC link voltage	140 Vdc
PWM frequency	20 kHz

Table 7.4: Experimental test parameters

Speed [r/min]	250	500	500	1000
Torque output [Nm]	5	5	2	2
Turn-on angle [mechanical deg.]	0	0	0	0
Turn-off angle [mechanical deg.]	15	17	15	19
Advance angle [mechanical deg.]	0	0	0	5

sition instrument, DEWE-43. The PWM carrier frequency for creating the smooth voltage during the turn-off stage was set to 20 kHz, and the control interval of the control system was 66.67 μs. Chapter 3, which compare different SRM topologies, found that the 12/10 SSRM has the dominant mode of vibration at the second-order mode. Therefore, the main focus for reducing the emitted noise and vibration of the 12/10 SSRM is to decrease the high magnitude of acoustic noise and vibration at the second-order mode shape of the machine. The parameters of the motor and drive system are shown in Table 7.3.

The experimental test was implemented for four conditions with three rotational speeds of 250, 500, and 1000 r/min. The load torque output at 2 and 5 Nm of the load machine was applied to the SSRM at different speeds. Various angles of turn-on, turn-off, and advance were selected to achieve the desired torque output at different rotational speeds. Table 7.4 illustrates the detail of each dynamic testing. Three control techniques based on a hysteresis current control for acoustic noise and

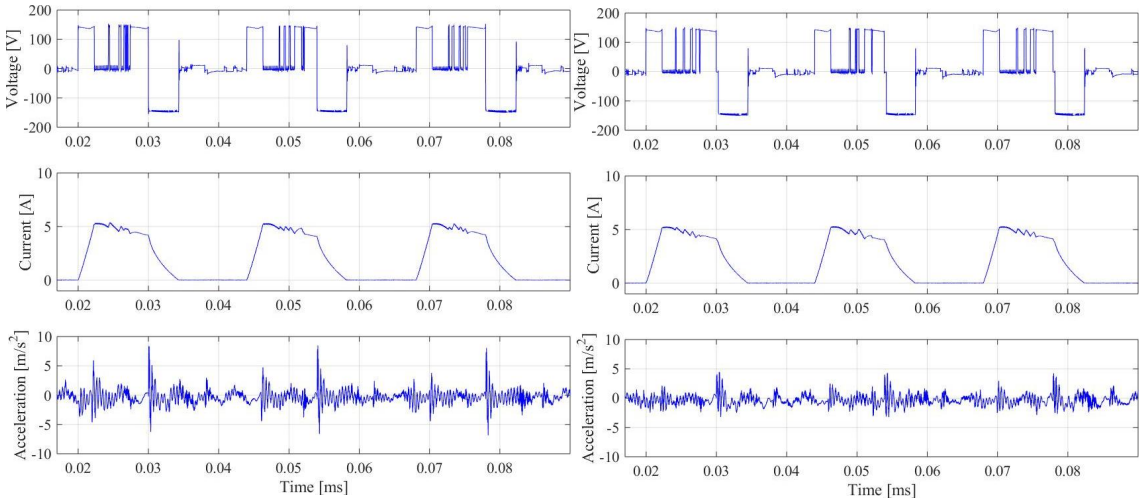

Figure 7.16: Comparison waveform of voltage, current, and acceleration at speed = 250 r/min with load torque = 5 Nm: soft chopping (left) and AVC with two-stage commutation (right)

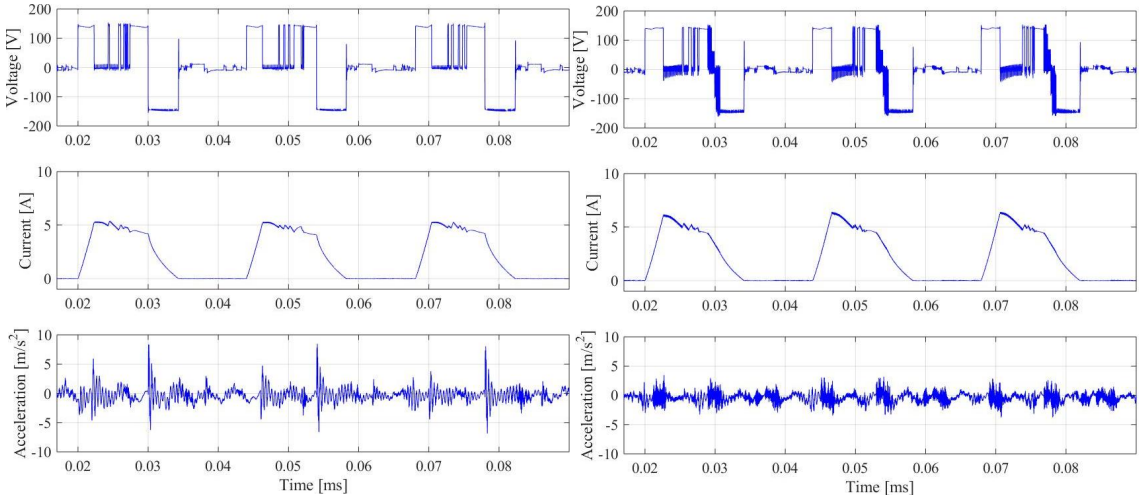

Figure 7.17: Comparison waveform of voltage, current, and acceleration at speed = 250 r/min with load torque = 5 Nm: soft chopping (left) and AVC with smooth voltage PWM (right)

vibration reduction, which are soft chopping, a conventional AVC technique with two-stage commutation, and the proposed method of AVC technique with smooth voltage PWM, were selected for the dynamic test to compare the acoustic noise and vibration in each technique. The ramp lengths of the varying PWM voltage in each stage of the proposed technique are 466.7 μs in the second stage, 200 μs in the third and fourth stages, and 333.35 μs in the fifth stage as shown in Fig. 7.13. These ramp

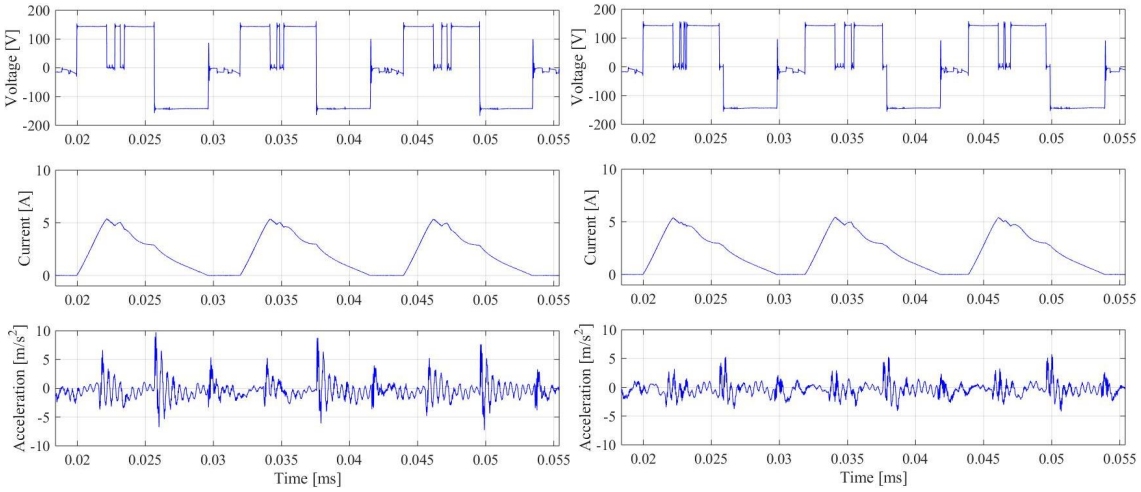

Figure 7.18: Comparison waveform of voltage, current, and acceleration at speed = 500 r/min with load torque = 5 Nm: soft chopping (left) and AVC with two-stage commutation (right)

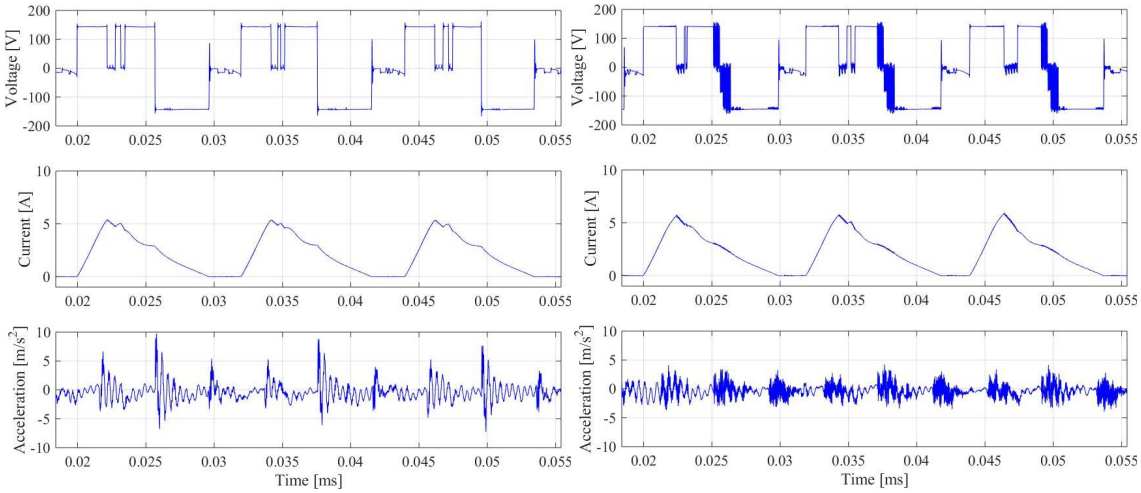

Figure 7.19: Comparison waveform of voltage, current, and acceleration at speed = 500 r/min with load torque = 5 Nm: soft chopping (left) and AVC with smooth voltage PWM (right)

lengths can be optimised to achieve the low vibration and RMS current, depending on the phase voltage level and the damping ratio of the machines.

The experimental dynamic test was performed with 2 and 5 Nm of load. The no-load testing condition was not implemented in this testing because it gives low emitted noise and vibration compared to load-testing. The hard and soft chopping techniques of the conventional hysteresis current control are simple methods of SRM

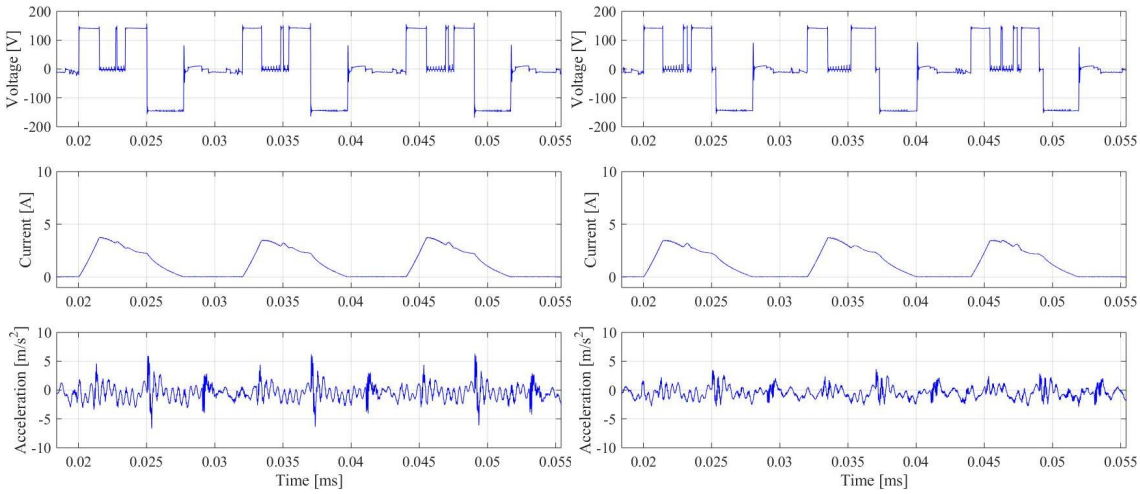

Figure 7.20: Comparison waveform of voltage, current, and acceleration at speed = 500 r/min with load torque = 2 Nm: soft chopping (left) and AVC with two-stage commutation (right)

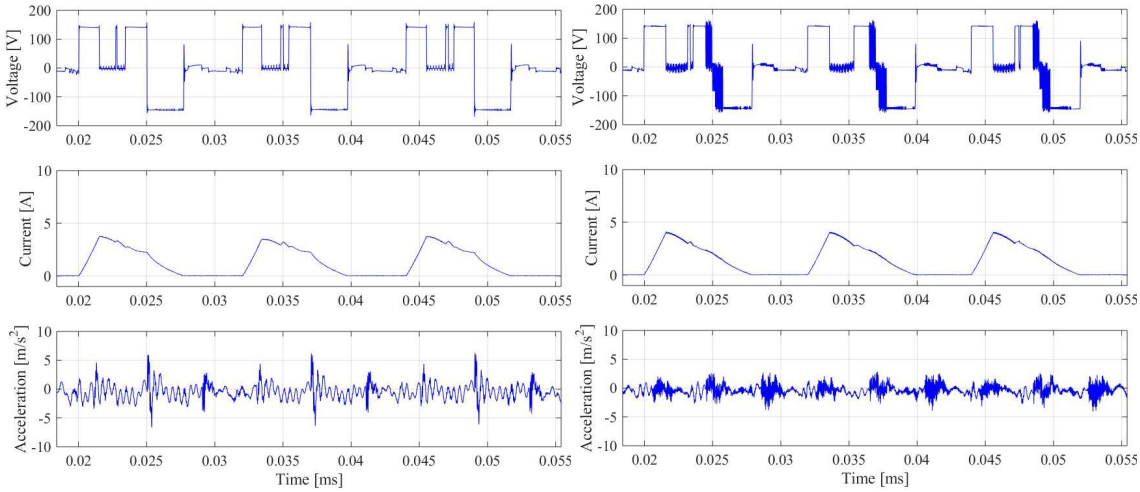

Figure 7.21: Comparison waveform of voltage, current, and acceleration at speed = 500 r/min with load torque = 2 Nm: soft chopping (left) and AVC with smooth voltage PWM (right)

operation. However, the hard chopping method generally creates a high torque ripple and more emitted noise and vibration compared to the soft chopping, as predicted in the simulation section. The conventional soft chopping method was set as a standard of SRM operation instead of hard chopping method for this comparison.

The first dynamic test applied 5 Nm of load torque at 250 r/min of rotational speed using a conventional hysteresis current control with soft chopping and two

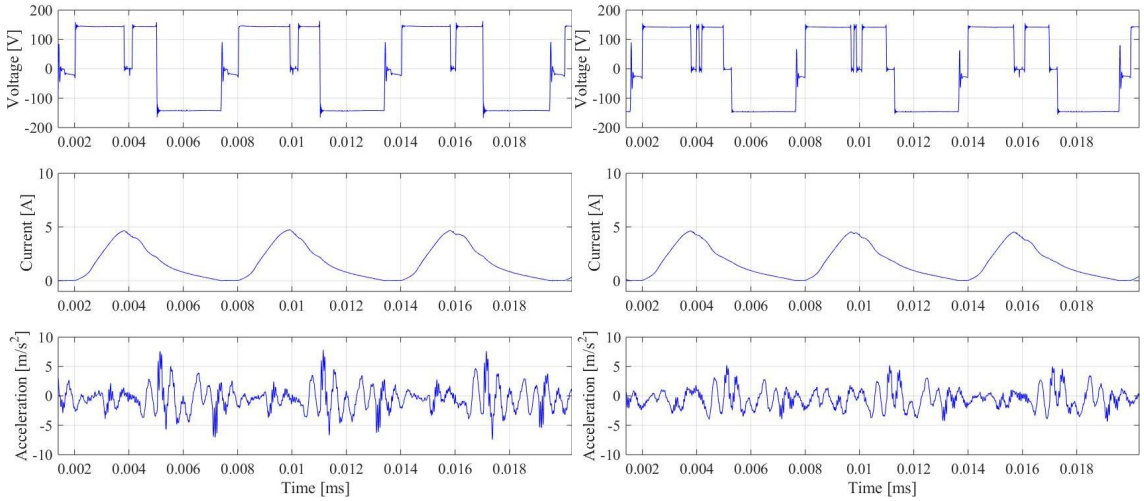

Figure 7.22: Comparison waveform of voltage, current, and acceleration at speed = 1000 r/min with load torque = 2 Nm: soft chopping (left) and AVC with two-stage commutation (right)

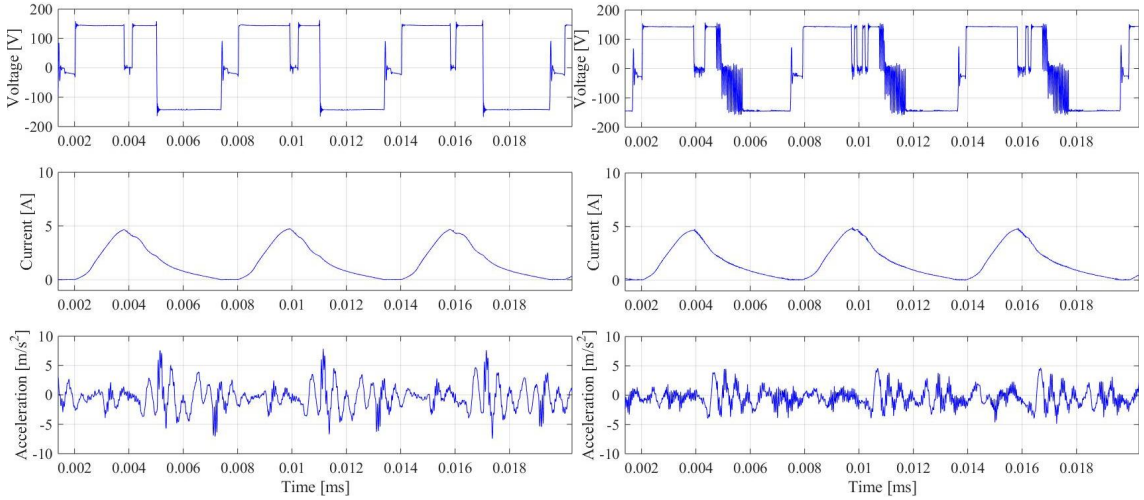

Figure 7.23: Comparison waveform of voltage, current, and acceleration at speed = 1000 r/min with load torque = 2 Nm: soft chopping (left) and AVC with smooth voltage PWM (right)

AVC techniques of noise and vibration reduction. Then each result with the AVC method was compared with the conventional technique with soft chopping as illustrated in Fig. 7.16 and 7.17. The soft chopping produces the maximum acceleration level at 8.46 m/s^2 while the two AVC techniques, namely the technique with two-stage commutation and the technique with smooth voltage PWM method, give maximum acceleration levels of 4.39 and 3.47 m/s^2, respectively. The results of the

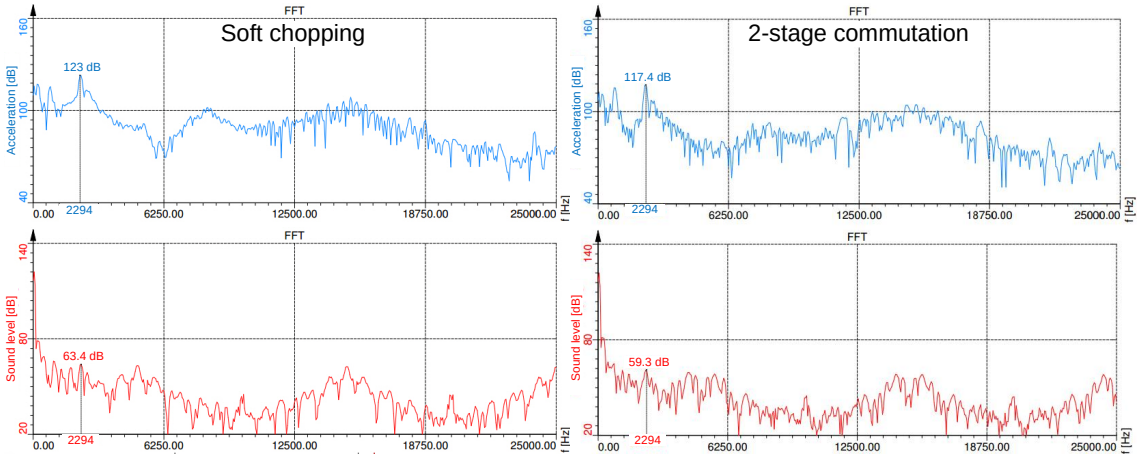

Figure 7.24: Comparison of measured acceleration and noise spectra at speed = 250 r/min with load torque = 5 Nm: soft chopping (left) and AVC with two-stage commutation (right)

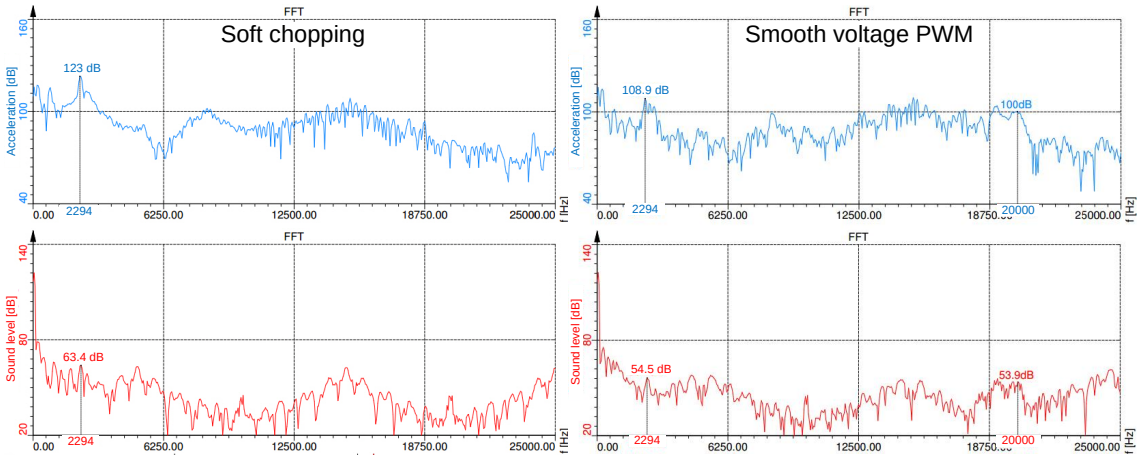

Figure 7.25: Comparison of measured acceleration and noise spectra at speed = 250 r/min with load torque = 5 Nm: soft chopping (left) and AVC with smooth voltage PWM (right)

two AVC techniques confirm the simulation result that these AVC techniques can decrease the vibration of the SRM when compared to the conventional soft chopping method. The two-stage commutation method can reduce the maximum acceleration of the soft chopping by 48.12 % while the smooth voltage PWM method can reduce it by 58.98 %. When comparing both the two-stage commutation and smooth voltage PWM methods, the smooth voltage PWM method also decreases the maximum acceleration of the two-stage commutation by 20.96 %. On the other hand, in terms

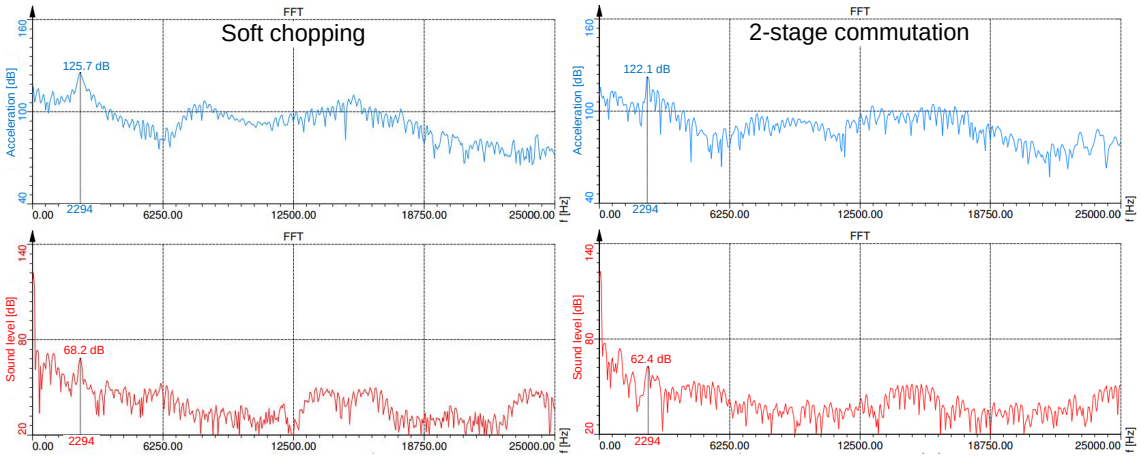

Figure 7.26: Comparison of measured acceleration and noise spectra at speed = 500 r/min with load torque = 5 Nm: soft chopping (left) and AVC with two-stage commutation (right)

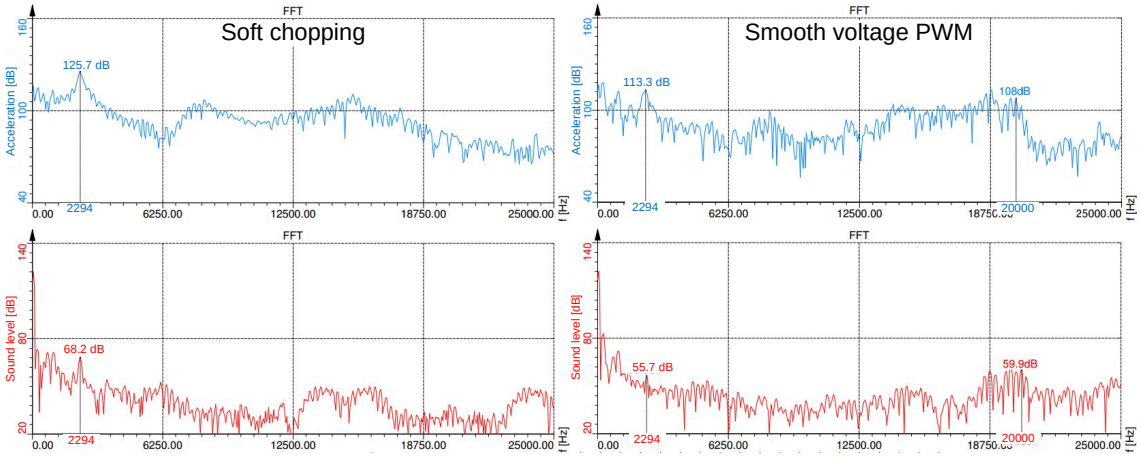

Figure 7.27: Comparison of measured acceleration and noise spectra at speed = 500 r/min with load torque = 5 Nm: soft chopping (left) and AVC with smooth voltage PWM (right)

of power consumption, the smooth voltage PWM generates a high peak of phase current to compensate the long decay of the current, which tends to create negative torque. For this reason, the RMS current of the smooth voltage PWM method is higher than that of the other techniques, causing higher copper losses in the machine. The RMS current of the smooth voltage PWM method increases by 3.75 and 3.40 % compared to the soft chopping and two-stage commutation methods, respectively.

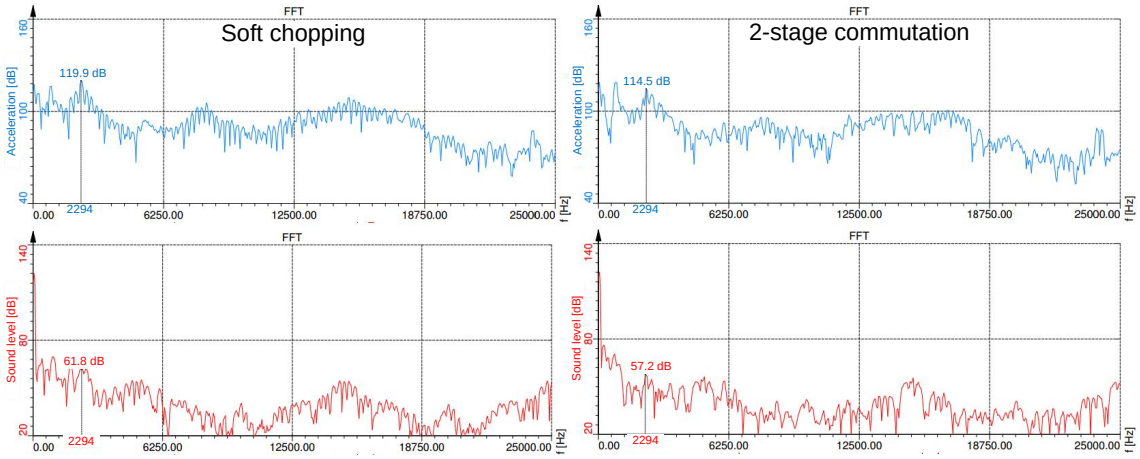

Figure 7.28: Comparison of measured acceleration and noise spectra at speed = 500 r/min with load torque = 2 Nm: soft chopping (left) and AVC with two-stage commutation (right)

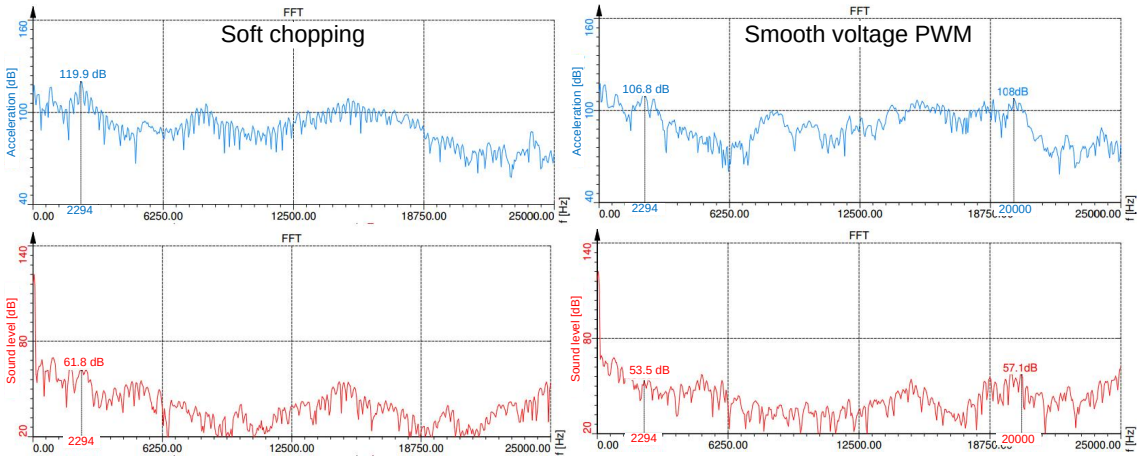

Figure 7.29: Comparison of measured acceleration and noise spectra at speed = 500 r/min with load torque = 2 Nm: soft chopping (left) and AVC with smooth voltage PWM (right)

In the second test, the rotational speed of the SRM was increased from 250 to 500 r/min with the same load torque of 5 Nm. The voltage, current and acceleration signals are shown in Fig. 7.18 and 7.19. Both AVC techniques are also compared with the conventional soft chopping. The maximum acceleration level of the soft chopping techniques rises by 6.03 % when increasing the rotational speed. Using the AVC method, the maximum acceleration of the soft chopping can be decreased by 35.79 % with two-stage commutation and by 52.95 % with smooth voltage PWM.

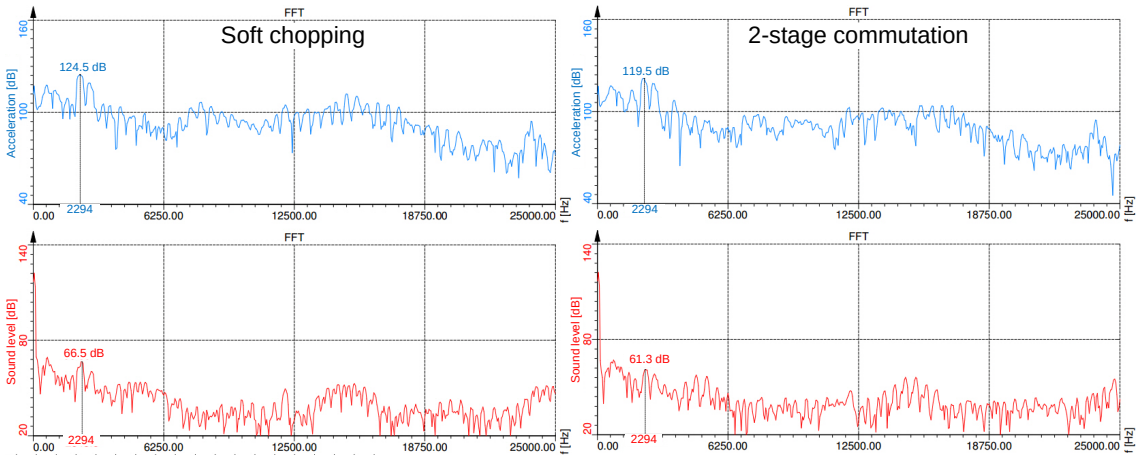

Figure 7.30: Comparison of measured acceleration and noise spectra at speed = 1000 r/min with load torque = 2 Nm: soft chopping (left) and AVC with two-stage commutation (right)

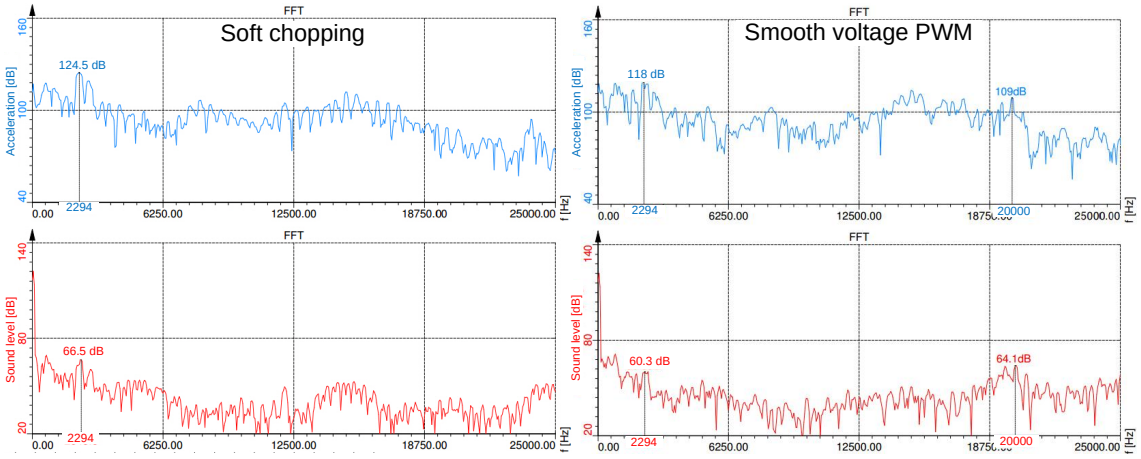

Figure 7.31: Comparison of measured acceleration and noise spectra at speed = 1000 r/min with load torque = 2 Nm: soft chopping (left) and AVC with smooth voltage PWM (right)

Similarly to the previous testing, the peak and RMS current of the smooth voltage PWM method is still high compared with the other methods. It increases by 2.93 and 2.55 % compared to the soft chopping and two-stage commutation methods, respectively.

The third dynamic testing, maintained a rotational speed of 500 r/min, but the load torque was reduced from 5 to 2 Nm. The level of maximum acceleration in the soft chopping method decreases by 29.65 % from 8.97 m/s^2 at 5 Nm of load torque

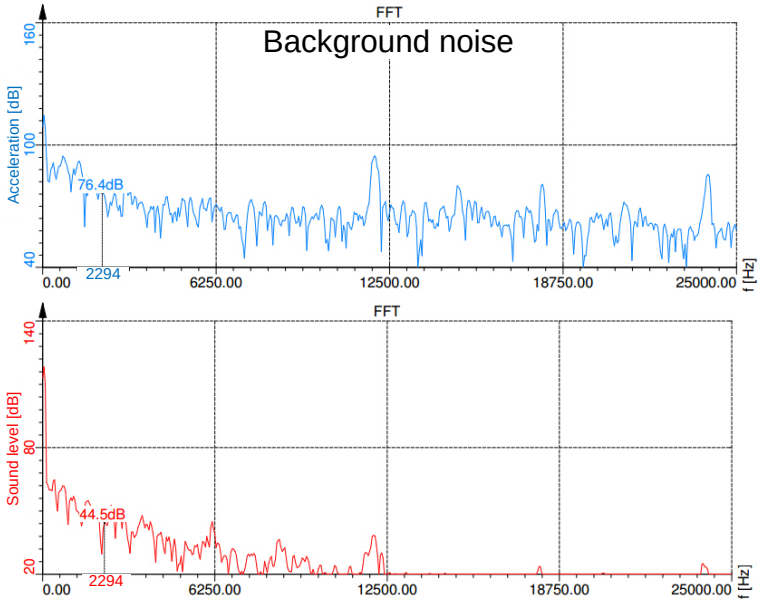

Figure 7.32: Background acceleration and noise spectra

Table 7.5: Decibel reference level (ISO R 1683)

Quantity	Definition, dB	Reference = 0 dB
Vibratory acceleration level	$L_a = 20\text{Log}_{10}(a/a_0)$ dB	$a_0 = 10^{-6}$ m/s^2
Vibratory velocity level	$L_v = 20\text{Log}_{10}(v/v_0)$ dB	$v_0 = 10^{-9}$ m/s
Vibratory force level	$L_F = 20\text{Log}_{10}(F/F_0)$ dB	$F_0 = 10^{-6}$ N

to 6.31 m/s^2 at 2 Nm. In addition, in the soft chopping method the RMS current reduces by 33.3% when decreasing the load torque. The smooth voltage PWM method is still capable of vibration reduction in the SRM, reducing the maximum of acceleration level by 54.52 % and 21.8 % compared with the soft chopping and two-stage commutation methods, respectively. However, the RMS current of the proposed method increases by 7.14 % and 5.98 % compared with the soft chopping and two-stage commutation methods, respectively, as shown in Fig. 7.20 and 7.21.

The final test condition was at a rotational speed of 1000 r/min with the same load torque of 2 Nm. Fig. 7.22 and 7.23 show experimental results of the three control techniques when increasing the speed from 500 to 1000 r/min. The soft chopping method generates the maximum level of acceleration at 7.83 m/s^2, which represents an increase of by 24.1 % compared to that at the rotational speed of 500 r/min. The proposed method can reduce the maximum of the acceleration level of

Table 7.6: Experimental results at applied load torque = 5 Nm (ambient noise = 44.5 dB)

Speed 250 r/min Load torque 5 Nm				
Control technique	Maximum Acce. [m/s^2]	Acceleration [dB]	Sound level [dB]	RMS current [A]
Soft chopping	8.46	123.0	63.4	2.93
2-stage commutation	4.39	117.4	59.3	2.94
Smooth voltage PWM	3.47	108.9	54.5	3.04
Speed 500 r/min Load torque 5 Nm				
Control technique	Maximum Acce. [m/s^2]	Acceleration [dB]	Sound level [dB]	RMS current [A]
Soft chopping	8.97	125.7	68.2	2.73
2-stage commutation	5.76	122.1	62.4	2.74
Smooth voltage PWM	4.22	113.3	55.7	2.81

the soft chopping and two-stage commutation methods by 40.74 % and 11.45 %, respectively. The RMS current is still high in the proposed method compared with the other methods, rising by 2.65 % and 1.3 % compared to the soft chopping and two-stage commutation methods, respectively.

In terms of frequency domain analysis, the proposed method can reduce the magnitude of noise and vibration by 8.9 dB of sound level and 14.1 dB of acceleration compared with the conventional soft chopping method at 250 r/min of rotational speed with 5 Nm of load torque. The two-stage commutation method can reduce the magnitude of noise and vibration by 4.1 dB of sound level and 5.6 dB of acceleration compared with the conventional method as shown in Fig. 7.24 and 7.25. In the frequency domain, the magnitude of acceleration is calculated according to the decibel reference level in ISO R 1683, as described in Table 7.5.

When increasing the rotational speed to 500 r/min at the same torque level of 5 Nm, the sound and vibration level increases in the soft chopping method by 4.8 dB of sound level and 2.7 dB of acceleration compared with that at 250 r/min. The

Table 7.7: Experimental results at applied load torque = 2 Nm (ambient noise = 44.5 dB)

Speed 500 r/min Load torque 2 Nm				
Control technique	Maximum Acce. [m/s^2]	Acceleration [dB]	Sound level [dB]	RMS current [A]
Soft chopping	6.31	119.9	61.8	1.82
2-stage commutation	3.67	114.5	57.2	1.84
Smooth voltage PWM	2.87	106.8	53.5	1.95
Speed 1000 r/min Load torque 2 Nm				
Control technique	Maximum Acce. [m/s^2]	Acceleration [dB]	Sound level [dB]	RMS current [A]
Soft chopping	7.83	124.5	66.5	2.26
2-stage commutation	5.24	119.5	61.3	2.29
Smooth voltage PWM	4.64	118.0	60.3	2.32

sound and vibration levels in the proposed technique are lower than in the other methods. Compared with the soft chopping method, the proposed technique reduces the sound level by an additional 12.5 dB and the acceleration by an additional 12.4 dB. Compared to the two-stage commutation method, the proposed technique creates a low magnitude of sound and vibration, reducing sound level by 6.7 dB and acceleration by 8.8 dB as shown in Fig. 7.26 and 7.27.

When decreasing the load torque to 2 Nm at the same rotational speed of 500 r/min, the magnitude of the sound and vibration level also reduces. In the soft chopping method, the magnitude of sound level decreases by 6.4 dB from 68.2 to 61.8 dB, and the magnitude of acceleration decreases by 5.8 dB from 125.7 to 119.9 dB. The proposed technique reduces the magnitude of sound and vibration level of the soft chopping by 8.3 dB of sound level and 13.1 dB of acceleration. Furthermore, the smooth voltage PWM method also generates less magnitude of sound and vibration compared with the two-stage commutation method by 3.7 dB of sound level and 7.7 dB of acceleration as shown in Fig. 7.28 and 7.29.

In the conventional soft chopping method, increasing the rotational speed to 1000 r/min at the same load torque of 2 Nm resulted in the magnitude of the sound level going up by 4.7 dB from 61.8 dB at 500 r/min to 66.5 dB at 1000 r/min. The vibration level went up by 4.6 dB from 119.9 dB at 500 r/min to 124.5 dB at 1000 r/min. At 1000 r/min, the magnitude of the sound and vibration with the soft chopping method can be reduced by using the proposed technique and the two-stage commutation method. The two-stage commutation method can reduce the magnitude by 5.2 dB of sound level and by 5 dB of acceleration, whereas the proposed method can decrease the magnitude by 6.2 dB of sound level and 6.5 dB of acceleration as shown in Fig. 7.30 and 7.31. Moreover, the high amplitude of the harmonic component of acoustic noise and vibration at 20 kHz appears when using the AVC with smooth voltage PWM method. This occurs as a result of using a high PWM switching frequency to generate a smooth average phase voltage with this technique. The experimental results are summarised in Table 7.6 and 7.7.

7.3 Conclusion

This chapter focuses on an investigation of control techniques for acoustic noise and vibration reduction in an SRM. High vibration in the SRM is generated during the turn-off stage due to the rate change of phase voltage, and the amplitude of vibration depends on the rate change of the phase voltage level. A simple effective control method for reducing emitted noise and vibration is an active vibration cancellation technique. The principle of the AVC technique is creating another vibration signal to cancel the main vibration signal. In this chapter both simulation and experimental testing was implemented to investigate and compare each control technique to eliminate an acoustic noise and vibration in a 12/10 SSRM. The AVC technique has been reported that it is very effective in SRM control with regard to vibration reduction with single-pulse voltage control, but less effective under current control.

Five different control methods for the SRM, (hard chopping, soft chopping, AVC with two-stage commutation, AVC with two-stage and PWM, and AVC with smooth voltage PWM technique based on hysteresis current control) were simulated for

an initial study of the control effect on vibration in a 12/10 SSRM using MATLAB/Simulink and a magnetic finite element method. Hard chopping generates the highest vibration level, while the two proposed methods (AVC with two-stage commutation and PWM and AVC with smooth voltage PWM technique) produce a low vibration level compared with the other methods. The most effective control method in the simulation is the AVC with smooth voltage PWM technique. This technique uses the PWM method with a high switching frequency to vary the average phase voltage. This variance affects the amplitude of the vibration signal during the turn-off stage. The smooth average phase voltage is controlled by the varying duty ratio of PWM according to the damping ratio of the vibration signal of the machine.

In experimental dynamic testing, the three control methods of soft chopping, AVC with two-stage commutation, and AVC with smooth voltage PWM method were selected. Increasing load torque and rotational speed of the machine have a significant effect on generating noise and vibration. The implementation of dynamic testing was performed under three different rotational speeds (250, 500, and 1000 r/min) and two load torque conditions (2 and 5 Nm).

The experimental results in the time and frequency domain confirm that the AVC with smooth voltage PWM technique generates a low level of emitted noise and vibration compared to any other methods. The results also confirm that the conventional soft chopping produces a higher level of acoustic noise and vibration. However, the proposed method generates a high level of the RMS current compared with any other methods because it requires a high level of peak phase current to compensate for the long decay of the phase current, which tends to produce a negative torque output. Furthermore, using a high switching PWM frequency, creates a high amplitude of the harmonic component of noise and vibration at the PWM frequency, so the PWM switching frequency should be as high as possible (more than 20 kHz). The benefits and drawbacks of the AVC with a smooth voltage PWM method are summarised below.

The advantages of the proposed method are as follows:

- Does not require knowledge of the resonant frequency of the SRM structure

- Simple and can be applied to any SRM control technique
- Tolerant of the temperature effect of vibration. Temperature testing of the stator prototype shows that the resonant frequency of the stator goes down to a low frequency when temperature increases, but this method is not sensitive to resonant frequency.

The drawbacks of the proposed method are as follows:

- Higher RMS current
- Increased switching losses
- Suitable for a high switching power semiconductor device such as MOSFETs

Chapter 8.
Conclusions and Future Works

In accordance with the aims and objectives of this project, the radial magnetic force, which is the origin of the vibration and acoustic noise generation in an SRM, has been investigated, including the study of control and structure parameters and a comparison of radial magnetic force between different SRM topologies. Furthermore, techniques for mitigation of vibration and acoustic noise in an SRM have been developed. Computation techniques have been developed to determine mechanical material properties, thereby improving the accuracy of the structural simulation model. Simulation and testing methods have enabled calculation of stator structure stiffness and control techniques, which have been shown to be effective for vibration and acoustic noise reduction.

8.1 Background Literature

A review of past research work has revealed information about vibration and acoustic noise in an SRM. The origin of vibration and acoustic noise is radial magnetic force of attraction between the stator and rotor. Severe vibration occurs when a large harmonic component of the radial magnetic force coincides with the dominant resonant frequency of the SRM stator. Techniques to reduce the vibration and acoustic noise in SRM are divided into two methods.

The first method is a SRM control technique associated with the high vibration which occurs during the phase excitation turn-off stage. An active vibration cancellation technique is applied to minimise vibrations during turn-off stage. Another control technique is current shaping control by modifying the shape of the SRM phase current to reduce the amplitude of radial magnetic force harmonic compo-

nents. The second method is modifying the SRM stator and rotor structures. The main purpose of this technique is to increase the stiffness of the stator structure. Recommendation methods to increase the stiffness of the stator are: increasing the stator yoke thickness, modifying the stator yoke structure as the hexagon-round shape and redesigning the teeth, introducing fillet radius and tapered stator poles.

An initial simulation showed that increasing the stiffness of the SRM structures by increased the yoke thickness and frame can shift the dominant resonant frequency of the stator structure to a higher frequency range. Moreover, the SRM control parameters such as turn-on and turn-off angle and phase current shape were predicted to have a significant impact on generating of vibration and acoustic noise in SRM.

8.2 Magnetic Force and Vibration Behaviour

Four SRM topologies (a 12/8 conventional SRM with a short-pitched winding, a 12/8 conventional SRM with a fully-pitched winding, a 12/8 segmental rotor SRM, and a 12/10 single-tooth wound segmental rotor SRM), which have different winding arrangements and different structures, were chosen for comparative study of a radial magnetic force generation. The geometries and dimensions of each SRM topology are the same and they were tested with the same conditions of control parameters, output power and rotational speed.

The simulation results showed that changing of winding arrangement of 12/8 conventional SRM from short-pitched to fully-pitched winding does not improve the vibration and acoustic noise problem. Modifying both the SRM stator/rotor structure and winding arrangement to a 12/8 segmental rotor SRM can reduce vibration when compared with a 12/8 conventional SRM with the short or fully-pitched windings. As a result of this the topology generates continuous radial force waveforms which have lower amplitudes of the high order harmonic components and also have a low ripple rate of sum of radial force. Although, a SRM with a segmental rotor can reduce the amplitude of radial force harmonic components and produce a low ripple rate of sum of radial force, it still generates a high vibration, due to its dominant resonant frequency which occurs in the low-frequency range of a 12/10

single-tooth wound segmental rotor SRM. This topology has the dominant resonant frequency mode of the second order mode of vibration mode shape, compared with 12/8 segmental rotor SRM which has fourth order mode shape. The low order mode shape of vibration can coincide with a lower harmonic component of radial force, which often has high amplitude. This suggests that the design of the SRM structure for low noise emission should have as a higher dominant resonant frequency as possible.

8.3 Mechanical Material Property

To improve the accuracy of simulation models of structural analysis of SRMs, the mechanical material properties are important inputs which affect the results of the simulation for the resonant frequency. The semi-finite element technique, which uses both finite element analysis and analytical methods was developed to determine the mechanical material property of the Young's modulus and Poisson's ratio of the stator lamination core. The comparative results of different steel thicknesses show that the steel sheet thickness and steel volume fraction have a significant impact to Young's modulus in the axial direction. Comparison of the results of the resonant frequency between experimental modal tests and the structural simulation model, with having material properties from the proposed technique, show that both results are similar.

8.4 Techniques of Vibration Measurement

Two methods of vibration measurement were implemented, with 12/10 single-tooth wound segmental rotor SRM, for calculating the resonant frequency and damping ratio of its structures. The first technique is the electromagnetic excitation method which uses the control unit for force excitation and the second is the impact hammer method, where force excitation is applied by the hammer. Both methods give a similar result. The accelerometer, which was mounted on the stator casing is a vibration sensor. The vibration signal was captured for computing of resonant

frequency, using Fast Fourier transform method, and for the damping ratio. Furthermore, the mounting techniques of the SRM, such as a flange-mounted support or an elastic rope support, along with the front and end covers, have a significant impact on the resonant frequency of the SRM structure. Conversely, the rotor does not affect the resonant frequency.

8.5 Stator deformation in Segmented Core

Eight stator prototypes of an SRM segmented stator core have been studied, with different segment joints and an aluminium casing, where the shrink fitting technique was investigated, in terms of, stiffness and modal testing. Simulation and experimental test were developed to evaluate the stiffness of the SRM stator structure. Simulation results provided the average compressive hoop stress and stiffness of each stator model with different interference fits from 20-100 μm. Increasing the interference fit between the stator and casing can increase the stiffness of the segmented stator. However, it also creates a high compressive stress leading to increasing the iron losses in the stator core. The stiffness testing results confirm that the stiffness of the stator structures is reduced by at least 31 % when making a stator core as a segmented core. Moreover, to build a segmented stator with a shrink fitting technique, a high interference fit should be applied to compensate for the high error of tolerance of the manufacturing processes. Varying temperature also has an impact on the resonant frequency and the modal damping ratio. The resonant frequency of the stator structure drops with increasing temperature, whereas damping ratio rise.

8.6 Control Techniques for Vibration Reduction

The development of control techniques for vibration and acoustic noise reduction in the SRM is presented and compared with conventional control methods. The proposed technique is hysteresis current control, with smooth voltage PWM, based on the active vibration cancellation technique. The PWM technique is used to reduce the rate change of voltage during the turn-off stage, where the high vibration signal

appears. The proposed method was implemented experimentally and compared with a conventional method, and was shown to reduce the acoustic noise by 8.9 dB, 8.3 dB, and 6.2 dB at the rotational speed of 250, 500, and 1000 r/min, respectively, at the same load condition.

8.7 Future Academic Work

This academic works has resulted in suggestions for the following areas of further study:

8.7.1 Building Prototype for Verification

Some parts of this project need a further experimental testing. In this project, the comparative study of magnetic force, vibration and acoustic noise at different SRM topologies was only performed in simulation. The SRM prototype for comparative study should be constructed and tested to verify the simulation results.

To enhance an investigation of stator deformation, the lamination segmented stator core of each prototype should be built for the verification of the modal testing. The segmented stator prototypes in this project were built using solid steel to investigate the deformation of the stator. However, in the modal testing, the damping ratio of the building stator prototype between solid steel and a laminated core is very different. In future, laminated cores should be used for this testing.

8.7.2 Mechanical Material Property of the Lamination Core

In the process of building the stator lamination core, the steel sheets are bonded together with epoxy and assembled into a stack using a hydraulic press. The lamination stack was then baked under pressure for several hours, finally leaving it at room temperature for cooling. During the manufacturing processes of the stator lamination core, the mechanical material properties change. This project focuses on the stator lamination core with an adhesive bonding technique. The calculation technique of mechanical material properties for this lamination core was developed

Figure 8.1: Laminated stator core using a welding technique

using structural finite element analysis software. Often other stator assembly techniques, other than bonding alone is used. Sometimes after adhesive bonding, welding is applied to increase the stiffness of the stator stack. At other times, the assembled stack still is welded directly, without the use of adhesive bonding, as shown in Fig. 8.1. By doing this, the mechanical material properties of the lamination core are changed and will be different to that of adhesive bonding. Further work in this area should consider the welded outer stator surface and its development into the structural simulation model.

The analytical method developed for the mechanical material properties of the coil winding should be improved and incorporated into the structural simulation model. This project used the mechanical material data of the coil winding from the equation which was obtained using experimental tests [74]. Coil winding materils in the stator slot consist of solid copper, insulating varnish, insulating sheet and enamel. The percentage of the space factor is very difficult to estimate. There is research [76, 77] on using compressed coil windings to increase the fill factor in the motor slots. The fill factor can be increased to over 70 % using compressed coil techniques. In these cases of high fill factor, the Young's modulus of the compressed

coil can be assumed to be equal to that of solid copper.

To verify this assumption, the SRM with a compressed coil winding should be constructed and tested and then compared to a conventionally wound SRM to improve the structural simulation model.

8.7.3 Control Techniques for Vibration Reduction

The proposed control technique in this project use a PWM technique to reduce the rate of change of phase voltage during the turn-off stage with the PWM switching frequency at 20 kHz. The PWM frequency has an influence on the vibration signal. Therefore, the PWM frequency should be selected to be above the human ear perception (20 Hz - 20 kHz). PWM frequencies above 20 kHz should be selected to implement the proposed SRM control technique-the higher the frequency the better. This will enhance the smoothness of the phase voltage. Also at high frequencies and current chopping control, the vibration signal will be chopped.

Whilst under these strategies, vibration cannot develop high amplitudes. However, the negative effects of using high switching PWM frequencies are that it generates electromagnetic interference which has a detrimental effect on the drive control system. There effects can cause damage to the power semiconductor devices and the CPU operation. Additionally, it will increase the switching losses in the power converter and increase the device cost.

The challenge of this technique is how to develop the SRM converter to use with a high switching PWM frequency? There are now many power electronic devices which can operate at high-frequency and generate low switching losses, and there are many grades of microcontroller which can operate in a highly disturbed environment.

References

[1] J. F. Gieras, C. Wang, and J. C. Lai, *Noise of Polyphase Electric Motors*. CRC Press, Dec. 2005.

[2] P. Vijayraghavan and R. Krishnan, "Noise in electric machines: a review," *IEEE Transactions on Industry Applications*, vol. 35, no. 5, pp. 1007–1013, 1999.

[3] P. L. Timr, *Noise and vibration of electrical machines*. Elsevier Science Pub. Co., 1989.

[4] S. J. Yang, "Effects of Voltage/Current Harmonics on Noise Emission from Induction Motors," in *Vibrations and Audible Noise in Alternating Current Machines*, ser. NATO ASI Series, R. Belmans, K. J. Binns, W. Geysen, and A. Vandenput, Eds. Springer Netherlands, 1988, no. 148, pp. 457–468.

[5] P. J. Lawrenson, J. M. Stephenson, P. T. Blenkinsop, J. Corda, and N. N. Fulton, "Variable-speed switched reluctance motors," *IEE Proceedings B - Electric Power Applications*, vol. 127, no. 4, pp. 253–265, July 1980.

[6] P. Lawrenson, "Switched-reluctance motor drives," *Electronics and Power*, vol. 29, no. 2, pp. 144–147, February 1983.

[7] T. J. E. Miller, *Switched Reluctance Motors and Their Control*, ser. Monographs in Electrical and Electronic Engineering. Oxford, New York: Oxford University Press, Jul. 1993.

[8] R. Krishnan and P. Vijayraghavan, "State of the art: acoustic noise in switched reluctance motor drives," in *Proceedings of the 24th Annual Conference of the*

IEEE Industrial Electronics Society, IECON '98, vol. 2, Aug. 1998, pp. 929–934.

[9] R. B. Inderka and R. W. A. A. D. Doncker, "DITC-direct instantaneous torque control of switched reluctance drives," *IEEE Transactions on Industry Applications*, vol. 39, no. 4, pp. 1046–1051, Jul. 2003.

[10] C.-Y. Wu and C. Pollock, "Analysis and reduction of vibration and acoustic noise in the switched reluctance drive," *IEEE Transactions on Industry Applications*, vol. 31, no. 1, pp. 91–98, Jan. 1995.

[11] J. W. Lee, H. S. Kim, B. I. Kwon, and B.-t. Kim, "New rotor shape design for minimum torque ripple of SRM using FEM," *IEEE Transactions on Magnetics*, vol. 40, no. 2, pp. 754–757, 2004.

[12] B. Mecrow, J. Finch, E. El-Kharashi, and A. Jack, "Switched reluctance motors with segmental rotors," *Electric Power Applications, IEE Proceedings* -, vol. 149, no. 4, pp. 245–254, Jul. 2002.

[13] D. Cameron, J. Lang, and S. Umans, "The origin of acoustic noise in variable-reluctance motors," in *Conference Record of the 1989 IEEE Industry Applications Society Annual Meeting*, vol. 1, 1989, pp. 108–115.

[14] ——, "The origin and reduction of acoustic noise in doubly salient variable-reluctance motors," *IEEE Transactions on Industry Applications*, vol. 28, no. 6, pp. 1250–1255, 1992.

[15] C. Pollock and C.-Y. Wu, "Acoustic noise cancellation techniques for switched reluctance drives," *IEEE Transactions on Industry Applications*, vol. 33, no. 2, pp. 477–484, Mar. 1997.

[16] G. E. Horst, "Noise reduction in a switched reluctance motor by current profile manipulation," U.S. Patent US5 461 295 A, Oct., 1995.

[17] ——, "Current decay control in switched reluctance motor," U.S. Patent US5 446 359 A, Aug., 1995.

[18] A. Michaelides and C. Pollock, "Reduction of noise and vibration in switched reluctance motors: new aspects," in *, Conference Record of the 1996 IEEE Industry Applications Conference, 1996. Thirty-First IAS Annual Meeting, IAS '96*, vol. 2, Oct. 1996, pp. 771–778 vol.2.

[19] X. Liu, Z. Q. Zhu, M. Hasegawa, A. Pride, and R. Deodhar, "Investigation of PWMs on vibration and noise in SRM with sinusoidal bipolar excitation," in *2012 IEEE International Symposium on Industrial Electronics (ISIE)*, 2012, pp. 674–679.

[20] J. Lecointe, R. Romary, J.-F. Brudny, and M. McClelland, "Analysis and active reduction of vibration and acoustic noise in the switched reluctance motor," *Electric Power Applications, IEE Proceedings*, vol. 151, no. 6, pp. 725–733, 2004.

[21] P. Pillay, R. Samudio, M. Ahmed, and R. Patel, "A chopper-controlled SRM drive for reduced acoustic noise and improved ride-through capability using supercapacitors," *IEEE Transactions on Industry Applications*, vol. 31, no. 5, pp. 1029–1038, 1995.

[22] A. Hofmann, A. Al-Dajani, M. Bsing, and R. W. D. Doncker, "Direct instantaneous force control: A method to eliminate mode-0-borne noise in switched reluctance machines," in *Electric Machines Drives Conference (IEMDC), 2013 IEEE International*, May 2013, pp. 1009–1016.

[23] F. C. Lin and S. M. Yang, "An Approach to Producing Controlled Radial Force in a Switched Reluctance Motor," *IEEE Transactions on Industrial Electronics*, vol. 54, no. 4, pp. 2137–2146, Aug. 2007.

[24] J. Li, H. Sun, and Y. Liu, "New rotor structure mitigating vibration and noise in switched reluctance motor," in *2010 International Conference on Information, Networking and Automation (ICINA)*, vol. 2, Oct 2010, pp. V2–80–V2–84.

[25] M. Sanada, S. Morimoto, Y. Takeda, and N. Matsui, "Novel rotor pole design of switched reluctance motors to reduce the acoustic noise," in *Conference*

Record of the 2000 IEEE Industry Applications Conference. Thirty-Fifth IAS Annual Meeting and World Conference on Industrial Applications of Electrical Energy (Cat. No.00CH37129), vol. 1, 2000, pp. 107–113 vol.1.

[26] J. O. Fiedler, K. A. Kasper, and R. W. D. Doncker, "Acoustic noise in switched reluctance drives: an aerodynamic problem?" in *IEEE International Conference on Electric Machines and Drives, 2005.*, May 2005, pp. 1275–1280.

[27] K. Kiyota, T. Kakishima, A. Chiba, and M. A. Rahman, "Cylindrical rotor design for acoustic noise and windage loss reduction in switched reluctance motor for hev applications," *IEEE Transactions on Industry Applications*, vol. 52, no. 1, pp. 154–162, Jan 2016.

[28] J.-P. Hong, K.-H. Ha, and J. Lee, "Stator pole and yoke design for vibration reduction of switched reluctance motor," *IEEE Transactions on Magnetics*, vol. 38, no. 2, pp. 929–932, March 2002.

[29] M. N. Anwar and I. Husain, "Design perspectives of a low acoustic noise switched reluctance machine," in *Conference Record of the 2000 IEEE Industry Applications Conference, 2000*, vol. 1, 2000, pp. 99–106 vol.1.

[30] T. Kakishima, K. Kiyota, S. Nakano, and A. Chiba, "Pole selection and vibration reduction of switched reluctance motor for hybrid electric vehicles," in *2014 IEEE Conference and Expo Transportation Electrification Asia-Pacific (ITEC Asia-Pacific)*, Aug 2014, pp. 1–4.

[31] P. Rasmussen, J. Andreasen, and J. Pijanowski, "Structural stator spacers-a solution for noise reduction of switched reluctance motors," *IEEE Transactions on Industry Applications*, vol. 40, no. 2, pp. 574–581, 2004.

[32] K. Takayama and I. Miki, "Design of switched reluctance motor to reduce acoustic noise," in *2016 International Symposium on Power Electronics, Electrical Drives, Automation and Motion (SPEEDAM)*, June 2016, pp. 425–429.

[33] O. N. Samani and B. Ganji, "Noise reduction of switched reluctance motors," in *2017 8th Power Electronics, Drive Systems Technologies Conference (PEDSTC)*, Feb 2017, pp. 300–304.

[34] H.-Y. Yang, Y.-C. Lim, and H.-c. Kim, "Acoustic Noise/Vibration Reduction of a Single-Phase SRM Using Skewed Stator and Rotor," *IEEE Transactions on Industrial Electronics*, vol. 60, no. 10, pp. 4292–4300, 2013.

[35] C. Gan, J. Wu, M. Shen, S. Yang, Y. Hu, and W. Cao, "Investigation of skewing effects on the vibration reduction of three-phase switched reluctance motors," *IEEE Transactions on Magnetics*, vol. 51, no. 9, pp. 1–9, Sept 2015.

[36] P. Rasmussen, F. Blaabjerg, J. Pedersen, and F. Jensen, "Switched reluctance-shark machines-more torque and less acoustic noise," in *Conference Record of the 2000 IEEE Industry Applications Conference*, vol. 1, 2000, pp. 93–98.

[37] M. Abbasian, M. Moallem, and B. Fahimi, "Double-Stator Switched Reluctance Machines (DSSRM): Fundamentals and Magnetic Force Analysis," *IEEE Transactions on Energy Conversion*, vol. 25, no. 3, pp. 589–597, 2010.

[38] R. Krishnan, *Switched Reluctance Motor Drives: Modeling, Simulation, Analysis, Design, and Applications*. CRC Press, Jun. 2001.

[39] M. Van der Giet, E. Lange, D. Correa, I. Chabu, S. Nabeta, and K. Hameyer, "Acoustic Simulation of a Special Switched Reluctance Drive by Means of Field-Circuit Coupling and Multiphysics Simulation," *IEEE Transactions on Industrial Electronics*, vol. 57, no. 9, pp. 2946–2953, 2010.

[40] J. Fiedler, K. Kasper, and R. De Doncker, "Calculation of the Acoustic Noise Spectrum of SRM Using Modal Superposition," *IEEE Transactions on Industrial Electronics*, vol. 57, no. 9, pp. 2939–2945, 2010.

[41] J. Li, X. Song, and Y. Cho, "Comparison of 12/8 and 6/4 Switched Reluctance Motor: Noise and Vibration Aspects," *IEEE Transactions on Magnetics*, vol. 44, no. 11, pp. 4131–4134, Nov. 2008.

[42] J. Li and Y. Cho, "Investigation into Reduction of Vibration and Acoustic Noise in Switched Reluctance Motors in Radial Force Excitation and Frame Transfer Function Aspects," *IEEE Transactions on Magnetics*, vol. 45, no. 10, pp. 4664–4667, Oct. 2009.

[43] F. dos Santos, J. Anthonis, F. Naclerio, J. Gyselinck, H. Van der Auweraer, and L. Goes, "Multiphysics NVH Modeling: Simulation of a Switched Reluctance Motor for an Electric Vehicle," *IEEE Transactions on Industrial Electronics*, vol. 61, no. 1, pp. 469–476, 2014.

[44] R. Colby, F. M. Mottier, and T. J. E. Miller, "Vibration modes and acoustic noise in a four-phase switched reluctance motor," *IEEE Transactions on Industry Applications*, vol. 32, no. 6, pp. 1357–1364, 1996.

[45] C. S. Edrington, D. C. Kaluvagunta, J. Joddar, and B. Fahimi, "Investigation of electromagnetic force components in srm under single and multiphase excitation," *IEEE Transactions on Industry Applications*, vol. 41, no. 4, pp. 978–988, July 2005.

[46] W. Jiang, M. Moallem, B. Fahimi, and S. Pekarek, "Qualitative investigation of force density components in electromechanical energy conversion process," in *IECON 2006 - 32nd Annual Conference on IEEE Industrial Electronics*, Nov 2006, pp. 1113–1118.

[47] M. N. Anwar and I. Husain, "Radial force calculation and acoustic noise prediction in switched reluctance machines," in *Conference Record of the 1999 IEEE Industry Applications Conference. Thirty-Forth IAS Annual Meeting (Cat. No.99CH36370)*, vol. 4, 1999, pp. 2242–2249 vol.4.

[48] W. Wang, C. Lin, and B. Fahimi, "Comparative analysis of double stator switched reluctance machine and permanent magnet synchronous machine," in *2012 IEEE International Symposium on Industrial Electronics*, May 2012, pp. 617–622.

[49] A. Isfahani and B. Fahimi, "Multi-physics analysis of double stator switched reluctance machines," in *2013 IEEE Energy Conversion Congress and Exposition (ECCE)*, Sep. 2013, pp. 2827–2833.

[50] ——, "Comparison of Mechanical Vibration Between a Double-Stator Switched Reluctance Machine and a Conventional Switched Reluctance Machine," *IEEE Transactions on Magnetics*, vol. 50, no. 2, pp. 293–296, Feb. 2014.

[51] S. D. Garvey, J. E. Penny, M. J. Friswell, and C. N. Glew, "Modelling the vibrational behaviour of stator cores of electrical machines with a view to successfully predicting machine noise," in *IEE Colloquium on Modeling the Performance of Electrical Machines (Digest No: 1997/166)*, Apr 1997, pp. 3/1–313.

[52] L. Zhu, B. Wang, R. Yan, Q. Yang, Y. Yang, and X. Zhang, "Electromagnetic vibration of motor core including magnetostriction under different rotation speeds," *IEEE Transactions on Magnetics*, vol. 52, no. 3, pp. 1–4, March 2016.

[53] K. Delaere, W. Heylen, R. Belmans, and K. Hameyer, "Comparison of induction machine stator vibration spectra induced by reluctance forces and magnetostriction," *IEEE Transactions on Magnetics*, vol. 38, no. 2, pp. 969–972, Mar 2002.

[54] S. D. Garvey and C. N. Glew, "Magnetostrictive excitation of vibration in machines-a modal approach," in *1999. Ninth International Conference on Electrical Machines and Drives (Conf. Publ. No. 468)*, 1999, pp. 169–173.

[55] B. Weiser, H. Pfutzner, and J. Anger, "Relevance of magnetostriction and forces for the generation of audible noise of transformer cores," *IEEE Transactions on Magnetics*, vol. 36, no. 5, pp. 3759–3777, Sep 2000.

[56] L. Vandevelde and J. A. A. Melkebeek, "Magnetic forces and magnetostriction in electrical machines and transformer cores," *IEEE Transactions on Magnetics*, vol. 39, no. 3, pp. 1618–1621, May 2003.

[57] A. Moses, "Measurement of magnetostriction and vibration with regard to transformer noise," *IEEE Transactions on Magnetics*, vol. 10, no. 2, pp. 154–156, Jun 1974.

[58] P. Pillay and W. Cai, "An investigation into vibration in switched reluctance motors," *IEEE Transactions on Industry Applications*, vol. 35, no. 3, pp. 589–596, May 1999.

[59] C. Lin and B. Fahimi, "Prediction of Radial Vibration in Switched Reluctance Machines," *IEEE Transactions on Energy Conversion*, vol. 28, no. 4, pp. 1072–1081, Dec. 2013.

[60] ——, "Prediction of Acoustic Noise in Switched Reluctance Motor Drives," *IEEE Transactions on Energy Conversion*, vol. 29, no. 1, pp. 250–258, Mar. 2014.

[61] B. C. Mecrow, "Fully pitched-winding switched-reluctance and stepping-motor arrangements," *IEE Proceedings B - Electric Power Applications*, vol. 140, no. 1, pp. 61–70, Jan 1993.

[62] B. Mecrow, E. El-Kharashi, J. Finch, and A. Jack, "Segmental rotor switched reluctance motors with single-tooth windings," *Electric Power Applications, IEE Proceedings* -, vol. 150, no. 5, pp. 591–599, Sep. 2003.

[63] J. Widmer and B. Mecrow, "Optimized Segmental Rotor Switched Reluctance Machines With a Greater Number of Rotor Segments Than Stator Slots," *IEEE Transactions on Industry Applications*, vol. 49, no. 4, pp. 1491–1498, Jul. 2013.

[64] C. Laudensack and D. Gerling, "Vibration and noise analyses of canned switched reluctance machines with different winding topologies," in *AFRICON, 2013*, Sep. 2013, pp. 1–5.

[65] I. Husain, A. Radun, and J. Nairus, "Unbalanced force calculation in switched-reluctance machines," *IEEE Transactions on Magnetics*, vol. 36, no. 1, pp. 330–338, Jan 2000.

[66] J. O. Fiedler and R. W. De Doncker, "Simplified Calculation of Radial Force Spectrum in SRM for Acoustic Noise Prediction in Preliminary Machine Design," in *The 3rd IET International Conference on Power Electronics, Machines and Drives, 2006*, Apr. 2006, pp. 652–656.

[67] M. Takiguchi, H. Sugimoto, N. Kurihara, and A. Chiba, "Acoustic noise and vibration reduction of srm by elimination of third harmonic component in sum of radial forces," *IEEE Transactions on Energy Conversion*, vol. 30, no. 3, pp. 883–891, Sept 2015.

[68] Z. Tang, P. Pillay, A. Omekanda, C. Li, and C. Cetinkaya, "Young's modulus for laminated machine structures with particular reference to switched reluctance motor vibrations," *IEEE Transactions on Industry Applications*, vol. 40, no. 3, pp. 748–754, May 2004.

[69] ——, "Effects of material properties on switched reluctance motor vibration determination," in *Industry Applications Conference, 2003. 38th IAS Annual Meeting. Conference Record of the*, vol. 1, Oct. 2003, pp. 235–241 vol.1.

[70] W. Cai, P. Pillay, Z. Tang, and A. Omekanda, "Low-vibration design of switched reluctance motors for automotive applications using modal analysis," *IEEE Transactions on Industry Applications*, vol. 39, no. 4, pp. 971–977, Jul. 2003.

[71] W. Cai, P. Pillay, and Z. Tang, "Impact of stator windings and end-bells on resonant frequencies and mode shapes of switched reluctance motors," *IEEE Transactions on Industry Applications*, vol. 38, no. 4, pp. 1027–1036, Jul. 2002.

[72] S. Long, Z. Zhu, and D. Howe, "Vibration behaviour of stators of switched reluctance motors," *Electric Power Applications, IEE Proceedings* -, vol. 148, no. 3, pp. 257–264, May 2001.

[73] S. Noda, S. Mori, F. Ishibashi, and K. Itomi, "Effect of Coils on Natural Frequencies of Stator Cores in Small Induction Motors," *IEEE Transactions on Energy Conversion*, vol. EC-2, no. 1, pp. 93–99, Mar. 1987.

[74] K. Itori, S. Noda, F. Ishibashi, and H. Yamawaki, "Young's modulus of windings on finite element method for natural frequency analysis of stator core in induction motor," *Transactions of the Japan Society of Mechanical Engineers*, vol. 68, no. 669, pp. 1–6, 2002.

[75] M. van der Giet, K. Kasper, R. De Doncker, and K. Hameyer, "Material parameters for the structural dynamic simulation of electrical machines," in *2012 XXth International Conference on Electrical Machines (ICEM)*, Sep. 2012, pp. 2994–3000.

[76] J. D. Widmer, R. Martin, and B. C. Mecrow, "Precompressed and stranded aluminum motor windings for traction motors," *IEEE Transactions on Industry Applications*, vol. 52, no. 3, pp. 2215–2223, May 2016.

[77] M. C. Kulan, N. J. Baker, and J. D. Widmer, "Design and analysis of compressed windings for a permanent magnet integrated starter generator," *IEEE Transactions on Industry Applications*, vol. PP, no. 99, pp. 1–1, 2017.

[78] S. D. Garvey, "The vibrational behaviour of laminated components in electrical machines," in *1989 Fourth International Conference on Electrical Machines and Drives Conf. Publ. No. ??)*, Sep 1989, pp. 226–231.

[79] R. M. Jones, *Mechanics Of Composite Materials*, 2nd ed. Philadelphia, PA: CRC Press, Jul. 1998.

[80] Z. Gurdal, R. T. Haftka, and P. Hajela, *Design and Optimization of Laminated Composite Materials*. John Wiley & Sons, Jan. 1999.

[81] Z. Tang, P. Pillay, and A. Omekanda, "Vibration prediction in switched reluctance motors with transfer function identification from shaker and force hammer tests," *IEEE Transactions on Industry Applications*, vol. 39, no. 4, pp. 978–985, Jul. 2003.

[82] W. Cai, P. Pillay, Z. Tang, and A. Omekanda, "Vibration measurements in the switched reluctance motor," in *Conference Record of the 2001 IEEE Industry*

Applications Conference, 2001. Thirty-Sixth IAS Annual Meeting, vol. 1, Sep. 2001, pp. 11–17 vol.1.

[83] Z. Tang, P. Pillay, and A. Omekanda, "Analysis of mounting effects on vibrations of switched reluctance motors," in *Electric Machines and Drives Conference, 2003. IEMDC'03. IEEE International*, vol. 1, Jun. 2003, pp. 97–103 vol.1.

[84] K. W. Klontz and H. Li, "Reducing core loss of segmented laminations," in *Power Transmission Engineering 2009*, vol. 3, oct 2009, pp. 26–32.

[85] B. C. Mecrow and A. G. Jack, "The modelling of segmented laminations in three dimensional eddy current calculations," *IEEE Transactions on Magnetics*, vol. 28, no. 2, pp. 1122–1125, Mar 1992.

[86] J. L. Besnerais, "Effect of lamination asymmetries on magnetic vibrations and acoustic noise in synchronous machines," in *2015 18th International Conference on Electrical Machines and Systems (ICEMS)*, Oct 2015, pp. 1729–1733.

[87] D. Miyagi, K. Miki, M. Nakano, and N. Takahashi, "Influence of compressive stress on magnetic properties of laminated electrical steel sheets," *IEEE Transactions on Magnetics*, vol. 46, no. 2, pp. 318–321, Feb 2010.

[88] L. Bernard and L. Daniel, "Effect of stress on magnetic hysteresis losses in a switched reluctance motor: Application to stator and rotor shrink fitting," *IEEE Transactions on Magnetics*, vol. 51, no. 9, pp. 1–13, Sept 2015.

[89] R. Wrobel, P. H. Mellor, and D. Holliday, "Thermal modeling of a segmented stator winding design," *IEEE Transactions on Industry Applications*, vol. 47, no. 5, pp. 2023–2030, Sept 2011.

[90] A. Sakuma, M. Kadowaki, H. Ukigai, I. Miki, T. Okamoto, and T. Segawa, "Stator structure for noise reduction of switched reluctance motor," in *2012 15th International Conference on Electrical Machines and Systems (ICEMS)*, Oct 2012, pp. 1–4.

[91] T. Kotegawa and I. Miki, "Stator structure for reducing noise in switched reluctance motor," in *2013 15th European Conference on Power Electronics and Applications (EPE)*, Sept 2013, pp. 1–9.

[92] D. Miyagi, N. Maeda, Y. Ozeki, K. Miki, and N. Takahashi, "Estimation of iron loss in motor core with shrink fitting using fem analysis," *IEEE Transactions on Magnetics*, vol. 45, no. 3, pp. 1704–1707, March 2009.

[93] A. J. Moses and H. Rahmatizadeh, "Effects of stress on iron loss and flux distribution of an induction motor stator core," *IEEE Transactions on Magnetics*, vol. 25, no. 5, pp. 4003–4005, Sep 1989.

[94] K. Fujisaki and S. Satoh, "Numerical calculations of electromagnetic fields in silicon steel under mechanical stress," *IEEE Transactions on Magnetics*, vol. 40, no. 4, pp. 1820–1825, July 2004.

[95] R. A. Serway, *Physics for scientists and engineers*, 4th ed., ser. Saunders golden sunburst series. Philadelphia: Saunders College Pub., 1996.

[96] A. Klein-Hessling, A. Hofmann, and R. W. D. Doncker, "Direct instantaneous torque and force control: A novel control approach for switched reluctance machines," in *2015 IEEE International Electric Machines Drives Conference (IEMDC)*, May 2015, pp. 922–928.

[97] N. Kurihara, J. Bayless, H. Sugimoto, and A. Chiba, "Noise reduction of switched reluctance motor with high number of poles by novel simplified current waveform at low speed and low torque region," *IEEE Transactions on Industry Applications*, vol. 52, no. 4, pp. 3013–3021, July 2016.

[98] J. Bayless, N. Kurihara, H. Sugimoto, and A. Chiba, "Acoustic noise reduction of switched reluctance motor with reduced rms current and enhanced efficiency," *IEEE Transactions on Energy Conversion*, vol. 31, no. 2, pp. 627–636, June 2016.

[99] D. Panda and V. Ramanarayanan, "Reduced acoustic noise variable dc-bus-voltage-based sensorless switched reluctance motor drive for hvac applica-

tions," *IEEE Transactions on Industrial Electronics*, vol. 54, no. 4, pp. 2065–2078, Aug 2007.

[100] H. Makino, T. Kosaka, and N. Matsui, "Digital pwm-control-based active vibration cancellation for switched reluctance motors," *IEEE Transactions on Industry Applications*, vol. 51, no. 6, pp. 4521–4530, Nov 2015.

[101] A. Tanabe and K. Akatsu, "Vibration reduction method in srm with a smoothing voltage commutation by pwm," in *2015 9th International Conference on Power Electronics and ECCE Asia (ICPE-ECCE Asia)*, June 2015, pp. 600–604.

[102] S. A. Long, Z. Q. Zhu, and D. Howe, "Effectiveness of active noise and vibration cancellation for switched reluctance machines operating under alternative control strategies," *IEEE Transactions on Energy Conversion*, vol. 20, no. 4, pp. 792–801, Dec 2005.

[103] Z. Q. Zhu, X. Liu, and Z. Pan, "Analytical model for predicting maximum reduction levels of vibration and noise in switched reluctance machine by active vibration cancellation," *IEEE Transactions on Energy Conversion*, vol. 26, no. 1, pp. 36–45, March 2011.

Appendix A.
Extended Results of Chapter 2

A.1 Simulation Models

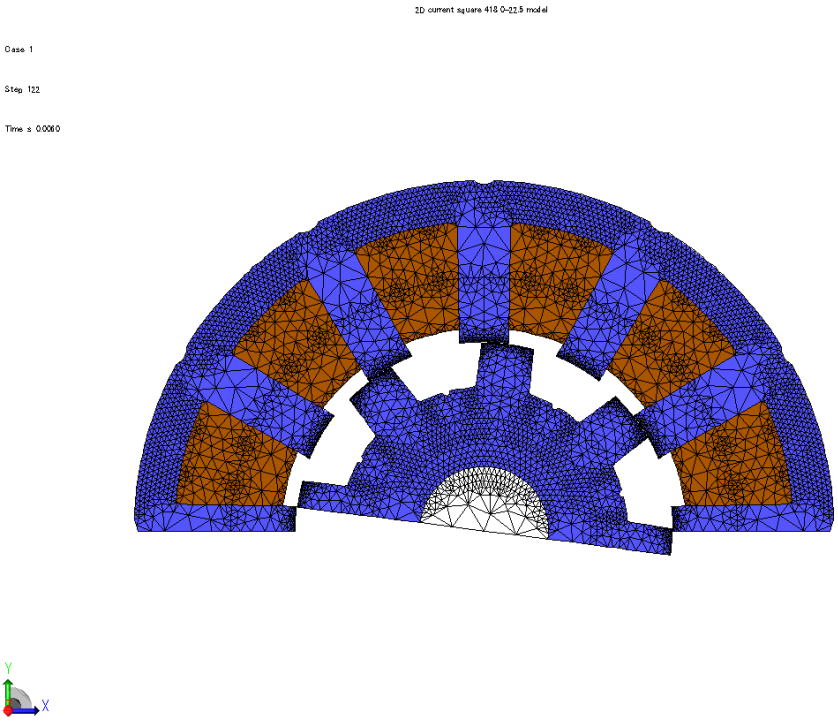

Figure A.1: Meshing of the 2D 12/8 conventional SRM model

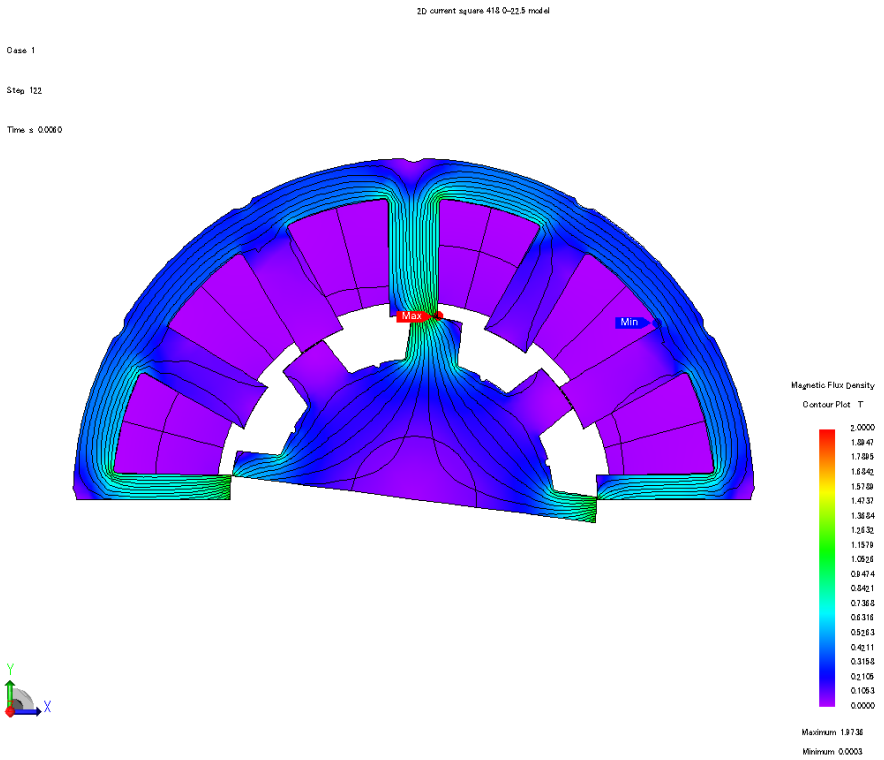

Figure A.2: Flux density and flux line of the 2D 12/8 conventional SRM model

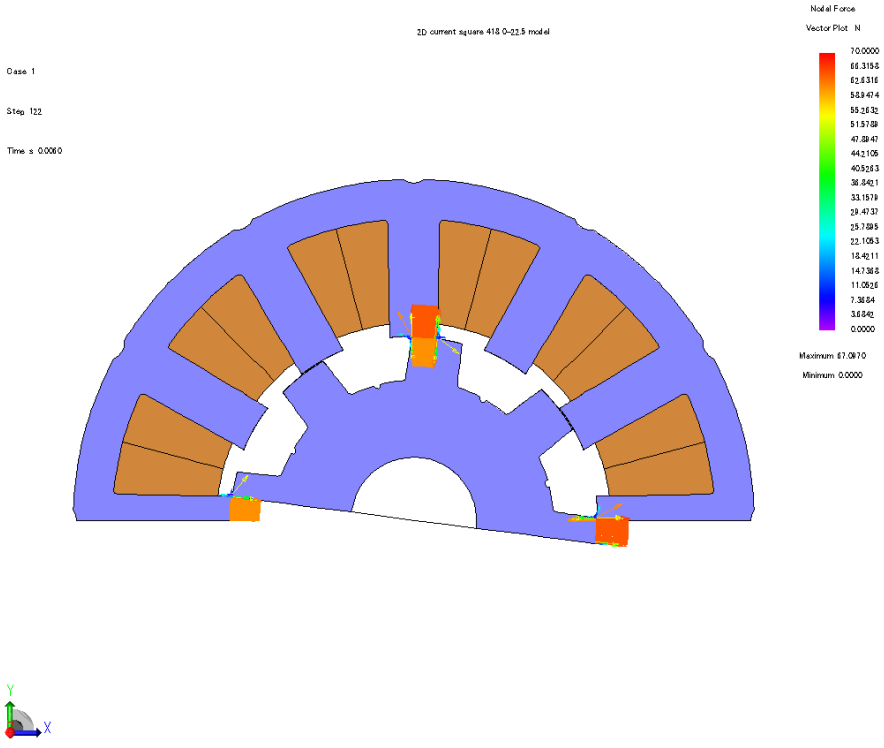

Figure A.3: Magnetic force distribution of the 2D 12/8 conventional SRM model

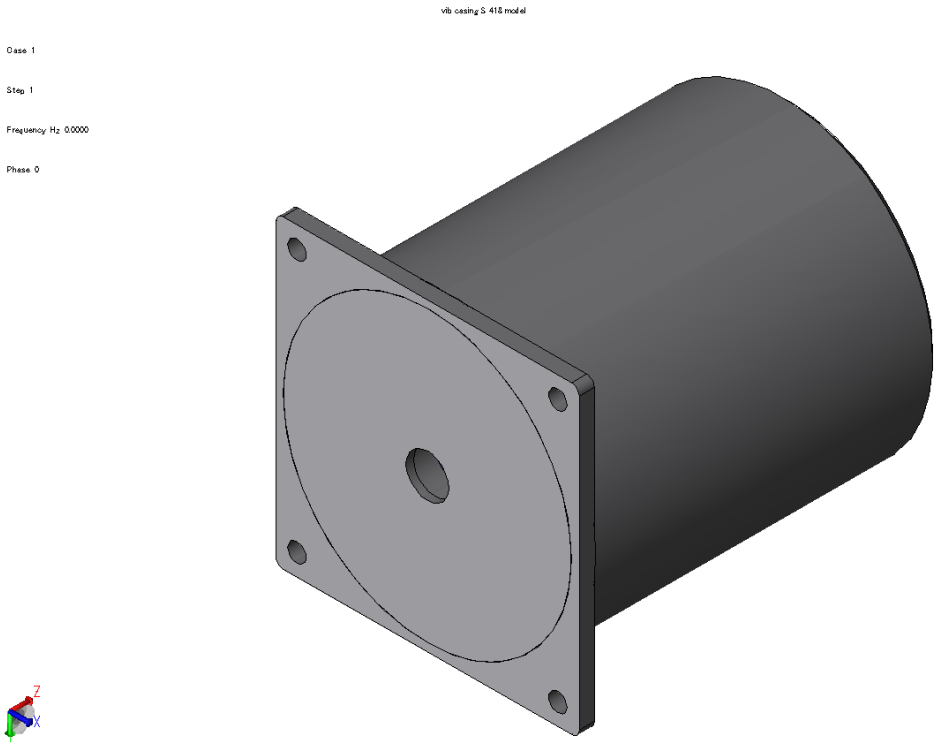

Figure A.4: Frame of the 3D 12/8 conventional SRM model

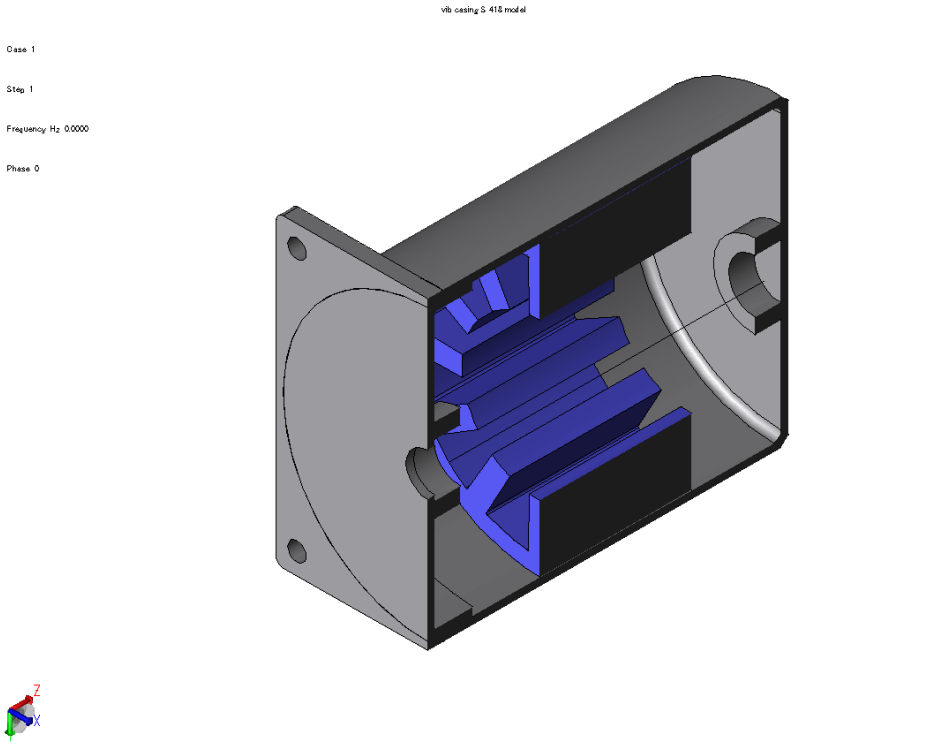

Figure A.5: Cross-section of the 3D 12/8 SRM (frame and stator) model

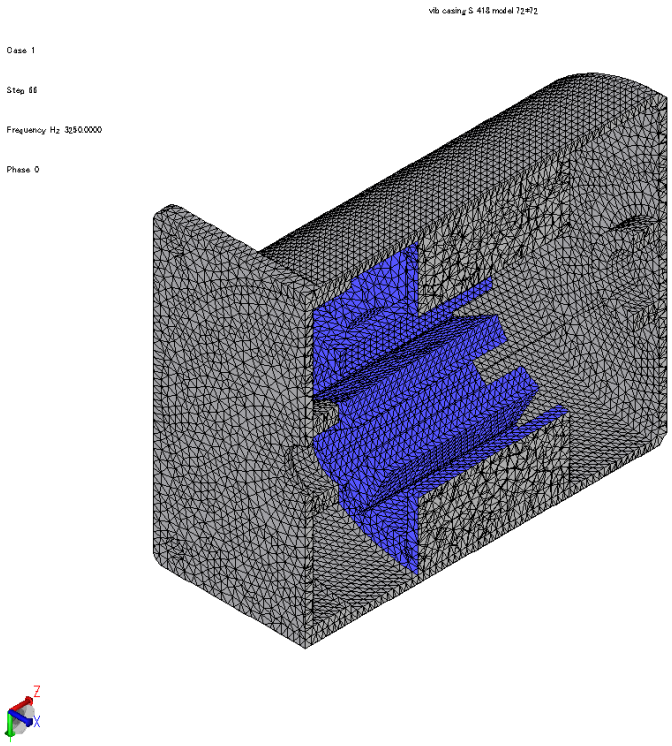

Figure A.6: Meshing of the 3D 12/8 conventional SRM (frame and stator) model

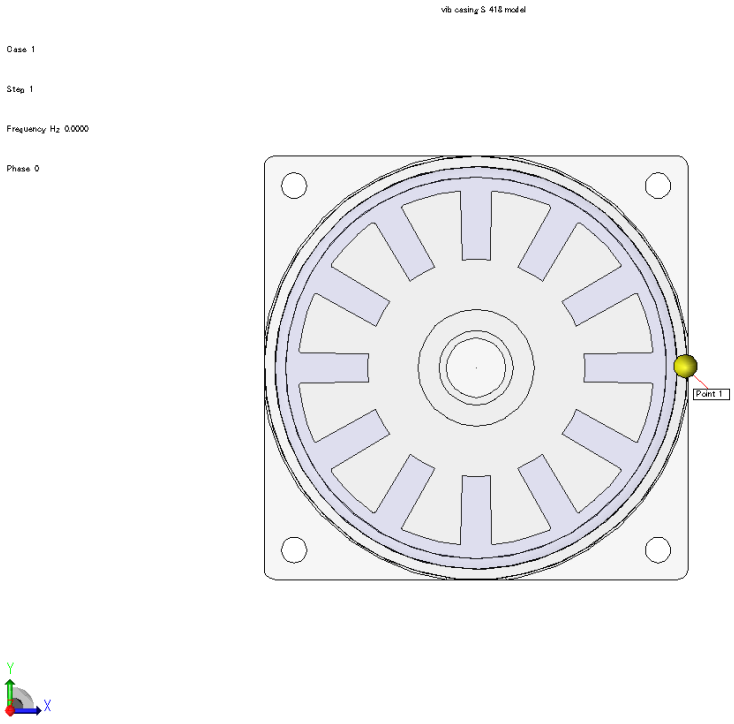

Figure A.7: Probing point of acceleration of the 3D 12/8 conventional SRM model

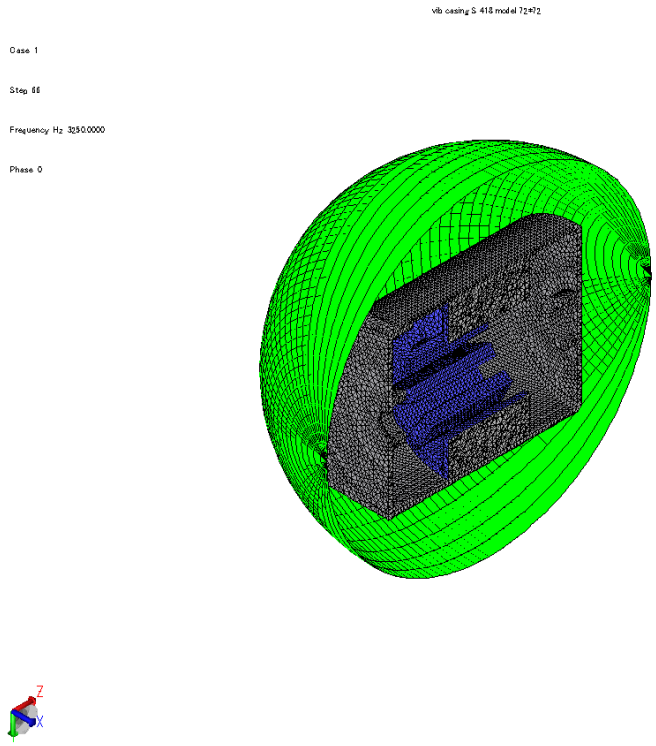

Figure A.8: Meshing for sound pressure analysis of the 3D 12/8 SRM model

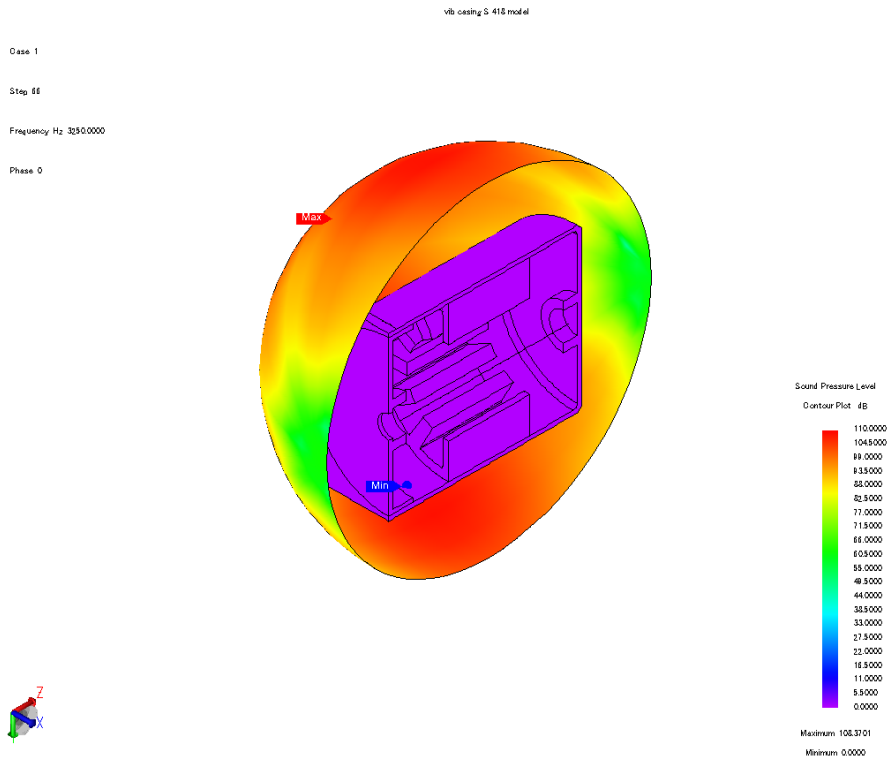

Figure A.9: Sound pressure distribution of the 3D 12/8 conventional SRM model

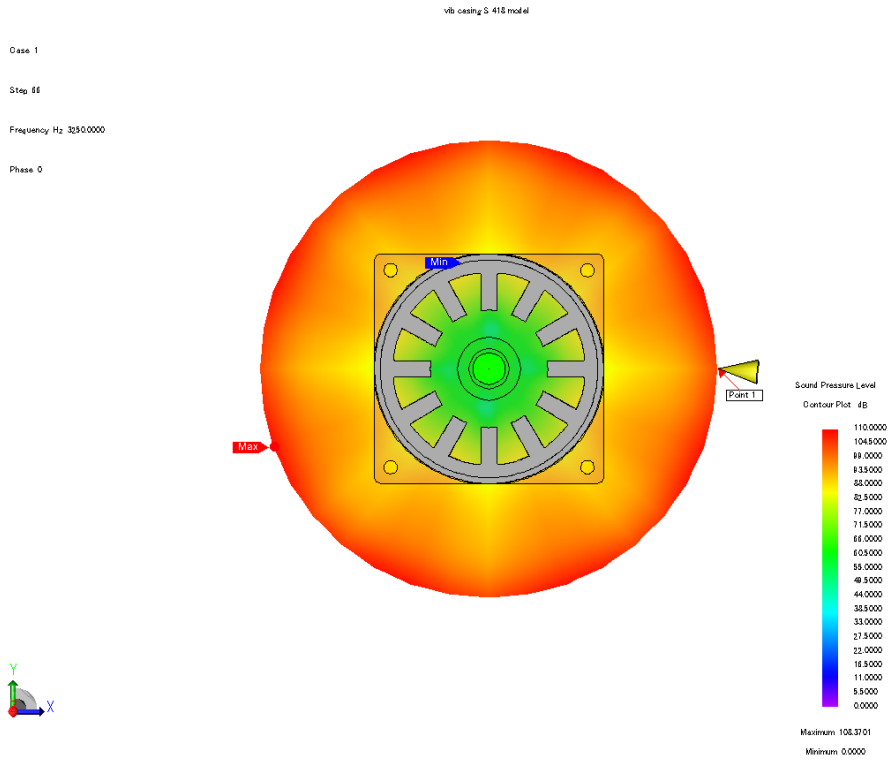

Figure A.10: Probing point of sound pressure level of the 3D 12/8 SRM model

A.2 Simulation Results

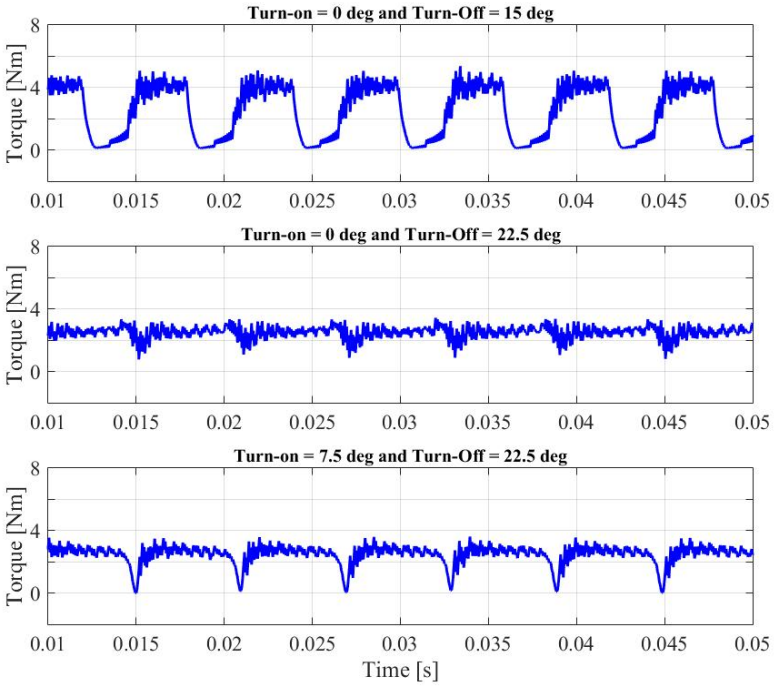

Figure A.11: Total torque of different turn-on and turn-off angles at 418 r/min

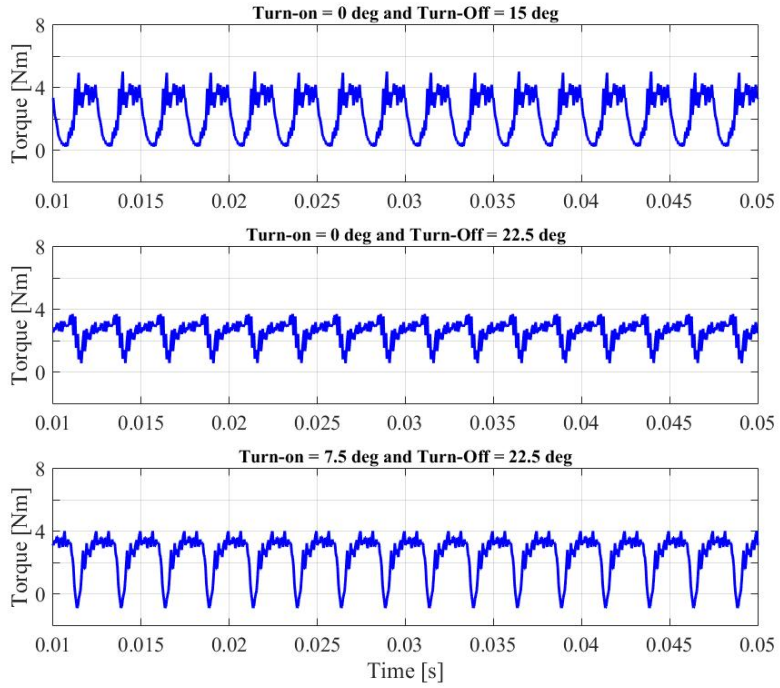

Figure A.12: Total torque of different turn-on and turn-off angles at 1000 r/min

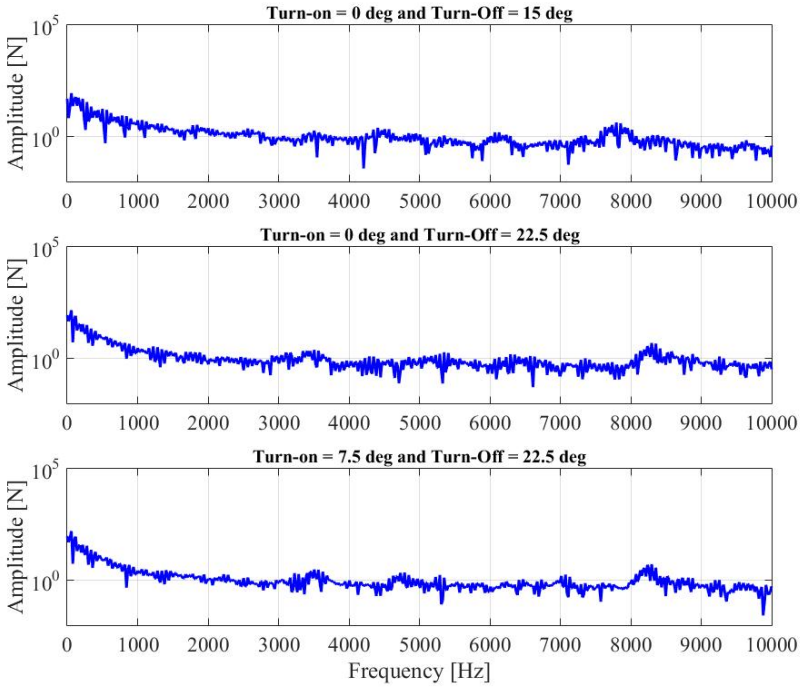

Figure A.13: Radial forces acting on the single stator pole in frequency domain of different turn-on and turn-off angles at 418 r/min

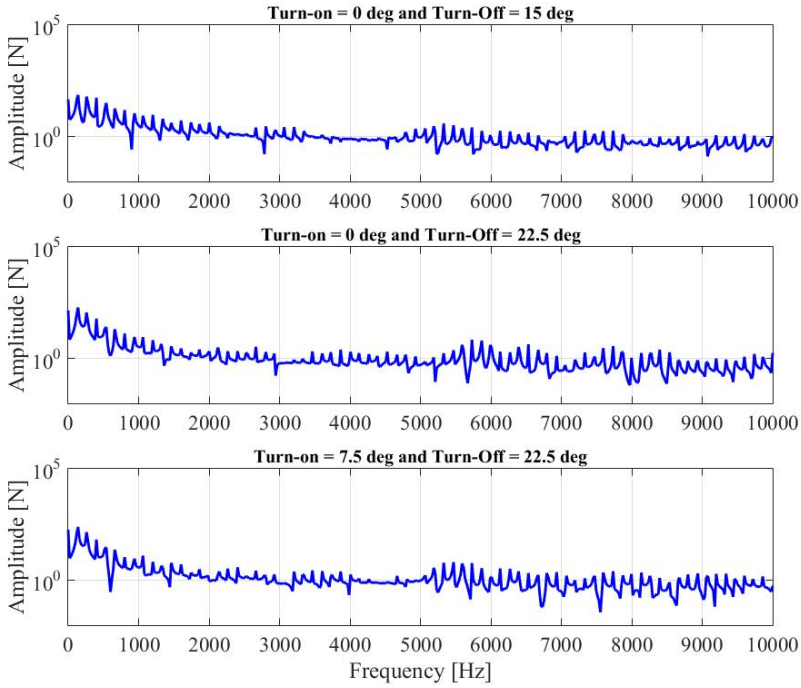

Figure A.14: Radial forces acting on the single stator pole in frequency domain of different turn-on and turn-off angles at 1000 r/min

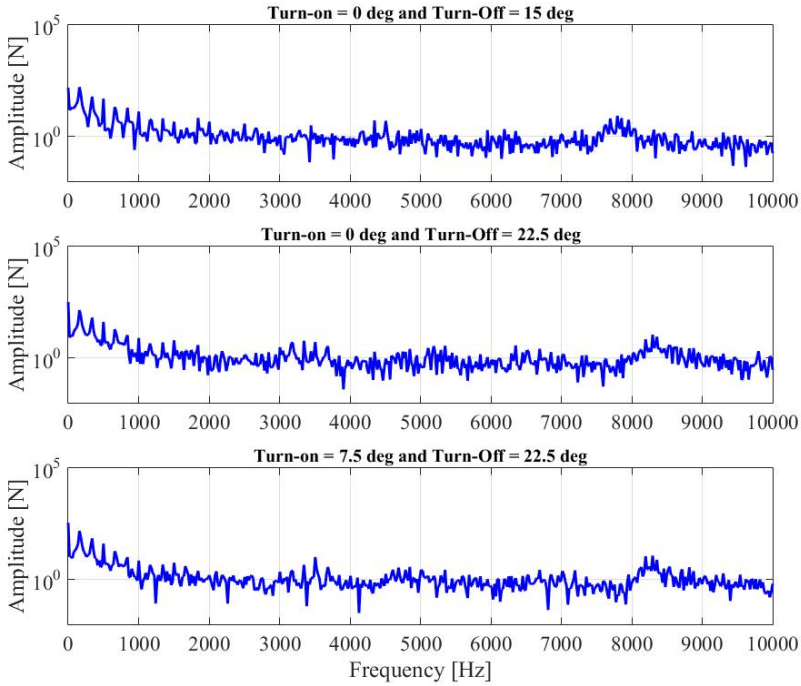

Figure A.15: Sum of radial forces on the stator in frequency domain of different turn-on and turn-off angles at 418 r/min

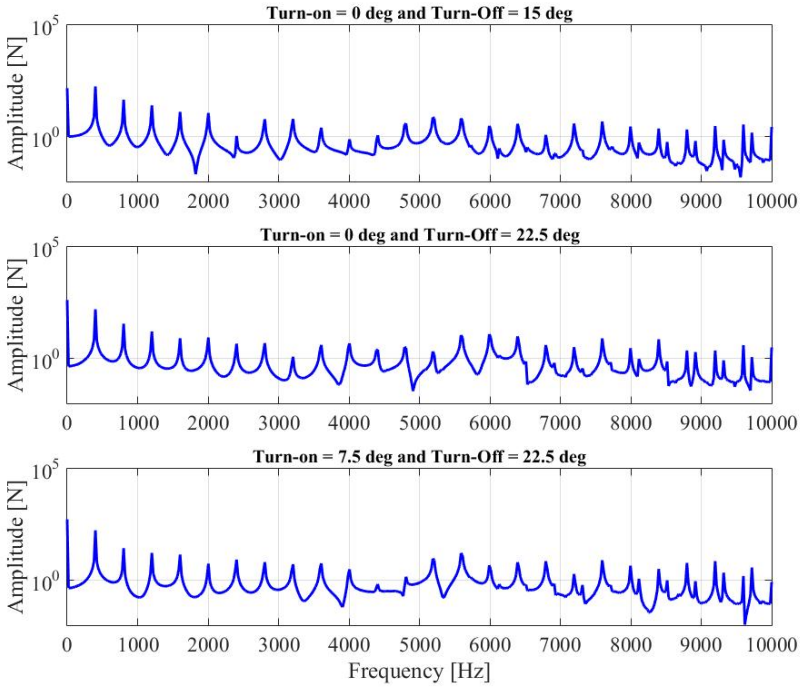

Figure A.16: Sum of radial forces on the stator in frequency domain of different turn-on and turn-off angles at 1000 r/min

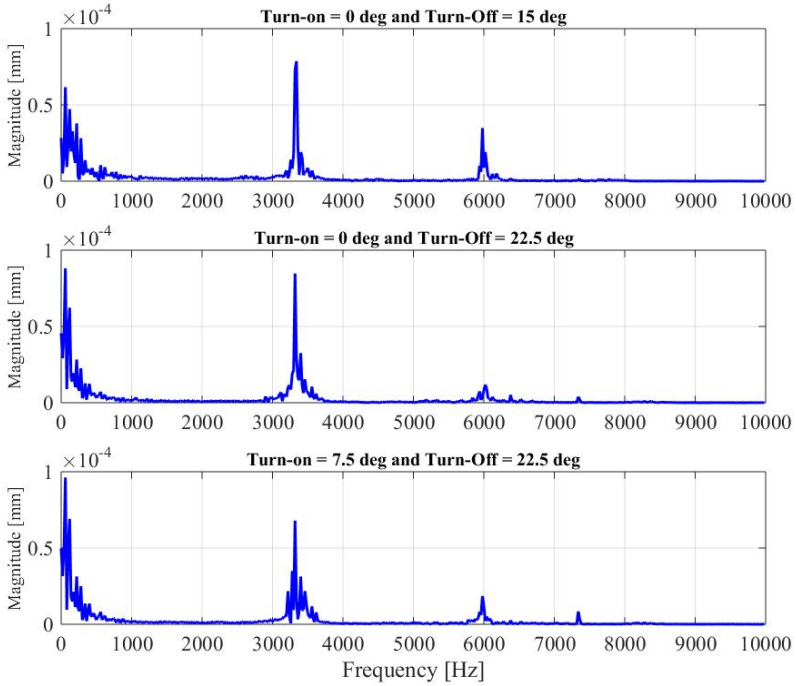

Figure A.17: Magnitude of displacement of three different turn-on and turn-off angles at 418 r/min

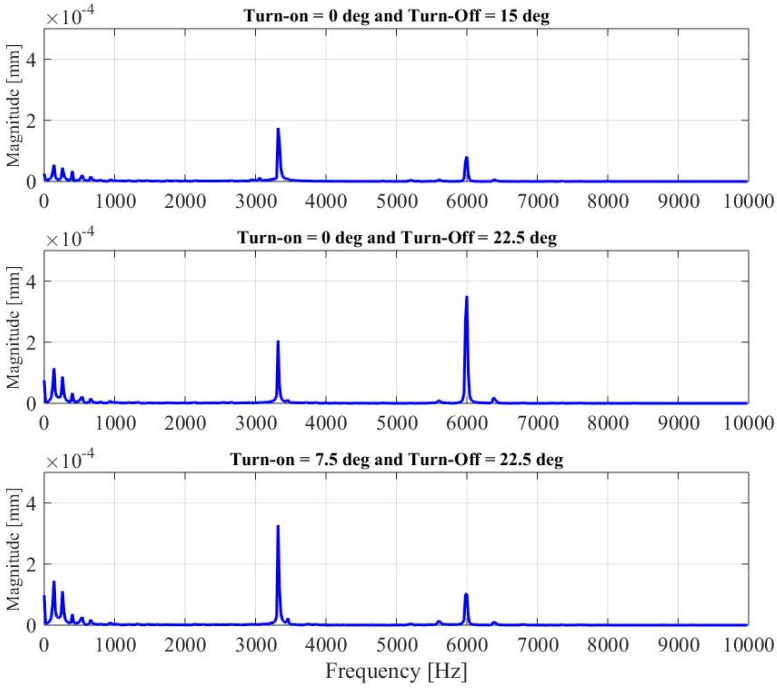

Figure A.18: Magnitude of displacement of three different turn-on and turn-off angles at 1000 r/min

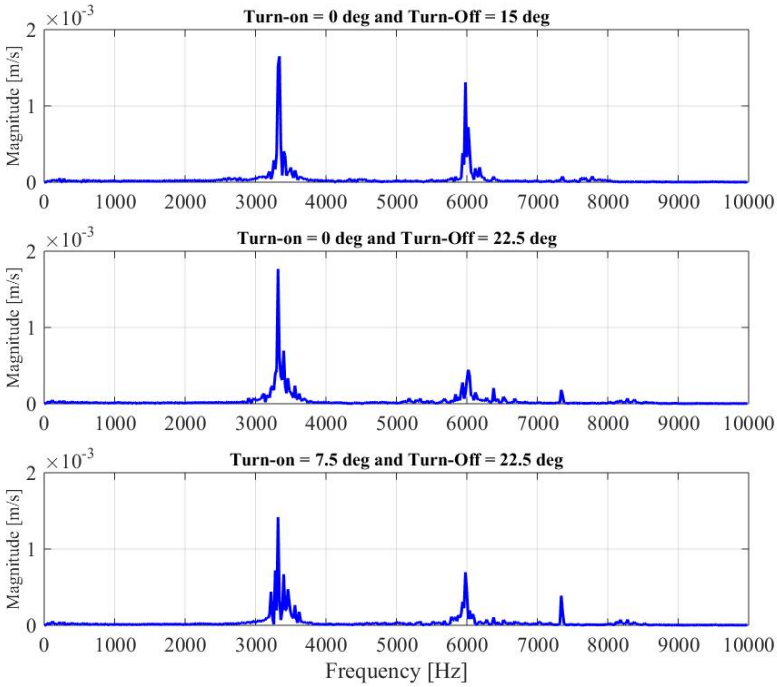

Figure A.19: Magnitude of velocity of different turn-on and turn-off angles at 418 r/min

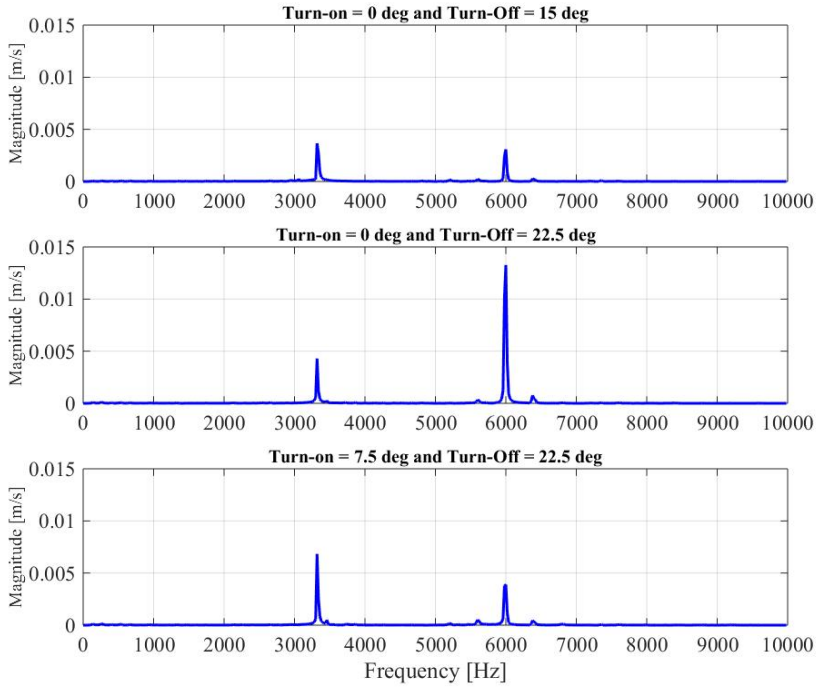

Figure A.20: Magnitude of velocity of different turn-on and turn-off angles at 1000 r/min

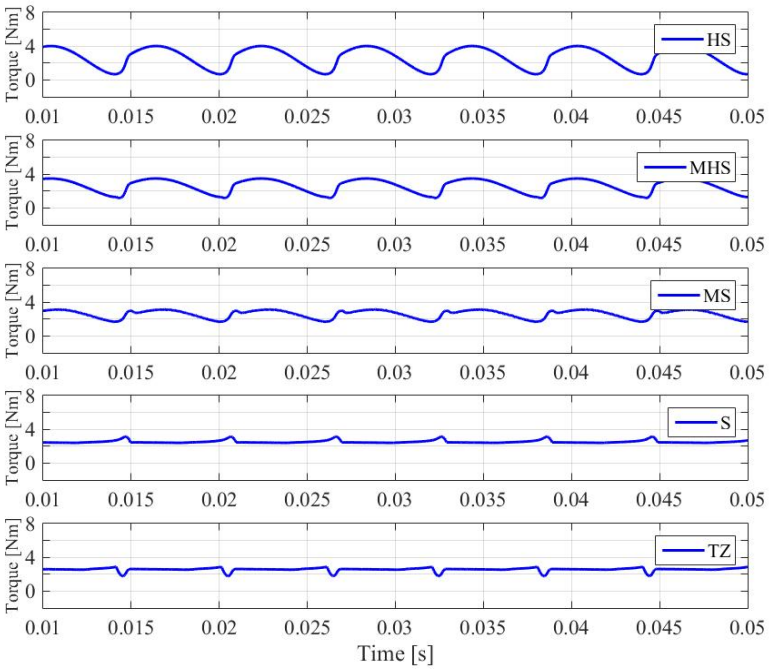

Figure A.21: Total torque of different current shapes at 418 r/min

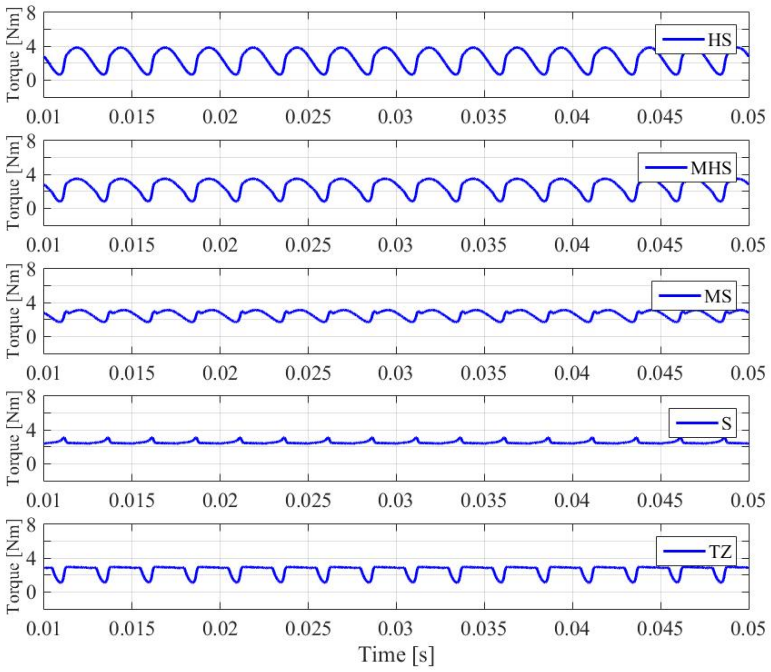

Figure A.22: Total torque of different current shapes at 1000 r/min

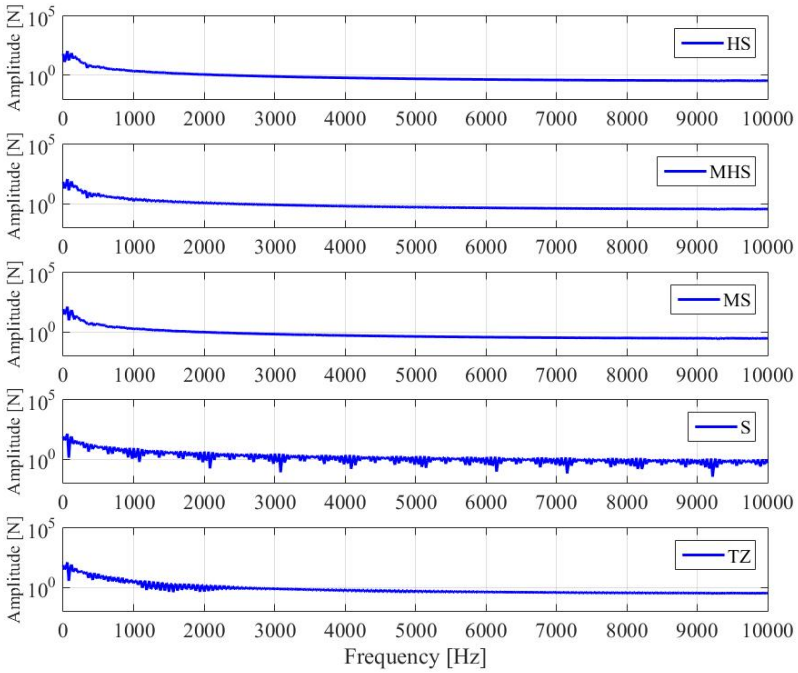

Figure A.23: Radial forces acting on the single stator pole in frequency domain of different current shapes at 418 r/min

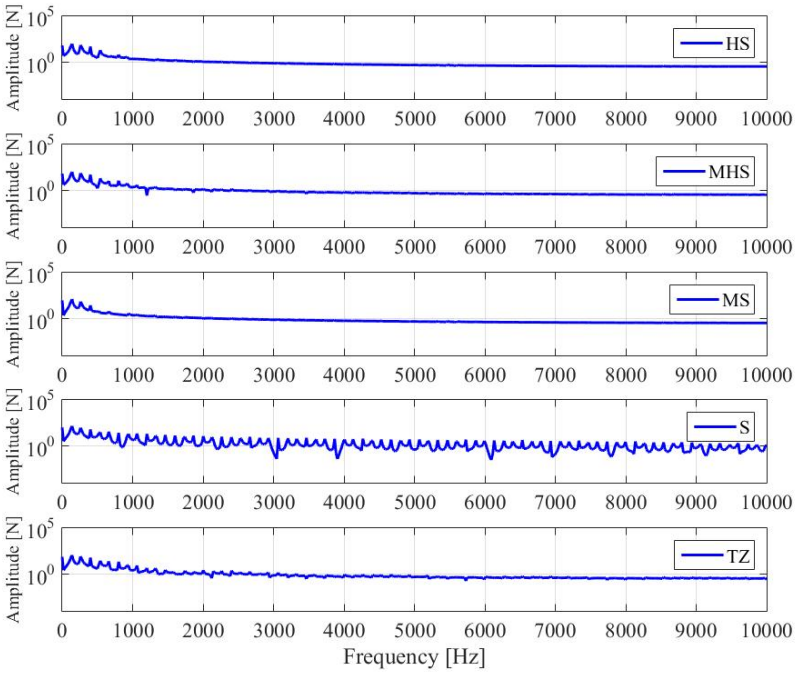

Figure A.24: Radial forces acting on the single stator pole in frequency domain of different current shapes at 1000 r/min

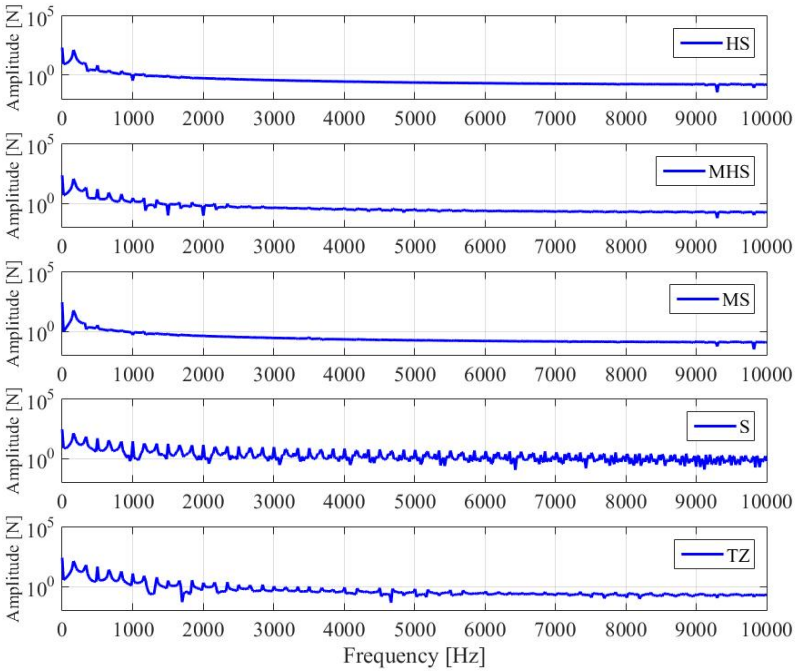

Figure A.25: Sum of radial forces on the stator in frequency domain of different current shapes at 418 r/min

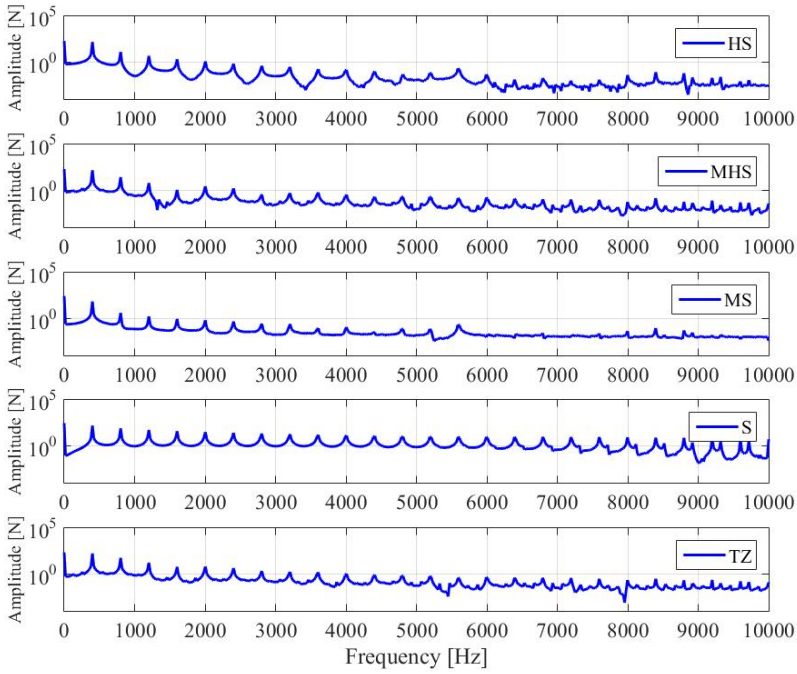

Figure A.26: Sum of radial forces on the stator in frequency domain of different current shapes at 1000 r/min

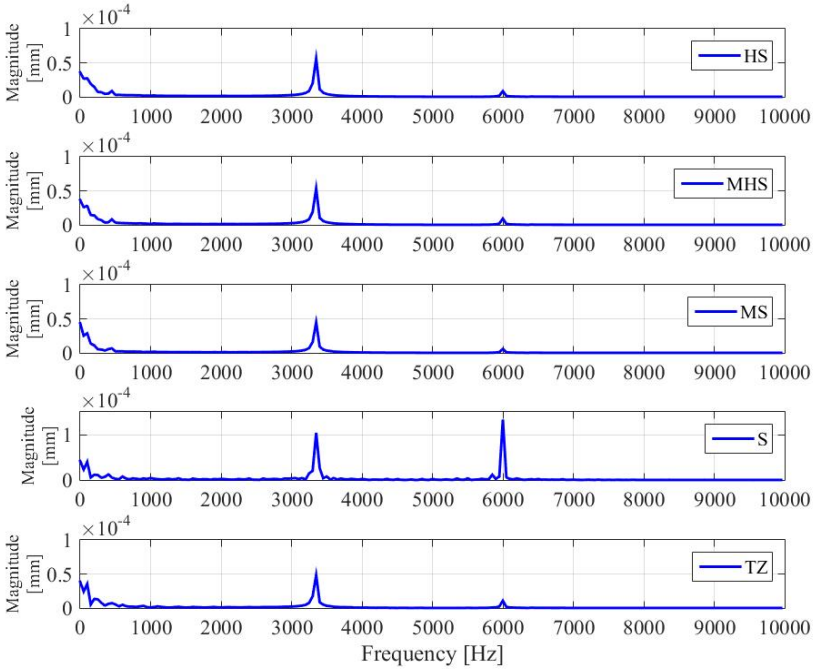

Figure A.27: Magnitude of displacement of different current shapes at 418 r/min

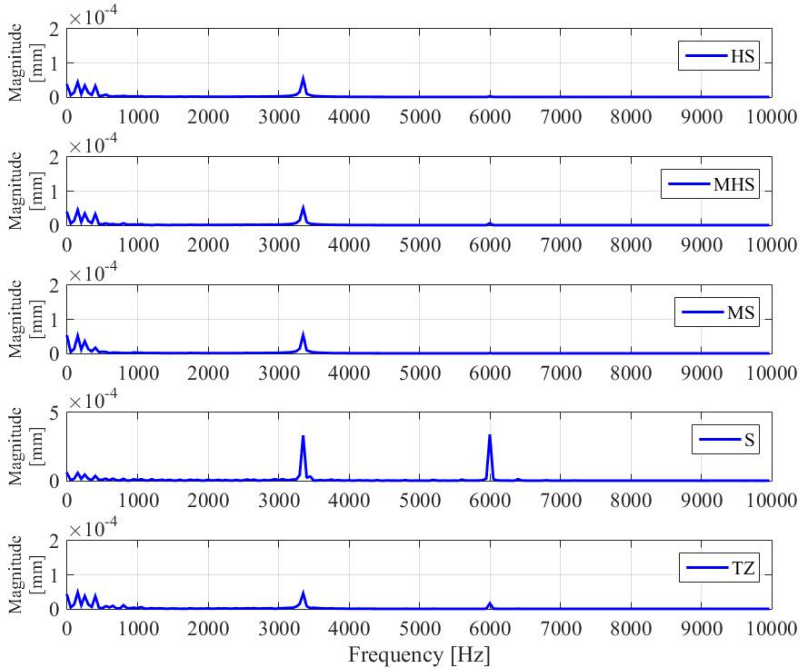

Figure A.28: Magnitude of displacement of different current shapes at 1000 r/mine

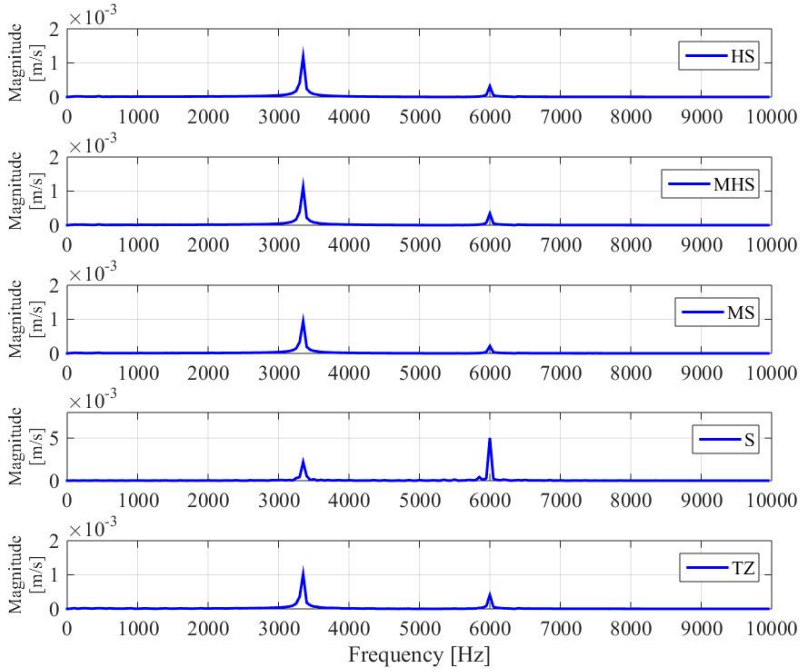

Figure A.29: Magnitude of velocity of different current shapes at 418 r/min

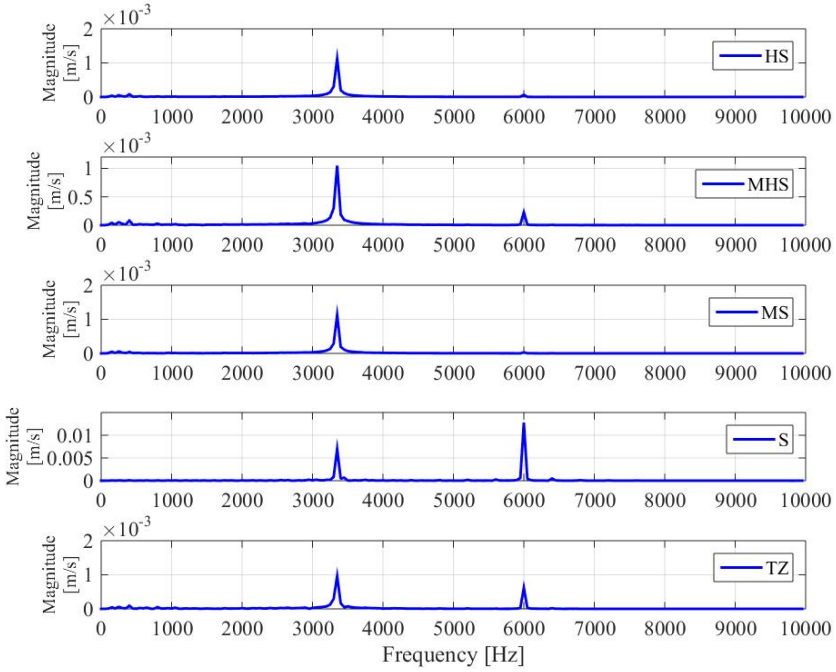

Figure A.30: Magnitude of velocity of different current shapes at 1000 r/min

Appendix B. Extended Results of Chapter 3

B.1 Simulation Models

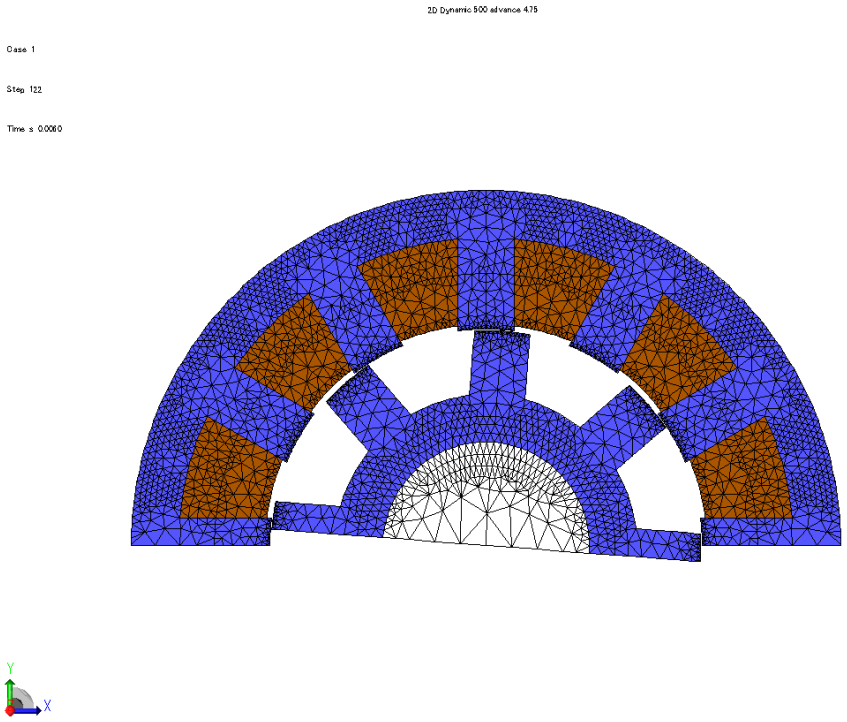

Figure B.1: Meshing of the 2D 12/8 CON SP model

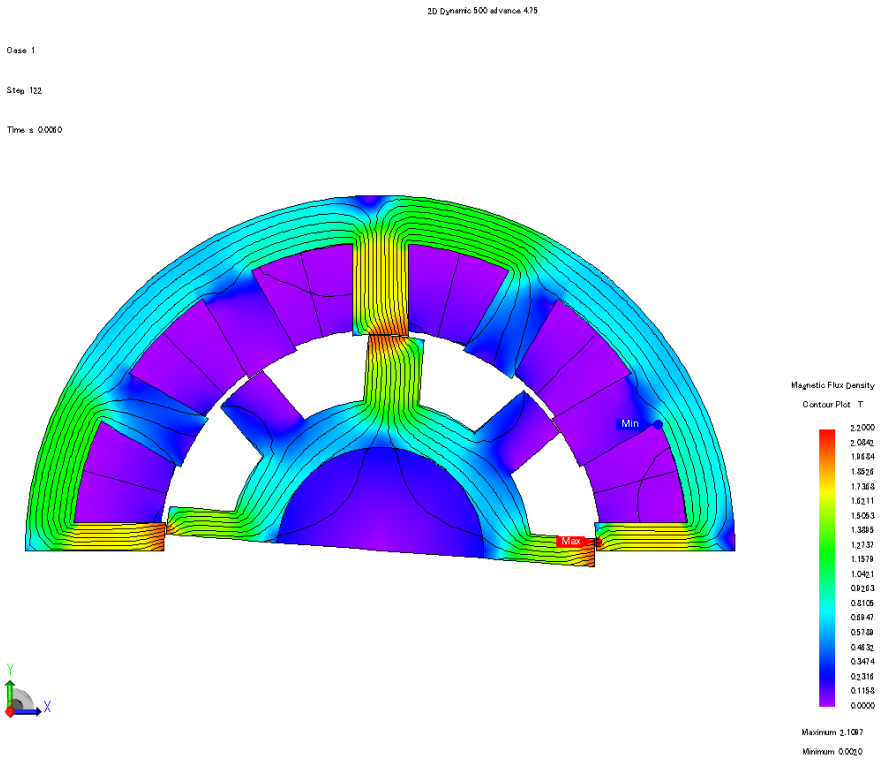

Figure B.2: Flux density and flux line of the 2D 12/8 CON SP model

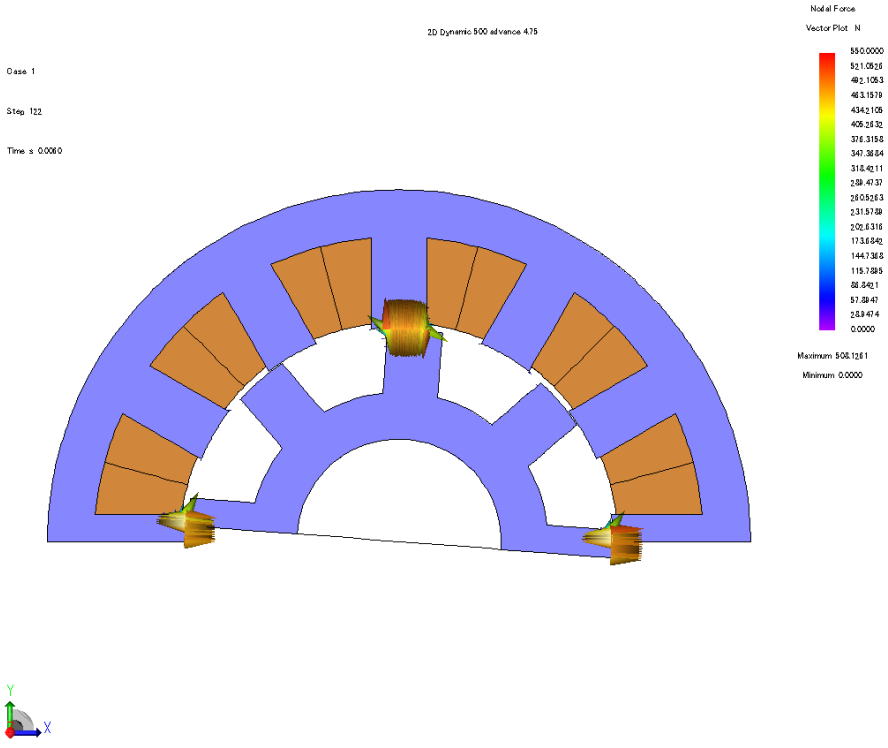

Figure B.3: Magnetic force distribution of the 2D 12/8 CON SP model

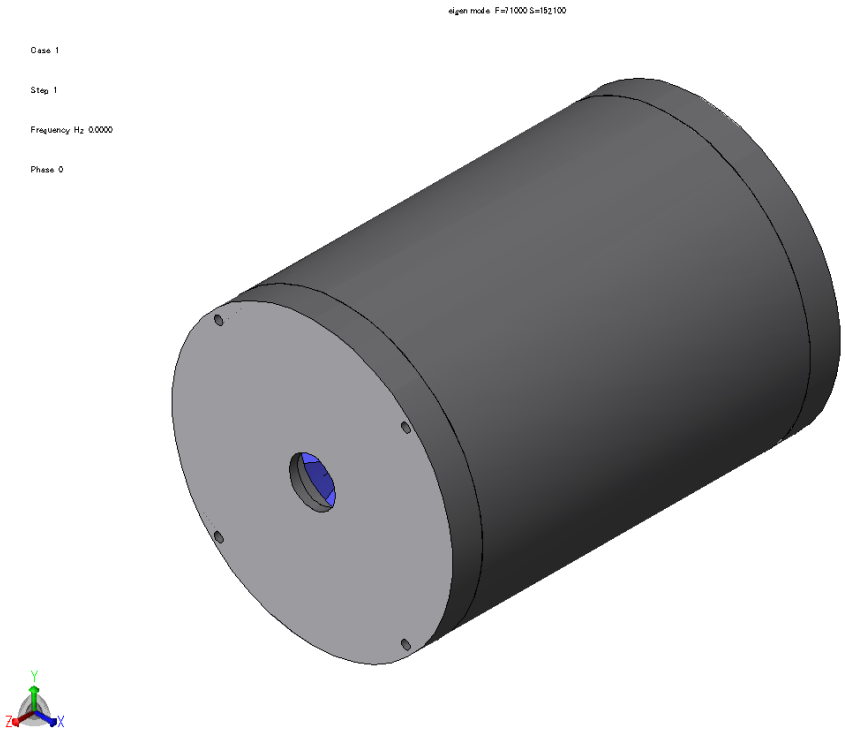

Figure B.4: Frame of the 3D 12/8 CON SP model

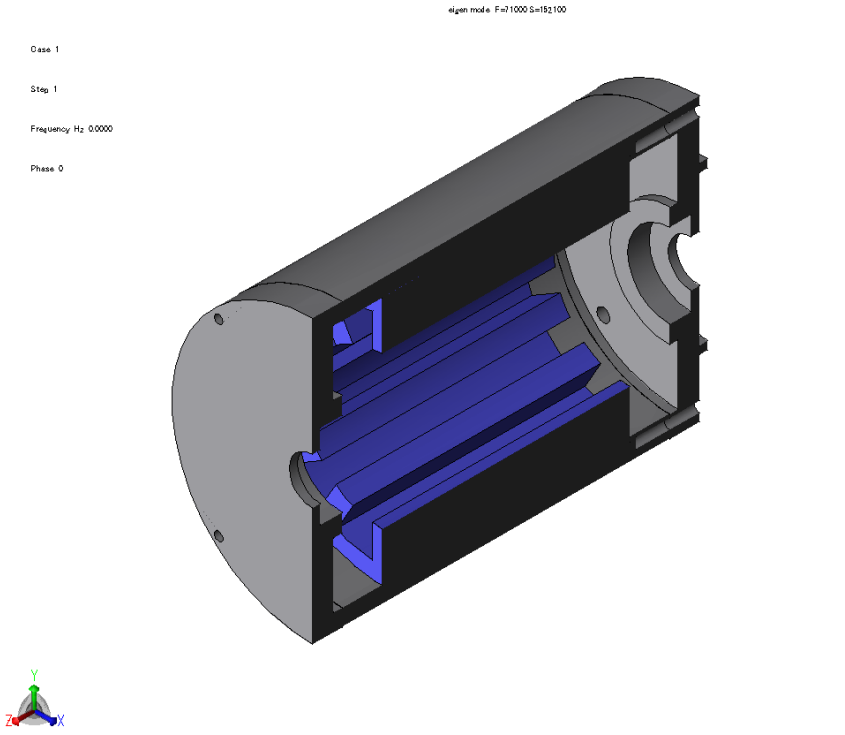

Figure B.5: Cross-section of the 3D 12/8 CON SP (frame and stator) model

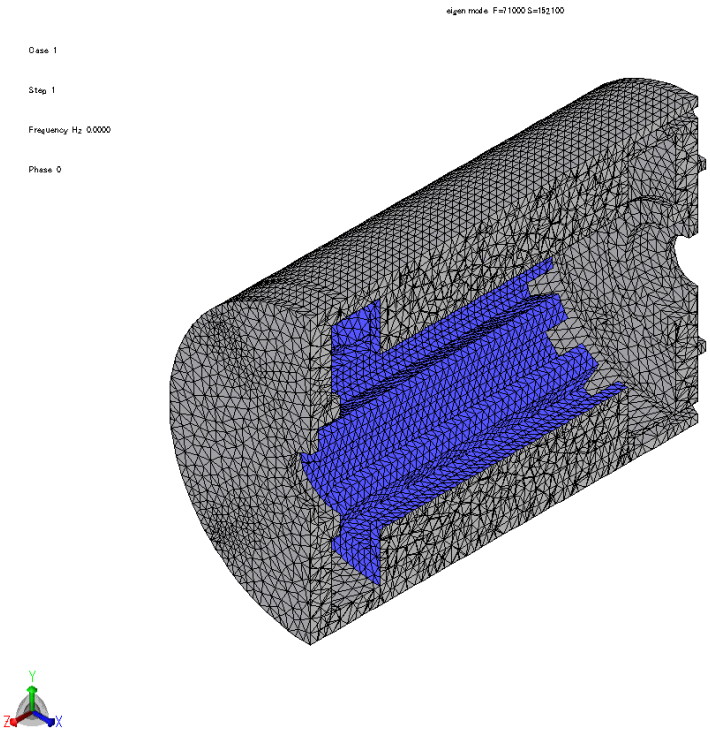

Figure B.6: Meshing of the 3D 12/8 CON SP (frame and stator) model

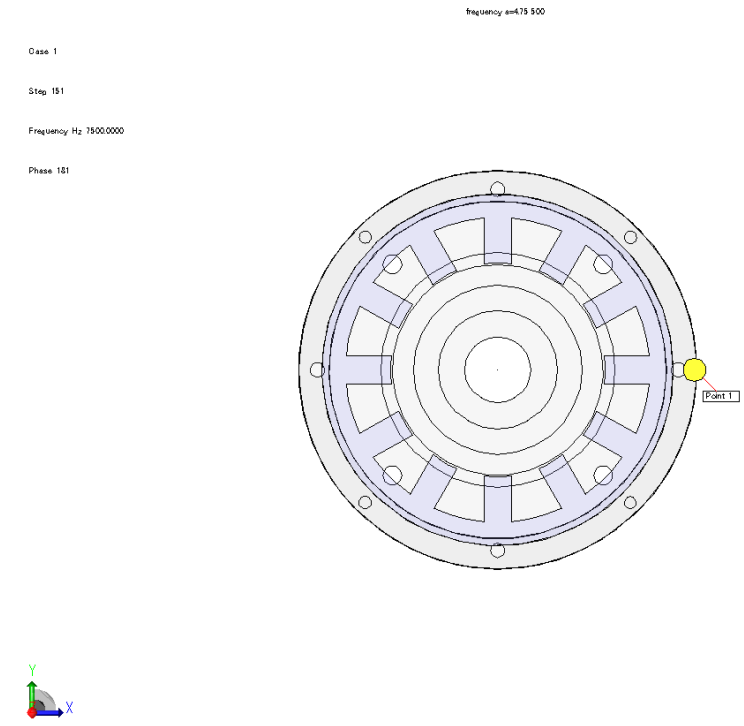

Figure B.7: Probing point of acceleration of the 3D 12/8 CON SP model

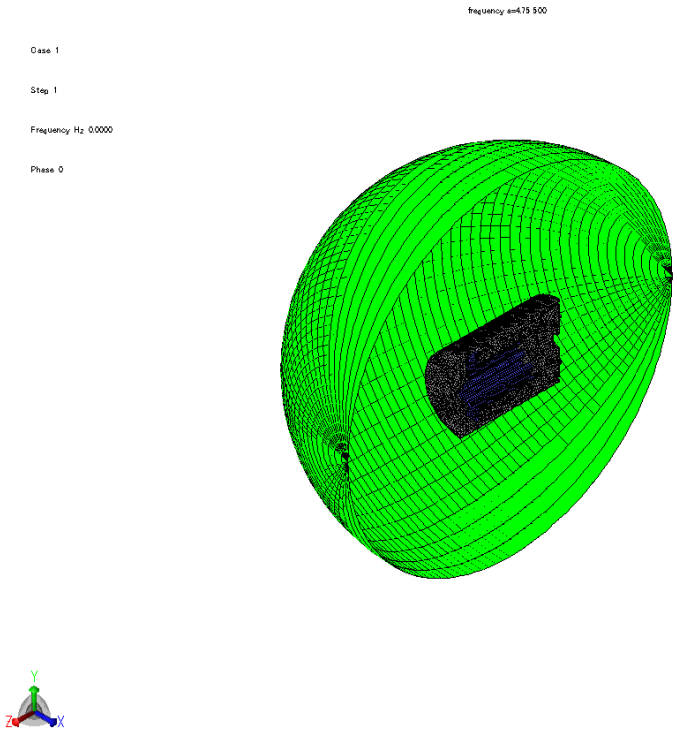

Figure B.8: Meshing for sound pressure analysis of the 3D 12/8 CON SP model

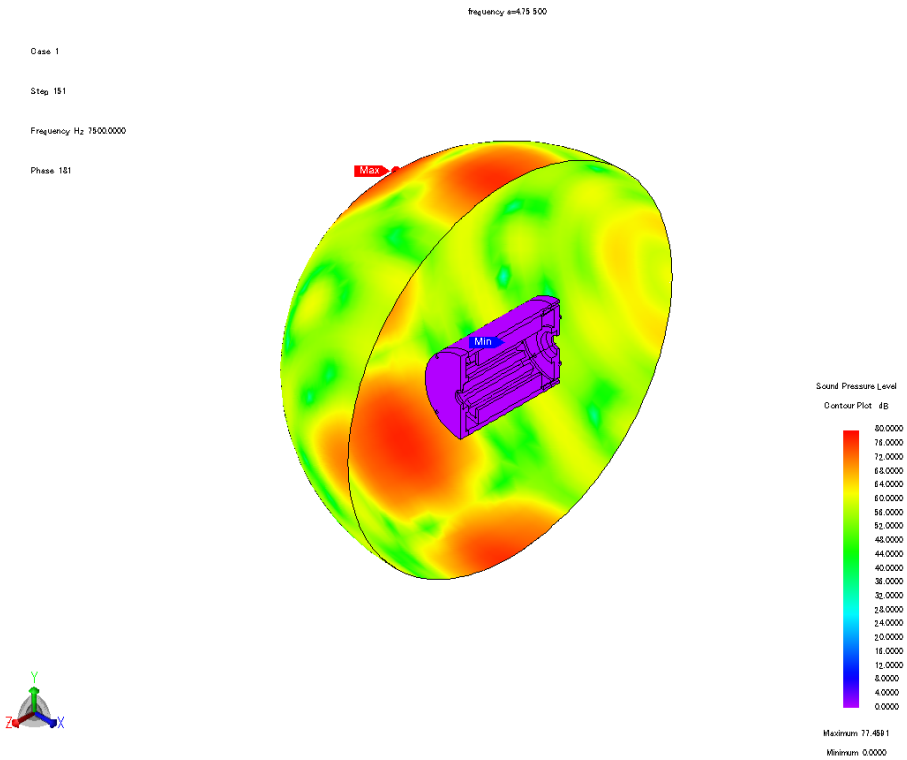

Figure B.9: Sound pressure distribution of the 3D 12/8 CON SP model

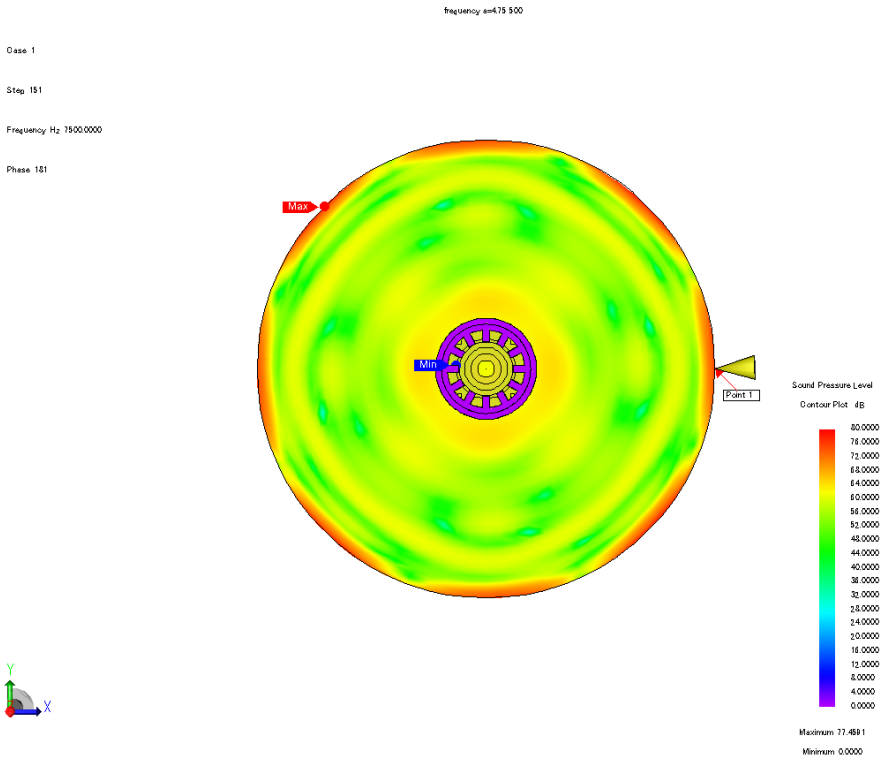

Figure B.10: Probing point of sound pressure level of the 3D 12/8 CON SP model

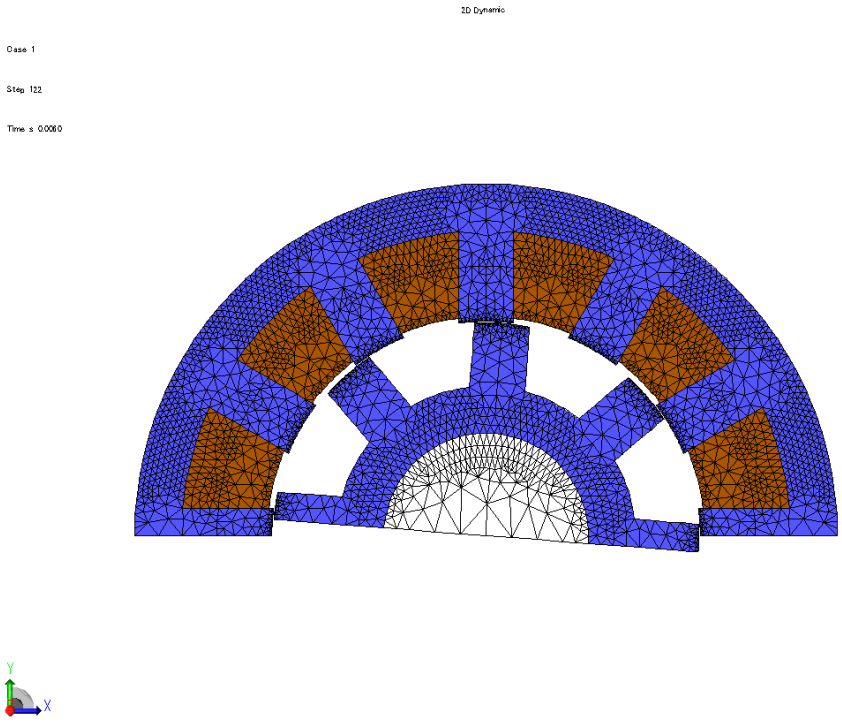

Figure B.11: Meshing of the 2D 12/8 CON FP model

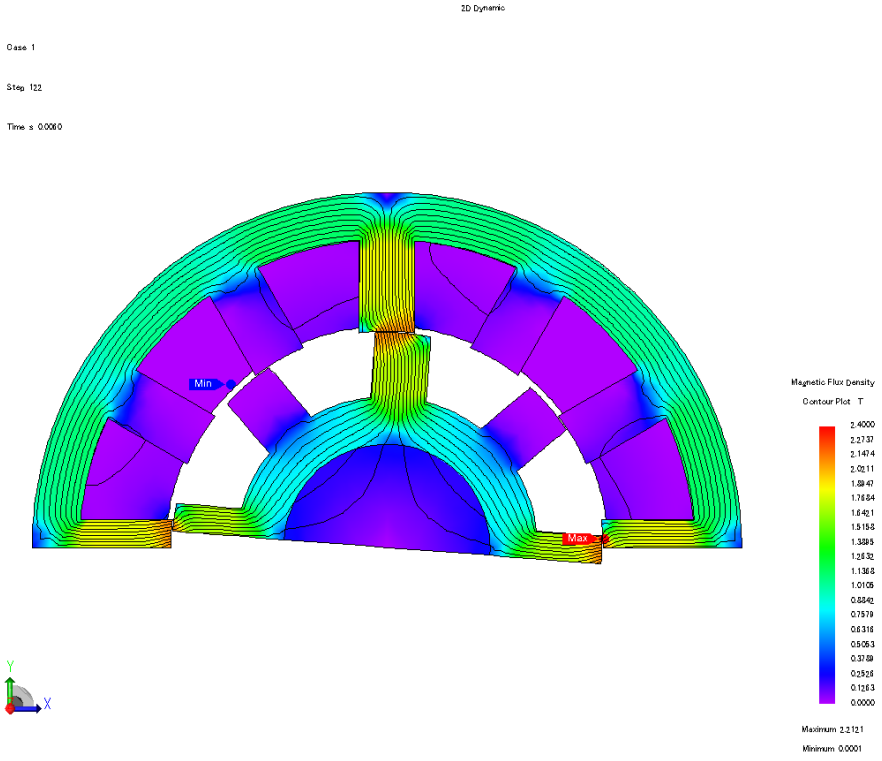

Figure B.12: Flux density and flux line of the 2D 12/8 CON FP model

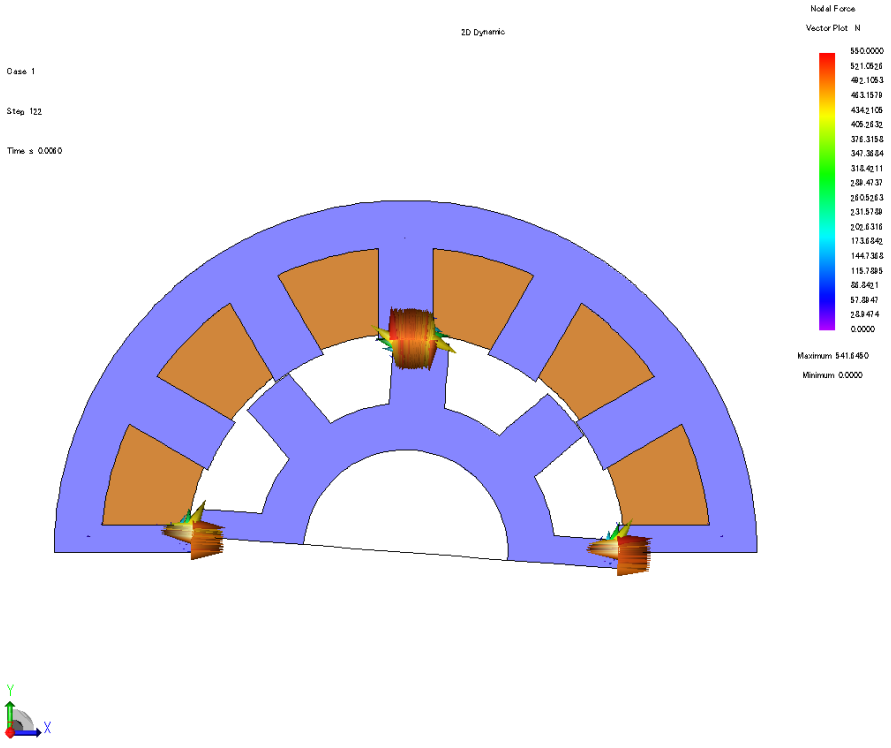

Figure B.13: Magnetic force distribution of the 2D 12/8 CON FP model

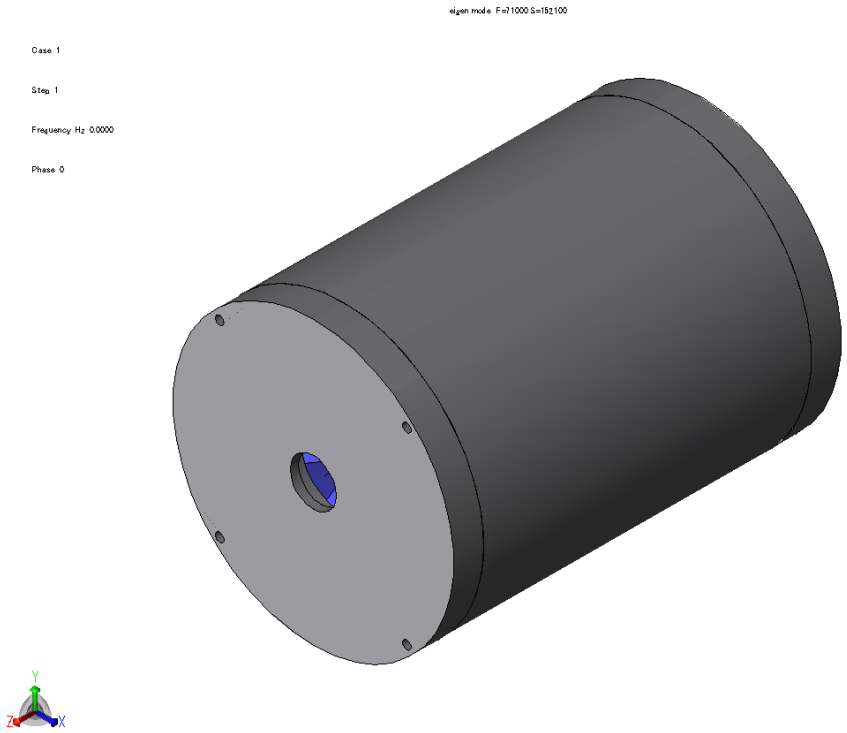

Figure B.14: Frame of the 3D 12/8 CON FP model

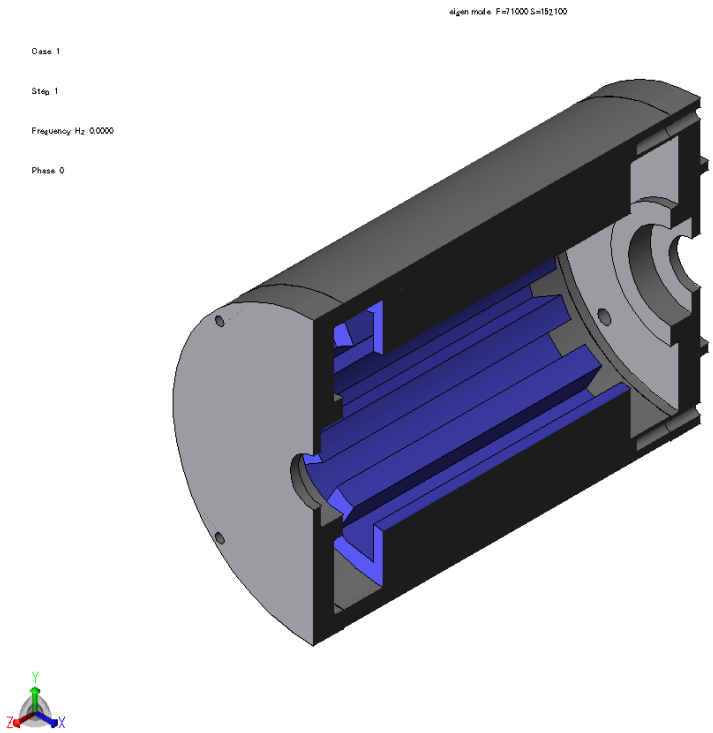

Figure B.15: Cross-section of the 3D 12/8 CON FP (frame and stator) model

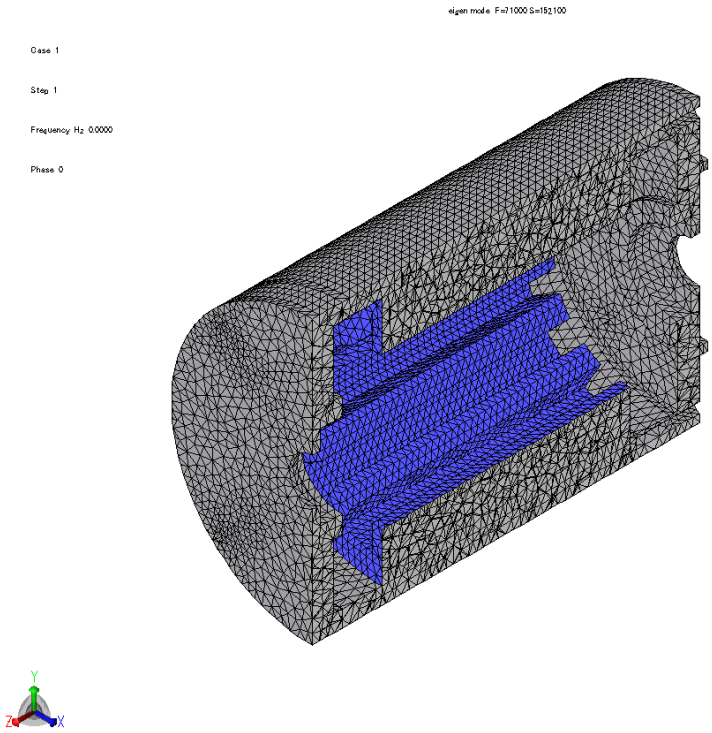

Figure B.16: Meshing of the 3D 12/8 CON FP (frame and stator) model

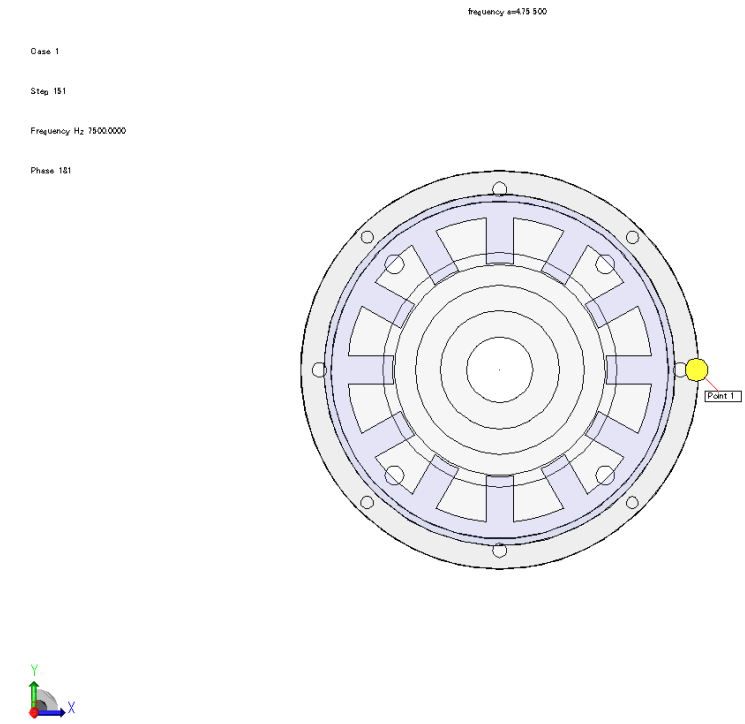

Figure B.17: Probing point of acceleration of the 3D 12/8 CON FP model

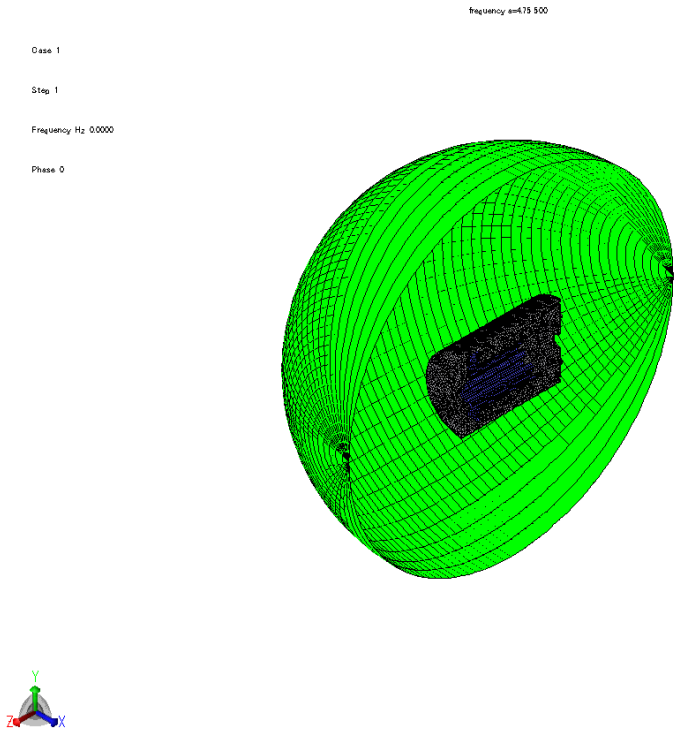

Figure B.18: Meshing for sound pressure analysis of the 3D 12/8 CON FP model

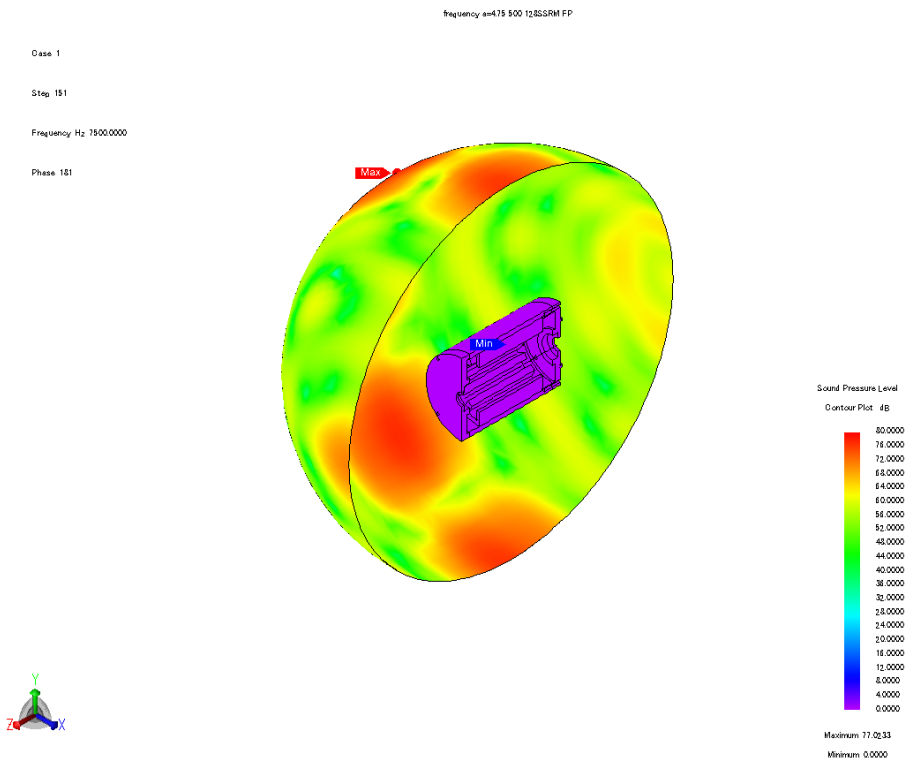

Figure B.19: Sound pressure distribution of the 3D 12/8 CON FP model

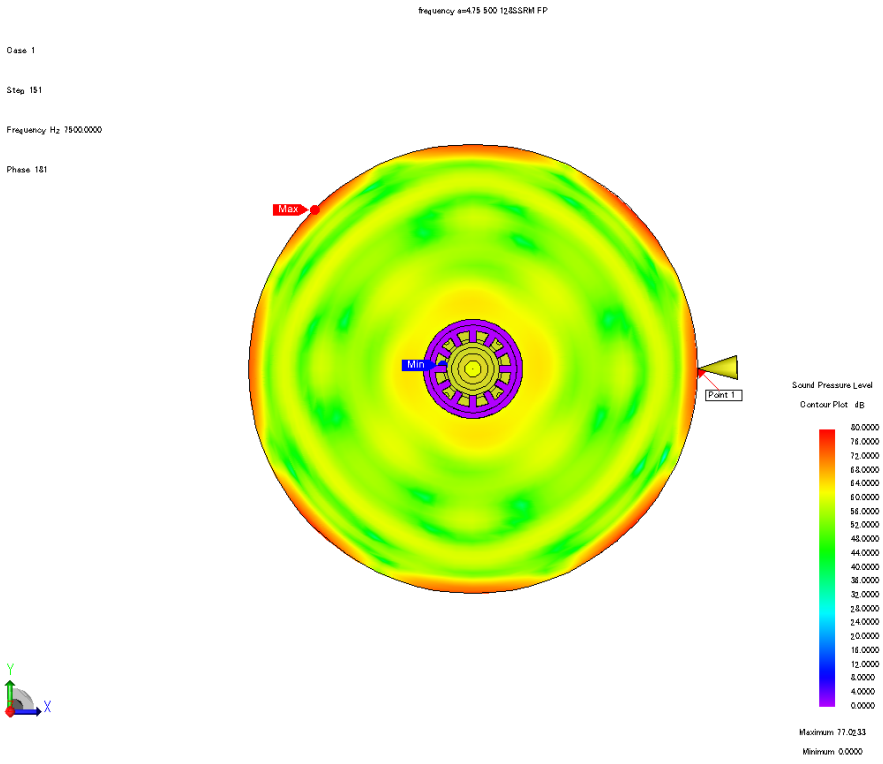

Figure B.20: Probing point of sound pressure level of the 3D 12/8 CON FP model

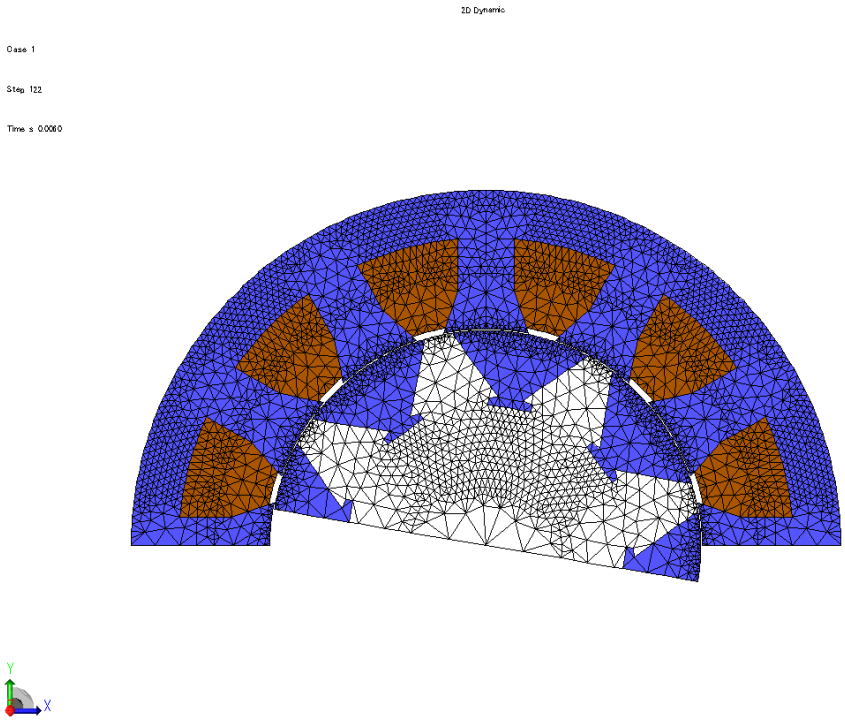

Figure B.21: Meshing of the 2D 12/8 SSRM model

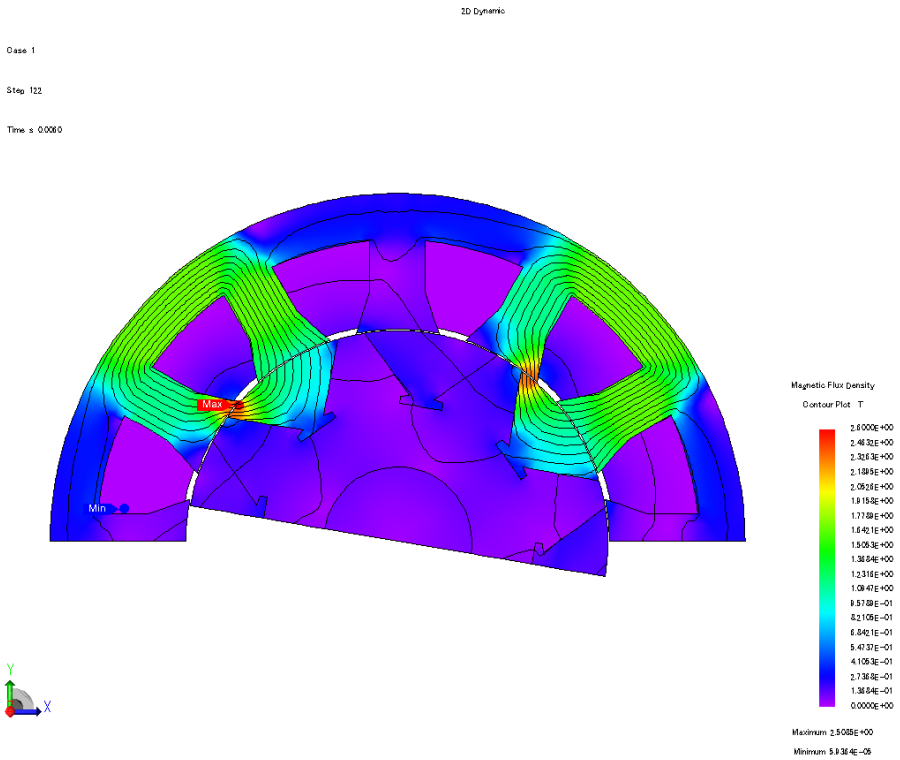

Figure B.22: Flux density and flux line of the 2D 12/8 SSRM model

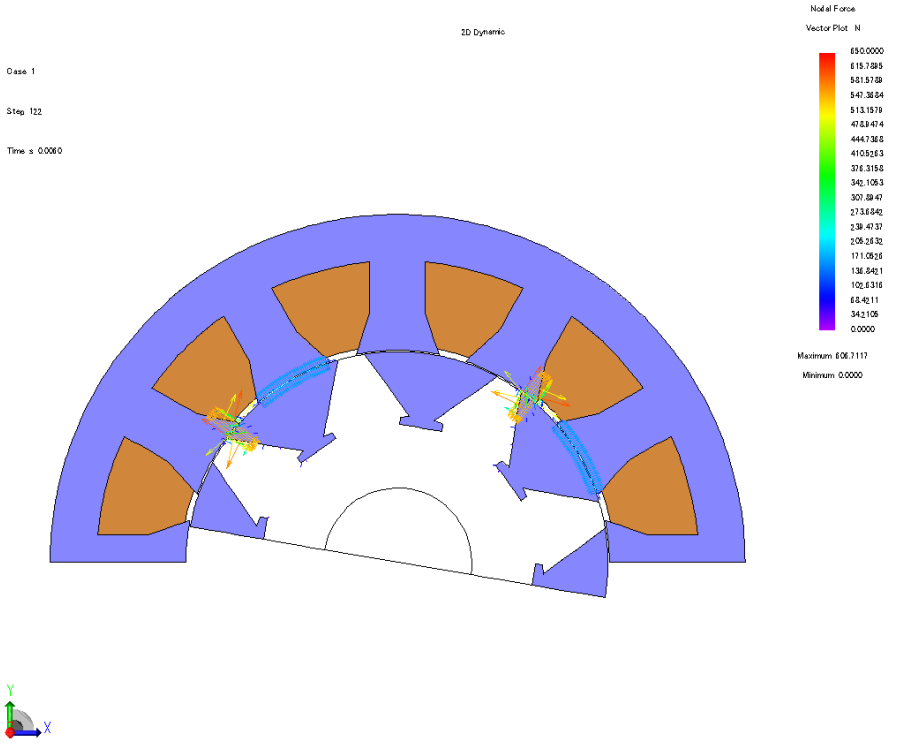

Figure B.23: Magnetic force distribution of the 2D 12/8 SSRM model

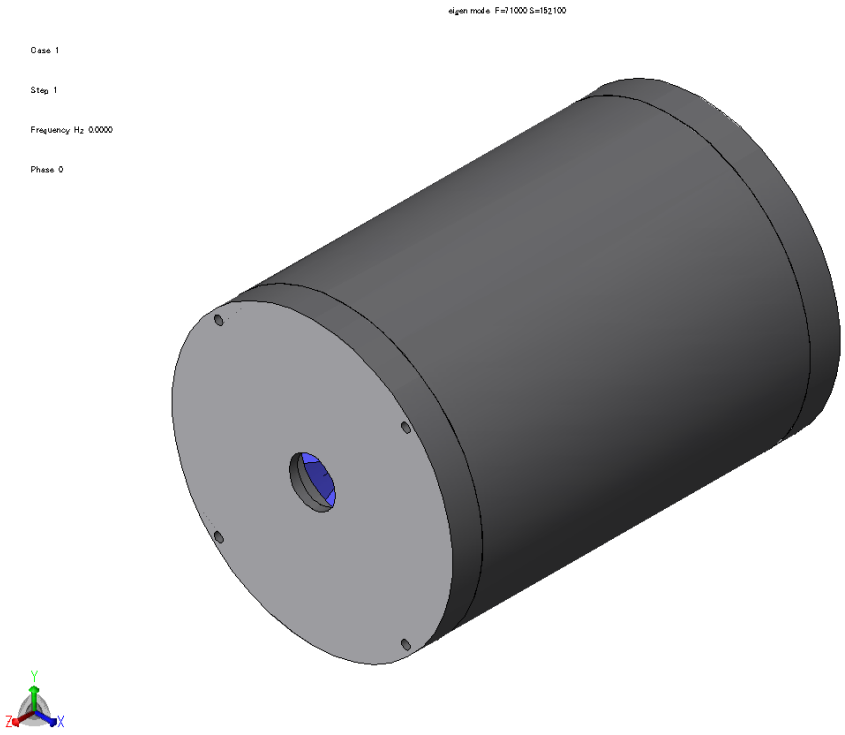

Figure B.24: Frame of the 3D 12/8 SSRM model

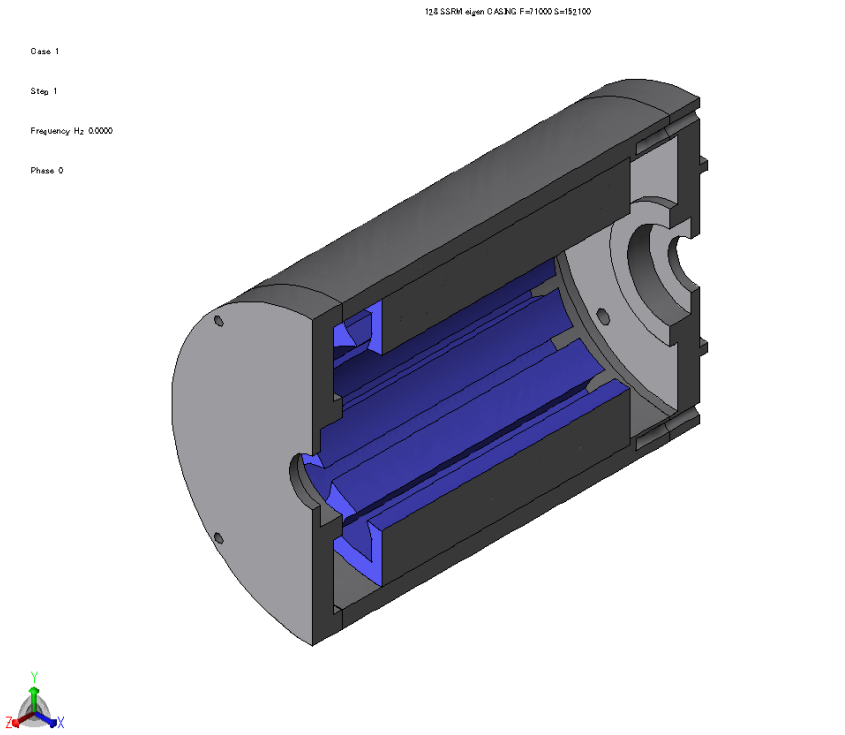

Figure B.25: Cross-section of the 3D 12/8 SSRM (frame and stator) model

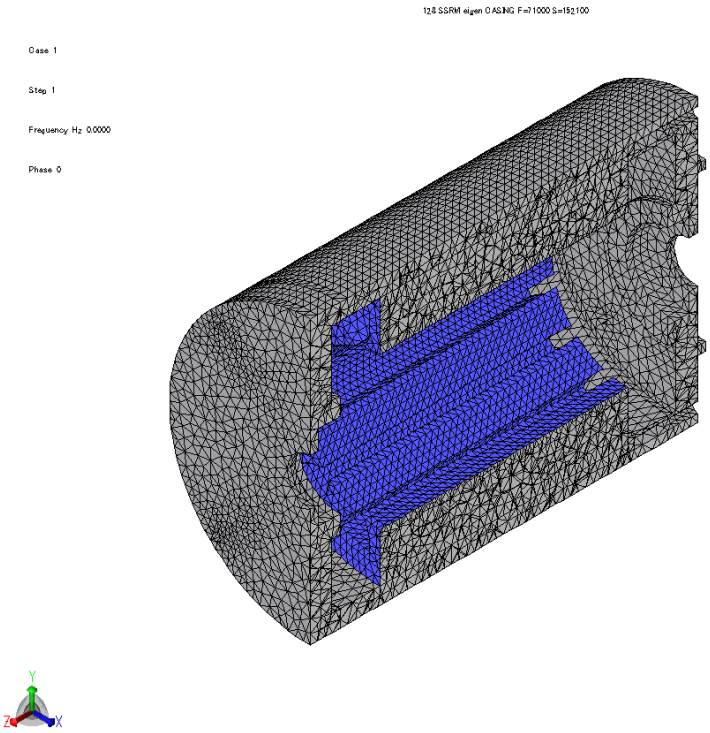

Figure B.26: Meshing of the 3D 12/8 SSRM (frame and stator) model

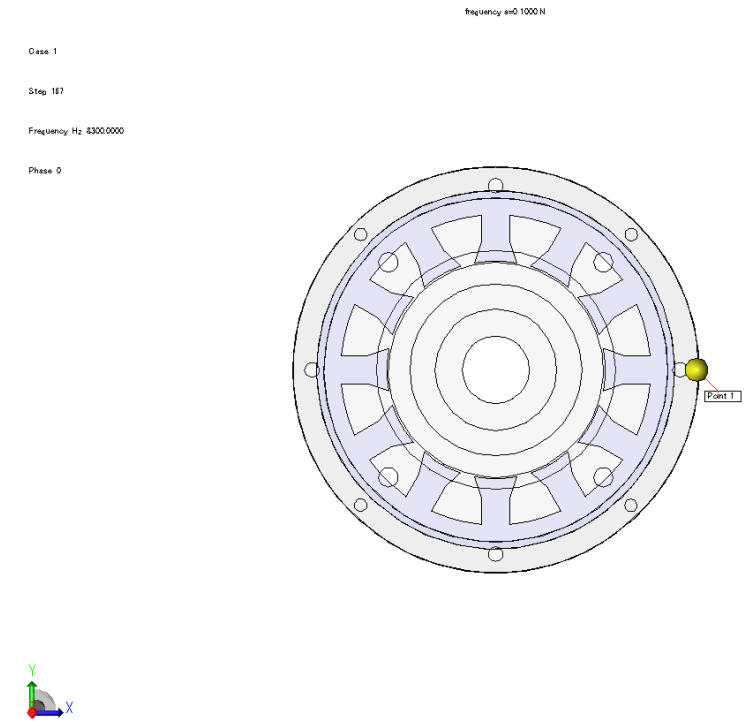

Figure B.27: Probing point of acceleration of the 3D 12/8 SSRM model

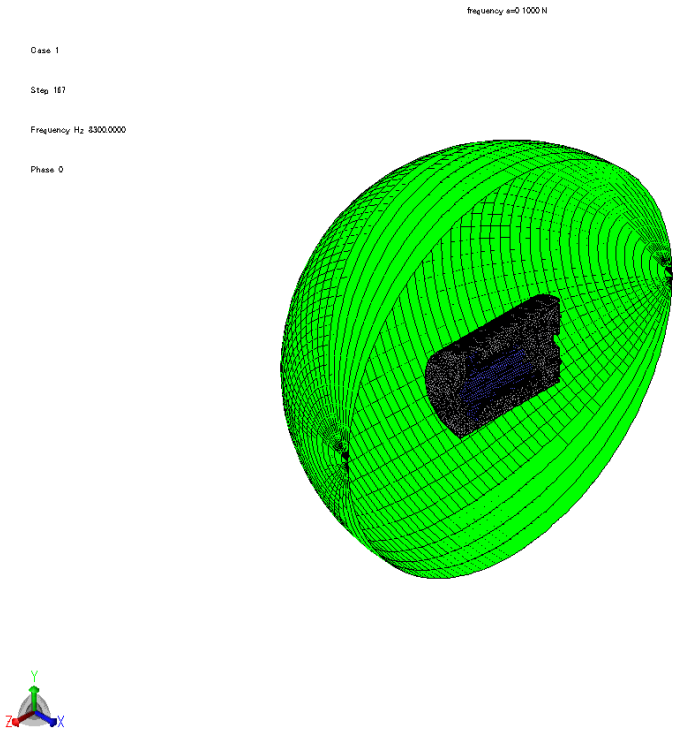

Figure B.28: Meshing for sound pressure analysis of the 3D 12/8 SSRM model

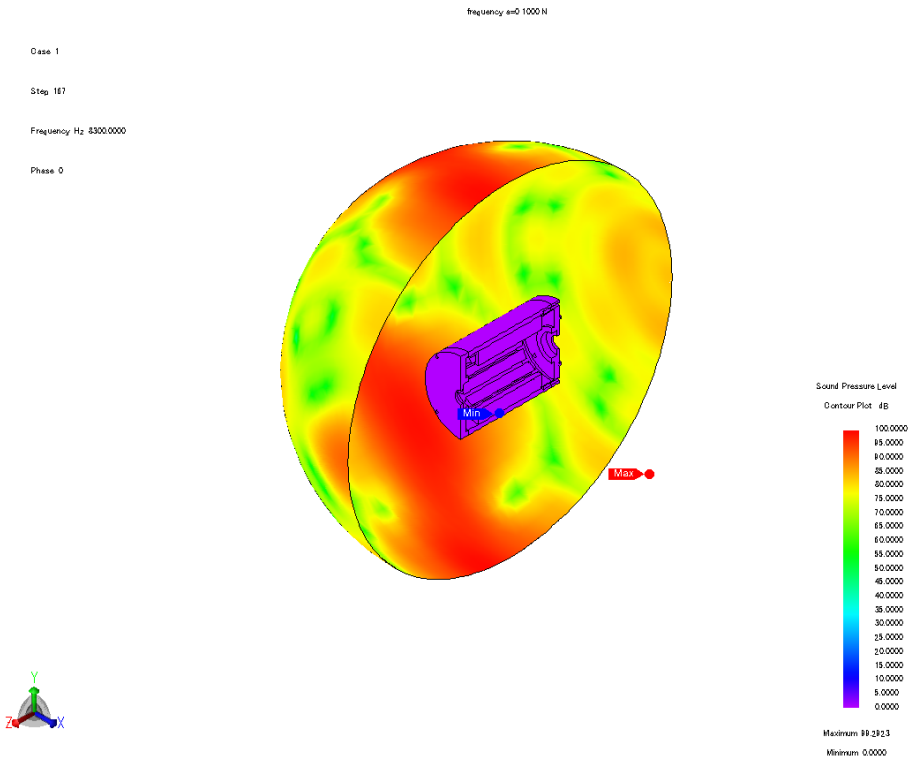

Figure B.29: Sound pressure distribution of the 3D 12/8 SSRM model

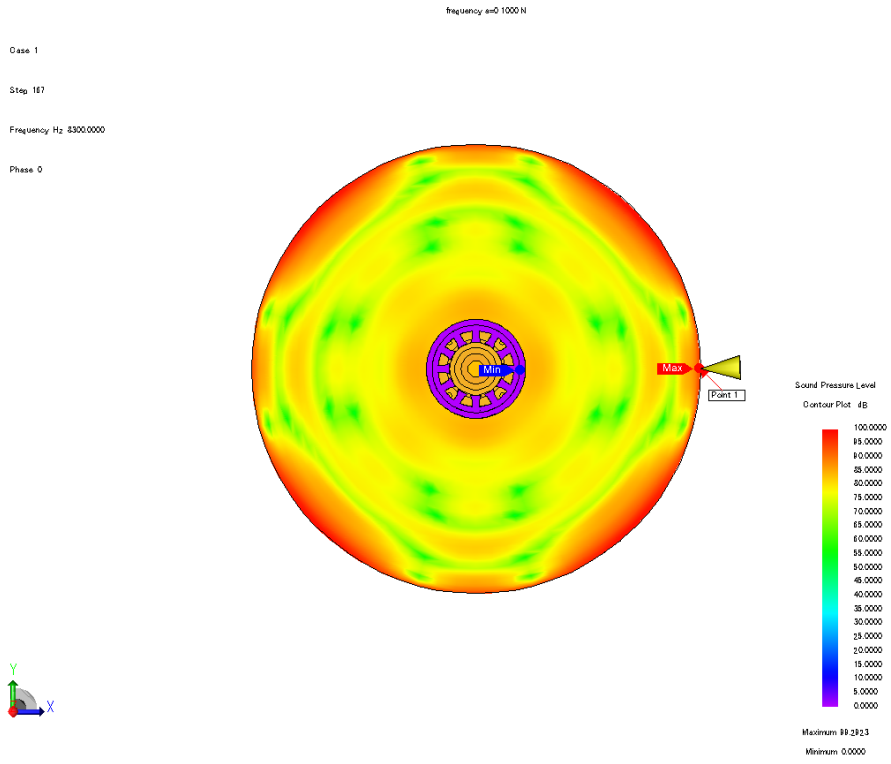

Figure B.30: Probing point of sound pressure level of the 3D 12/8 SSRM model

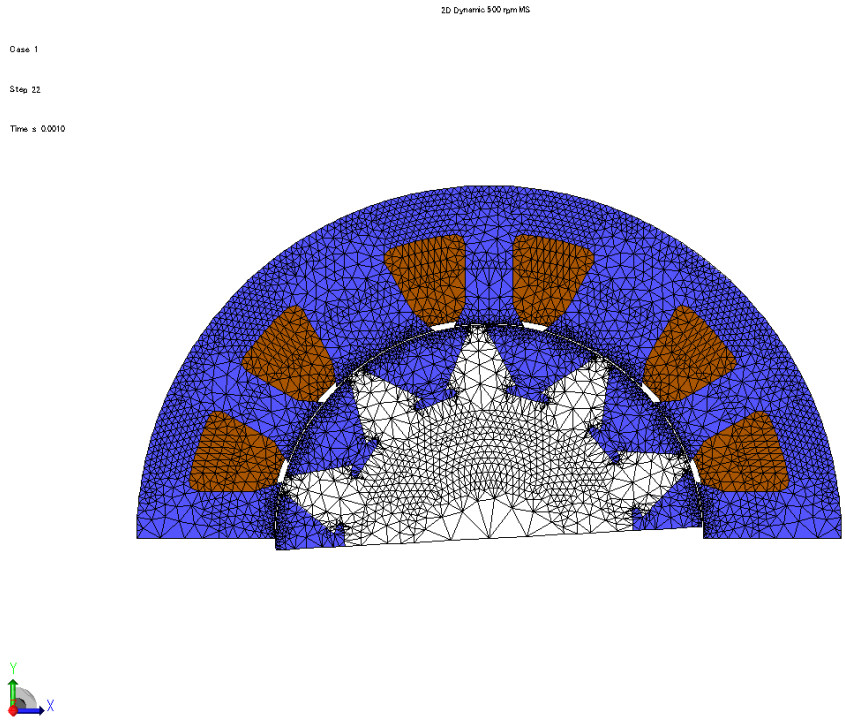

Figure B.31: Meshing of the 2D 12/10 SSRM model

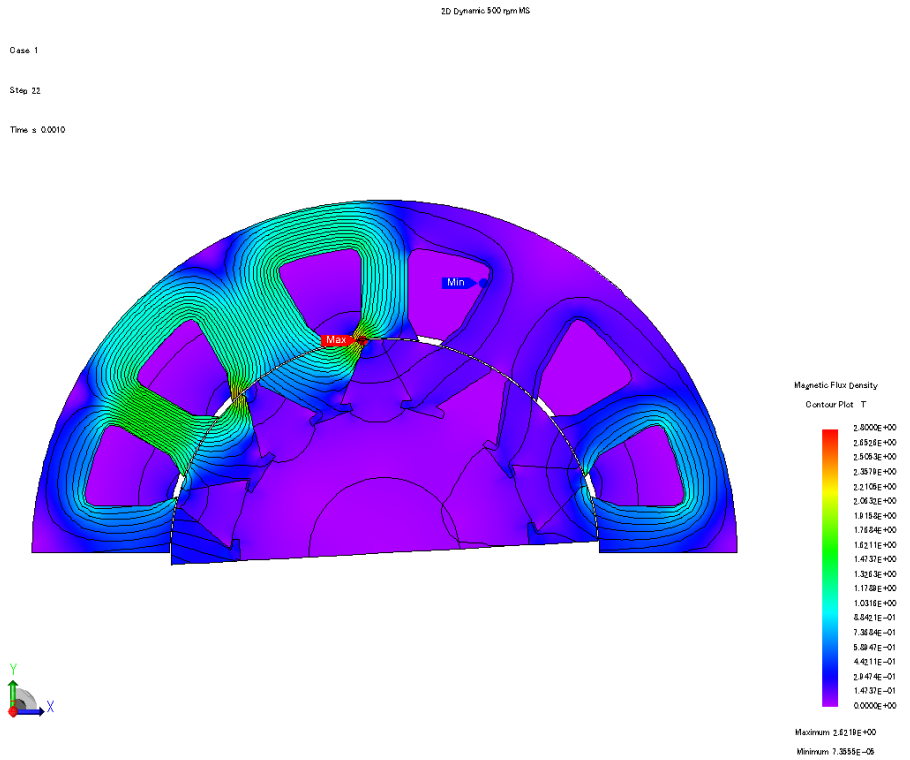

Figure B.32: Flux density and flux line of the 2D 12/10 SSRM model

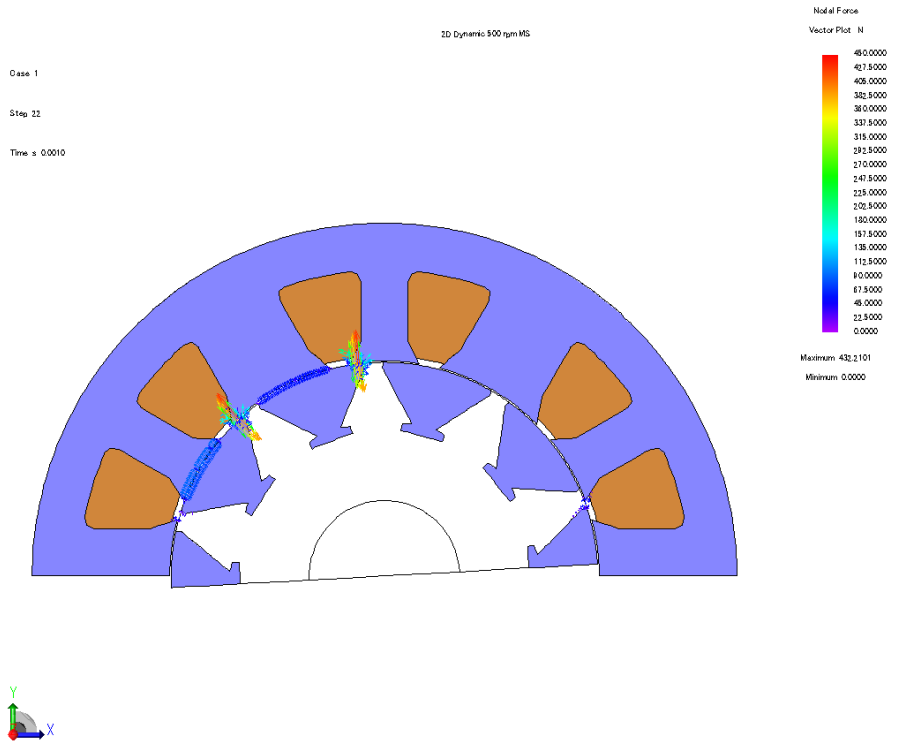

Figure B.33: Magnetic force distribution of the 2D 12/10 SSRM model

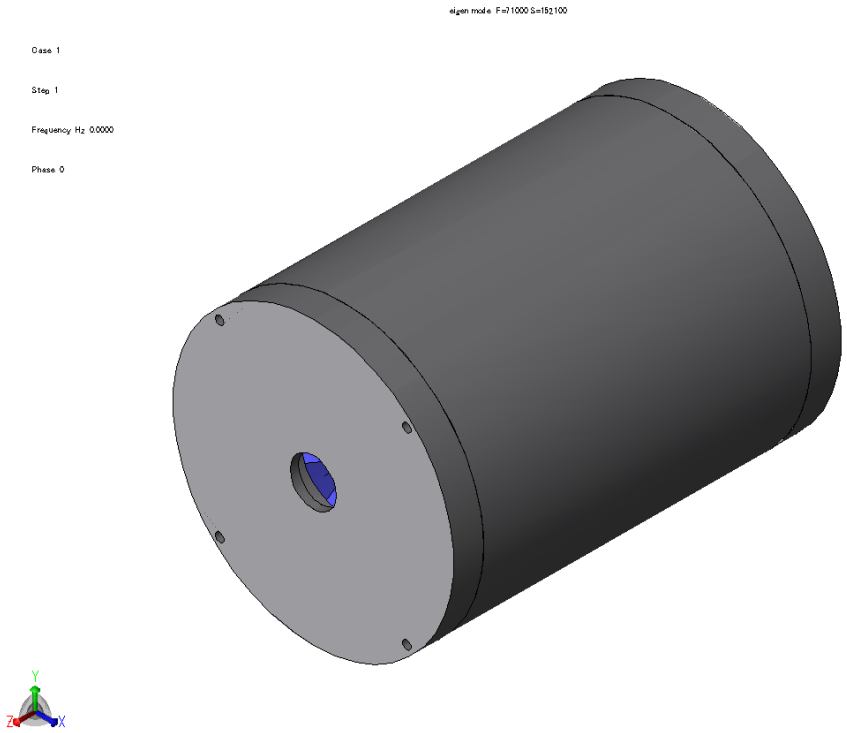

Figure B.34: Frame of the 3D 12/10 SSRM model

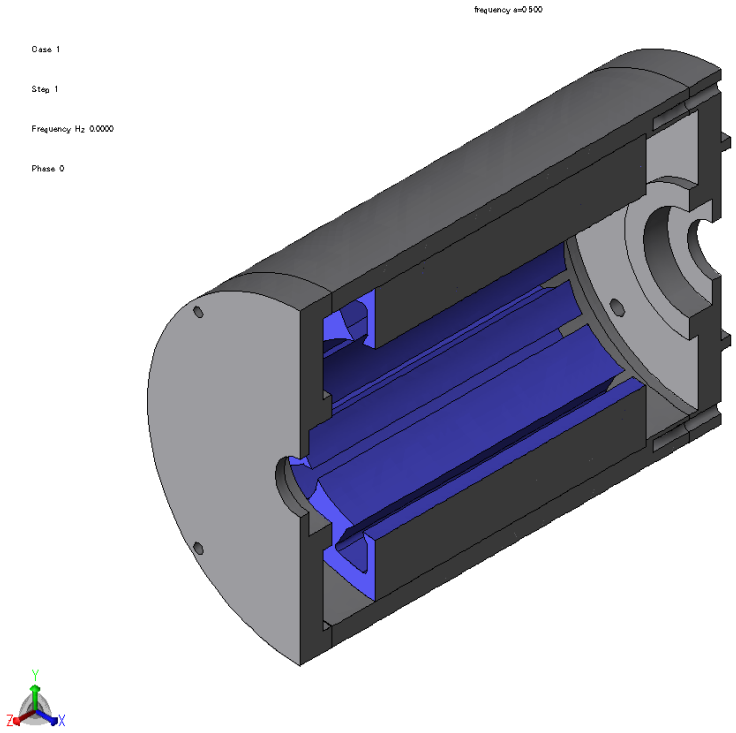

Figure B.35: Cross-section of the 3D 12/10 SSRM (frame and stator) model

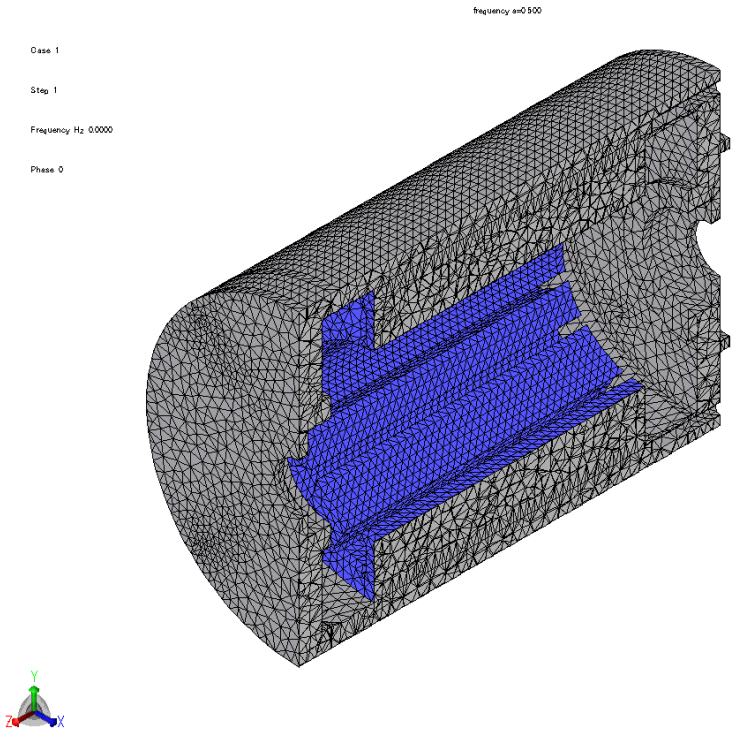

Figure B.36: Meshing of the 3D 12/10 SSRM (frame and stator) model

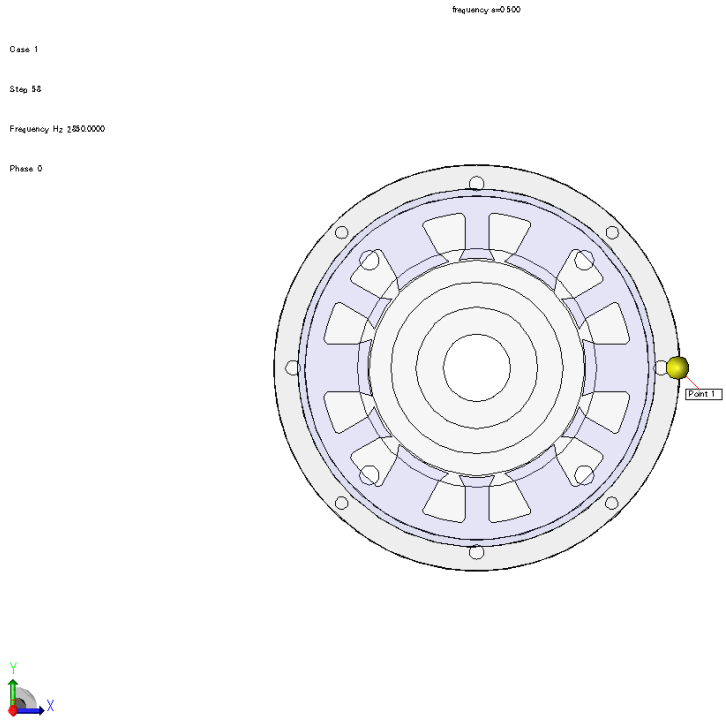

Figure B.37: Probing point of acceleration of the 3D 12/10 SSRM model

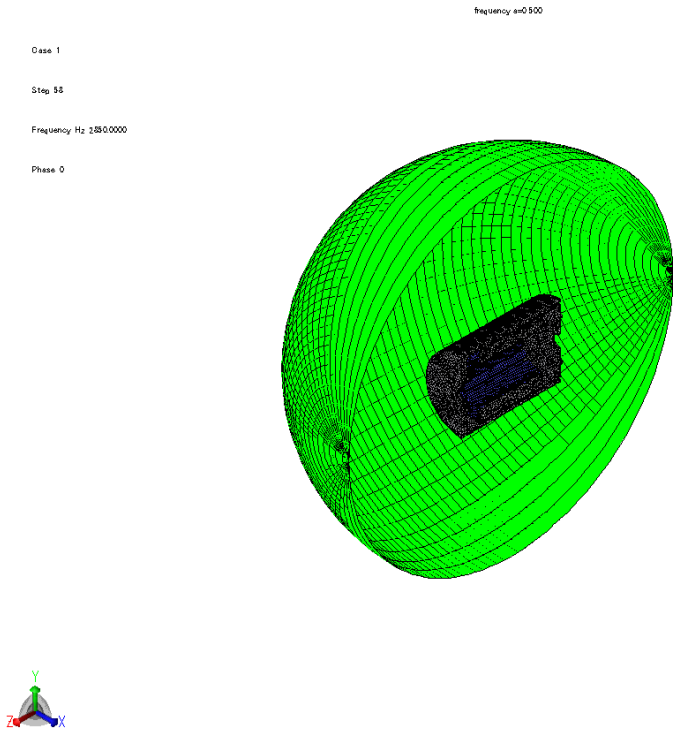

Figure B.38: Meshing for sound pressure analysis of the 3D 12/10 SSRM model

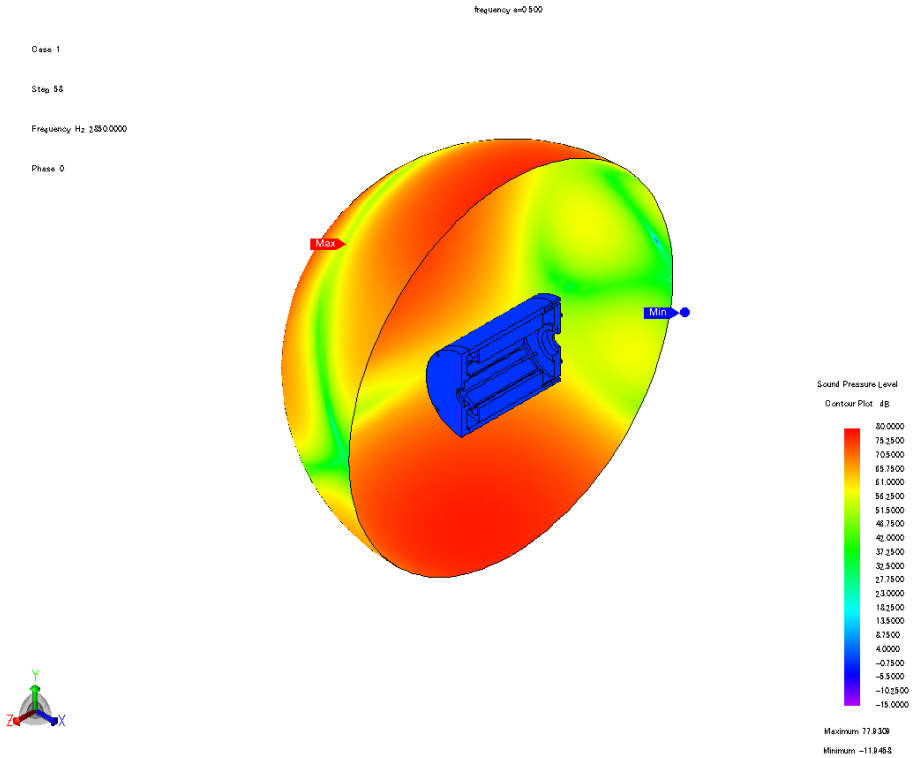

Figure B.39: Sound pressure distribution of the 3D 12/10 SSRM model

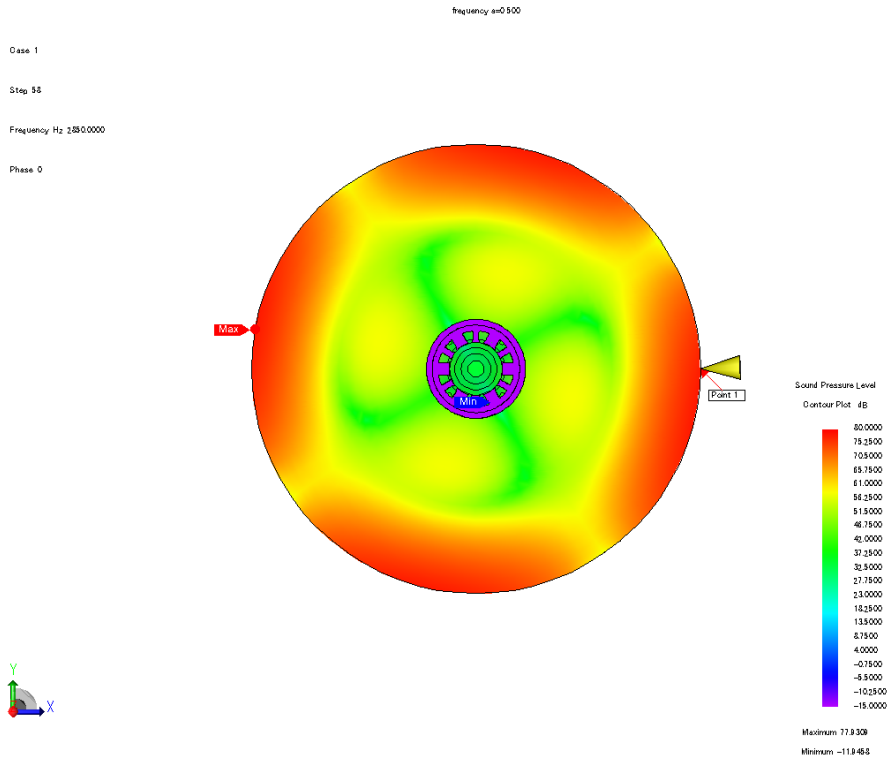

Figure B.40: Probing point of sound pressure level of the 3D 12/10 SSRM model

Appendix C.
Extended Results of Chapter 4

C.1 Simulation Models

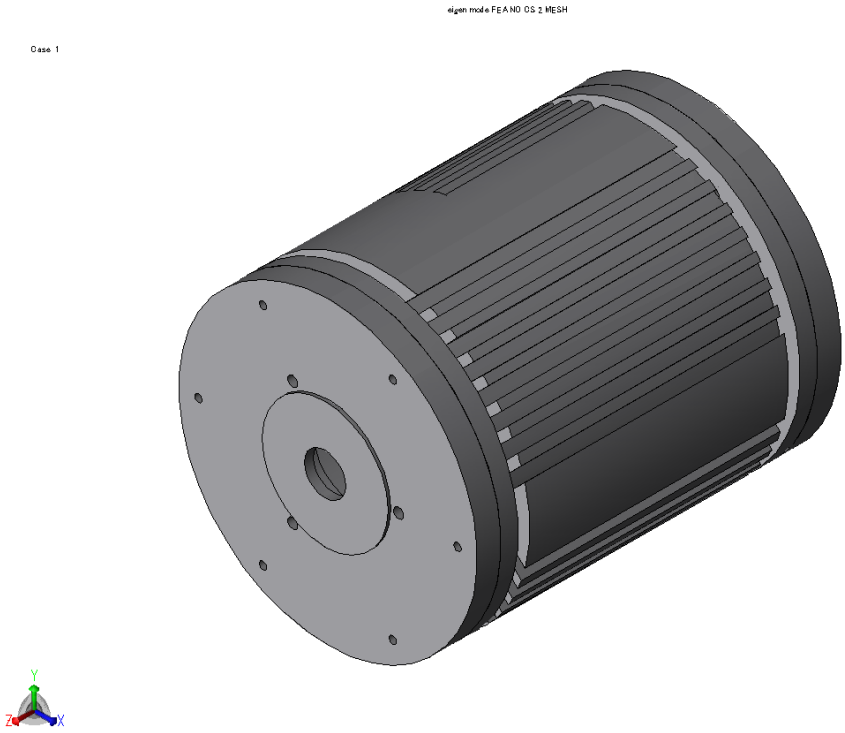

Figure C.1: Frame of the 3D 12/10 SSRM model

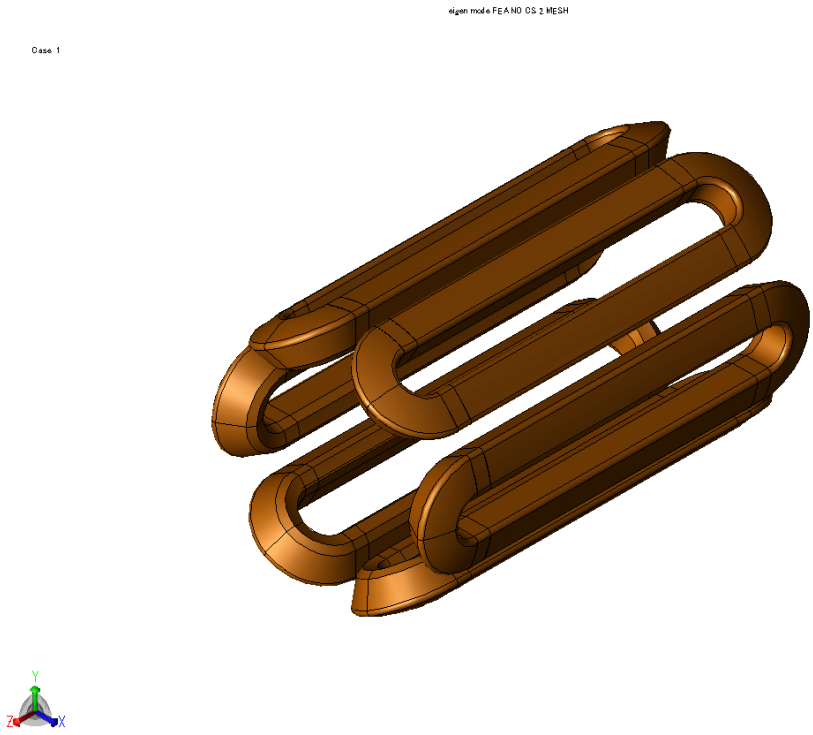

Figure C.2: Coils of the 3D 12/10 SSRM model

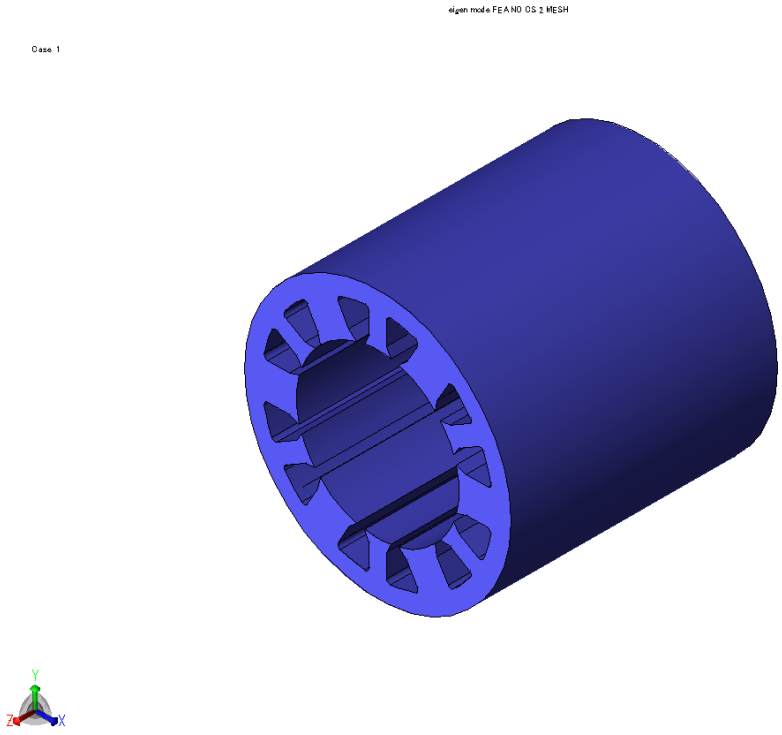

Figure C.3: Stator core of the 3D 12/10 SSRM model

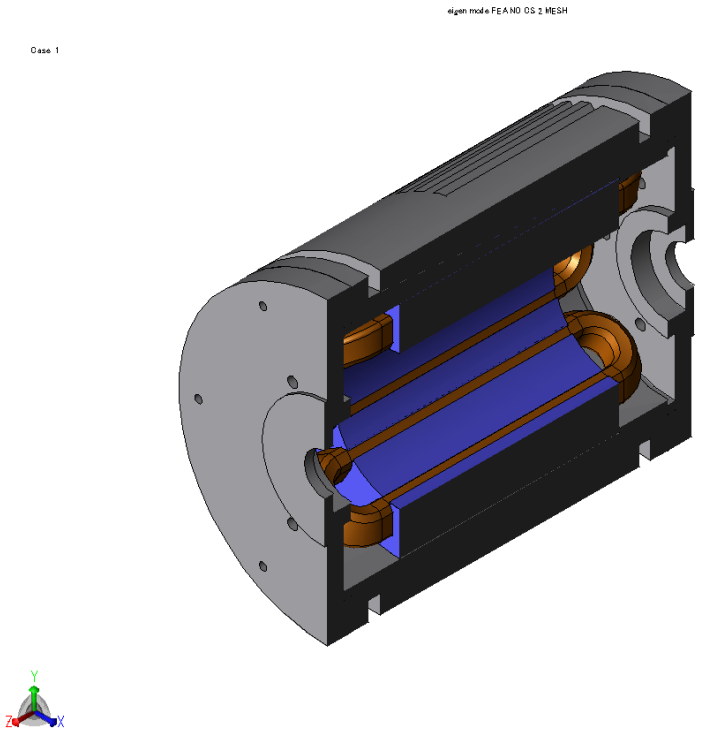

Figure C.4: Cross-section of the 3D 12/10 SSRM model (frame, coils, and stator)

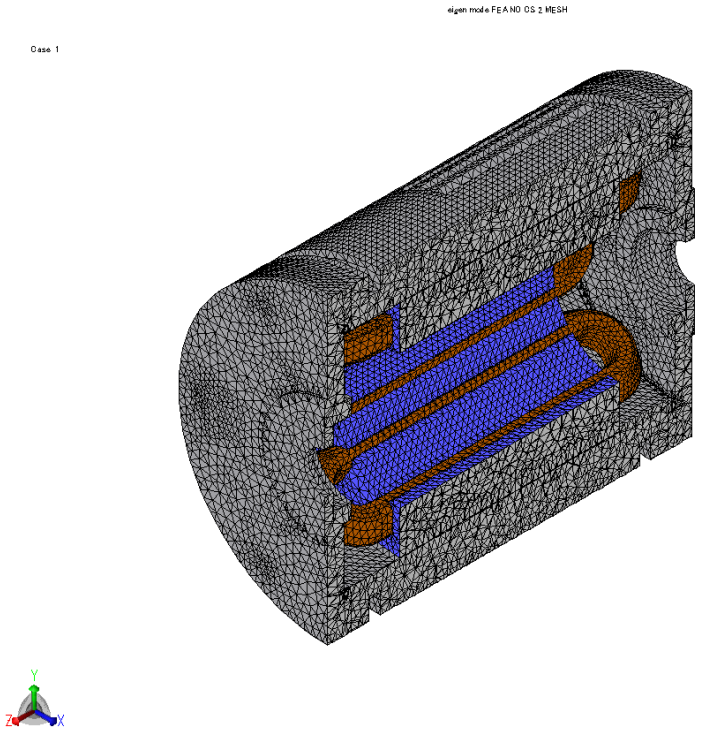

Figure C.5: Meshing of the 3D 12/10 SSRM model (frame, coils, and stator)

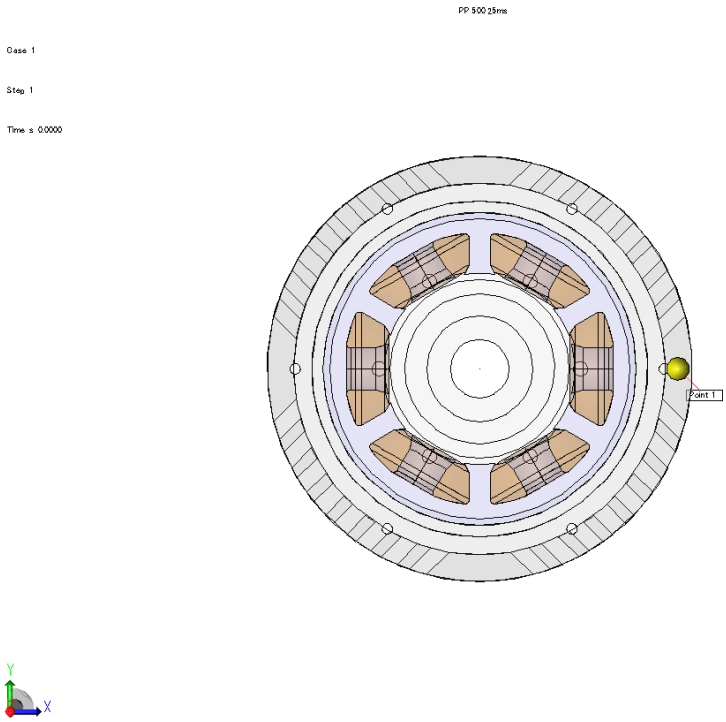

Figure C.6: Probing point of acceleration of the 3D 12/10 SSRM model (frame, coils, and stator)

Appendix D. Extended Results of Chapter 6

D.1 Experimental Results of Temperature Test

Table D.1: The resonant frequency of the stator M1, M2, M3, and M4 model at different temperatures

Temperature [°C]	Resonant frequency [Hz]			
	M1@60μm	M2@100μm	M3@60μm	M4@60μm
20	2256.7	2120.3	2057.3	1863.6
30	2249.4	2097.8	1999.5	1791.2
40	2241.2	2069.7	1905.1	1636.6
50	2231.5	2032.5	1767.6	1496.6
60	2211.1	1986.7	1559.2	1268.7
70	2185.9	1912.8	1359.9	1062.0

Table D.2: The resonant frequency of the stator M5, M6, M7, and M6 NEW model at different temperatures

Temperature [°C]	Resonant frequency [Hz]			
	M5@60μm	M6@60μm	M7@60μm	M6 NEW@60μm
20	1268.7	1000.1	2096.4	1005.9
30	1014.8	950.5	2041.0	975.8
40	699.1	900.1	1946.6	931.0
50	522.5	829.3	1836.8	884.6
60	437.0	712.9	1679.7	806.48
70	373.5	544.4	1479.5	637.2

Table D.3: The modal damping ratio of the stator M1, M2, M3, and M4 model at different temperatures

Temperature [°C]	Resonant frequency [Hz]			
	M1@60μm	M2@100μm	M3@60μm	M4@60μm
20	0.0013	0.0019	0.0037	0.0072
30	0.0014	0.0021	0.0052	0.0079
40	0.0016	0.0024	0.0079	0.0085
50	0.0018	0.0032	0.0097	0.0120
60	0.0019	0.0036	0.0141	0.0210
70	0.0024	0.0047	0.0195	0.0243

Table D.4: The modal damping ratio of the stator M5, M6, M7, and M6 NEW model at different temperatures

Temperature [°C]	Resonant frequency [Hz]			
	M5@60μm	M6@60μm	M7@60μm	M6 NEW@60μm
20	0.0204	0.0062	0.0018	0.0056
30	0.0375	0.0074	0.0020	0.0085
40	0.0491	0.0100	0.0034	0.0110
50	0.0512	0.0126	0.0051	0.0115
60	0.0530	0.0200	0.0075	0.0195
70	0.0653	0.0404	0.0118	0.0377